Location, Location, Location: Insights from Spatially-Resolved Observations of Marine Seep Carbonate Ecosystems and Carbonaceous Chondrite Surfaces

Thesis by

Sergio Alexander Parra

In Partial Fulfillment of the Requirements for
the Degree of
Doctor of Philosophy in Geobiology

CALIFORNIA INSTITUTE OF TECHNOLOGY
Pasadena, California

2025
(Defended December 4th, 2024)

Sergio Alexander Parra
ORCID: 0000-0002-2637-7960

...But, beneath the waves,
there are many dominions yet to be visited,
and kingdoms to be discovered;
and he who venturously brings up from the abyss
enough of their inhabitants to display
the physiognomy of the country,
will taste that cup of delight,
the sweetness of whose draught
those only who have made a discovery know.

- E. Forbes,
  The Natural History of the European Seas (1859)

ACKNOWLEDGEMENTS

This work would not have been possible if my thesis advisor, Dr. Victoria Orphan, had not taken a chance on a freshly-graduated chemical engineer with a newly discovered passion for research in earth and planetary sciences. Over 6.5 years, it has been a privilege to be a member of her laboratory and leverage the wide array of amazing tools she has skillfully collected to tackle questions in marine microbial ecology. I have learned much from her, including how to pitch my science, find collaborations in unexpected places, and foster a supportive and inclusive workplace.

In this, I am especially lucky, for the members of the Orphan Lab can each claim a part in shaping the problem-solver I've become. I am eternally grateful to them for their lessons, patience, and availability. I thank Daan Speth, for allowing me to be his barnacle when I was still a newbie and sharing many belly laughs that kept me floating when things got tough. My thanks also to Kriti Sharma, for sharing her microscopy secrets and poetic insights into the human condition with the same twinkle in her eyes. I thank Magdi Mayr, for joining me on our "land cruises" as we sawed rocks in a forgotten sub-basement for days, in addition to her generous time in guiding my work and reviewing several of the chapters in this thesis. I also thank Dan Utter, for always making the time to share his measured and careful opinions on everything from phylogenetics to writing manuscripts (including Chapter 2!). And of course, I am ever grateful to Stephanie Connon, for sharing the deep well of wisdom and expertise in everything from protocols to labware that only comes with managing a successful laboratory for many years. I also thank her for taking care of us at all times — keeping the lights on and instruments working, bringing snacks to stress-eat, and even making us her famous seasonal candles. There are so many other names and faces that made the lab a stronghold of support and a reliable source of laughter: Sujung Lim, Fran Martinez, Ranjani Murali, Aditi Narayanan, Manet Peña Salinas, Alon Philosof, Haley Sapers, and Rebecca Wipfler among so many wonderful people, thank you. Where it once might've been terrifying to swim in the open ocean of life in research, being an Orphan labbie taught me how to surf.

I was also privileged to moonlight as a spectroscopist under the auspices of Dr. Bethany Ehlmann. While my work in geobiology took the main stage, it was a privilege to collaborate on a project with the world-renown planetary scientist I'd looked up to before I came to Caltech. Beyond how to divine minerals from squiggly lines on a graph, she taught me how to identify and focus on the important details, as well as how to move quickly and decisively. I thank her for making the time to point me in the right directions and even looking out for me as I sought out a different professional direction outside of academia. Though brief, I cherished my time in the

Ehlman Lab and all its amazing people that taught me so much about how we study the worlds beyond our own. I thank Rebecca Greenberger, first for keeping an eye out on me as I wrangled the spectrometer at NASA's Jet Propulsion Laboratory, but also for her analytical eye, helpful tips, and many wonderful conversations. I am indebted to her for her patience as we troubleshooted data on/off for several years. She always knew when to check in and make sure I was doing alright. I am also especially grateful to Eva Scheller (who is now a professor of her own!) for her years of friendship and conversation in the Ehlmann Lab.

Of course, I am also grateful to the rest of my thesis advisory committee. My thanks to Dr. Woody Fischer, for his contagious excitement about a wide array of topics in geobiology and his confidence in my ability to finish this degree. Being his teaching assistant was a joy, and I'll miss our instructional trips to Death Valley. I'd also like to thank Dr. Christof Meile at the University of Georgia, for his kind support and enthusiasm as I tackled a multi-year project that was far more ambitious than I could have predicted.

I'd be remiss not to also honor the teachers and mentors who played critical roles in nurturing my curiosity and shaping my work ethic in science, even before I set foot on campus at Caltech. I am especially grateful to Dr. Sarah Milkovich, who gave me the chance to Dare Mighty Things at JPL and be in the same room with the folks exploring the Martian surface. I also thank Dr. James Wray, who took a chance on a chemical engineering student at Georgia Tech with no research background and let him mess around with satellite spectra from Mars. My thanks also to Dr. William Whitman at the University of Georgia, for entertaining a high-schooler's cold email and setting me on a winding path to environmental science. Of course, I must also thank Tim Harbin, who first sparked my love of microbiology in high school and whose back room I took over for my first science fair project studying methanogens in pond sediments. I'm also thankful to Greg Marr, Scott Mitchell, and Janna Penn, who challenged me constantly and helped me achieve more than I thought I could. And last but not least I thank Dr. David Pauli, whose instruction first drove me to pursue higher education in science. This thesis exists because of you all.

My trajectory at Caltech was not what I had planned when I showed up to the basement offices for the first-years in 2018, also known as the "Pit". There, I made friendships that feel like they were iron-forged in the trials and triumphs that we experienced as Ph.D. hopefuls. I am forever grateful I met Elliott Mueller, Philip Woods, Makayla Betts, Xenia Boyes, Emily Miaou, Juliet Ryan-Davis, and Shaelyn Silverman. Together, they taught me to believe in myself as a scientist and were a constant reminder that I was never alone. We also laughed a lot. *A LOT*. I can't wait to laugh again with them in the years to come. In particular, I express my gratitude for the close friendship of Elliott Mueller. Over the years, I've admired his constant drive, sharp wit, and incredible thoughtfulness. I look forward to more shared adventures.

I also am deeply grateful to other dear (doctor!) friends — Gillian Kyne, James Tuttle Keane and James Haber especially — for their encouragement and friendship, even from afar. I finally did it, guys!

More personally, I would like to thank my partner, Jake. 5 years ago, I watched and learned as he walked down this very road and earned his Ph.D. Since then, through the wild chaos of a global pandemic, elections, and general uncertainty in life, he has been an unwavering source of love, strength, comfort, and laughter that I would not trade for the world. Life is sweeter and more colorful with him, and I am ever a better man for it.

Finally, I could not have gotten to this point in my life without the undying love and support of my family. Despite the separation of 3 time zones and a completely unfamiliar field of study, they have not once doubted in my success, and I owe much of who I am today to them. I would not be here without my sister (and now also graduate student!), Ayleen, who has been my constant cheerleader since I was 2.5 years old. She inspires me *every day* with her fierce determination, intelligence, and heart for service.

I am also ever grateful to my mother, Aylen, from whom I inherited my pragmatism and sharp sense of humor that have saved me many a time. She, too, has been a source of inspiration as an immigrant who forged her own path as a brilliant and beloved teacher (with a Master's degree to boot!). Her prayers, hugs, meals, and frequent video calls were the wind beneath my wings. Her distinctly Latin mom-coded maxims were (and are!) the voice of reason in my mind. *Te amo muchísimo, mamá!*

And last but never least, I am grateful to my father, Sergio, to whom I ultimately dedicate this thesis. To write a proper thank you would require another thesis (and perhaps a memoir), but instead I view many, if not all, of my successes as a testament to his immense role in my life. Beyond the trials that come with immigration to a new country with a foreign language, he was the first of his family to graduate from college and the first to get a Ph.D. Year after year, I watched him make innumerable sacrifices to build a better life for himself and my family — never without a smile. In this, he was my first teacher. It is from him that I get my excitement to learn new things. It is from him I learned attention to detail, precision, and organization. It is from him I that first learned to believe in myself. It is from him that I learned that anything I did, I should do with all my heart and soul. I am forever indebted to him. *Gracias mil, papá, por todo.*

ABSTRACT

Spatially heterogeneous, multi-component systems are prevalent topics of study in geobiology and planetary science. However, previous studies of these systems often represent limited measurements that abstract or separate the sample from its localized context, thereby obscuring or precluding insights into the drivers ultimately shaping these systems. This challenge motivates the work presented in this thesis, where we provide an extensive and spatially-resolved examination of two complex, heterogeneous systems in geobiology and planetary science: marine seep carbonates and carbonaceous chondrite surfaces, respectively. In marine seep systems worldwide, seep carbonates are a mineral byproduct of a microbial metabolism (the anaerobic oxidation of methane, or AOM) and can continue hosting metabolically active microbial communities, including methane-oxidizing microbes. However, much of our understanding of these endolithic microbial communities stems from bulk, centimeter-scale evaluations of microbial identity and/or metabolic activity across a limited number of samples. As such, the range of structural and environmental conditions that ultimately shape the degree and extent of microbial activity in seep carbonates, including AOM, remains relatively under-constrained. To address this gap, Chapters 1-3 investigate carbonate-hosted microbial communities at a methane seep site in Santa Monica. In Chapter 1, we explore carbonate 'nodules' from methane seep sediments at and below the sulfate-methane transition zone (SMTZ), analyzing their mineral composition, internal structures, and hosted microbial communities compared to their host sediment communities and porewater chemistry. We also discuss key implications of the connectivity of seep sediments to nodules over geologic timescales and the preservation of microbial 'thumbprints'. Chapter 2 describes rare tripartite associations between two groups of anaerobic methanotrophic archaea (ANME-1 and ANME-2) and a bacterial partner within seep carbonate crusts and other substrates at the seafloor, with implications towards understudied diversity in the syntrophic interactions governing AOM beyond seep carbonates. Chapter 3 examines the impact of seep carbonate internal

structure on endolithic communities from various carbonate crusts, revealing similarities and differences between surface and interior communities that may reflect the importance of pore networks in maintaining favorable local environments. In Chapter 4, we pivot to an extensive analysis of spectra from carbonaceous chondrite surfaces. Carbonaceous chondrites (CCs) are a group of meteorites that represent the oldest materials in the solar system, whose mineralogy preserves a record of early alteration processes thought to be shared with certain asteroids. However, most studies connecting specific CCs to specific asteroids have relied on spectroscopic measurements of bulk powder CCs, which are spatially unresolved and destroy textures, thereby hindering tying shared spectral features to particular phases, petrologic contexts, and alteration histories. As such, Chapter 4 presents an analysis of CCs measured using microimaging hyperspectral visible-and-shortwave-infrared (VSWIR) spectroscopy, where we capture chondrite surfaces features at high spatial resolution. We also compare CC spectral features with asteroids using the Expanded Bus-DeMeo taxonomy, which provides a systematic framework to examine and identify shared drivers of spectral diversity within this spectral range, including Fe-bearing minerals from both original and terrestrial alteration processes. Together, these studies emphasize the importance of spatially-resolved sampling across disciplines, specifically in geobiology and planetary science, thereby capturing and highlighting the heterogenous nature of key systems in these fields and bettering our understanding of the factors shaping them.

PUBLISHED CONTENT AND CONTRIBUTIONS

Parra, S. A., Mayr, M. J., Mullahoo, J., Quinn, L.K., Wipfler, R. L., Orphan, V. J., 2025. Diversity and single-cell activity of endolithic microbes in sediment-hosted carbonate nodules within and below the sulfate-methane transition zone. bioRxiv. https://doi.org/10.1101/2025.02.26.640391. Submitted to *ASM Journal of Applied and Environmental Microbiology*.

S. A. Parra helped conceptualize the study (with V.J.O.), acquired financial support for the study (with V.J.O.), processed and analyzed data presented in the study, including nodule selection, porewater sulfide measurements, DIC/δ^{13}C measurements, x-ray diffraction, DNA extraction, 16S rRNA sequence analyses, fluorescence microscopy, and BONCAT incubations. S. A. Parra also wrote the original draft and incorporated edits (from all authors) before and during the publication stage.

Parra, S. A., Greenberger, R. N., Ehlmann, B. L., 2025. Microimaging Spectroscopy of Carbonaceous Chondrites and a Comparison to the Spectral Diversity of Asteroids. Submitted to *AGU Journal of Geophysical Research: Planets*.

S. A. Parra helped conceptualize the study (with B.L.E.), acquired financial support for the study (with B.L.E.), selected carbonaceous chondrite samples, performed all imaging, coding, software pipeline validation, and data analysis (with support from R.N.G.). S. A. Parra also wrote the original draft and incorporated edits (from all authors) before and during the publication stage.

TABLE OF CONTENTS

LIST OF ILLUSTRATIONS

LIST OF TABLES

Introduction

Spatially heterogeneous systems necessitate spatially-resolved data sets

To understand the connective tissue between the chapters presented in this work, we first begin at the 10,000-ft view of current topics of study in geobiology and planetary sciences. While disparate at first glance (indeed, what does a microbe have to do with an asteroid?), many ongoing investigations in these fields ultimately strive to define and interpret a complex network of natural processes (e.g., cell metabolisms or rock weathering reactions) that all talk to, overlap, and overwrite each other to produce an observable subject (e.g., a microbial ecosystem or minerals on a rock surface). Geobiologists and planetary scientists study these subjects to piece together the intricate, integrated systems that made them and the ways these processes have shaped everything from a microscopic environment at the bottom of Earth's oceans to an entire solar system.

A persistent challenge in studying these subjects is that they are often spatially and/or temporally heterogeneous systems of their own, with diverse elements that can change over time. Depending on when, what part, and how much of the system is sampled, geobiologists and planetary scientists risk missing traces of certain natural processes that are essential to understanding the larger picture. In this work, we present case studies that target missing, or understudied parts of spatially heterogeneous systems in geobiology and planetary science. By expanding where and how closely we look at these systems, we are able to resolve the traces of natural processes that improve our understanding of these systems as a whole. We begin with the first example, by diving down to the seafloor…

Part I: Microbes work together to consume methane at the seafloor

Methane (CH_4) is the most abundant hydrocarbon in Earth's atmosphere and an important greenhouse gas informing ongoing dialogue in climate science. While it is only one of many forms carbon naturally takes, it is often the end result of biomass decay and is produced in many of the planet's natural systems, including coastal marine sediments (Dean et al., 2018). In marine sediments, however, much of this continuously generated methane is consumed by a microbially-mediated process known as the anaerobic oxidation of methane (AOM). In fact, this process, which converts methane to bicarbonate (HCO_3^-) in the absence of oxygen, is responsible for consuming 80-90% of subsurface-generated methane, an estimated 382.4×10^{12} g/yr worldwide (Reeburgh, 2007). Fascinating advances in ocean exploration technology, coupled with breakthroughs in high-throughput genetic sequencing, geochemical measurements, and fluorescence microscopy techniques have allowed us to investigate this phenomenon in increasing detail over the last 20-30 years.

Through these methods, we now know much of this global methane consumption through AOM occurs in concert with the microbial reduction of sulfate (SO_4^{2-}), naturally found in seawater, to sulfide (HS^-, shown in Eq. 1) and is accomplished by a unique, symbiotic partnership (or 'consortium') between anaerobic, methanotrophic (ANME) archaea and sulfate-reducing bacteria (SRB; Hoehler et al., 1994; Hinrichs et al., 1999; Boetius et al., 2000; Orphan et al., 2001; Michaelis et al., 2002; Nauhaus et al., 2002; Orphan et al., 2002).

$$CH_4(g) + SO_4^{2-}(aq) \longrightarrow HCO_3^{-}(aq) + HS^{-}(aq) + H_2O(l) \qquad (1)$$

In this partnership, ANME and SRB form lobate or spherical biofilms, or 'aggregates', that more recent studies have suggested allow them to participate in direct, interspecies electron transfer (DIET), thereby directly coupling the archaeal oxidation of subsurface methane ($CH_4 \rightarrow HCO_3^-$) to the bacterial reduction of seawater sulfate ($SO_4^{2-} \rightarrow HS^-$; McGlynn et al., 2015; Wegener et al., 2015; Scheller et al., 2016). While better defining this unique mechanism of interaction still remains the focus of much study, what is clear is that this microbial metabolic symbiosis acts on a global scale to mitigate the flux of methane entering Earth's atmosphere. This mitigation, however, does not occur without leaving a trace. Interestingly, microbially-mediated AOM can be identified in the fossil record. How?

Methane-consuming microbes also bury themselves alive

With sufficient conversion of methane to bicarbonate, the buildup of dissolved bicarbonate in marine sediments (referred to, along with sulfide and other dissolved proton acceptors, as 'alkalinity') often triggers the precipitation of carbonate minerals in marine sediments, including calcium- and magnesium-bearing aragonite and calcite ($(Ca, Mg)CO_3$, e.g., Eq. 2).

$$Ca^{2+}(aq) + Mg^{2+}(aq) + 4HCO_3^-(aq) \rightarrow$$

$$CaMg(CO_3)_2\,(s) + \ 2CO_2(g) + 2H_2O(l) \quad (2)$$

In fact, carbonate precipitation is estimated to sequester 14% of the methane oxidized through AOM in these marine settings (Greinert et al., 2001). Over geologic timescales (e.g., 1000s of years), AOM is thus thought to continue feeding the growth of these carbonates, leading to distinct, km-scale formations of carbonates found at sites of past and current methane ‘seepage’ around the world (Ritger et al., 1987; Greinert et al., 2001; Reitner et al., 2005; Naehr et al., 2007; Sahling et al., 2008; Klaucke et al., 2012). This precipitation and gradual transformation to solid rock, also known as diagenesis, effectively entombs the sediment-hosted microbial community, including the ANME-SRB consortia that produced it, but also preserves chemical and mineral signatures that bear evidence of the carbonate’s microbial origins and subsequent geologic history. In turn, these signatures enable us to look into the past and study AOM in ancient marine environments (Aharon et al., 1997; Peckmann & Thiel, 2004; Teichert et al., 2005; Naehr et al., 2007; Haas et al., 2010).

Studies within the last decade, however, have observed that these globally distributed, marine ‘seep’ carbonates are not just records of past AOM, but continue to host active microbial communities still capable of oxidizing methane and thus represent an under-characterized methane ‘sink’ distinct from the sediments in which they originate (Marlow et al., 2014b, 2015, 2021). These observations bear many still undefined implications for how these seep carbonates are studied, as they suggest that the record of AOM as indicated by the carbonates may not reflect a passive, integrative history, but a dynamic and overprinted record of past and current AOM. This complex record is difficult to interpret and recent studies have only just begun to address how microbial communities within these carbonates across various hypothesized stages of formation may change (or not) across time and location (Marlow et al., 2014a; Mason et al., 2015; Case et al., 2015; Yanagawa et al., 2019; Schroedl et al., 2024). As in marine sediments, the AOM-capability of rock-hosted, or 'endolithic' communities are still impacted by environmental conditions, including methane transport from deeper in the sediment and sulfate delivery from the overlying seawater that ultimately define a zone of habitability (also known as the 'sulfate-methane transition zone', or SMTZ) and thus constrain the spatiotemporal extent to which AOM in seep carbonates is still possible. Here, we arrive at two key aspects of current and future studies addressing the dynamic nature and extent of AOM in seep carbonates: space and time.

Carbonate-hosted methane consumption is a function of space and time

For AOM to continue optimally, the ANME-SRB consortia that mediate this process must have access to the methane and sulfate that form a key vertical gradient in marine sediments known as the SMTZ. This gradient is spatially and temporally variable — shallowing and deepening, expanding and contracting (vertically), and widening and narrowing (laterally) over time to create localized, three-dimensional regions of heightened or reduced AOM activity (Tryon et al., 2002; Treude et al., 2003; Heeschen et al., 2005). These patches of activity are often discernible at the seafloor, where carpets of colorful microbial ‘mats’, tubeworms, and bivalve clams subsisting on the ambient fluxes of methane and sulfate or sulfide are 2D markers of an active seep ecosystem hosted in the underlying sediments. However, these patches can move, grow, shrink, appear, and disappear between a given sampling period — indicative of the shifting SMTZ beneath.

Temporal variability stems from the waxing and waning of methane delivery from the deeper subsurface, resulting in distinct ‘high activity’, ‘low activity’, and ‘inactive’ periods that can last from days to centuries (Tryon et al., 2002; Treude et al., 2003; Heeschen et al., 2005). Such variability at these coastal methane seeps is often dependent on the mechanism of methane generation or mobilization, whether from microbes performing the last step of anaerobic biomass decay (i.e., methanogenesis), thermogenic hydrocarbon production (including natural gas and other fossil fuels), or the decomposition of water-bound methane ‘ice’ in seep sediments (also known as gas hydrates, or clathrates) (e.g., Bernard et al., 1978; Hein et al., 2006; Reeburgh, 2007; Dean et al., 2018).

Similarly, the SMTZ can occur across a wide range of spatial scales, from meters to millimeters, dependent on the volumetric methane flux (i.e., how much methane is being generated or released?), transport limitations informed by the medium (i.e., can the methane or sulfate travel through the pores and voids?) and the metabolic activity of the local microbial community (i.e., is all the methane or sulfate being consumed before it can travel far?). Elevated methane fluxes at marine seeps (1-10s of L/m^2

day, e.g., Reeburgh et al., 2007) are often caused by gas hydrate decomposition and lead to advective transport regimes, where vigorous bubbling and perfusion of porewater through seep sediments and porous carbonates move methane quickly towards the seawater-seafloor interface, thereby shallowing the SMTZ and starving deeper sediments and buried carbonates of sulfate as it is wholly consumed by microbes performing AOM (e.g., 99 mmol/m^2 day in sediments, Treude et al., 2003, refs. therein) closer to the seafloor surface. Indeed, the most active seep sites are often marked by visible bubble plumes above the seafloor, indicative of incomplete methane drawdown. By contrast, weaker methane fluxes (<<1 L/m^2 day, e.g., Reeburgh et al., 2007) tend to be more diffusive regimes, where sulfate is drawn down much more slowly due to more methane-limited rates of AOM in sediments (<2 mmol/m^2 day, e.g., Iversen & Jorgensen, 1985; Joye et al., 2004), leading to a vertical expansion and/or deepening of the SMTZ as methane is more gradually consumed at depth.

Until now, limited sampling has largely prevented us from better understanding exactly how, when, and where seep carbonate-hosted AOM persists in these dynamic conditions. Indeed, much of our current understanding of AOM in seep carbonates comes from centimeter-scale (‘bulk’) evaluations of microbial identity and/or metabolic activity across a patchwork of samples that have not yet encompassed or resolved the range of structural and environmental conditions experienced by microbial communities in seep carbonates (Marlow et al., 2014ab, 2021; Mason et al., 2015; Case et al., 2015; Yanagawa et al., 2019). Recent studies, including multimodal imaging data sets collected by Schroedl et al. (2024) have begun to explore patterns in seep carbonate composition, structure, and microbial community identity at finer (sub-centimeter) scale resolution, but much more work remains to untangle the complex record of past and current AOM activity hosted by seep carbonates in order to better define the role this metabolic phenomenon plays in how methane moves through marine sediments worldwide.

This thesis examines spatial trends in methane-derived marine carbonates

The first three chapters presented in this thesis are therefore a step towards expanding our understanding of microbial communities and potential AOM associated with, and hosted by, methane seep carbonates. Specifically, these works add to the spatial extent and resolution at which we are able to observe these carbonate-hosted microbial communities and represent some of the most comprehensive examinations of seep carbonates from a single site.

In Chapter 1, we explored the mineral compositions, internal structures, and hosted microbial communities of several sediment-hosted carbonate ‘nodules’ — centimeter-scale, porous concretions in methane seep sediments within and below the SMTZ. We contextualized these observations with centimeter-scale profiles of surrounding sediment porewater chemistry and microbial communities. Combined with lab-based observations of microbial activity, we observed strong similarities between the communities hosted in the nodules and sediments, suggestive of ongoing exchange well after carbonate precipitation. These similarities persisted below the

SMTZ and in one site, even suggested nodules could be hosting methane production (methanogenesis) instead of methane consumption. Lab-based incubations of these associations with an amino acid analog (known as BONCAT) revealed that nodules coming from these regions below the SMTZ did not re-adapt to high sulfate and methane concentrations and participate in AOM, which may underscore how slowly, if at all, these energy-limited microbial communities grow and change over time.

In Chapter 2, we used genetic sequencing and fluorescence microscopy to identify rare, morphologically diverse tripartite associations between two distinct groups of anaerobic methanotrophic archaea (ANME-1 and ANME-2) and a bacterial partner occurring within and underneath a seep carbonate crust at the seafloor. We also found that these associations were not just limited to the seep carbonate at the seafloor, but occurred in sediments and sediment-hosted carbonates at Santa Monica Basin. Furthermore, sitewide abundances of candidate members forming these associations, as well as close genetic relationships with other, globally distributed ANME sequences and morphological resemblances to common ANME-SRB consortia suggested these associations might not be specialized behavior, but instead a likely recurrent, optional behavior accessible to many different ANME groups. Here, BONCAT incubations of these associations with an amino acid analog also showed that ANME-2 was active while ANME-1 was not, suggestive of competitive advantages for ANME-2 in these unique associations. Collectively, these findings broaden our understanding of ANME-SRB consortia, highlighting the flexibility and ecological significance of ANME interactions performing AOM at methane seeps.

In Chapter 3, we revisited the seep carbonate bearing the tripartite associations and included additional seep carbonate crusts, or 'pavements' to examine how the carbonate structure might impact the spatial distribution of these communities at the µm- and mm-scale. Here, we assessed the carbonates' porosities and typical pore size dimensions, as well as their mineralogy. We also used genetic sequencing and fluorescence microscopy from millimeter-sized vertical carbonate transects to produce microbial community and cellular abundance profiles with sample depth. Communities were found to differ between the outer surfaces and the interior, with higher microbial diversity and cellular abundance near the surface. Porosity, in particular, was linked to the ability of the pavements to host biomass and facilitate nutrient exchange, which ultimately impacts methane consumption. Together, our findings further supported spatially resolved differences in the microbial community hosted by seep carbonates. Based on these results, we also discussed additional avenues to better resolve habitation and activity in these seep carbonates.

Ultimately, the central theme of these studies is the importance of spatially resolved and extensive sampling in our approaches to untangle how AOM is recorded and persists in the carbonates that form at marine methane seeps. Through this approach, we can not only better constrain the nature and extent of carbonate-hosted AOM, but even shed light on rarer seep-associated phenomena that promise to expand our understanding of AOM in marine sediments as a whole and shape the role this microbially mediated process plays in global methane cycling.

Part II: Spatially-resolved trends in records from the early Solar System

While notably distinct from the first three chapters of this work, Chapter 4 represents another study, this time in planetary science, that underscores the value of spatially-resolved data sets in studies of spatially heterogeneous systems. In this particular application, we studied fine-scale spatial variations in the infrared spectroscopic properties of the diverse clasts and matrix materials that comprise carbonaceous chondrites — a class of meteorites that are remnants of the protoplanetary disk from the early solar system. These meteorites are thought to originate from ‘primitive’ asteroids, or larger fragments from the protoplanetary disk that together with carbonaceous chondrites allow us to explore the ancient record of aqueous and thermal alteration processes in these ‘planetesimals’. This shared record primarily stems from reflectance spectroscopy, or the measurement of similarities in light reflection profiles (‘spectra’) from different components that allow us to interpret evidence of shared chemical changes. This record, however, is not fully understood due to the limited spatial resolution afforded by both ground observations of asteroid surfaces (i.e., one spectrum for an entire asteroid surface), as well as ‘bulk’ powder observations of carbonaceous chondrites in the lab (i.e., 1-10’s of spectra for an entire, pulverized, meteorite surface).

In this study, we used microimaging, hyperspectral spectroscopy in the visible and shortwave infrared (VSWIR) range to capture the spectral diversity of 20 carbonaceous chondrites, resulting in almost 700,000 spectra collected at an ~80 μm/pixel resolution. To systematically compare these chondrite spectra to asteroid spectra, we also used the Expanded Bus-DeMeo asteroid taxonomy, a statistically-driven framework that uses the most varying spectral features from a collection of 371 asteroids to spatially cluster similarly varying spectra.

Through this framework, we found direct connections between distinct chondrite compositional groups and asteroid spectral classes (e.g., CM2 chondrites and Cgh-class asteroids; CV3 chondrites and L-class asteroids) that further support shared origins and alteration histories from previous bulk-scale analyses. Furthermore, this framework highlighted compositional similarities between localized chondrite components and asteroid classes beyond those traditionally associated with carbonaceous chondrites, including unaltered, iron-bearing silicates (e.g., olivine, low-Ca pyroxene) more commonly observed in asteroids with different formation histories. Together, these findings also underscore the impact of strength and abundance of spectrally active components, such as iron, in shaping the observable record of alteration contained in asteroids and carbonaceous chondrites. Thus, while not the major focus of this work, Chapter 4 represents another instance where spatially-resolved data sets of composition and process records expand our understanding of past and current natural phenomena.

References

Aharon, P., Schwarcz, H.P., Roberts, H.H., 1997. Radiometric dating of submarine hydrocarbon seeps in the Gulf of Mexico. GSA Bulletin 109, 568—579. https://doi.org/10.1130/0016-7606(1997)109<0568:RDOSHS>2.3.CO;2

Bernard, B.B., Brooks, J.M., Sackett, W.M., 1978. Light hydrocarbons in recent Texas continental shelf and slope sediments. Journal of Geophysical Research: Oceans 83, 4053–4061. https://doi.org/10.1029/JC083iC08p04053

Boetius, A., Ravenschlag, K., Schubert, C.J., Rickert, D., Widdel, F., Gieseke, A., Amann, R., Jørgensen, B.B., Witte, U., Pfannkuche, O., 2000. A marine microbial consortium apparently mediating anaerobic oxidation of methane. Nature 407, 623—626. https://doi.org/10.1038/35036572

Case, D.H., Pasulka, A.L., Marlow, J.J., Grupe, B.M., Levin, L.A., Orphan, V.J., 2015. Methane Seep Carbonates Host Distinct, Diverse, and Dynamic Microbial Assemblages. mBio 6. https://doi.org/10.1128/mBio.01348-15

Dean, J.F., Middelburg, J.J., Röckmann, T., Aerts, R., Blauw, L.G., Egger, M., Jetten, M.S.M., de Jong, A.E.E., Meisel, O.H., Rasigraf, O., Slomp, C.P., in't Zandt, M.H., Dolman, A.J., 2018. Methane Feedbacks to the Global Climate System in a Warmer World. Reviews of Geophysics 56, 207—250. https://doi.org/10.1002/2017RG000559

Greinert, J., Bohrmann, G., Suess, E., 2001. Gas Hydrate-Associated Carbonates and Methane-Venting at Hydrate Ridge: Classification, Distribution, and Origin of Authigenic Lithologies, in: Natural Gas Hydrates: Occurrence, Distribution, and Detection. American Geophysical Union (AGU), pp. 99—113. https://doi.org/10.1029/GM124p0099

Haas, A., Peckmann, J., Elvert, M., Sahling, H., Bohrmann, G., 2010. Patterns of carbonate authigenesis at the Kouilou pockmarks on the Congo deep-sea fan. Marine Geology 268, 129—136. https://doi.org/10.1016/j.margeo.2009.10.027

Heeschen, K.U., Collier, R.W., de Angelis, M.A., Suess, E., Rehder, G., Linke, P., Klinkhammer, G.P., 2005. Methane sources, distributions, and fluxes from cold vent sites at Hydrate Ridge, Cascadia Margin. Global Biogeochemical Cycles 19. https://doi.org/10.1029/2004GB002266

Hein, J.R., Normark, W.R., McIntyre, B.R., Lorenson, T.D., Powell, C.L., II, 2006. Methanogenic calcite, 13C-depleted bivalve shells, and gas hydrate from a mud volcano offshore southern California. Geology 34, 109–112. https://doi.org/10.1130/G22098.1

Hinrichs, K.-U., Hayes, J.M., Sylva, S.P., Brewer, P.G., DeLong, E.F., 1999. Methane-consuming archaebacteria in marine sediments. Nature 398, 802—805. https://doi.org/10.1038/19751

Hoehler, T.M., Alperin, M.J., Albert, D.B., Martens, C.S., 1994. Field and laboratory studies of methane oxidation in an anoxic marine sediment: Evidence for a methanogen-sulfate reducer consortium. Global Biogeochemical Cycles 8, 451—463. https://doi.org/10.1029/94GB01800

Iversen, N., Jorgensen, B.B., 1985. Anaerobic methane oxidation rates at the sulfate-methane transition in marine sediments from Kattegat and Skagerrak

(Denmark). Limnology and Oceanography 30, 944–955. https://doi.org/10.4319/lo.1985.30.5.0944

Joye, S.B., Boetius, A., Orcutt, B.N., Montoya, J.P., Schulz, H.N., Erickson, M.J., Lugo, S.K., 2004. The anaerobic oxidation of methane and sulfate reduction in sediments from Gulf of Mexico cold seeps. Chem. Geol. 205, 219–238. https://doi.org/10.1016/j.chemgeo.2003.12.019

Klaucke, I., Weinrebe, W., Linke, P., Kläschen, D., Bialas, J., 2012. Sidescan sonar imagery of widespread fossil and active cold seeps along the central Chilean continental margin. Geo-Mar Lett 32, 489—499. https://doi.org/10.1007/s00367-012-0283-1

Marlow, J., Peckmann, J., Orphan, V., 2015. Autoendoliths: a distinct type of rock-hosted microbial life. Geobiology 13, 303—307. https://doi.org/10.1111/gbi.12131

Marlow, J.J., Hoer, D., Jungbluth, S.P., Reynard, L.M., Gartman, A., Chavez, M.S., El-Naggar, M.Y., Tuross, N., Orphan, V.J., Girguis, P.R., 2021. Carbonate-hosted microbial communities are prolific and pervasive methane oxidizers at geologically diverse marine methane seep sites. PNAS 118. https://doi.org/10.1073/pnas.2006857118

Marlow, J.J., Steele, J.A., Case, D.H., Connon, S.A., Levin, L.A., Orphan, V.J., 2014a. Microbial abundance and diversity patterns associated with sediments and carbonates from the methane seep environments of Hydrate Ridge, OR. Front. Mar. Sci. 1. https://doi.org/10.3389/fmars.2014.00044

Marlow, J.J., Steele, J.A., Ziebis, W., Thurber, A.R., Levin, L.A., Orphan, V.J., 2014b. Carbonate-hosted methanotrophy represents an unrecognized methane sink in the deep sea. Nature Communications 5, 5094. https://doi.org/10.1038/ncomms6094

Mason, O.U., Case, D.H., Naehr, T.H., Lee, R.W., Thomas, R.B., Bailey, J.V., Orphan, V.J., 2015. Comparison of Archaeal and Bacterial Diversity in Methane Seep Carbonate Nodules and Host Sediments, Eel River Basin and Hydrate Ridge, USA. Microb Ecol 70, 766—784. https://doi.org/10.1007/s00248-015-0615-6

McGlynn, S.E., Chadwick, G.L., Kempes, C.P., Orphan, V.J., 2015. Single cell activity reveals direct electron transfer in methanotrophic consortia. Nature 526, 531—535. https://doi.org/10.1038/nature15512

Michaelis, W., Seifert, R., Nauhaus, K., Treude, T., Thiel, V., Blumenberg, M., Knittel, K., Gieseke, A., Peterknecht, K., Pape, T., Boetius, A., Amann, R., Jørgensen, B.B., Widdel, F., Peckmann, J., Pimenov, N.V., Gulin, M.B., 2002.

Microbial Reefs in the Black Sea Fueled by Anaerobic Oxidation of Methane. Science 297, 1013—1015. https://doi.org/10.1126/science.1072502

Naehr, T.H., Eichhubl, P., Orphan, V.J., Hovland, M., Paull, C.K., Ussler, W., Lorenson, T.D., Greene, H.G., 2007. Authigenic carbonate formation at hydrocarbon seeps in continental margin sediments: A comparative study. Deep Sea Research Part II: Topical Studies in Oceanography, Authigenic Mineral Formation in the Marine Environment; Pathways, Processes and Products 54, 1268—1291. https://doi.org/10.1016/j.dsr2.2007.04.010

Nauhaus, K., Boetius, A., Krüger, M., Widdel, F., 2002. In vitro demonstration of anaerobic oxidation of methane coupled to sulphate reduction in sediment from a marine gas hydrate area. Environmental Microbiology 4, 296—305. https://doi.org/10.1046/j.1462-2920.2002.00299.x

Orphan, V.J., House, C.H., Hinrichs, K.-U., McKeegan, K.D., DeLong, E.F., 2002. Multiple archaeal groups mediate methane oxidation in anoxic cold seep sediments. Proceedings of the National Academy of Sciences 99, 7663—7668. https://doi.org/10.1073/pnas.072210299

Orphan, V.J., House, C.H., Hinrichs, K.-U., McKeegan, K.D., DeLong, E.F., 2001. Methane-Consuming Archaea Revealed by Directly Coupled Isotopic and Phylogenetic Analysis. Science 293, 484—487. https://doi.org/10.1126/science.1061338

Peckmann, J., Thiel, V., 2004. Carbon cycling at ancient methane—seeps. Chemical Geology, Geomicrobiology and Biogeochemistry of Gas Hydrates and Hydrocarbon Seeps 205, 443—467. https://doi.org/10.1016/j.chemgeo.2003.12.025

Reeburgh, W.S., 2007. Oceanic Methane Biogeochemistry. Chem. Rev. 107, 486—513. https://doi.org/10.1021/cr050362v

Reitner, J., Peckmann, J., Blumenberg, M., Michaelis, W., Reimer, A., Thiel, V., 2005. Concretionary methane-seep carbonates and associated microbial communities in Black Sea sediments. Palaeogeography, Palaeoclimatology, Palaeoecology, Geobiology of Ancient and Modern Methane-Seeps 227, 18—30. https://doi.org/10.1016/j.palaeo.2005.04.033

Ritger, S., Carson, B., Suess, E., 1987. Methane-derived authigenic carbonates formed by subduction-induced pore-water expulsion along the Oregon/Washington margin. GSA Bulletin 98, 147—156. https://doi.org/10.1130/0016-7606(1987)98<147:MACFBS>2.0.CO;2

Sahling, H., Masson, D.G., Ranero, C.R., Hühnerbach, V., Weinrebe, W., Klaucke, I., Bürk, D., Brückmann, W., Suess, E., 2008. Fluid seepage at the continental margin offshore Costa Rica and southern Nicaragua. Geochemistry, Geophysics, Geosystems 9. https://doi.org/10.1029/2008GC001978

Scheller, S., Yu, H., Chadwick, G.L., McGlynn, S.E., Orphan, V.J., 2016. Artificial electron acceptors decouple archaeal methane oxidation from sulfate reduction. Science 351, 703—707. https://doi.org/10.1126/science.aad7154

Schroedl, P., Silverstein, M., DiGregorio, D., Blättler, C.L., Loyd, S., Bradbury, H.J., Edwards, R.L., Marlow, J., 2024. Carbonate chimneys at the highly productive point Dume methane seep: Fine-scale mineralogical, geochemical, and microbiological heterogeneity reflects dynamic and long-lived methane-metabolizing habitats. Geobiology 22, e12608. https://doi.org/10.1111/gbi.12608

Teichert, B.M.A., Bohrmann, G., Suess, E., 2005. Chemoherms on Hydrate Ridge — Unique microbially-mediated carbonate build-ups growing into the water column. Palaeogeography, Palaeoclimatology, Palaeoecology, Geobiology of Ancient and Modern Methane-Seeps 227, 67—85. https://doi.org/10.1016/j.palaeo.2005.04.029

Treude, T., Boetius, A., Knittel, K., Wallmann, K., Barker Jørgensen, B., 2003. Anaerobic oxidation of methane above gas hydrates at Hydrate Ridge, NE Pacific Ocean. Mar. Ecol. Prog. Ser. 264, 1—14. https://doi.org/10.3354/meps264001

Tryon, M.D., Brown, K.M., Torres, M.E., 2002. Fluid and chemical flux in and out of sediments hosting methane hydrate deposits on Hydrate Ridge, OR, II: Hydrological processes. Earth and Planetary Science Letters 201, 541—557. https://doi.org/10.1016/S0012-821X(02)00732-X

Wegener, G., Krukenberg, V., Riedel, D., Tegetmeyer, H.E., Boetius, A., 2015. Intercellular wiring enables electron transfer between methanotrophic archaea and bacteria. Nature 526, 587—590. https://doi.org/10.1038/nature15733

Yanagawa, K., Shiraishi, F., Tanigawa, Y., Maeda, T., Mustapha, N.A., Owari, S., Tomaru, H., Matsumoto, R., Kano, A., 2019. Endolithic Microbial Habitats Hosted in Carbonate Nodules Currently Forming within Sediment at a High Methane Flux Site in the Sea of Japan. Geosciences 9, 463. https://doi.org/10.3390/geosciences9110463

Chapter 1

DIVERSITY AND SINGLE-CELL ACTIVITY OF ENDOLITHIC MICROBIAL COMMUNITIES IN SEDIMENT-HOSTED CARBONATE NODULES WITHIN AND BELOW THE SULFATE-METHANE TRANSITION ZONE

Sergio A. Parra[a], Magdalena J. Mayr[a,b], James Mullahoo[a], Laura K. Quinn[c],
Rebecca L. Wipfler[a], Victoria J. Orphan[a,b]

[a]Division of Geological and Planetary Sciences, California Institute of Technology,
Pasadena, California, USA

[b]Division of Biology and Biological Engineering, California Institute of Technology,
Pasadena, California, USA

[c]Division of Chemistry and Chemical Engineering, California Institute of Technology,
Pasadena, California, USA

as submitted to the ASM Journal of Applied and Environmental Microbiology

Abstract

Authigenic carbonate concretions (‘nodules’) precipitate in marine seep sediments as a result of anaerobic oxidation of methane (AOM). These rocks host active endolithic microbial communities and persist as important methane sinks. Still, how these communities and their activity differ from those in adjacent seep sediments, particularly as a function of proximity to the sulfate-methane transition zone (SMTZ), remains understudied. Here, we sampled sediments and nodules within and below the SMTZ (0-57 cm deep) at four active deep-sea seep areas in Santa Monica Basin, CA. Measurements of high nodule porosities (43-51%) coupled to strong similarities between sediment and nodule 16S rRNA-based community profiles, including below the SMTZ, suggest continued perfusion and exchange between buried nodules and surrounding sediment. Shared, depth-dependent transitions in methanotrophic taxa (ANME-1, ANME-2, ANME-3) and methanogenic taxa (*Methanofastidiosales*) below the SMTZ were also consistent with trends in porewater methane and sulfate concentrations, porewater DIC, and nodule δ13C values — underscoring the impact of different geochemical conditions on community structure and suggestive of under-characterized physiological plasticity in ANME-1. Laboratory-based BONCAT incubations of nodules within the SMTZ over ~14-weeks revealed active sulfide production and translationally active endolithic microorganisms. However, cells from parallel nodule incubations recovered below the SMTZ showed weak-to-negligible BONCAT-based activity despite similar cell abundances — suggestive of low activity on shorter timescales or dormancy. Together, these data challenge the interpretation of passively recorded microbiological signatures in seep sediment-hosted carbonate nodules and expand our understanding of how these endolithic communities may be actively shaped by past and present conditions.

Importance

This study advances earlier investigations of microbial communities in buried seep carbonate nodules by integrating microbiological profiles of nodules and sediments, sediment geochemistry, single-cell activity measurements, and nodule mineral, geochemical, and physical characteristics within and below the sulfate-methane transition zone in deep-sea methane seeps. This approach allows us to view how nodule-hosted, endolithic microbial communities change relative to their surrounding sediments across multiple geochemical contexts and better understand how formation history and environmental conditions might affect community identity and metabolic function. Results indicate that the seep nodule and surrounding sediment communities are closely linked across diverse geochemical conditions. This connectivity between sediments and carbonate nodules is distinct from that observed in exhumed seep carbonates, with implications regarding how microbial community composition within these nodules are interpreted, suggesting that instead of a passive recorder of the communities at the time of formation, these nodules appear to retain diverse, metabolically viable communities.

1. Introduction

Authigenic carbonates at marine methane seeps form as the result of microbially-mediated anaerobic oxidation of methane (AOM) in sediments, which draws down a substantial amount of the subsurface methane produced at these seeps (1, 2). Because these deposits persist over geologic timescales, these carbonates have been interpreted as a record of past AOM activity in ancient marine environments (3–7).

However, several lab-based measurements of elevated methane oxidation rates in recovered seep carbonates demonstrate that these rocks continue to host viable microorganisms and AOM activity, representing a persistent methane sink whose activity and ecology remains under-studied compared to seep sediments (8–11).

In particular, vuggy carbonate concretions, or ‘nodules’ observed in seep sediments (12–15) have not been investigated as thoroughly as denser, seafloor-exposed seep carbonates — whose metabolically diverse, endolithic communities have been observed to differ significantly from sediments and sediment-hosted nodules collected from the same sites, e.g., (16). As such, seep nodules represent a unique opportunity to study seep carbonate microbial community structure and activity in comparison to their host sediments in geochemical context.

For example, AOM in marine sediments primarily occurs within a distinct redox regime known as the sulfate-methane transition zone (SMTZ), where syntrophic activity between anaerobic, methanotrophic (ANME) archaea and sulfate-reducing bacteria (SRB) act to consume porewater methane and sulfate (17–20). This zone of AOM activity varies in depth and thickness largely controlled by methane flux, e.g., (21), transitioning from methane-poor, sulfate-rich overlying sediment horizons to deeper sulfate-poor, methane-rich sediments. The impact of relative proximity to the SMTZ on the endolithic community structure and activity within sediment-hosted carbonate nodules remains poorly characterized, with limited sampling from existing studies focusing exclusively within this zone (14–16, 22). In sediments, this geochemical stratification often results in regimes of distinct ANME/SRB lineages indicative of niche differentiation (22–29), where the observed persistence of certain ANME clades in sulfate-depleted seep sediments remains an area of active investigation (30–32). As such, the SMTZ represents a useful comparative framework in which to study the similarities and differences with co-occurring carbonate nodules across this globally important geochemical transition zone.

Previous work examining nodules recovered from seep sediments reported high similarities in the 16S rRNA diversity and community structure with host sediments (14–16). However, the extent to which these DNA-based community profiles represent extant, metabolically viable communities actively exchanged with host sediment or preserved, ancient sediment communities remains unclear (14, 15), with implications how different traces of AOM are ultimately interpreted and/or preserved in sediment-hosted nodules.

In this study, we expanded the characterization of sediment-hosted authigenic carbonate nodules from four methane seep areas at Santa Monica Mounds 800 and 863 within the Santa Monica Basin (33). Specifically, we integrated the biological and porewater geochemical profiles of 1 m long, ROV-deployed sediment cores within active deep-sea seeps with the structural and microbiological profiles of seep carbonate nodules, effectively capturing changes in both sediment and associated nodules within and well below the SMTZ. Laboratory microcosm experiments were also used to characterize differences in bulk respiration and cellular anabolic activity by the endolithic community across this transition zone using geochemical assays and single cell bioorthogonal non-canonical amino acid tagging (BONCAT) incubations. This combined approach allows us to probe the historical and current capacity of seep carbonate nodules as hosts for continued AOM activity in geochemical context, compared to their surrounding sediments.

2. Results

Sediment and nodule sampling within Santa Monica Basin methane seeps

Nodules and sediment push cores in this study were collected in May 2021 during the WF05-21 Southern California oceanographic expedition on the *R/V Western Flyer* using the *ROV Doc Ricketts*, both owned and operated by the Monterey Bay Aquarium Research Institute (MBARI). 93 samples (7 cores, 82 sediment horizons, 11 nodule horizons) were recovered in total from two active methane seep sites within the Santa Monica Basin: Santa Monica Mound Site 800 (SMM 800: 33.799438N /118.64672E; 805m depth; also known as the NE mound) and Santa Monica Mound Site 863 (SMM 863: 33.7888N /118.6683W; 863 m; also known as the SW mound); (33, 34). At these sites, we investigated 4 distinct seep areas: SMM 800-I, SMM 800-II, SMM 800-III, and SMM 863 (Fig. 1.1). Within each seep area, 1-2 sediment cores were collected, including 3, 1.22 m long cores (LC) and 4, standard, 30 cm long push cores (PC), with quasi-duplicate (‘paired’) cores taken in close spatial proximity (~30-50 cm apart) to capture comparable environments, where possible. One sediment core (PC64, SMM 800-II) was collected during a previous cruise and sampled from the same microbial mat within 5 m from the 2021 sampling location (Supplemental Material).

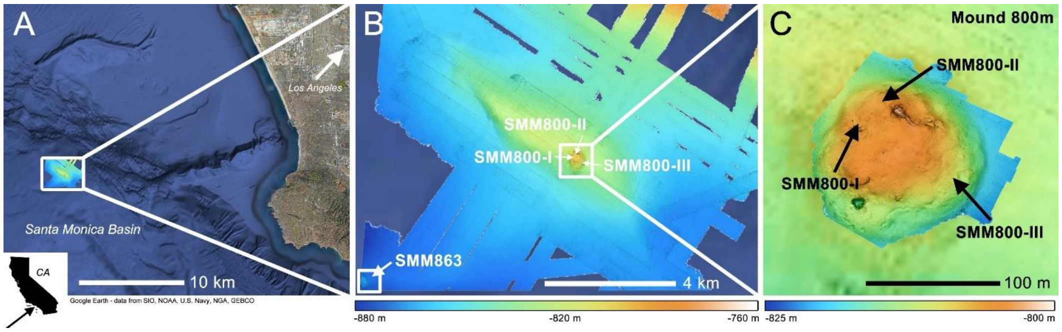

Fig. 1.1 – A) General location of the Santa Monica Basin seep sites (NE Mound, 800m, and SW mound, 863m) sampled for this study; B) Multi-beam bathymetry map of the sampling seep areas at SMM 800 and SMM 863; C) higher-resolution bathymetry map of the seep areas sampled at SMM 800: SMM 800-I, SMM 800-II, and SMM 800-III. Bathymetry colors in B) and C) correspond to mapped depth. Bathymetry maps were collected by MBARI in 2018.

Morphological diversity in seep sediment-hosted nodules

Across both short and long sediment push cores from all four seep areas, we observed distinct depth intervals of hardened, grey-brown calcitic material ranging in size from <cm rubble to >cm concretions, or nodules. Representative nodules from the four seep areas are shown in Fig. 1.2, with a complete list of the nodule-bearing sediment horizons included in this study summarized in Table 1.5. We observed strong morphological differences between the nodules recovered from cores at SMM 800 and SMM 863. Nodules from SMM 800 (Fig. 1.2A-C) were rougher, more irregularly shaped, and featured a greater number of mm to cm-sized voids. These nodules were also less friable, with lobate, grey-brown, coarse-grained growths often covering black, thin bivalve shell fragments. These features were consistent between the three seep areas sampled at SMM 800, as well as down core (7 nodule-bearing horizons total). In contrast, nodules from SMM 863 (Fig. 1.2D) were less irregularly shaped, with a less porous, finer grained, brown-colored material that resembled packed sediment hosting smaller lithics within. This morphology was also consistently observed between cores and across the five nodule-bearing horizons sampled at SMM 863.

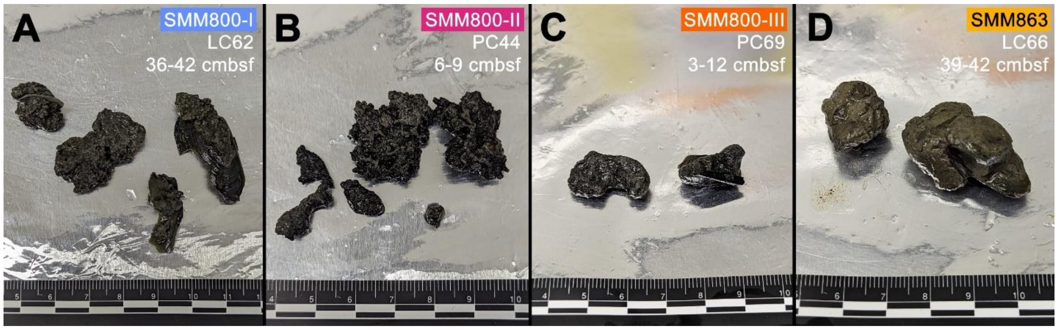

Fig. 1.2 – Characteristic nodules recovered from each of the four seep areas in this study; Nodule morphology is remarkably consistent with depth (expressed as centimeters below seafloor, cmbsf); ruler markings are in cm; A) Nodules recovered from LC62's 36-42-cmbsf horizons at SMM 800-I; B) Nodules from PC44's 6-9-cmbsf horizon at SMM 800-II; C) Nodules recovered from PC69 (3-12-cmbsf) at SMM 800-III; D) Nodules recovered from the 39-42-cmbsf horizon of LC66 at SMM 863.

Nodule porosity differences and pore size distributions

Open porosity is defined as the volume of connected pores relative to the volume of bulk solid, effectively representing the pore space that can freely exchange with the surrounding sediment environment. Water intrusion analyses of a subset of nodules (Table 1.1) revealed that the open porosities of two nodules sampled from SMM 800 (800-I, 800-II) were substantially higher than that of the nodule from SMM 863.

Table 1.1
Water intrusion-derived open porosities for select nodules

Seep Area	**SMM 800-I**	**SMM 800-II**	**SMM 863**
Core ID	LC62	PC44	LC66
Core Horizon (cmbsf)	36-42	9-12	39-42
Open Porosity (%)	51.36±0.84	49.52±1.33	43.03±0.78

Hg-porosimetry enabled the measurement of pore size distributions between 6 and 350 μm, revealing several pore-size regimes within a SMM 863 nodule collected at depth (39-42 cmbsf), including peaks corresponding to 11, 30, and 300 µm, and a slightly higher proportion of pores with sizes >100 µm (Fig. 1.3). A similarly deep-sourced nodule from SMM 800-I had fewer, although more evenly distributed pore sizes in the observed range. We also saw a smaller peak of pore diameters at 90 µm and fewer pore diameters above 100 µm compared to the nodule from SMM 863. A shallower nodule from SMM 800-II (9-12 cmbsf) also had a relatively low, but even pore-size distribution below 100 µm, in addition to the occurrence of pore sizes between 100 and 250 µm, with minor peaks at 300 and 350 µm.

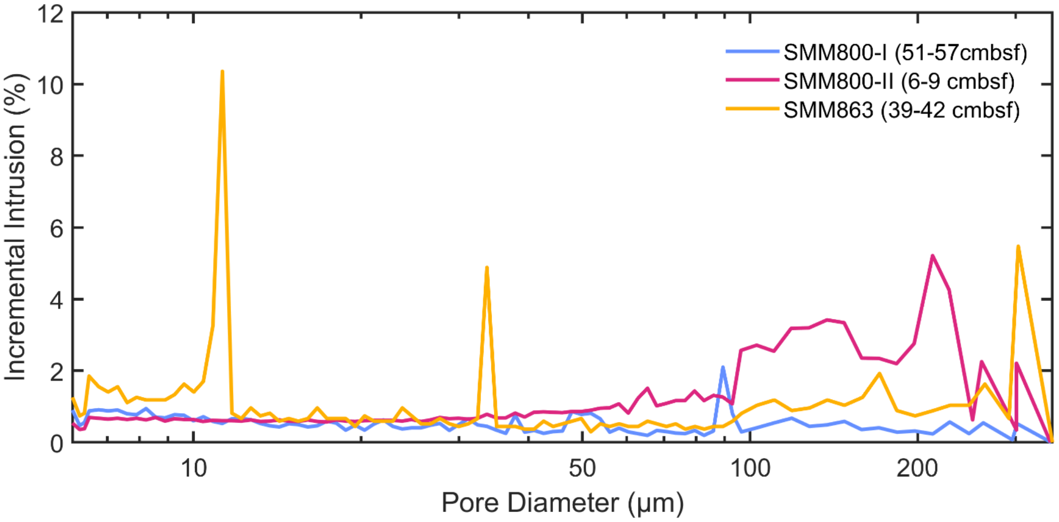

Fig. 1.3 – Hg-porosimetry curves detailing pore diameter versus incremental intrusion for three nodules sampled from SMM 800-I, SMM 800-II, and SMM 863. Pore sizes observable with porosimetry range from 6- to 350-µm. The three nodules shed information on the three distinct nodule-featuring regions identified in this data set: 1) SMM 800 deep sediment (LC62), 2) SMM 800 shallow sediment (PC44), and 3) SMM 863 deep sediment (LC66)

Aragonite dominates nodule carbonate mineralogy, with increased Mg-calcite fractions in deeper nodules

Bulk powder XRD-derived mineralogies showed SMM 800 nodules were largely composed of aragonite (>78.2%), with minor contributions from Mg-calcite, calcite, and dolomite (Table 1.2). Conversely, nodules from SMM 863 were more aragonite-poor (<43.1%) and featured greater contributions from Mg-calcite (45.1%, 65.1%) than the nodules from SMM 800. Collectively, however, we did observe a greater proportion of Mg-calcite in the nodules sourced from deeper sediment horizons.

Table 1.2
Key mineral phases for select nodules, as determined by XRD

Seep Area	Core ID	Depth (cmbsf)	Aragonite	Mg-Calcite[a]	Calcite	Dolomite	Quartz
SMM 800-I	LC62	24-27	85.2%	4.5%	0.6%	3.3%	6.4%
		48-51	78.2%	11.3%	3.8%	0.03%	6.7%
SMM 800-II	PC44	9-12	90.2%	2.1%	2%	1.6%	3.3%
SMM 800-III	PC69	3-12	97%	0.1%	1.3%	0.8%	0.9%
SMM 863	LC74	33-39	43.1%	45.1%	0.5%	4.8%	0.5%
	LC66	39-42	26.1%	65.1%	7.1%	1.6%	0.03%

a: Mg-Calcite corresponds to $(Ca_{0.9}Mg_{0.1})O_3$*, as measured by* (35)

Geochemical localization of the SMTZ and δ^{13}C trends in porewater DIC and nodules

To characterize the geochemical environments at SMM 800 and SMM 863, we focused on the vertical trends of three characteristic porewater species that inform the sulfate-methane transition zone (SMTZ): methane (CH_4), sulfate (SO_4^{2-}), and sulfide (H_2S), shown in Fig. 1.4. At SMM 800-I (LC62) collected within a sulfur-oxidizing microbial mat (Fig. 1.11), porewater extracts revealed high AOM activity, with a near-complete drop in sulfate concentration by 6-9 cmbsf, which remained low down core (Fig. 1.4A). This drop was matched by a concurrent rise in porewater sulfide and methane, although we observed more dynamic behavior in the sulfide and methane concentrations with depth, including a notable decrease in both species below their peaks at 6-9 cmbsf. SMM 800-II (PC64) showed a similar sulfate profile, reaching its minimum by 3-4 cmbsf, with values measured at ~3 mM to the base of the short core at 9 cmbsf (Fig. 1.4B). Similarly, this drop was accompanied by a steep rise in porewater methane and sulfide, although as with SMM 800-I, we observed a subsequent drop in concentration below the 3-4 cmbsf horizon. At SMM 800-III (PC43), also collected in a sulfur-oxidizing microbial mat (Fig. 1.13), the peak in AOM activity also occurred at shallower depths (4-5 cmbsf), and, distinct from SMM 800-II, sulfate concentration dropped below detection below this depth (Fig. 1.4C). At SMM 863 (LC66), only porewater sulfate concentrations were measured. However, compared to the seep areas at SMM 800, we observed a much deeper penetration of sulfate into the sediment, dropping below detection by 21-24 cmbsf in this microbial mat habitat, suggestive of a lower methane flux (Fig. 1.4D).

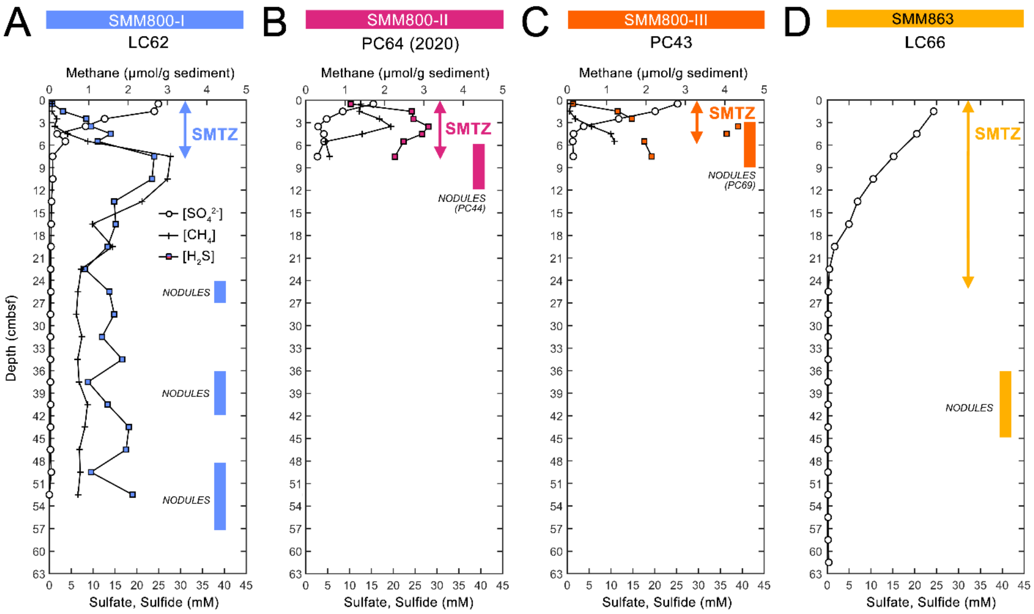

Fig. 1.4 – Sulfate, methane, and sulfide concentration profiles collected for sediment porewaters at the seep areas (A-D) investigated in this study. We plot the median depth in centimeters below seafloor (cmbsf), where concentrations represent 3-cm depth horizons. The sulfate-methane transition zones (SMTZ), as determined by near-complete(<<1mM) sulfate drawdown in each core, are also demonstrated with colored arrows. Colored bars represent the horizons where nodules were recovered for further analysis. Nodules recovered from a different, co-located core at the seep area are also specified. PC64 from SMM 800-II was collected a year previously. We note that there are greater uncertainties with measured sulfide concentrations above the detection limit (>25mM, e.g.,

in PC43 from SMM 800-III). Only sulfate porewater concentration was collected for the core at SMM 863.

Porewater concentrations and the $\delta^{13}C$ values of dissolved inorganic carbon (DIC, $\delta^{13}C_{pw}$) in addition to the inorganic carbon isotopic concentration of the nodules ($\delta^{13}C_{nod}$) were also measured across the four areas in this study (Fig. 1.5). These data provide additional information into active AOM horizons where highly ^{13}C-depleted bicarbonate is produced during methane oxidation and subsequently serves as the source of precipitation of authigenic carbonates (36). At SMM 800-I (LC62), porewater DIC concentrations steeply increased from <10mM to as high as ~42mM in the shallow subsurface (0-6 cmbsf) before stabilizing down core. Interestingly, this occurred in two distinct stages at SMM 800-I, which experienced a second rise in DIC to ~36mM at 15-18 cmbsf to the base of the core at 54 cmbsf (Fig. 1.5A). At both SMM 800-I and SMM 800-III (PC43), this shallow spike in DIC concentration was paired with the peak in negative $\delta^{13}C_{pw}$, reaching values as low as -59.20‰, followed by a steady increase in $\delta^{13}C$ values down core. This indicated a peak in AOM in the shallow sediment horizons, consistent with the depth of the sulfate minima. SMM 800-II (PC64) exhibited a different trend, with comparatively less $\delta^{13}C_{pw}$ (-46.24‰, Fig. 1.5B). Notably, both DIC concentration and $\delta^{13}C_{pw}$ increased with depth, perhaps reflective of a mixture of both heterotrophic sulfate reduction and AOM at this site (37, 38). In comparison, $\delta^{13}C_{nod}$ exhibited a wide range of values across all four seep areas (-30.09‰ to -53.79‰). Notably, nodules from shallower depths at both SMM 800-I and SMM863 had greater ^{13}C enrichment than the nodules recovered deeper in the cores, where the $\delta^{13}C_{nod}$ at SMM 800-I was slightly more ^{13}C-depleted (-46.03‰) than its surrounding porewater (-41.26‰).

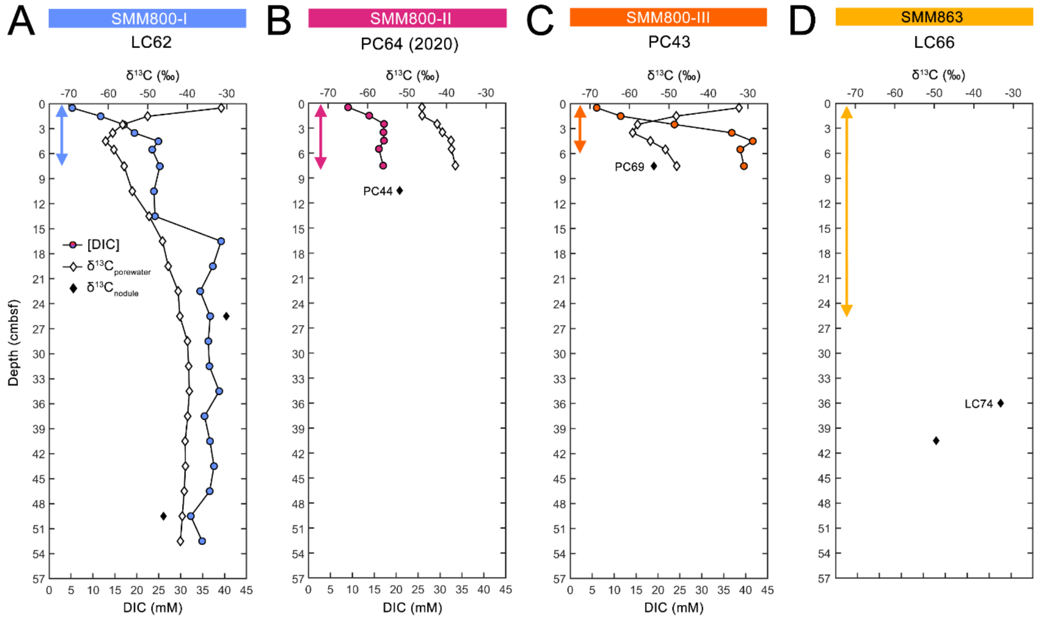

Fig. 1.5 – Sediment porewater DIC, $\delta^{13}C_{porewater}$, and $\delta^{13}C_{nodule}$ profiles collected at the seep areas investigated in this study. We plot the median depth in centimeters below seafloor (cmbsf), where values represent multiple depth horizons. Because of the <3‰ spread between $\delta^{13}C_{nodule}$ replicates, values are simply averaged for comparison (individual values are included in Table 1.6). Colored arrows indicate an estimate for the location of the SMTZ, as in Fig. 1.4. PC64 from SMM 800-II was collected a year previously. Only $\delta^{13}C_{nodule}$ was able to be collected for the cores at SMM 863.

16S rRNA gene comparison of phylum-level diversity in nodules and host sediments

Dominant microbial phyla across all sampled sediment and nodules (Fig. 1.16-1.22) broadly resembled reports from other carbonate-bearing methane seep environments from Hydrate Ridge, OR and Eel River Basin, CA, which were often dominated by members of the *Halobacteriota* (putative methane-oxidizers largely affiliated with ANME archaea lineages), *Euryarchaeota*, and *Desulfobacterota* phyla (14, 16, 22). Additionally, members of the archaeal *Thermoplasmatota*, *Asgardarchaeota*, and *Crenarchaeota* were consistently recovered above 1% relative abundance. Of the bacterial phyla, *Desulfobacterota* were consistently present, with additional representation by members of the *Chloroflexi* and *Caldatribacteriota* (the latter exclusively associated with JS1, Supplementary Data, Table T2), and occasional detection (>1%) of taxa belonging to the *Planctomycetota*, *Acidobacteriota*, and *Fermentibacterota*. Notably, members from the *Fermentibacterota,* first characterized in anaerobic digesters by (39), were only substantially recovered in three nodules (1.05-2.28% relative abundance) at both the SMM 800-II and SMM 800-III seep areas and rarely recovered (<<1%) within the associated host sediments (Fig. 1.19, 1.21).

Similar 16S rRNA community profiles between sediments and nodules from shallow sediment horizons

In the shorter push cores from seep areas SMM 800-II and 800-III, *Halobacteriota* lineages consistently present in seep sediments were ANME-1a, ANME-2b, and ANME-2c (Fig. 1.6). Interestingly, these lineages persisted past the shallow zone of sulfate depletion in these cores. ANME-2c relative abundances were largely consistent with depth through 9-12 cmbsf at both SMM 800-II and 800-III. However, we observed contrasting patterns in ANME-2b and ANME-1a abundances. Deeper horizons in SMM 800-II (PC44) showed a drop in the relative abundance of ANME-2b, concurrent with an increase in ANME-1a below 6 cmbsf. In the cores from SMM 800-III (PC43 and PC69) however, ANME-2b relative abundance and comparatively less ANME-1a were recovered from the deeper horizons, although this trend was much weaker in PC69 (Fig 1.6C). Within the three nodules recovered from these push cores, the dominant *Halobacteriota* lineages largely resembled those of their parent sediment horizons, where notable exceptions include an enrichment of ANME-1a (>20%) in the nodules from PC44 at SMM 800-II. Still, Shannon-Wiener and Inverse Simpson indices based on archaeal 16S ASV proportional abundances (Table 1.7) showed that archaeal diversity was greater in the sediment communities from SMM 800-II and SMM 800-III than in the nodules.

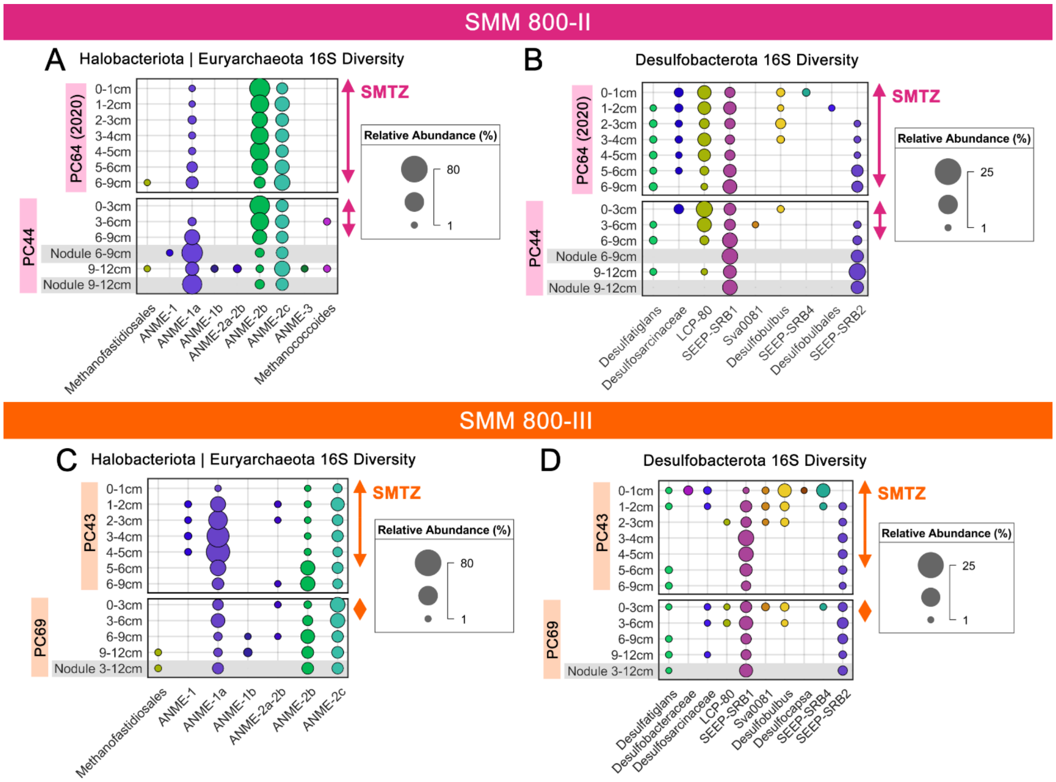

Fig. 1.6 – Bubble plots summarizing the depth-resolved, 16S relative abundances for groups within *Halobacteriota* (featuring ANME), *Euryarchaeota* (featuring methanogens, e.g., *Methanofastidiosales*), and *Desulfobacterota* (featuring sulfate-reducing partners to ANME) in PC64 and PC44 at SMM 800-II (A, B), as well as PC43 and PC69 at SMM 800-III (C, D) . Where possible, ASVs within these phyla were grouped at the genus-level, or at the next highest taxonomic level possible, and then cut off below a minimum 1% relative abundance. Communities extracted from nodules are highlighted in grey and often represent larger depth horizons. The location of the sulfate-methane transition zone (SMTZ) according to porewater sulfate concentrations from the same or co-located sediment core is indicated with the colored arrows.

Dominant *Desulfobacterota* lineages within these shallow sediment horizons at SMM 800-II and 800-III included two main sulfate-reducing bacterial lineages, Seep-

SRB1 and Seep-SRB2, that have been previously documented to form syntrophic associations with ANME (40–43), where their respective abundances appeared to covary with those of their ANME partners (Fig. 1.6BD). In the sulfate-rich, near-seafloor sediments (0-3 cmbsf) at both seep areas, a large diversity of other putative sulfate-reducing bacterial groups was also detected above 1%. These SRB lineages were largely affiliated with groups not known to directly participate in syntrophic AOM. By comparison, *Desulfatiglans* (not currently known to be involved in AOM) was recovered from both seep areas at low abundances as deep as 12 cmbsf, including within the nodule from PC69 at SMM 800-III. While uncommon in seep ecosystems, this group has been observed in cold seep sediments in the Okinawa Trough that also harbor ANME-1 (29). Shannon-Wiener and Inverse Simpson indices based on bacterial 16S ASV proportional abundances (Table 1.7) indicated that the sediments surrounding the nodules from these seep areas had higher diversity, as found with the Archaea.

Deeper sediment and nodule 16S rRNA surveys show persistence of *Halobacteriota* and *Desulfobacterota* and putative methanogenic lineages

Similarly to SMM 800-II and 800-III, SMM 800-I (LC62) had a shallow SMTZ (sulfate depleted by 5-6 cmbsf) and both sediments and nodules were enriched in *Halobacteriota*, *Euryarchaeota*, and *Desulfobacterota* lineages within and well below the sulfate depletion depth. Archaeal diversity was largely dominated by ANME-1a (up to 66.5% relative abundance) which was recovered throughout the core at depths below 3 cmbsf. In the deeper horizons, this group was accompanied by ANME-1b at lower relative abundance (Fig. 1.7). Notably, within this long core, we also documented two distinct transitions in both archaeal and bacterial community composition, which occurred between 4-27 cmbsf and between 33-57 cmbsf, representing the base of the core.

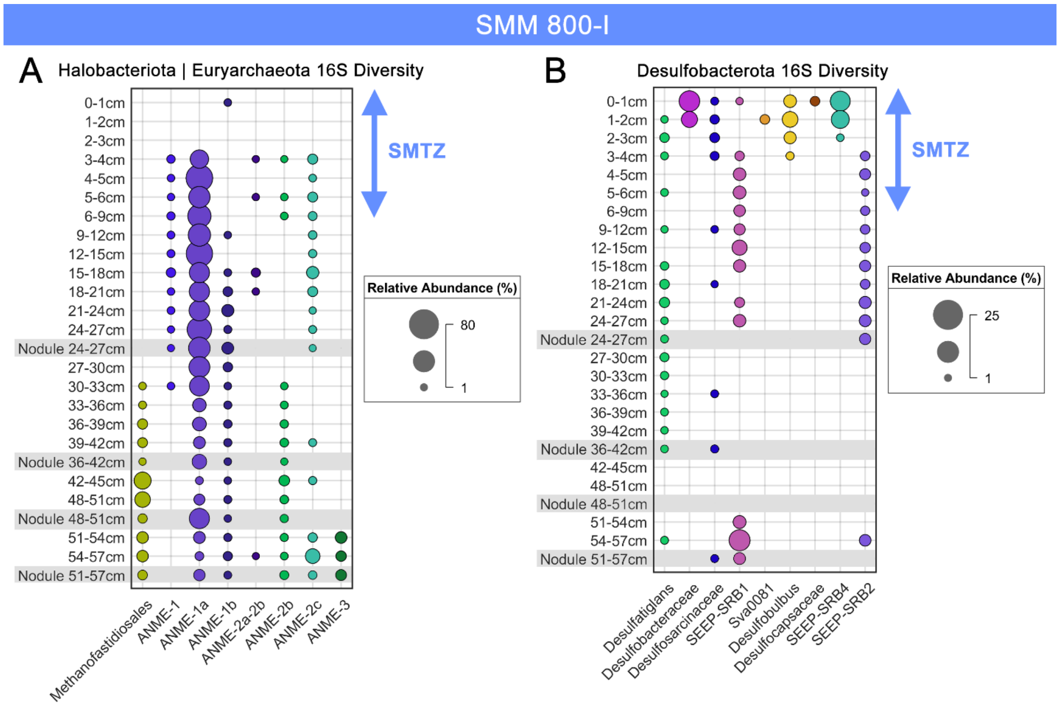

Fig. 1.7 – Bubble plots summarizing the depth-resolved, 16S relative abundances for groups within *Halobacteriota*, *Euryarchaeota*, and *Desulfobacterota* in LC62 at SMM 800-I. Where possible, ASVs within these phyla were grouped at the genus-level, or at the next highest taxonomic level possible, and then cut off below a minimum 1% relative abundance. Communities extracted from nodules are highlighted in grey and often represent larger depth horizons. The location of the sulfate-methane transition zone (SMTZ) according to porewater sulfate concentrations from the same or co-located sediment core is indicated with the colored arrows. A) Relative abundances within prominent phyla *Halobacteriota* (featuring ANME) and *Euryarchaeota* (featuring methanogens such as *Methanofastidiosales*). B) Relative abundances within *Desulfobacterota* – the phylum with sulfate-reducing partners to ANME.

The first transition showed a shift from the consistent presence of ANME-2c (1-10% relative abundance), an unclassified ANME-1 lineage, and the putative syntrophic sulfate-reducing bacterial lineages Seep-SRB1 and Seep-SRB2 in the shallow sediment down to 27 cmbsf to an underlying zone ~24 cm thick where each of these groups, with the exception of sporadic occurrence of ANME-2c, were below detection (Fig. 1.7). The second transition, occurring between 33-57 cmbsf (well below the SMTZ), was marked by the emergence of ANME-2b and a putative methylotrophic methanogen lineage *Methanofastidiosales* (formerly the WSA2 group, <20% relative abundance) largely dominated by a singular ASV (Supplementary Data, Table T2). The *Methanofastidiosales* are a poorly characterized group originally described from anaerobic sludge digesters (44) and observed in hydrothermal systems, gas hydrates, methane seeps, and methane-rich coastal sediments (29, 32, 45–48). This ASV was also detected above 1% abundance in the shallower push core sediments from SMM 800-II (PC464, PC44) and 800-III (PC69), including a nodule in PC69 (Fig. 1.6AC). A similar transition was observed for *Desulfobacterota* lineages, where the dominance of ANME partners Seep-SRB1 and Seep-SRB2 was succeeded by the persistent, though minor (<10%) presence of *Desulfatiglans* (Fig. 1.7B).

Additional transitions in the archaeal and bacterial communities occurred in the uppermost 3 cm and deepest horizons of the core below 51 cmbsf, with the near seafloor sediments largely devoid of ANME lineages, but supporting a high diversity of *Desulfobacterota* not recovered in deeper horizons, including Seep-SRB4 and Desulfobulbus lineages, while the deepest horizons (51-54 cmbsf) showed an increase in *Halobacteriota* diversity, with the reappearance of members of the ANME-2c and detection of ANME-3, alongside the reoccurrence of Seep-SRB1. Compared to ANME-2c ASVs, the dominant Seep-SRB1 ASVs in the deepest core interval were different from the dominant ASVs in the intermediate depth horizons

(3-27 cmbsf), although we observed a few shared Seep-SRB1 ASVs between these regions (Supplementary Data, Table T2).

Direct comparisons of the carbonate nodules (n=4) with paired sediments across these transitions revealed strong similarities between representative archaeal and bacterial taxa, including major members within *Halobacteriota* and *Desulfobacterota,* down to the ASV level (Fig. 1.7, Supplementary Data, Table T2). Beyond these taxa, both Shannon-Wiener and Inverse Simpson indices suggested the sampled nodule bacterial communities were consistently more diverse than their surrounding sediments, though this trend did not extend to the archaeal communities (Table 1.7).

The long cores recovered from SMM 863 revealed a slightly different community structure from SMM 800-I. Across both SMM 863 cores (LC74, LC66), we observed a clear transition in the dominant ANME and putative sulfate-reducing bacterial groups around 21-24 cmbsf (Fig. 1.8), aligned with the approximate depth of the SMTZ at this site. Here, members of the *Halobacteriota* above this transition zone were dominated by ANME-2c and known syntrophic partners belonging to the Seep-SRB1 as well as other uncharacterized lineages within the *Desulfosarcinaceae*. We also identified ANME-3 at varying abundances in the upper (<12 cmbsf) sediment in both cores. Below the transition at 21-24 cmbsf, ANME-2c was succeeded by lineages within ANME-1, primarily ANME-1b (up to 75% relative abundance). This transition corresponded with the appearance of the Seep-SRB2 lineage, previously observed to partner with ANME-1 (43, 49, 50). This depth distribution pattern was distinct from the other main ANME syntrophic partner, Seep-SRB1, which was consistently detected above 1% throughout both cores (Fig. 1.8B). Interestingly, we observed another transition in both cores, beginning at 36-39 cmbsf in LC74 and at 42-45 cmbsf in LC66, where ANME-2c reappeared alongside ANME-3. Here, the lower abundance of ANME-2c at depth was represented by the same dominant ANME-2c ASVs recovered in the upper sediment, while the ANME-3 ASVs at depth largely differed from those recovered near the top of the core (Supplementary Data, Table T2). Nodules sampled from this transition (n=3) revealed similar ANME-1b and ANME-1a lineages as in the surrounding sediments, down to the ASV level (Fig. 1.8A, Supplementary Data, Table T2), but lacked consistent representation from the other minor ANME lineages, including the uncharacterized ANME-1 group (in LC66) and ANME-2c (in both LC66 and LC74). Similarities were notably less apparent among the *Desulfobacterota*, where lineages present in the host sediment were often absent from the nodules (i.e., Seep-SRB1 and Seep-SRB2) and lineages not observed in the immediate sediment horizon were observed in the hosted nodule (e.g., *Desulfatiglans* in LC66).

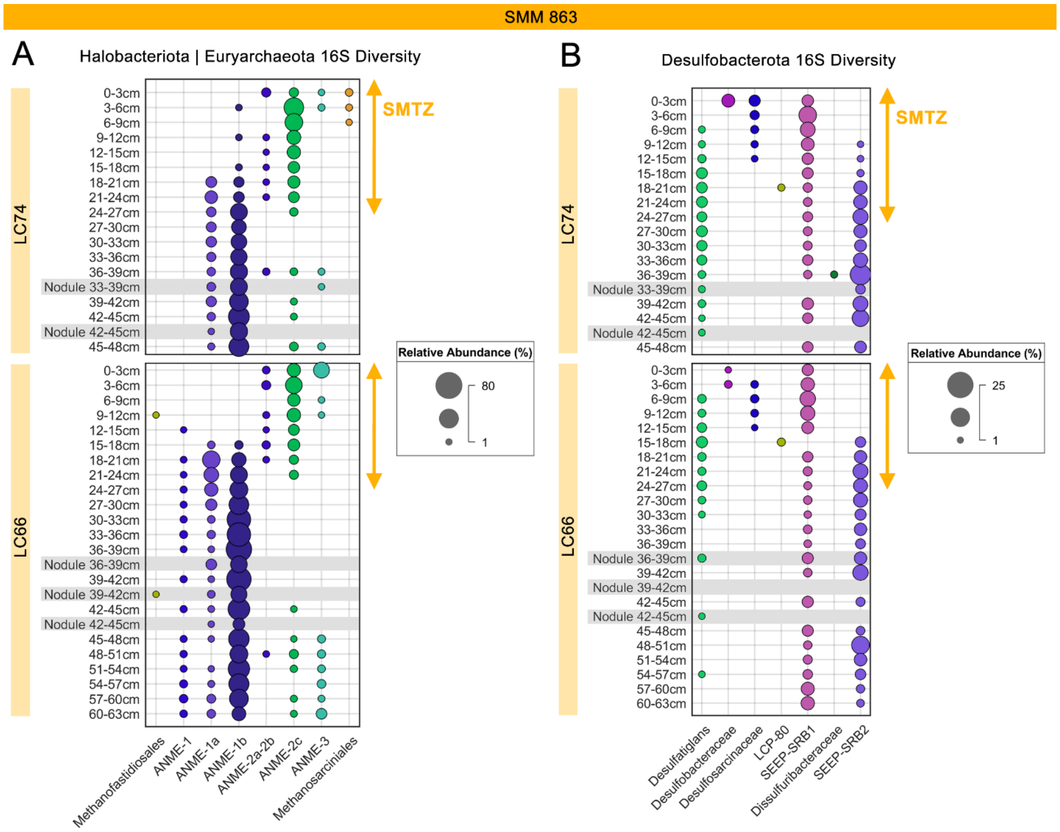

Fig. 1.8 – Bubble plots summarizing the depth-resolved, 16S relative abundances for groups within *Halobacteriota*, *Euryarchaeota*, and *Desulfobacterota* in LC74 and LC66 at SMM 863. Where possible, ASVs within these phyla were grouped at the genus-level, or at the next highest taxonomic level possible, and then cut off below a minimum 1% relative abundance. Communities extracted from nodules are highlighted in grey and often represent larger depth horizons. The location of the sulfate-methane transition zone (SMTZ) according to porewater sulfate concentrations from the same or co-located sediment core is indicated with the colored arrows. A) Relative abundances within prominent phyla *Halobacteriota* (featuring ANME) and *Euryarchaeota* (featuring methanogens such as *Methanofastidiosales*). B) Relative abundances within *Desulfobacterota* – the phylum with sulfate-reducing partners to ANME.

Cell abundance and fluorescence *in situ* hybridization (FISH) in nodules and sediments

Quantification of SYBR Gold®-stained cells and cell aggregates (cell associations > 5 µm) extracts were consistently higher (often 1-2 orders of magnitude) in sediment compared with nodules across the sites, with typical single cell abundances ranging between 10^6-10^7 cells mg^{-1} in sediments compared with 10^5-10^6 cells mg^{-1} in nodules (Table 1.3). While differences in cell abundance between sediments and nodules were observed, a substantial decrease in cell abundance between the deeper sediment horizons (e.g., 2.7 x10^7 at 54-57 cmbsf) compared with shallower depths (e.g., 3.59 x10^7 at 9-12 cmbsf) was not detected.

Table 1.3
Aggregate/single-cell/cell clump SYBR Gold counts in nodules and paired sediment horizons

Seep Area	Core ID	Core Horizon (cmbsf)	Avg Single Cells per mg Sample	SE	Avg Aggregates per mg Sample	SE
SMM 800-I	LC62	36-39	9.53×10^{6}	3.69×10^{5}	8.00×10^{3}	1.58×10^{3}
		39-42	1.30×10^{7}	4.05×10^{5}	1.02×10^{4}	1.60×10^{3}
		(Nodule) 36-42	3.89×10^{5}	1.86×10^{4}	5.65×10^{2}	1.73×10^{2}
		51-54	2.98×10^{7}	2.36×10^{6}	4.63×10^{4}	6.63×10^{3}
		54-57	2.70×10^{7}	2.18×10^{6}	3.11×10^{4}	1.89×10^{3}
		(Nodule) 51-57	5.11×10^{5}	1.73×10^{4}	2.56×10^{3}	2.78×10^{2}
SMM 800-II	PC44	6-9	4.05×10^{7}	2.10×10^{6}	8.28×10^{4}	2.17×10^{4}
		(Nodule) 6-9	4.21×10^{5}	1.54×10^{4}	4.63×10^{3}	7.19×10^{2}
		9-12	3.59×10^{7}	2.01×10^{6}	2.88×10^{4}	8.87×10^{3}
		(Nodule) 9-12	1.15×10^{6}	7.56×10^{4}	2.89×10^{3}	4.11×10^{2}
SMM 800-III	PC69	3-6	5.50×10^{7}	3.78×10^{6}	3.62×10^{4}	9.54×10^{3}
		6-9	4.42×10^{7}	2.64×10^{6}	4.14×10^{4}	1.61×10^{4}
		9-12	3.97×10^{7}	1.84×10^{6}	3.63×10^{4}	1.24×10^{4}
		(Nodule) 3-12	1.09×10^{6}	6.52×10^{4}	1.77×10^{3}	2.38×10^{2}
SMM863	LC66	42-45	3.01×10^{7}	9.51×105	2.64×10^{4}	3.02×10^{3}
		(Nodule) 42-45	1.70×10^{6}	8.68×10^{4}	4.01×103	9.20×10^{2}
	LC74	42-45	7.45×10^{6}	4.70×10^{5}	3.16×10^{4}	4.11×10^{3}
		(Nodule) 42-45	1.60×10^{6}	1.54×10^{5}	1.08×10^{4}	1.51×10^{3}

The spatial associations in aggregates and morphology of Bacteria, Archaea, and ANME-1 cells were also examined within the recovered nodules by fluorescence *in situ* hybridization (FISH); (Fig. 1.9). The persistence of highly auto-fluorescent material within the long cores from seep areas SMM 800-I and SMM 863 made it difficult to clearly discern a positive fluorescence signal from FISH, however we were able to observe positive hybridization with the ANME-1 probe, supporting 16S rRNA results. Notably, we observed large aggregates with morphology consistent with ANME-SRB consortia reported from seep sediments at a higher frequency within nodules recovered from the shallower sediment horizons (< 9-12 cmbsf) at seep areas SMM 800-II and 800-III, compared to the nodules recovered from deeper sediment intervals at SMM 800-I and SMM 863, where the FISH signal from cells was dimmer and cell aggregates were more loosely bound in an exopolymeric matrix (Fig. 1.9FG, Fig. 1.24).

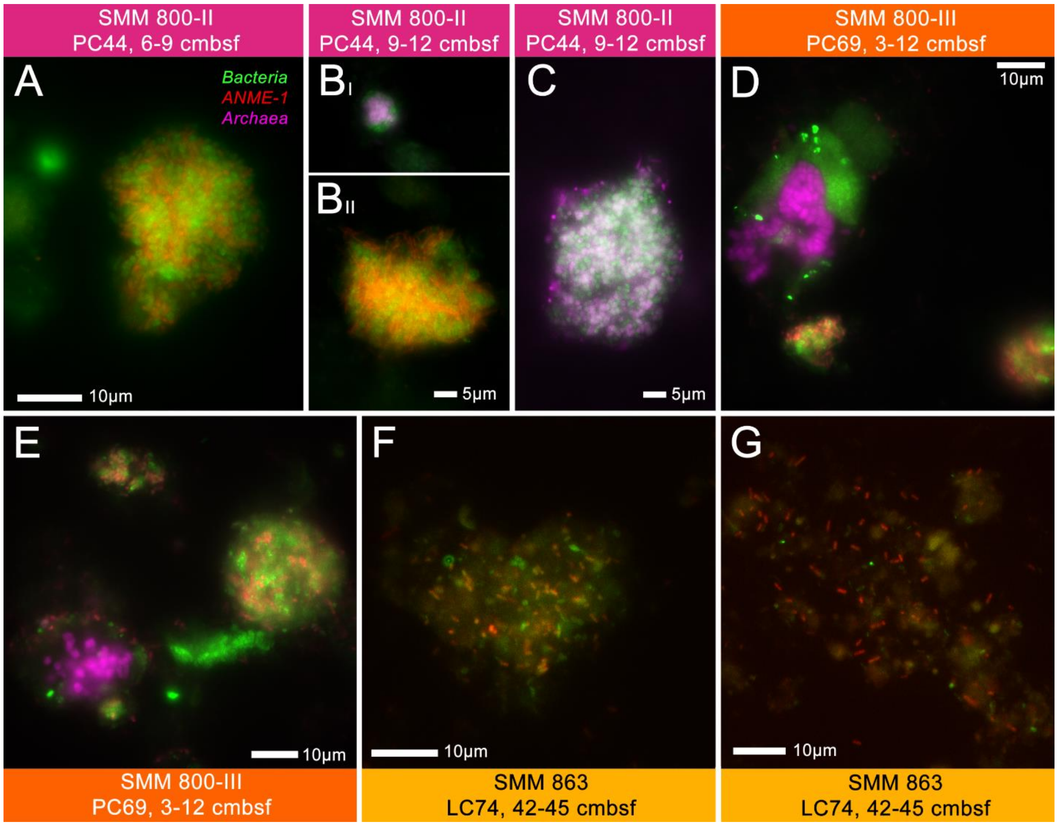

Fig. 1.9 – Representative examples of carbonate nodule associated cells and aggregates recovered from SMM 800-II, 800-III, and 863, visualized by fluorescence in situ hybridization (FISH) using probes targeting *Bacteria* (EUB338 I-III, in green), ANME-1 (ANME1-350, ANME1-728; in red), and *Archaea* (ARCH915, in pink). Cell extracts for nodules from SMM 800-I were not shown due to strong interference from auto-fluorescent exopolymeric material.

Single-cell translational activity measurements (BONCAT) show large shift in nodule endolithic activity between shallow sediments and deeper horizons below the SMTZ

A subset of nodules (n=7) from 5 sediment cores were separated from their host sediment and incubated with the methionine analog HPG under sulfate- and methane-rich conditions to examine translational activity by endolithic microorganisms using biorthogonal noncanonical amino acid tagging (BONCAT), e.g., (49, 51, 52). Nodules were recovered after a 14-week incubation at 4ºC, and BONCAT analysis of carbonate-associated cells showed high heterogeneity in activity for both single cells and cell aggregates between nodules, ranging from less than 1% up to 39% of the recovered cells. The relative fraction of extracted cells and cell aggregates (>5 µm) with a confirmed BONCAT signal compared to those without is provided in Table 1.4. Representative examples of BONCAT stained cells and aggregates from each of the seep areas are shown in Fig. 1.10.

Table 1.4
Proportion of BONCAT-active cells to non-BONCAT-active cells from incubated nodules

Seep Area	Core ID	Nodule Horizons (cmbsf)	BONCAT-Active Single Cells	BONCAT-Active Aggregates
SMM 800-I	LC62	36-42	<1% (n = 765)	*no aggregates observed*
		51-57	<1% (n = 767)	0% (n=1)
SMM 800-II	PC44	6-9	39% (n = 792)	60% (n = 10)
		9-12	14% (n = 1011)	40% (n = 5)
SMM 800-III	PC69	3-12	4% (n = 1041)	62% (n = 21)
SMM863	LC66	42-45	<1% (n = 1062)	*no aggregates observed*
	LC74	42-45	7% (n = 857)	100% (n = 2)

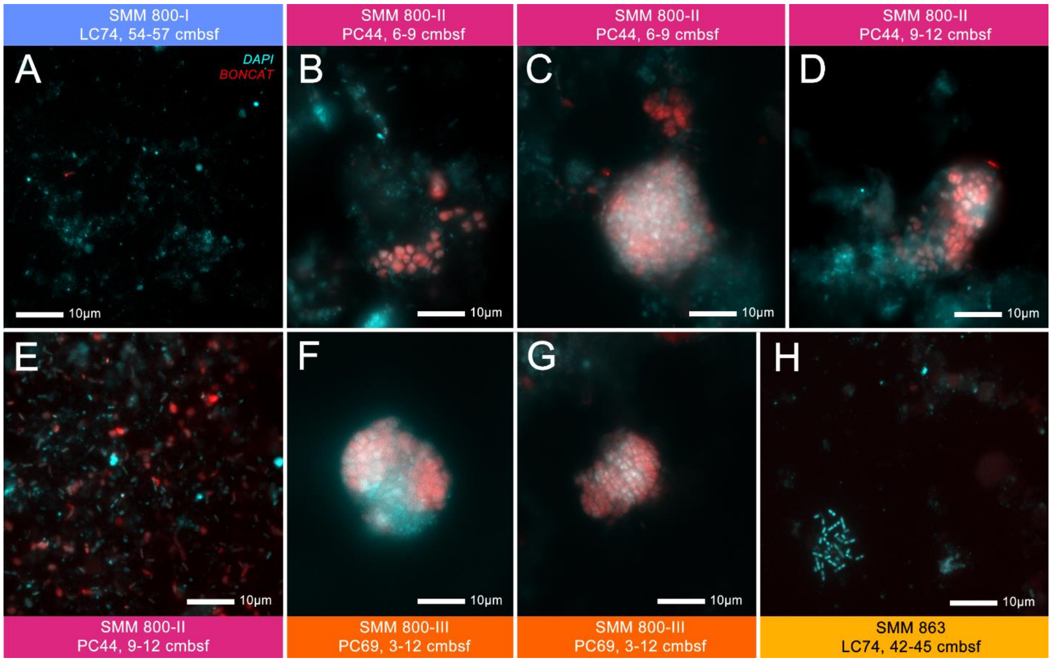

Fig. 1.10 – Cell extracts from recovered carbonate nodules at all four seep areas, displaying the presence/absence of newly synthesized proteins with BONCAT (in red) after a 14-week incubation with methionine analog, L-Homopropargylglycine (HPG). DAPI staining of nucleic acids indicating cells is in cyan. Positive BONCAT signal was consistently observed in all extracts from the shallower nodules at SMM 800-II and 800-III, compared to the consistent lack of signal at SMM 800-I and 863.

Nodule-hosted cells recovered from SMM 800-I (LC62, 36-42 and 51-57 cmbsf, both well below the SMTZ), did not exhibit evidence of HPG assimilation among the >700 cells examined per sample. Additionally, these nodules lacked cell aggregates commonly found in shallower sediment horizons. The absence of a BONCAT signal aligns with the minimal sulfide production observed prior to the HPG incubation period (Fig. 1.25). We observed similar results with a deep nodule recovered from SMM863 below the SMTZ (LC66, 42-45 cmbsf). However, the nodule recovered from the parallel core (LC74) from the same depth horizon did show a weak BONCAT signal (7% of total cells screened) in single cells and aggregates, despite lack of observed sulfide production prior to HPG incubation (Fig. 1.25). This signal indicated that these endolithic habitats below the SMTZ continued to support viable microorganisms (Table 1.4).

The low microbial activity and lack of cell aggregates observed in the majority of nodule incubations from the deeper sediment intervals contrasted with the nodules recovered from the shallow horizons within the SMTZ (between 3-12 cm) at SMM 800-II and 800-III. Here, we observed active HPG assimilation for both single cells and cell aggregates, with up to 39% of the single cells (n=792) and 62% of aggregates (n=21) showing a positive BONCAT signal (Table 4). FISH-based identification of BONCAT positive cells indicated a large fraction of these active cells were Archaea (ARCH915 probe, Fig. 1.26). These samples actively produced sulfide prior to the incubation, reaching values as high as 8 mM after 30 days (Fig. 1.25), supporting their likely involvement in sulfate-coupled methane oxidation.

3. Discussion

In this study, increased depth sampling directly within active seeps using ROV-deployed long cores provided a window into microbial community transitions within and below the SMTZ. We sampled seven sediment cores containing carbonate nodules directly within microbial mat-associated, active seep habitats from four seep areas associated with two carbonate mounds in the Santa Monica Basin. The three seep areas at SMM 800 showed consistent geochemical profiles with high, sulfate-coupled AOM activity characterized by a shallow (<9 cmbsf), sharply defined SMTZ, whereas the two long cores from SMM 863 instead revealed a much deeper (~21 cmbsf) sulfate depletion zone suggestive of lower methane flux and AOM activity (21). Carbonate nodules recovered from all four seep areas across these distinct geochemical zones enabled us to investigate the physical properties, along with the diversity and metabolic activity of nodule-hosted microbial communities relative to their host sediments, with implications for the degrees to which these incipient carbonate nodules preserve records of past AOM and continue to serve as habitats for *in situ* endolithic communities.

Closely-linked sediment and nodule-hosted microbial communities indicate ongoing exchange throughout and below the SMTZ

16S rRNA-based community profiles from recovered nodules at all the characterized seep areas reinforced a close similarity to those of their host sediments, regardless of depth and geochemical regime. Non-metric multidimensional scaling (NMDS) ordination of all sediment and nodule-derived ASVs (Fig. 1.23) also showed a consistent, area-specific clustering between nodules and sediments. This coupling generally agrees with previous studies comparing various carbonate substrates, including nodules, from seep sites at Hydrate Ridge, OR; Eel River Basin, CA; and the Sea of Japan (14–16, 22).

Collectively, these shared microbial community profiles across major geochemical transition zones are strong evidence of continuous colonization and response to *in situ* conditions which collectively influence nodules and sediments, rather than a time-integrated, microbial ‘thumbprint’ of the surrounding sediment.

This is further supported by the high open porosities measured for the nodules in this study, regardless of depth and pore size distributions (< 350 µm), which likely facilitate continuous colonization by surrounding seep sediments. Indeed, 13-month seafloor colonization experiments of sterilized carbonate substrates within and on the periphery of deep-sea methane seeps previously demonstrated active colonization by seep sediment microorganisms, including ANME-1 (16). Although the mechanisms of potential exchange between nodules and sediments remain unknown — especially since motility has not been definitively observed in ANME — previous studies have hypothesized the involvement of fluid advection and/or methane ebullition in facilitating active carbonate colonization (14, 16, 53, 54).

Further, the high nodule open porosities support sufficient connectivity for methane and sulfate perfusion, along with the diffusion of small organic molecules (e.g., HPG, used in BONCAT experiments). As such, these nodules likely experience very similar, current geochemical pressures as the surrounding sediments, which supports the shared microbial community transitions observed in both sediments and nodules from SMM 800 and SMM 863. Indeed, subsurface methane fluxes can vary over periods that can last from days to centuries (55–57), where changes in geochemical stratification exert an active role in structuring the sediment microbial communities performing AOM and facilitating authigenic carbonate precipitation (1, 14, 36, 58–60).

Isotopic and mineral signatures from the nodules recovered below the SMTZ also record carbonate precipitation in different geochemical regimes from the present environments observed. Despite being a sulfate-depleted environment, the consistently depleted $\delta^{13}C$ values for these nodules — below that of marine organic carbon, -25‰ (61) — support at least a partly AOM-driven origin, and thus preclude exclusive precipitation under the current geochemical conditions. Indeed, all the nodules at SMM 800-I were aragonite-rich (78.2-85.2%), suggestive of a history largely informed by shallower, sulfate-bearing sediments (62, 63). By contrast, the greater Mg-calcite content (45.1-65.1%) in the nodules from SMM 863 support a longer-lived interval in a deeper, more sulfate-limited AOM environment (6, 59, 64, 65). Together, these data suggest that the nodules recovered at depth are likely to have experienced microbial community shifts to reflect communities better adapted to *in situ* conditions, which agrees with a model of continued colonization from the surrounding sediments.

Persistence of ANME lineages suggest potential adaptation or survival under sulfate-poor conditions below SMTZ

Long cores collected from both SMM 800-I and SMM 863 revealed the consistent dominance of ANME-1 lineages over ANME-2 in the deeper sulfate-depleted sediments and nodules, consistent with several previous studies that have noted this general pattern in seep ecosystems worldwide (24, 26, 28, 30–32, 66, 67). The occurrence of ANME-1 lineages well below the SMTZ, frequently representing the same ASVs as those found within zones of high AOM activity, may reflect thus greater physiological plasticity among this archaeal lineage.

Interestingly, the difference in community profiles below the SMTZ between SMM 800-I (LC62) and SMM 863 (LC74, LC66) attests to additional environmental factors driving niche differentiation in seep sediments and nodules in this geochemical zone. While the dominance of ANME-1b below the SMTZ at SMM 863 may be linked in part to AOM with known ANME partners Seep-SRB1 and Seep-SRB2, the low abundance (<1%) of *Desulfobacterota* sequences below the SMTZ at SMM 800-I suggest that the ANME-1a cells at depth may persist without a sulfate-reducing partner. FISH data from several environments have documented the occurrence of ANME-1 as single cells without an attached bacterial partner (23, 66, 68–71), further supportive of ANME-1's metabolic flexibility beyond sulfate-coupled AOM.

Notably, the occurrence of putative methylotrophic methanogens within the *Methanofastidiosales* at depth supports the transition to a methanogenic regime below the SMTZ, where ANME-1a and *Caldatribacteriota* (exclusively JS1, Supplementary Data, Table T2) were found to co-occur. JS1 has been previously identified in anaerobic and/or methanogenic seep sediments worldwide (16, 26, 72–74), and hypothesized to participate in hydrocarbon degradation that may supply key substrates for methanogenesis (44, 73–75). Indeed, it has also been hypothesized that at least some members of the ANME-1 may be capable of methanogenesis (31, 70, 76–80). Although porewater methane concentrations do not conclusively support methane production, previous methane measurements at SMM 800 (33) do support a biological origin for methane, based on the purity and isotopic signature (-70.8‰ $\delta^{13}C$). Similarly, the observed rise in porewater DIC and associated $\delta^{13}C$ in the deeper sediment horizons at SMM 800-I (LC62) may be explained by ^{13}C-enriched DIC produced during methanogenesis (81, 82). Enriched ^{13}C content associated with an increased dolomite fraction in a deeper nodule from SMM 800-I (LC62, 24-27 cmbsf) also agrees with carbonate formation in historically methanogenic sediment regimes below the SMTZ (6, 64) — a phenomenon additionally observed for a sub-SMTZ nodule recovered from SMM 863 (LC74, 33-39 cmbsf).

Beyond methanogenesis, the observed co-occurrences of ANME-1 lineages, *Methanofastidiosales*, and JS1 may also attest to Fe-coupled AOM below the SMTZ at SMM 800-I. Fe-coupled AOM has been observed in sulfate-depleted marine sediments (29, 83–91), where explicit associations between ANME-1a/1b, JS1, and *Methanofastidiosales* have been statistically supported within seep sediments likely hosting Fe-AOM (29). Further, the detection of ANME-3 in the lower (51-57 cmbsf) horizons of core LC62 at SMM 800-I aligns with observations of ANME-3 in sulfate-depleted marine sediments and microcosms supporting Fe-AOM (83, 85). Ultimately, lack of dissolved iron concentrations for the sediment or discernible iron mineral content in the nodules precludes geochemical support for Fe-AOM at SMM 800-I. Still, past observations of this metabolic regime and its connection to frequently observed microbial taxa in globally-distributed seep sediments below the SMTZ — including sediments and nodules at the seep areas in this study — suggest that the extent of AOM below the SMTZ at active seeps may be under-constrained.

More broadly, the co-occurrence of both ANME/SRB and methanogenic lineages at SMM 800-I may also suggest *in situ* mixing of AOM and methanogenic regimes. These regimes have been hypothesized to co-occur in marine sediments (92) and have been reported for sediments in the Bothnian Sea (87). Significant correlations between ANME clades and methanogen groups from sulfate-depleted sediments at the Okinawa Trough have also suggested a degree of cryptic methane cycling (29). Collectively, these studies underscore the complexity of resolving distinct metabolic regimes in seep sediments.

Interestingly, the weaker-to-negligible BONCAT signal in incubated nodules from below the SMTZ at SMM 800-I and SMM 863 under sulfate and methane-replete conditions indicates that substrate concentrations alone may be insufficient to stimulate measurable AOM activity in nodules at depth over the time period of the incubation (3.5 months). This was despite recovering high cell abundances that included both single cells and aggregate morphologies consistent with ANME (including FISH-detectable ANME-1) in the deeper nodules. Together, these data suggest that measuring metabolic activity for incubated nodules recovered at depth may require longer observation periods, or more sensitive measurements.

In this regard, the minimal activity observed for carbonate nodules below the SMTZ may be compared to that of seafloor carbonates in low-activity seep areas. Indeed, *in situ* experiments transplanting seafloor-exposed carbonates from low to high activity seepage areas by (16) reported shifts towards microbial community structures enriched in lineages involved in AOM and sulfur-based metabolisms after 13 months. Further, sulfide measurements from incubated low activity seafloor carbonates in (11) showed that reactivation of AOM in hosted endolithic communities could take months to years. By contrast, previous $^{14}CH_4$ radiotracer measurements of methane oxidation rates from low-activity seep carbonates, incubated under similar conditions, showed detectable, if low methane oxidation (<200 nmol after 7 days) after the introduction of AOM-favorable conditions (8).

Collectively, these data may also point to the understudied nature of metabolic dormancy in seep microbial communities. Previous studies have diverged on interpretation of gene-based profiles of seep sediments and buried seep carbonates, where relict, or 'fossil' DNA has been proposed to persist in marine sediments (93–95) and cited in buried seep carbonate crusts (58, 59, 90), such that community profiles are not representative of metabolically viable cells. However, recent studies have suggested that 'fossil' DNA negligibly affects taxonomic surveys of environmental samples, especially in marine sediments below the bioturbation zone and even across systems where physical protection of DNA (e.g., seep carbonates) may generate bias (96, 97). As such, we consider 16S rRNA-based nodule community profiles to largely reflect the intact cell assemblage observed in nodules from all depths, with clear variation in metabolic activity with increasing depth below the SMTZ, representing a mixture of dormant and active microorganisms within this endolithic habitat.

Future investigations at methane seeps should therefore seek to better characterize the role of AOM in both the sediment and nodules below the SMTZ, which remains poorly understood. Longer (>1 year), lab-based studies examining the dynamics and range of metabolisms leveraged in these methane-rich, sulfate-poor conditions may shed additional information on factors driving metabolic activity in low-energy seep environments and how sensitive these communities are to the types of geochemical changes characteristic of transient methane seep activity.

Mechanisms, timescales for sediment community entrapment or exchange in nodules remain underexplored

Although continued exposure and exchange between seep nodules and sediments is strongly supported by the observations presented in this study, the processes or conditions that may act to decouple the nodule environment from its surroundings remain to be more clearly defined. Minor offsets observed between sediment and nodule communities in NMDS ordination of all sediment and nodule-derived ASVs (Fig. 1.23) may reflect subtle substrate-level differences in community structure. Further, we observed higher community richness in shallow sediments compared to nodules at SMM 800-II and 800-III (Table 1.7). This trend has also been observed previously in methane seeps at Hydrate Ride, OR (14, 22), and may suggest a local environment more favorable to certain microbial taxa. Indeed, lower cell and cell aggregate abundances in the nodules from SMM 800 and SMM 863 relative to the surrounding sediments may result from niche-specific differences and/or likelihood of some barriers to free exchange between sediments and porous carbonate nodules.

Minor discrepancies between sediment-nodule pairs have also been hypothesized to originate from translocation events that disrupt the original emplacement of incipient seep carbonates. These translocation events act on a local basis and may be driven by sudden gas hydrate decomposition or ebullition events (14). Still, the prevalence of this phenomenon is not known, as the formation and depositional history of seep nodules remains poorly constrained. Sediment-hosted seep carbonates are thought to be continuously subject to burial by continuous sediment transport from nearby coasts, uplift from tectonic movements or gas hydrate accumulation (6, 33, 64), and dissolution from nearby sulfide oxidation and/or aerobic methane oxidation (98–103). In addition to precipitation dynamics, these forces are all expected to shape the duration and nature of exchange between sediments and hosted carbonate nodules in ways that outline future paths of investigation. Although the ages of the nodules in this study remain unconstrained (though loosely estimated at 10^2-10^3 years, (33)), the data presented in this study suggest that over the interval since their formation, diagenetic forces have not acted to significantly decouple sediment and nodule microbial communities.

Additional sampling of seep sediment-hosted nodules should seek to more clearly define the time-constrained formation and diagenetic history captured by these understudied carbonates relative to their surrounding sediments, especially in instances where nodule-hosted microbial communities and surrounding sediment communities differ. Uranium-thorium (U-Th) dating, combined with $\delta^{13}C$ and X-ray diffraction (XRD) characterizations of these sediment-hosted carbonates can better address their age, provenance, and subsequent diagenetic history. In turn, these studies can advance our understanding of controls informing continued microbial habitation in seep sediment-hosted nodules.

4. Conclusions

In this study, we integrated microbiological and geochemical analyses of paired seep carbonate nodules and host sediments spanning the SMTZ and below at two previously described seep sites in the Santa Monica Basin, CA. We extend prior characterizations of seep sediment-hosted nodules with this integrated analysis, mapping changes in nodule-hosted microbial community structure and activity of these endolithic microorganisms across steep geochemical and microbiological transitions. By sampling within and below the SMTZ, we captured similar community transitions in both nodules and sediments, suggestive of continued perfusion and exchange between nodules and surrounding sediments, regardless of geochemical conditions. Porosity and mineralogy measurements also indicated sediment-nodule connectivity was feasible and had likely persisted throughout the nodule's formation, regardless of formation environment. Unique community structures beneath the SMTZ also attested to different metabolic regimes captured in both sediments and nodules, with the potential for co-occurrence of methanogenesis and AOM. Still, BONCAT activity measurements under sulfate/methane-rich conditions showed that the deeper nodules collected below the SMTZ were slow or no longer capable of producing measurable evidence of AOM within the 14-week incubation period compared to nodules from near-seabed horizons supporting active, sulfate-coupled AOM. Future investigations should explore the range of AOM and non-AOM metabolisms feasible in seep sediment ecosystems in wider detail and seek to more accurately constrain the range of diagenetic histories captured by seep nodules to better constrain the past and current degree of AOM activity recorded in these endolithic habitats.

5. Materials and Methods

Sample collection

Sediment cores were collected with the manipulator arm using the *ROV Doc Ricketts* during dives DR1329 and DR1333 during the WF05-21 Southern California cruise on the *R/V Western Flyer*. Additionally, we included data from one core (PC64) collected on dive DR1248 by ROV *Doc Ricketts* at SMM 800 in February 2020 during the WF02-20 Southern California cruise on the *R/V Western Flyer*. Additional information on site contexts and additional sample recovery details may be found in the Supplemental Material. A further detailed summary of all the sediment and nodules in the study is also included in Supplementary Data, Table T1.

Upon recovery, all cores were kept in a 4°C walk-in cooler until processing. Within hours of collection, sediment cores were documented and sectioned shipboard into 1- or 3-cm horizons by upward extrusion. Nodules were manually identified during core sectioning and kept within the associated sediment horizons. These horizons were then bagged in sterile Whirl-Pak bags, sealed in Ar-flushed Mylar bags (IMPAK Corporation), and maintained in cold storage at 4°C for, and during, transport to the laboratory.

In the laboratory (<2 weeks after sample collection), nodules >1cm in diameter were manually extracted from the bagged, anoxic sediment horizons under N_2 and rinsed three times in 0.22 μm-filtered, 3X phosphate-buffered saline (PBS, as in (104)) to remove any adhered sediment. After rinsing, nodules from each horizon were then sub-sampled for various physical, geochemical, microbiological analyses (further detailed by section titled in the Supplemental Material). Due to limited sample available for multiple analyses, some nodules were combined across adjacent sediment horizons and treated as the representation of a larger segment of the sediment core collected (Supplementary Data, Table T1). We conducted a second cleaning step for the rinsed nodules used for DNA-based community analysis and visualization by fluorescence microscopy to minimize sediment contamination following the optimized protocol for DNA extraction from carbonate nodules described in (14). In (14), rigorous testing for sufficient removal of surface contamination from the sediment hosted nodules was tested using *E. coli* as a tracer, with the following protocol demonstrating complete removal of DNA from the exogenously introduced microbes. Briefly, this surface treatment included additional rinses with cold, 0.22 μm-filtered 3X PBS, sonication, and centrifugation (additional details are provided in the Supplemental Material). Rinsed nodules designated for activity measurements with bioorthogonal non-canonical amino acid tagging (BONCAT) (51) were immediately transferred to separate, sterile, acid-washed media bottles, submerged in cold, 0.22 μm-filtered, N_2-sparged artificial seawater (media composition available in Supplemental Material Table 1.10), and stoppered with an acid-treated butyl rubber stopper (Th. Geyer GmbH & Co. KG). After immersion, bottle headspaces were flushed with pure CH_4 for 1 minute with a needle and then pressurized to 2 bar. Samples were incubated in the dark at 4°C.

Methane measurements

On both the WF05-21 and WF0-20 cruises, sediment methane samples were collected by 1 mL cut off syringe from each sediment core horizon and immediately transferred into 3 mL of 5M NaOH in a pre-weighed gas-tight 10 mL Restek vial, shaken to mix, and then stored upside down at room temperature until analysis. In the laboratory, methane concentrations in the headspace of the vials were measured with a Hewlett Packard (HP) 5890 Series II Plus Gas Chromatography system with a flame ionization detector, connected to a HP 7694 Headspace Sampler with a 1 mL sample loop. The GC column was a 30 m HP-Plot/Q column with inner diameter (I.D.) of 0.32 mm. The software used for analysis was Agilent GC ChemStation (version A.09.03 [1417]). A calibration series ranging from 250 ppm (v/v) to 5000 ppm (v/v) was run immediately prior to samples using lab grade CH_4 gas (100%) injected into sealed 10 mL Restek vials using a gas-tight syringe. Methane volumetric ppm values were converted to μmol assuming ideal gas behavior at standard temperature and pressure. These values were normalized relative to the mass of sediment added to the Restek vials during the cruise, where masses were corrected for porosity by weighing sediment from each horizon before and after drying in an oven.

Sulfate measurements

On both cruises, sediment porewater was collected in pressure-driven ‘squeezers’ (105), using argon to compress the sediment section against a 47 mm, 0.22 μm polycarbonate filter (Thermo Fisher) to recover sediment-free porewater in gas-tight, 60 mL syringes while minimizing exposure to air. Porewater from each sediment horizon was then filtered through a 0.22 μm polyethersulfone (PES) syringe filter (Tisch) into 2 mL Eppendorf tubes and stored at -20°C for later analysis. In the laboratory, the concentration of major ion species (e.g. sulfate) was determined by ion chromatography at the Resnick Sustainability Institute's Water and Environment Lab at the California Institute of Technology. Specifically, samples were run on a 250 mm Dionex IonPac instrument (Thermo Fisher) with AS19-4μm and CS16-4μm columns for anions and cations, respectively — each with 50 mm versions as guard columns. 100 μL of each porewater sample were diluted 50x in milliQ ultrapure DI water (final volume 5 mL) before running. Standard curves were generated using calibration standards diluted similarly to samples, with 100 μL of 500 mM NaCl added to mimic typical seawater sample peak behavior. Analyte peaks were automatically integrated and major ion species, including sulfate, were automatically calculated using the prepared standards with the Chromeleon Dionex IC (Thermo Fisher, v7.2.9) software, with manual inspection to ensure regular peak shapes.

Sulfide measurements

Samples for porewater sulfide concentrations were prepared by the addition of 0.5mL of 0.22 μm filtered porewater from each sediment horizon to 0.5 mL of 0.5M zinc acetate in a 1.5 mL Eppendorf tube to precipitate zinc sulfide. Due to its lability, sulfide samples were processed first after porewater collection from the squeezer apparatus. In the laboratory, the precipitated sulfide was quantified spectrophotometrically according to the Cline sulfide assay protocol (106). Briefly, this involved the acidification of the sample and reaction with N, N-dimethyl-p-phenylenediamine dihydrochloride in presence of ferric chloride. The resulting methylene blue solution’s absorbance was measured in duplicate at 670-nm wavelength with a microplate reader (Sunrise, Tecan). Concentrations were calculated after subtracting absorbance values from DI H_2O blanks from concurrently measured zinc sulfide standards prepared from sodium sulfide solutions (0.12 mM to 25 mM). We additionally measured 10x and 50x dilutions to allow for quantification of highly sulfidic samples within the linear color range.

DIC and $\delta^{13}C$ analyses

We measured dissolved inorganic carbon (DIC) concentrations and its $\delta^{13}C$ in porewater (C_{pw}), as well as the $\delta^{13}C$ of nodule (C_{nod}) where sufficient porewater or nodule material allowed. After extraction and rinsing, nodule samples were air dried and ground to a fine powder with an agate mortar and pestle, which was cleaned with DI water and ethanol between samples. Replicate subsamples of powdered nodules (0.45-0.65-mg) were added to 12 mL, acid-washed and combusted Exetainer vials (Labco). The vials were then flushed with helium for 2 minutes and acidified with 200 µL 43.5% phosphoric acid. To measure porewater DIC and $\delta^{13}C_{pw}$, 1 mL of extracted porewater was immediately added via syringe to 12 mL, acid-washed and combusted Exetainer vials (Labco) pre-flushed with helium and pre-loaded with 100 µL 43.5% phosphoric acid during the WF05-21 and WF02-20 cruises. In the laboratory, the released CO_2 gas was measured on a GasBench II coupled to a Delta

V Plus isotope ratio mass spectrometer (IRMS) at the Stable Isotope Facility at the California Institute of Technology.

Concentrations of DIC were determined based on comparison of the average total peak area of sample injections to replicate sodium bicarbonate standard curves. The 6-point dilution standard curves for the porewater DIC used ultrapure DI H_2O as a background standard and a solution series (1, 2.5, 5, 10, 20, and 30mM) of sodium bicarbonate (-2.9‰).

$\delta^{13}C_{nod}$ and $\delta^{13}C_{pw}$ values were corrected for instrument dependency on CO_2 concentration and then normalized to the VPDB scale with a two-point calibration (107) using the Merck ($\delta^{13}C$ = -49.2‰) and Carrara Marble (CM 2013, $\delta^{13}C$ = +2‰) carbonate standards. Here, we use solid carbonate powder isotope standards for both $\delta^{13}C_{nod}$ and $\delta^{13}C_{pw}$ on the basis of a quantitative conversion (i.e., total carbonate consumption) and since O isotopes are not considered for this study.

Nodule porosity & porosimetry

During nodule sub-sampling, select nodules (where sufficient material allowed) were additionally rinsed in deionized water to remove any salts and dried at room temperature for structural and mineralogical analysis. To characterize the internal structure of the recovered carbonate nodules, we determined their open porosity using a water intrusion (or Archimedes) method. We followed Method A of ASTM D792 (108), which collects the dry mass, the immersed mass (i.e., mass of fluid displaced), and the saturated mass (i.e., mass of fluid-saturated object) of a nodule sample with DI water, according to Eq. 1:

$$\mu_a = \frac{(m_3 - m_1)}{(m_3 - m_2)} \times 100 \tag{1}$$

where μ_a is the apparent, or open, porosity (expressed as a percentage of the sample bulk volume), m_1 is the dry mass, m_2 is the immersed mass, and m_3 is the saturated mass. This was achieved with a density apparatus attached to a fine scale (Mettler Toledo). Additionally, we measured the pore size distribution of paired samples with Hg-porosimetry. This method uses a pressurized, non-wetting liquid (mercury) to intrude the nodule pore spaces, where the cumulative volume of intruded mercury is recorded at each pressure interval, corresponding to a certain pore size (109). We used a Micromeritics AutoPore IV Mercury Intrusion Porosimeter to measure open pore size distribution between 6 and 350 µm by recording cumulative mercury intrusion volume at 90 intervals within a pressure range of 3.51 and 206 kPa.

XRD

Nodule subsamples for mineralogical characterization with X-ray diffraction (XRD) were air-dried and ground to fine powder with an agate mortar and pestle, cleaned with ethanol between each use. Resulting powders were analyzed with a Rigaku SmartLab powder diffractometer at the X-Ray Crystallography Facility in the Beckman Institute at the California Institute of Technology. We used a Cu Kα source at 50 kV and 40 mA. Scans were run from 5° to 70° 2θ at a scanning speed of 0.02° 2θ/s. Rigaku SmartLab Studio II was used to fit and identify peaks and the 2020

Crystallography Open Database was used for phase identification. The relative semi-quantification of clearly identifiable phases was calculated according to the reference intensity ratio (RIR) based on a corundum standard and documented in weight percent. For the phases, the RIR method used the (104) peak heights of calcite, Mg-calcite and dolomite, the (111) peak height of aragonite, and the (101) peak height for quartz. Here, Mg-calcite corresponds to $(Ca_{0.9}Mg_{0.1})O_3$, as measured by (35).

16S rRNA gene sequencing

To characterize and compare the diversity and composition of the microbial communities across the seep areas represented in the dataset, we sequenced the V4 and V5 regions of the 16S rRNA gene. Here, 2mL of sediment from each core horizon was sampled by sterile 1 mL cutoff disposable syringe into a 2 mL screwcap Eppendorf tube and immediately stored at -80°C for DNA extraction. In the laboratory, doubly rinsed nodules intended for sequencing were also finely ground and frozen at -80°C after extraction from sediment and cleaning as described above. DNA was extracted from 0.15-0.3 g (wet weight) of thawed sediment or finely ground nodule powder using the DNeasy PowerSoil Pro Kit (Qiagen). Target sequences were then amplified with a 2-step Illumina sequencing strategy (110). Briefly, this involved an initial amplification with 515f (5’-TCGTCGGCAGCGTCAGATGTGTATAAGAGACAG-GTGYCAGCMGCCGCGGTAA-3’) and 926r (5’-GTCTCGTGGGCTCGGAGATGTGTATAAGAGACAG-

CCGYCAATTYMTTTRAGTTT-3') primers, followed by a second amplification to include the necessary Illumina barcodes prior to being sequenced.

Adapters from paired-end sequences were removed using 'Cutadapt' (v2.9), (111). Trimmed reads were then input into QIIME2 (v2020.11), (112), where we used a DADA2 pipeline (v1.14.1), (113) to filter and denoise the reads as well as remove chimeric sequences. ASVs with assigned taxonomy were generated from the merged, non-chimeric sequences in QIIME2 using the Silva V138.1 SSURef database feature classifier (114). Classified, non-zero ASVs for all the sediment and nodules in the study are included in Supplementary Data, Table T2. Additional details on modified DNA extraction protocols, PCR amplification, gene sequencing, and read processing are also included in the Supplemental Material.

During subsequent analysis, we calculated Shannon-Wiener and Inverse Simpson diversity indices for archaeal and bacterial ASVs from the carbonate nodules and their host sediments. Further information on how these indices were calculated are detailed in the Supplemental Material. Additionally, we performed a non-metric multidimensional scaling (NMDS) ordination of all carbonate nodule and sediment-derived ASVs. Further details on how this ordination was performed is also detailed in the Supplemental Material.

Fluorescence in situ hybridization (FISH)

During sediment core sectioning, 0.5-0.7 mL sediment per horizon was immediately added to 0.5 mL of a 0.22 μm filtered 4% paraformaldehyde solution in 3X PBS and fixed overnight at 4°C. Afterwards, the sample was washed twice with 0.22 µm filtered 1X PBS and then re-suspended in a 50% ethanol: 1X PBS medium and stored at -20°C. During nodule extraction in the laboratory, doubly rinsed nodules were finely ground with a sterile agate mortar and pestle. Immediately after grinding, the ground nodules were also fixed and washed as was done for the sediments, but re-suspended in a 70% ethanol: 1X PBS medium prior to storage at -20°C. To visualize the cells with minimal interference from sediment and mineral particles, we then performed a density separation using percoll, based on a modified protocol outlined in (8, 23, 115). Briefly, 100-200 µL fixed sediment or carbonate was added to 400 µL of a chilled, 0.22 µm filtered 'combination' buffer made of 0.5% v/v Tween 20, 3 mM sodium pyrophosphate, and 0.35% wt/v PVP (116). Samples were then sonicated on ice over 3 cycles at amplitude 20 on a Q55 sonicator (Qsonica), with 10 seconds of active sonication and 10 seconds of rest in between to avoid overheating. Next, sample tubes were shaken on a vortex mixer (Vortex-Genie 2, Scientific Industries) for 30 minutes at room temperature. We then added 400 µL of chilled, 0.22 µm filtered 1X PBS before mixing and overlaying the mixed sample on 950 µL of a chilled percoll density gradient. The gradient tubes were then centrifuged at 18,000 x g for 25 minutes at 4ºC (Microfuge 18, Beckman Coulter). After centrifugation, the density gradient supernatant was transferred to a new set of sample tubes and centrifuged again at 16,000 x g for 3 minutes at 4ºC to form cell pellets. The pellets were washed twice with 0.22 µm filtered 1X PBS.

The washed cells were then stained with a SYBR® Gold (Thermo Fisher) solution at a 25X final concentration in ultrapure DI H_2O in the dark for 15 minutes at room temperature. After staining, the cells were centrifuged at 16,000 x g for 3 minutes at room temperature, re-suspended in ultrapure DI H_2O, and stored overnight at 4ºC. The next day, the cells were mounted via vacuum filtration onto a 0.2 µm black polycarbonate filter and a 5µm PVDF backing filter (Millipore Sigma). The filters were washed twice in ultrapure DI H_2O, air dried, and then stored in the dark at 4ºC until counting. Prior to coverslip placement, each filter received ~50 µL Vectashield® Antifade Mounting Medium (VectorLabs). For counts, we used an Olympus BX51 fluorescence microscope using a 100x objective lens (Olympus). Thirty fields of view per filtered sample were surveyed to determine the number of cell aggregates and single cells. For these counts, any association of cells larger than 5 µm were considered aggregates. Cell and aggregate counts were normalized per unit dry mass for all sample types.

To observe the presence and morphologies associated with particular taxa, we used fluorescence in situ hybridization (FISH). For FISH, the washed, percoll-extracted cells were re-suspended in ultrapure DI H_2O and stored overnight at 4ºC. The following day, cell suspensions were dried at room temperature onto separate 6 mm wells on PTFE- and L-lysine-coated glass slides (Tekdon). The hybridization probes EUB338 [5’-GCTGCCTCCCGTAGGAGT-3’ (117), 3’ conjugated Alexa Fluor™ 488 dye], EUB338 II [5’- GCAGCCACCCGTAGGTGT-3’ (118), dual-labeled Alexa Fluor™ 488 dye], EUB338 III [5’- GCTGCCACCCGTAGGTGT-3’ (118), dual-labeled Alexa Fluor™ 488 dye], ANME1-350 [5’-AGTTTTCGCGCCTGATGC-3’ (19), dual-labeled Alexa Fluor™ 546 dye], ANME1-728 [5’- GGTCTGGTCAGACGCCTT-3’, designed using ARB (119) to hit the ANME1 Clade of the Silva 138.1 database), 5’ conjugated Alexa Fluor™ 546 dye], and ARCH-915 [5’-GTGCTCCCCCGCCAATTCCT-3’ (120), dual-labeled Alexa Fluor™ 647 dye] were used for the mounted cell extracts. The hybridization probe mix was prepared in sterile, 40% formamide concentration, with final concentrations of 5-ng/µL for each probe (Integrated DNA Technologies). Each well on the slide then received 10 µL of probe mix and was hybridized in the dark, overnight at 46°C. The next day, the glass slides with hybridized cells were immersed and incubated in a pre-warmed hybridization wash in the dark for 10 minutes at 48°C. The slides were then rinsed in ultrapure DI H_2O and allowed to air dry (in the dark) completely. FISH hybridization probe and wash recipes are provided in Tables 1.8-1.9.

Prior to coverslip placement, each well also received 10 µL of a 90% Citifluor™ mounting medium (Electron Microscopy Sciences) with 4.5 ng/µL 4',6-diamidino-2-phenylindole (DAPI) for nucleic acid visualization. Hybridized cells were then visualized with an ELYRA S.1 / Axio Observer Z1 super resolution microscope using a 100x objective lens (Zeiss). For control experiments, each glass slide had a well with mounted cells subjected to the entire FISH protocol but used ultrapure DI H_2O instead of probes. For these wells, negligible signal was observed.

Single cell translational activity measurements with BONCAT

Translational activity was observed by amending a subset of the bottled nodules with an anoxic L-Homopropargylglycine (HPG) solution. HPG works as a methionine analog and is incorporated during protein synthesis without significantly altering community composition or metabolic activity (49, 51, 52). After incorporation, proteins containing HPG can be fluorescently labeled through copper-catalyzed azide-alkyne 'click' chemistry, which enables detection via fluorescence microscopy (49, 52, 121, 122).

In this study, the nodules previously maintained in N_2-sparged artificial seawater with a 2 bar CH_4 headspace were separated into replicate experimental and control bottles. Where possible, the nodules were selected to minimize mass differences between experimental and control groups. Each new sterile, acid-washed bottle received 50 mL of 0.22 μm-filtered, N_2-sparged artificial seawater of the same composition (Table 1.10, sufficient to immerse the nodules). Throughout transfer and immersion, all bottles were constantly maintained under active N_2 flow to minimize oxygen exposure. After immersion, all bottle headspaces were flushed with pure CH_4 for 1 minute and pressurized to 2 bar. Samples were then incubated in the dark at 4°C for a period of 5 weeks, during which the media was periodically sampled to monitor sulfide concentrations in control and experimental bottles. After determining comparable sulfide production between each control and experimental group (Fig. 1.25), the artificial seawater media was replaced with freshly prepared 0.22 μm-filtered, N_2-sparged artificial seawater. Additionally, each experimental bottle received aqueous 0.22 µm-filtered, N_2-sparged HPG to a final concentration of 200 µM. Throughout media replacement and HPG addition, all bottles were constantly maintained under active N_2 flow to minimize oxygen exposure. After immersion, all bottle headspaces were again flushed with pure CH_4 for 1 minute and pressurized to 2 bar. Samples were then incubated in the dark at 4°C for a period of 14 weeks to ensure sufficient HPG assimilation.

At the end of the incubation period, nodules from both control and experimental bottles were ground, fixed, and washed as previously described for FISH hybridization. Cells from each fixed, ground nodule were then extracted and mounted onto separate 6 mm wells on PTFE- and L-lysine-coated glass slides as previously described. For the BONCAT dye click reaction, the glass-mounted cell extracts were then dehydrated by sequential immersion in 50% (1 minute), 80% (3 minutes), and 90% (3 minutes) ethanol: DI H_2O baths and dried room temperature.

We used BONCAT azide dye Oregon Green 488 (VectorLabs) at a final concentration of 20 µM. 10-µL of the dye solution was then added to each well and incubated in the dark for 30 minutes. For the incubation, we flushed a lidded sample container with Ar, in which we placed the mounted cells to minimize oxygen exposure, which can reduce the fluorescent signal. After incubation, the slides were washed in 0.22 µm-filtered 1X PBS for 10 minutes (in the dark), quickly rinsed in ultrapure DI H_2O, and allowed to air dry in the dark prior to FISH hybridization. Hybridization probes EUB338 [5’ conjugated cyanine 3 dye], EUB338 II [3’ conjugated cyanine 3 dye], EUB338 III [5’ conjugated cyanine 3 dye], and ARCH-

915 [dual-labeled Alexa Fluor™ 647 dye] were used. Hybridization was done at 35% formamide. Washing and addition of DAPI-Citifluor® mounting medium was performed as previously described. BONCAT click reaction and FISH hybridization recipes are listed in Tables 1.11-1.13.

Click-dyed, hybridized cells were then visualized with an ELYRA S.1 / Axio Observer Z1 super resolution microscope using a 100x objective lens (Zeiss). Fraction of cells with HPG signal were evaluated by counting HPG-incubated, extracted cells with observable signal above a mean background threshold calculated from the control cells' auto-fluorescence in the same channel. For FISH and BONCAT control experiments, each glass slide had a well with mounted, non-HPG labeled cells subjected to the entire FISH protocol but used ultrapure DI H_2O instead of probes. For these cells in these negative control wells, a negligible signal was observed.

Data availability

The Santa Monica Mounds Low Altitude Survey System (LASS) survey was done in the Spring of 2018 using *ROV Ventana* on *R/V Rachel Carson*. The Santa Monica Mounds Mapping AUV surveys were done multiple times from *R/V Zephyr* and *R/V Carson*. Featured grids and photomosaics will be available at MGDS https://www.marine-geo.org/.

The raw DNA sequence reads generated from the SMM 800 sediment cores in this study were initially submitted to NCBI under project accession number

PRJNA1196099 (sample accession numbers: SAMN45814414-SAMN45814434; SAMN45814441- SAMN45814448) and are accessible at https://www.ncbi.nlm.nih.gov/bioproject/ PRJNA1196099. The rest of the raw DNA sequence reads generated for this study (SMM 800 nodules, SMM 863 samples, experimental controls) were submitted to NCBI under accession numbers PRJNA1207588 and accessible at https://www.ncbi.nlm.nih.gov/bioproject/PRJNA1207588.

Additional acknowledgements

We are indebted to the captain, crew, and pilots of the *ROV Doc Ricketts* from the WF05-21 cruise, who made this work possible. We also thank David Caress, Charles Paull, Eric Martin, and the Autonomous Systems Operations group at the Monterey Bay Aquarium Research Institute (MBARI), as well as the crews of *R/V Zephyr* and *R/V Carson* for collection, processing, and analysis of bathymetry maps of the Santa Monica Basin. We thank S. Lim (University of Nevada, Las Vegas), J.S. Magyar (Caltech), and S. Goffredi (Occidental College) for their help in sample collection and processing during the WF05-21 Southern California cruise of the *R/V Western Flyer*, S. Connon (Caltech) for technical support and barcoding of 16S amplicons for sequencing, D. Utter (Caltech) and H. Sapers (Northern Arizona University) for support during data processing.

S.A. Parra and V.J. Orphan conceptualized the study and acquired financial support for the study. J. Mullahoo analyzed dissolved porewater methane. L.K. Quinn analyzed nodule open porosity and Hg-porosimetry. R.L. Wipfler analyzed porewater sulfate concentrations. S.A. Parra processed and analyzed all other data presented in the study, including nodule selection, porewater sulfide measurements, DIC/δ^{13}C measurements, x-ray diffraction, DNA extraction, 16S rRNA sequence analyses, fluorescence microscopy, and BONCAT incubations. M.J. Mayr and V.J. Orphan supervised the study. S.A. Parra wrote the original draft and incorporated edits before and during the publication stage. M.J. Mayr, J. Mullahoo, L.K. Quinn, R.L. Wipfler, and V.J. Orphan all participated in critical review and commentary on the paper draft before and during the publication stage.

This work was supported in part by NASA's Interdisciplinary Consortia for Astrobiology Research (ICAR) program under Award Number AWD-005316-G4 (to V.J. Orphan), the National Science Foundation under Award Number 2048666 (to V.J. Orphan), and NASA's Future Investigators in NASA Earth and Space Science and Technology (FINESST) program under Award Number 80NSSC22K1336 (to S.A. Parra). This material is based upon work supported by the U.S. Department of Energy, Office of Science Biological and Environmental Research Program under Award Number DE-SC0022991 (to V.J. Orphan).

specific commercial product, process, or service by trade name, trademark, manufacturer, or otherwise does not necessarily constitute or imply its endorsement, recommendation, or favoring by the United States Government or any agency thereof. The views and opinions of authors expressed herein do not necessarily state or reflect those of the United States Government or any agency thereof.

6. References

1. Reeburgh WS. 2007. Oceanic Methane Biogeochemistry. Chem Rev 107:486–513.
2. Boetius A, Wenzhöfer F. 2013. Seafloor oxygen consumption fuelled by methane from cold seeps. 9. Nature Geosci 6:725–734.
3. Aharon P, Schwarcz HP, Roberts HH. 1997. Radiometric dating of submarine hydrocarbon seeps in the Gulf of Mexico. GSA Bulletin 109:568–579.
4. Peckmann J, Thiel V. 2004. Carbon cycling at ancient methane–seeps. Chemical Geology 205:443–467.
5. Teichert BMA, Bohrmann G, Suess E. 2005. Chemoherms on Hydrate Ridge — Unique microbially-mediated carbonate build-ups growing into the water column. Palaeogeography, Palaeoclimatology, Palaeoecology 227:67–85.
6. Naehr TH, Eichhubl P, Orphan VJ, Hovland M, Paull CK, Ussler W, Lorenson TD, Greene HG. 2007. Authigenic carbonate formation at hydrocarbon seeps in continental margin sediments: A comparative study. Deep Sea Research Part II: Topical Studies in Oceanography 54:1268–1291.
7. Haas A, Peckmann J, Elvert M, Sahling H, Bohrmann G. 2010. Patterns of carbonate authigenesis at the Kouilou pockmarks on the Congo deep-sea fan. Marine Geology 268:129–136.
8. Marlow JJ, Steele JA, Ziebis W, Thurber AR, Levin LA, Orphan VJ. 2014. Carbonate-hosted methanotrophy represents an unrecognized methane sink in the deep sea. 1. Nature Communications 5:5094.
9. Marlow J, Peckmann J, Orphan V. 2015. Autoendoliths: a distinct type of rock-hosted microbial life. Geobiology 13:303–307.

10. Marlow JJ, Hoer D, Jungbluth SP, Reynard LM, Gartman A, Chavez MS, El-Naggar MY, Tuross N, Orphan VJ, Girguis PR. 2021. Carbonate-hosted microbial communities are prolific and pervasive methane oxidizers at geologically diverse marine methane seep sites. PNAS 118.

11. Mayr MJ, Parra SA, Connon SA, Narayanan AK, Murali R, Cremiere A, Orphan VJ. 2025. Distinct Microbial Communities Within and On Seep Carbonates Support Long-term Anaerobic Oxidation of Methane and Novel pMMO Diversity. bioRxiv https://doi.org/10.1101/2025.02.04.636526.

12. Lein AYu. 2004. Authigenic Carbonate Formation in the Ocean. Lithology and Mineral Resources 39:1–30.

13. Watanabe Y, Nakai S, Hiruta A, Matsumoto R, Yoshida K. 2008. U–Th dating of carbonate nodules from methane seeps off Joetsu, Eastern Margin of Japan Sea. Earth and Planetary Science Letters 272:89–96.

14. Mason OU, Case DH, Naehr TH, Lee RW, Thomas RB, Bailey JV, Orphan VJ. 2015. Comparison of Archaeal and Bacterial Diversity in Methane Seep Carbonate Nodules and Host Sediments, Eel River Basin and Hydrate Ridge, USA. Microb Ecol 70:766–784.

15. Yanagawa K, Shiraishi F, Tanigawa Y, Maeda T, Mustapha NA, Owari S, Tomaru H, Matsumoto R, Kano A. 2019. Endolithic Microbial Habitats Hosted in Carbonate Nodules Currently Forming within Sediment at a High Methane Flux Site in the Sea of Japan. 11. Geosciences 9:463.

16. Case DH, Pasulka AL, Marlow JJ, Grupe BM, Levin LA, Orphan VJ. 2015. Methane Seep Carbonates Host Distinct, Diverse, and Dynamic Microbial Assemblages. mBio 6.

17. Hoehler TM, Alperin MJ, Albert DB, Martens CS. 1994. Field and laboratory studies of methane oxidation in an anoxic marine sediment: Evidence for a methanogen-sulfate reducer consortium. Global Biogeochemical Cycles 8:451–463.

18. Hinrichs K-U, Hayes JM, Sylva SP, Brewer PG, DeLong EF. 1999. Methane-consuming archaebacteria in marine sediments. Nature 398:802–805.

19. Boetius A, Ravenschlag K, Schubert CJ, Rickert D, Widdel F, Gieseke A, Amann R, Jørgensen BB, Witte U, Pfannkuche O. 2000. A marine microbial consortium apparently mediating anaerobic oxidation of methane. Nature 407:623–626.

20. Orphan VJ, House CH, Hinrichs K-U, McKeegan KD, DeLong EF. 2001. Methane-Consuming Archaea Revealed by Directly Coupled Isotopic and Phylogenetic Analysis. Science 293:484–487.

21. Borowski W, Paull C, Ussler W. 1996. Marine Pore-water Sulfate Profiles Indicate in situ Methane Flux from Underlying Gas Hydrate. Geology 655–658.

22. Marlow JJ, Steele JA, Case DH, Connon SA, Levin LA, Orphan VJ. 2014. Microbial abundance and diversity patterns associated with sediments and carbonates from the methane seep environments of Hydrate Ridge, OR. Front Mar Sci 1.

23. Orphan VJ, House CH, Hinrichs K-U, McKeegan KD, DeLong EF. 2002. Multiple archaeal groups mediate methane oxidation in anoxic cold seep sediments. Proceedings of the National Academy of Sciences 99:7663–7668.

24. Orphan VJ, Ussler W, Naehr TH, House CH, Hinrichs K-U, Paull CK. 2004. Geological, geochemical, and microbiological heterogeneity of the seafloor around methane vents in the Eel River Basin, offshore California. Chemical Geology 205:265–289.

25. Blumenberg M, Seifert R, Reitner J, Pape T, Michaelis W. 2004. Membrane lipid patterns typify distinct anaerobic methanotrophic consortia. Proceedings of the National Academy of Sciences 101:11111–11116.

26. Harrison BK, Zhang H, Berelson W, Orphan VJ. 2009. Variations in Archaeal and Bacterial Diversity Associated with the Sulfate-Methane Transition Zone in Continental Margin Sediments (Santa Barbara Basin, California). Applied and Environmental Microbiology 75:1487–1499.

27. Rossel PE, Elvert M, Ramette A, Boetius A, Hinrichs K-U. 2011. Factors controlling the distribution of anaerobic methanotrophic communities in marine environments: Evidence from intact polar membrane lipids. Geochimica et Cosmochimica Acta 75:164–184.

28. Yanagawa K, Sunamura M, Lever MA, Morono Y, Hiruta A, Ishizaki O, Matsumoto R, Urabe T, Inagaki F. 2011. Niche Separation of Methanotrophic Archaea (ANME-1 and -2) in Methane-Seep Sediments of the Eastern Japan Sea Offshore Joetsu. Geomicrobiology Journal 28:118–129.

29. Chen Y, Xu C, Wu N, Sun Z, Liu C, Zhen Y, Xin Y, Zhang X, Geng W, Cao H, Zhai B, Li J, Qin S, Zhou Y. 2022. Diversity of Anaerobic Methane Oxidizers in the Cold Seep Sediments of the Okinawa Trough. Front Microbiol 13.

30. Cui H, Su X, Chen F, Holland M, Yang S, Liang J, Su P, Dong H, Hou W. 2019. Microbial diversity of two cold seep systems in gas hydrate-bearing sediments in the South China Sea. Marine Environmental Research 144:230–239.

31. Chen J, Li Y, Zhong C, Xu Z, Lu G, Jing H, Liu H. 2023. Genomic Insights into Niche Partitioning across Sediment Depth among Anaerobic Methane-Oxidizing Archaea in Global Methane Seeps. mSystems 8:e01179-22.

32. Zhang C, Fang Y-X, Yin X, Lai H, Kuang Z, Zhang T, Xu X-P, Wegener G, Wang J-H, Dong X. 2023. The majority of microorganisms in gas hydrate-bearing subseafloor sediments ferment macromolecules. Microbiome 11:37.

33. Paull CK, Normark WR, Ussler W, Caress DW, Keaten R. 2008. Association among active seafloor deformation, mound formation, and gas hydrate growth and accumulation within the seafloor of the Santa Monica Basin, offshore California. Marine Geology 250:258–275.

34. Normark WR, Piper DJW, Sliter R. 2006. Sea-level and tectonic control of middle to late Pleistocene turbidite systems in Santa Monica Basin, offshore California. Sedimentology 53:867–897.

35. Althoff PL. 1977. Structural refinements of dolomite and a magnesian calcite and implications for dolomite formation in the marine environment. American Mineralogist 62:772–783.

36. Ussler W, Paull CK. 2008. Rates of anaerobic oxidation of methane and authigenic carbonate mineralization in methane-rich deep-sea sediments inferred from models and geochemical profiles. Earth and Planetary Science Letters 266:271–287.

37. Komada T, Burdige DJ, Li H-L, Magen C, Chanton JP, Cada AK. 2016. Organic matter cycling across the sulfate-methane transition zone of the Santa Barbara Basin, California Borderland. Geochimica et Cosmochimica Acta 176:259–278.

38. Tarnovetskii IY, Merkel AY, Kanapatskiy TA, Ivanova EA, Gulin MB, Toshchakov S, Pimenov NV. 2018. Decoupling between sulfate reduction and the anaerobic oxidation of methane in the shallow methane seep of the Black sea. FEMS Microbiology Letters 365:fny235.

39. Kirkegaard RH, Dueholm MS, McIlroy SJ, Nierychlo M, Karst SM, Albertsen M, Nielsen PH. 2016. Genomic insights into members of the candidate phylum Hyd24-12 common in mesophilic anaerobic digesters. The ISME Journal 10:2352–2364.

40. Schreiber L, Holler T, Knittel K, Meyerdierks A, Amann R. 2010. Identification of the dominant sulfate-reducing bacterial partner of anaerobic methanotrophs of the ANME-2 clade. Environmental Microbiology 12:2327–2340.

41. McGlynn SE, Chadwick GL, Kempes CP, Orphan VJ. 2015. Single cell activity reveals direct electron transfer in methanotrophic consortia. Nature 526:531–535.

42. Metcalfe KS, Murali R, Mullin SW, Connon SA, Orphan VJ. 2021. Experimentally-validated correlation analysis reveals new anaerobic methane oxidation partnerships with consortium-level heterogeneity in diazotrophy. ISME J 15:377–396.

43. Murali R, Yu H, Speth DR, Wu F, Metcalfe KS, Crémière A, Laso-Pèrez R, Malmstrom RR, Goudeau D, Woyke T, Hatzenpichler R, Chadwick GL, Connon SA, Orphan VJ. 2023. Physiological potential and evolutionary trajectories of syntrophic sulfate-reducing bacterial partners of anaerobic methanotrophic archaea. PLOS Biology 21:e3002292.

44. Nobu MK, Narihiro T, Kuroda K, Mei R, Liu W-T. 2016. Chasing the elusive Euryarchaeota class WSA2: genomes reveal a uniquely fastidious methyl-reducing methanogen. 10. ISME J 10:2478–2487.

45. Dhillon A, Lever M, Lloyd KG, Albert DB, Sogin ML, Teske A. 2005. Methanogen Diversity Evidenced by Molecular Characterization of Methyl Coenzyme M Reductase A (mcrA) Genes in Hydrothermal Sediments of the Guaymas Basin. Applied and Environmental Microbiology 71:4592–4601.

46. Teske A, Wegener G, Chanton JP, White D, MacGregor B, Hoer D, de Beer D, Zhuang G, Saxton MA, Joye SB, Lizarralde D, Soule SA, Ruff SE. 2021. Microbial Communities Under Distinct Thermal and Geochemical Regimes in Axial and Off-Axis Sediments of Guaymas Basin. Frontiers in Microbiology 12.

47. Lai H, Deng Y, Yang L, Liang J, Dai L, Li L, Fang Y, Liu L, Kuang Z. 2023. Origin of natural gas within the deep-sea uncompacted sediments of the Shenhu area, northern South China Sea: Geochemical and methanogenic cultivation results. Marine and Petroleum Geology 147:106015.

48. Coon GR, Duesing PD, Paul R, Baily JA, Lloyd KG. 2023. Biological methane production and accumulation under sulfate-rich conditions at Cape Lookout Bight, NC. Front Microbiol 14.

49. Hatzenpichler R, Connon SA, Goudeau D, Malmstrom RR, Woyke T, Orphan VJ. 2016. Visualizing in situ translational activity for identifying and sorting slow-growing archaeal−bacterial consortia. PNAS 113:E4069–E4078.

50. Krukenberg V, Riedel D, Gruber-Vodicka HR, Buttigieg PL, Tegetmeyer HE, Boetius A, Wegener G. 2018. Gene expression and ultrastructure of meso- and thermophilic methanotrophic consortia. Environmental Microbiology 20:1651–1666.

51. Hatzenpichler R, Scheller S, Tavormina PL, Babin BM, Tirrell DA, Orphan VJ. 2014. In situ visualization of newly synthesized proteins in environmental microbes using amino acid tagging and click chemistry. Environmental Microbiology 16:2568–2590.

52. Hatzenpichler R, Orphan VJ. 2016. Detection of Protein-Synthesizing Microorganisms in the Environment via Bioorthogonal Noncanonical Amino Acid Tagging (BONCAT), p. 145–157. *In* McGenity, TJ, Timmis, KN, Nogales, B (eds.), Hydrocarbon and Lipid Microbiology Protocols: Single-Cell and Single-Molecule Methods. Springer, Berlin, Heidelberg.

53. Schmale O, Leifer I, Deimling JS v., Stolle C, Krause S, Kießlich K, Frahm A, Treude T. 2015. Bubble Transport Mechanism: Indications for a gas bubble-mediated inoculation of benthic methanotrophs into the water column. Continental Shelf Research 103:70–78.

54. Crémière A, Lepland A, Chand S, Sahy D, Kirsimäe K, Bau M, Whitehouse MJ, Noble SR, Martma T, Thorsnes T, Brunstad H. 2016. Fluid source and methane-related diagenetic processes recorded in cold seep carbonates from the Alvheim channel, central North Sea. Chemical Geology 432:16–33.

55. Tryon MD, Brown KM, Torres ME. 2002. Fluid and chemical flux in and out of sediments hosting methane hydrate deposits on Hydrate Ridge, OR, II: Hydrological processes. Earth and Planetary Science Letters 201:541–557.

56. Treude T, Boetius A, Knittel K, Wallmann K, Barker Jørgensen B. 2003. Anaerobic oxidation of methane above gas hydrates at Hydrate Ridge, NE Pacific Ocean. Mar Ecol Prog Ser 264:1–14.

57. Heeschen KU, Collier RW, de Angelis MA, Suess E, Rehder G, Linke P, Klinkhammer GP. 2005. Methane sources, distributions, and fluxes from cold vent sites at Hydrate Ridge, Cascadia Margin. Global Biogeochemical Cycles 19.

58. Stadnitskaia A, Muyzer G, Abbas B, Coolen MJL, Hopmans EC, Baas M, van Weering TCE, Ivanov MK, Poludetkina E, Sinninghe Damsté JS. 2005. Biomarker and 16S rDNA evidence for anaerobic oxidation of methane and related carbonate precipitation in deep-sea mud volcanoes of the Sorokin Trough, Black Sea. Marine Geology 217:67–96.

59. Stadnitskaia A, Nadezhkin D, Abbas B, Blinova V, Ivanov MK, Sinninghe Damsté JS. 2008. Carbonate formation by anaerobic oxidation of methane: Evidence from lipid biomarker and fossil 16S rDNA. Geochimica et Cosmochimica Acta 72:1824–1836.

60. Lloyd KG, Albert DB, Biddle JF, Chanton JP, Pizarro O, Teske A. 2010. Spatial Structure and Activity of Sedimentary Microbial Communities Underlying a Beggiatoa spp. Mat in a Gulf of Mexico Hydrocarbon Seep. PLOS ONE 5:e8738.

61. Meister P, Liu B, Khalili A, Böttcher ME, Jørgensen BB. 2019. Factors controlling the carbon isotope composition of dissolved inorganic carbon

and methane in marine porewater: An evaluation by reaction-transport modelling. Journal of Marine Systems 200:103227.

62. Peckmann J, Reimer A, Luth U, Luth C, Hansen BT, Heinicke C, Hoefs J, Reitner J. 2001. Methane-derived carbonates and authigenic pyrite from the northwestern Black Sea. Marine Geology 177:129–150.

63. Magalhães VH, Pinheiro LM, Ivanov MK, Kozlova E, Blinova V, Kolganova J, Vasconcelos C, McKenzie JA, Bernasconi SM, Kopf AJ, Díaz-del-Río V, González FJ, Somoza L. 2012. Formation processes of methane-derived authigenic carbonates from the Gulf of Cadiz. Sedimentary Geology 243–244:155–168.

64. Greinert J, Bohrmann G, Suess E. 2001. Gas Hydrate-Associated Carbonates and Methane-Venting at Hydrate Ridge: Classification, Distribution, and Origin of Authigenic Lithologies, p. 99–113. *In* Natural Gas Hydrates: Occurrence, Distribution, and Detection. American Geophysical Union (AGU).

65. Aloisi G, Bouloubassi I, Heijs SK, Pancost RD, Pierre C, Sinninghe Damsté JS, Gottschal JC, Forney LJ, Rouchy J-M. 2002. CH4-consuming microorganisms and the formation of carbonate crusts at cold seeps. Earth and Planetary Science Letters 203:195–203.

66. Knittel K, Lösekann T, Boetius A, Kort R, Amann R. 2005. Diversity and Distribution of Methanotrophic Archaea at Cold Seeps. Applied and Environmental Microbiology 71:467–479.

67. Orcutt B, Boetius A, Elvert M, Samarkin V, Joye SB. 2005. Molecular biogeochemistry of sulfate reduction, methanogenesis and the anaerobic oxidation of methane at Gulf of Mexico cold seeps. Geochimica et Cosmochimica Acta 69:4267–4281.

68. Treude T, Knittel K, Blumenberg M, Seifert R, Boetius A. 2005. Subsurface Microbial Methanotrophic Mats in the Black Sea. Applied and Environmental Microbiology 71:6375–6378.

69. Treude T, Orphan V, Knittel K, Gieseke A, House CH, Boetius A. 2007. Consumption of Methane and CO2 by Methanotrophic Microbial Mats from Gas Seeps of the Anoxic Black Sea. Applied and Environmental Microbiology 73:2271–2283.

70. House CH, Orphan VJ, Turk KA, Thomas B, Pernthaler A, Vrentas JM, Joye SB. 2009. Extensive carbon isotopic heterogeneity among methane seep microbiota. Environmental Microbiology 11:2207–2215.

71. Ruff SE, Kuhfuss H, Wegener G, Lott C, Ramette A, Wiedling J, Knittel K, Weber M. 2016. Methane Seep in Shallow-Water Permeable Sediment Harbors High Diversity of Anaerobic Methanotrophic Communities, Elba, Italy. Frontiers in Microbiology 7.

72. Webster G, Parkes RJ, Fry JC, Weightman AJ. 2004. Widespread Occurrence of a Novel Division of Bacteria Identified by 16S rRNA Gene Sequences Originally Found in Deep Marine Sediments. Applied and Environmental Microbiology 70:5708–5713.

73. Lee YM, Hwang K, Lee JI, Kim M, Hwang CY, Noh H-J, Choi H, Lee HK, Chun J, Hong SG, Shin SC. 2018. Genomic Insight Into the Predominance of Candidate Phylum Atribacteria JS1 Lineage in Marine Sediments. Front Microbiol 9.

74. Chakraborty A, Ruff SE, Dong X, Ellefson ED, Li C, Brooks JM, McBee J, Bernard BB, Hubert CRJ. 2020. Hydrocarbon seepage in the deep seabed links subsurface and seafloor biospheres. PNAS 117:11029–11037.

75. Liu Y-F, Qi Z-Z, Shou L-B, Liu J-F, Yang S-Z, Gu J-D, Mu B-Z. 2019. Anaerobic hydrocarbon degradation in candidate phylum ‘Atribacteria’ (JS1) inferred from genomics. The ISME Journal 13:2377–2390.

76. Biddle JF, Cardman Z, Mendlovitz H, Albert DB, Lloyd KG, Boetius A, Teske A. 2012. Anaerobic oxidation of methane at different temperature regimes in Guaymas Basin hydrothermal sediments. ISME J 6:1018–1031.

77. Bertram S, Blumenberg M, Michaelis W, Siegert M, Krüger M, Seifert R. 2013. Methanogenic capabilities of ANME-archaea deduced from -labelling approaches. Environmental Microbiology 15:2384–2393.

78. Beulig F, Røy H, McGlynn SE, Jørgensen BB. 2019. Cryptic CH4 cycling in the sulfate–methane transition of marine sediments apparently mediated by ANME-1 archaea. The ISME Journal 13:250–262.

79. Kevorkian RT, Callahan S, Winstead R, Lloyd KG. 2021. ANME-1 archaea may drive methane accumulation and removal in estuarine sediments. Environ Microbiol Rep 13:185–194.

80. Chadwick GL, Skennerton CT, Laso-Pérez R, Leu AO, Speth DR, Yu H, Morgan-Lang C, Hatzenpichler R, Goudeau D, Malmstrom R, Brazelton WJ, Woyke T, Hallam SJ, Tyson GW, Wegener G, Boetius A, Orphan VJ. 2022. Comparative genomics reveals electron transfer and syntrophic mechanisms differentiating methanotrophic and methanogenic archaea. PLOS Biology 20:e3001508.

81. Conrad R. 2005. Quantification of methanogenic pathways using stable carbon isotopic signatures: a review and a proposal. Organic Geochemistry 36:739–752.

82. Chatterjee S, Dickens GR, Bhatnagar G, Chapman WG, Dugan B, Snyder GT, Hirasaki GJ. 2011. Pore water sulfate, alkalinity, and carbon isotope profiles in shallow sediment above marine gas hydrate systems: A numerical modeling perspective. Journal of Geophysical Research: Solid Earth 116.

83. Beal EJ, House CH, Orphan VJ. 2009. Manganese- and Iron-Dependent Marine Methane Oxidation. Science 325:184–187.

84. Riedinger N, Formolo MJ, Lyons TW, Henkel S, Beck A, Kasten S. 2014. An inorganic geochemical argument for coupled anaerobic oxidation of methane and iron reduction in marine sediments. Geobiology 12:172–181.

85. Oni OE, Miyatake T, Kasten S, Richter-Heitmann T, Fischer D, Wagenknecht L, Ksenofontov V, Kulkarni A, Blumers M, Shylin S, Costa B, Klingelhöfer G, Friedrich MW. 2015. Distinct microbial populations are tightly linked to the profile of dissolved iron in the methanic sediments of the Helgoland mud area, North Sea. Front Microbiol 6.

86. Sun Z, Wei H, Zhang X, Shang L, Yin X, Sun Y, Xu L, Huang W, Zhang X. 2015. A unique Fe-rich carbonate chimney associated with cold seeps in the Northern Okinawa Trough, East China Sea. Deep Sea Research Part I: Oceanographic Research Papers 95:37–53.

87. Egger M, Rasigraf O, Sapart CJ, Jilbert T, Jetten MSM, Röckmann T, van der Veen C, Bândă N, Kartal B, Ettwig KF, Slomp CP. 2015. Iron-Mediated Anaerobic Oxidation of Methane in Brackish Coastal Sediments. Environ Sci Technol 49:277–283.

88. Egger M, Hagens M, Sapart CJ, Dijkstra N, van Helmond NAGM, Mogollón JM, Risgaard-Petersen N, van der Veen C, Kasten S, Riedinger N, Böttcher ME, Röckmann T, Jørgensen BB, Slomp CP. 2017. Iron oxide reduction in methane-rich deep Baltic Sea sediments. Geochimica et Cosmochimica Acta 207:256–276.

89. Rooze J, Egger M, Tsandev I, Slomp CP. 2016. Iron-dependent anaerobic oxidation of methane in coastal surface sediments: Potential controls and impact. Limnology and Oceanography 61:S267–S282.

90. Li J, Peng X, Bai S, Chen Z, Van Nostrand JD. 2018. Biogeochemical processes controlling authigenic carbonate formation within the sediment column from the Okinawa Trough. Geochimica et Cosmochimica Acta 222:363–382.

91. Aromokeye DA, Kulkarni AC, Elvert M, Wegener G, Henkel S, Coffinet S, Eickhorst T, Oni OE, Richter-Heitmann T, Schnakenberg A, Taubner H, Wunder L, Yin X, Zhu Q, Hinrichs K-U, Kasten S, Friedrich MW. 2020. Rates and Microbial Players of Iron-Driven Anaerobic Oxidation of Methane in Methanic Marine Sediments. Front Microbiol 10.

92. Mitterer RM. 2010. Methanogenesis and sulfate reduction in marine sediments: A new model. Earth and Planetary Science Letters 295:358–366.

93. Dell’Anno A, Stefano B, Danovaro R. 2002. Quantification, base composition, and fate of extracellular DNA in marine sediments. Limnology and Oceanography 47:899–905.

94. Dell'Anno A, Danovaro R. 2005. Extracellular DNA Plays a Key Role in Deep-Sea Ecosystem Functioning. Science 309:2179–2179.

95. Torti A, Lever MA, Jørgensen BB. 2015. Origin, dynamics, and implications of extracellular DNA pools in marine sediments. Marine Genomics 24:185–196.

96. Lennon JT, Muscarella ME, Placella SA, Lehmkuhl BK. 2018. How, When, and Where Relic DNA Affects Microbial Diversity. mBio 9:10.1128/mbio.00637-18.

97. Torti A, Jørgensen BB, Lever MA. 2018. Preservation of microbial DNA in marine sediments: insights from extracellular DNA pools. Environmental Microbiology 20:4526–4542.

98. Cai W-J, Chen F, Powell EN, Walker SE, Parsons-Hubbard KM, Staff GM, Wang Y, Ashton-Alcox KA, Callender WR, Brett CE. 2006. Preferential dissolution of carbonate shells driven by petroleum seep activity in the Gulf of Mexico. Earth and Planetary Science Letters 248:227–243.

99. Himmler T, Brinkmann F, Bohrmann G, Peckmann J. 2011. Corrosion patterns of seep-carbonates from the eastern Mediterranean Sea. Terra Nova 23:206–212.

100. Matsumoto R. 1990. Vuggy carbonate crust formed by hydrocarbon seepage on the continental shelf of Baffin Island, northeast Canada. Geochemical Journal 24:143–158.

101. Carson B, Kastner M, Bartlett D, Jaeger J, Jannasch H, Weinstein Y. 2003. Implications of carbon flux from the Cascadia accretionary prism: results from long-term, in situ measurements at ODP Site 892B. Marine Geology 198:159–180.

102. Krause S, Aloisi G, Engel A, Liebetrau V, Treude T. 2014. Enhanced Calcite Dissolution in the Presence of the Aerobic Methanotroph Methylosinus trichosporium. Geomicrobiology Journal 31:325–337.

103. Leprich DJ, Flood BE, Schroedl PR, Ricci E, Marlow JJ, Girguis PR, Bailey JV. 2021. Sulfur bacteria promote dissolution of authigenic carbonates at marine methane seeps. ISME J 15:2043–2056.

104. Dulbecco R, Vogt M. 1954. PLAQUE FORMATION AND ISOLATION OF PURE LINES WITH POLIOMYELITIS VIRUSES. Journal of Experimental Medicine 99:167–182.

105. Reeburgh WS. 1967. An Improved Interstitial Water Sampler. Limnology and Oceanography 12:163–165.

106. Cline JD. 1969. Spectrophotometric Determination of Hydrogen Sulfide in Natural Waters. Limnology and Oceanography 14:454–458.

107. Coplen TB, Brand WA, Gehre M, Gröning M, Meijer HAJ, Toman B, Verkouteren RM. 2006. New Guidelines for δ13C Measurements. Anal Chem 78:2439–2441.

108. Standard Test Methods for Density and Specific Gravity (Relative Density) of Plastics by Displacement. https://www.astm.org/d0792-20.html. Retrieved 19 September 2024.

109. Giesche H. 2006. Mercury Porosimetry: A General (Practical) Overview. Particle & Particle Systems Characterization 23:9–19.

110. Kozich JJ, Westcott SL, Baxter NT, Highlander SK, Schloss PD. 2013. Development of a Dual-Index Sequencing Strategy and Curation Pipeline for Analyzing Amplicon Sequence Data on the MiSeq Illumina Sequencing Platform. Appl Environ Microbiol 79:5112–5120.

111. Martin M. 2011. Cutadapt removes adapter sequences from high-throughput sequencing reads. 1. EMBnet.journal 17:10–12.

112. Bolyen E, Rideout JR, Dillon MR, Bokulich NA, Abnet CC, Al-Ghalith GA, Alexander H, Alm EJ, Arumugam M, Asnicar F, Bai Y, Bisanz JE, Bittinger K, Brejnrod A, Brislawn CJ, Brown CT, Callahan BJ, Caraballo-Rodríguez AM, Chase J, Cope EK, Da Silva R, Diener C, Dorrestein PC, Douglas GM, Durall DM, Duvallet C, Edwardson CF, Ernst M, Estaki M, Fouquier J, Gauglitz JM, Gibbons SM, Gibson DL, Gonzalez A, Gorlick K, Guo J, Hillmann B, Holmes S, Holste H, Huttenhower C, Huttley GA, Janssen S, Jarmusch AK, Jiang L, Kaehler BD, Kang KB, Keefe CR, Keim P, Kelley ST, Knights D, Koester I, Kosciolek T, Kreps J, Langille MGI, Lee J, Ley R, Liu Y-X, Loftfield E, Lozupone C, Maher M, Marotz C, Martin BD, McDonald D, McIver LJ, Melnik AV, Metcalf JL, Morgan SC, Morton JT, Naimey AT, Navas-Molina JA, Nothias LF, Orchanian SB, Pearson T, Peoples SL, Petras D, Preuss ML, Pruesse E, Rasmussen LB, Rivers A, Robeson MS, Rosenthal P, Segata N, Shaffer M, Shiffer A, Sinha R, Song SJ, Spear JR, Swafford AD, Thompson LR, Torres PJ, Trinh P, Tripathi A, Turnbaugh PJ, Ul-Hasan S, van der Hooft JJJ, Vargas F, Vázquez-Baeza Y, Vogtmann E, von Hippel M, Walters W, Wan Y, Wang M, Warren J, Weber KC, Williamson CHD, Willis AD, Xu ZZ, Zaneveld JR, Zhang Y, Zhu Q, Knight R, Caporaso JG. 2019. Reproducible, interactive, scalable and extensible microbiome data science using QIIME 2. Nat Biotechnol 37:852–857.

113. Callahan BJ, McMurdie PJ, Rosen MJ, Han AW, Johnson AJA, Holmes SP. 2016. DADA2: High-resolution sample inference from Illumina amplicon data. Nature Methods 13:581–583.

114. Quast C, Pruesse E, Yilmaz P, Gerken J, Schweer T, Yarza P, Peplies J, Glöckner FO. 2013. The SILVA ribosomal RNA gene database project:

improved data processing and web-based tools. Nucleic Acids Research 41:D590–D596.

115. Mayr MJ, Orphan VJ. 2024. Extraction of microbial cells from methane-seep carbonate rocks for single-cell analyses (e.g. BONCAT-FISH) using “combination buffer” and percoll density centrifugation https://doi.org/10.17504/protocols.io.rm7vzjk55lx1/v1.

116. Eichorst SA, Strasser F, Woyke T, Schintlmeister A, Wagner M, Woebken D. 2015. Advancements in the application of NanoSIMS and Raman microspectroscopy to investigate the activity of microbial cells in soils. FEMS Microbiol Ecol 91:fiv106.

117. Amann RI, Binder BJ, Olson RJ, Chisholm SW, Devereux R, Stahl DA. 1990. Combination of 16S rRNA-targeted oligonucleotide probes with flow cytometry for analyzing mixed microbial populations. Applied and Environmental Microbiology 56:1919–1925.

118. Daims H, Brühl A, Amann R, Schleifer K-H, Wagner M. 1999. The Domain-specific Probe EUB338 is Insufficient for the Detection of all *Bacteria*: Development and Evaluation of a more Comprehensive Probe Set. Systematic and Applied Microbiology 22:434–444.

119. Westram R, Bader K, Prüsse E, Kumar Y, Meier H, Glöckner FO, Ludwig W. 2011. ARB: A Software Environment for Sequence Data, p. 399–406. *In* Handbook of Molecular Microbial Ecology I. John Wiley & Sons, Ltd.

120. Stahl DA, Amann R. 1991. Development and application of nucleic acid probes in bacterial systematics, p.205-248. *In* Stackebrandt, E. and Goodfellow, M., Eds., Nucleic Acid Techniques in Bacterial Systematics, John Wiley & Sons Ltd.

121. Dieterich DC, Link AJ, Graumann J, Tirrell DA, Schuman EM. 2006. Selective identification of newly synthesized proteins in mammalian cells using bioorthogonal noncanonical amino acid tagging (BONCAT). Proceedings of the National Academy of Sciences 103:9482–9487.

122. Sletten EM, Bertozzi CR. 2009. Bioorthogonal Chemistry: Fishing for Selectivity in a Sea of Functionality. Angewandte Chemie International Edition 48:6974–6998.

7. Supplemental Material

Site Descriptions and Sample Collection

Site Classification and Sample Collection

At all sampling locations, we confirmed local methane seep activity with in-situ observation of white or orange microbial mats, clam beds, and/or gas bubbling from the seafloor; this classification scheme is consistent with previous biological and geological surveys of seeps around the world (1–3). Sediment push cores (~7.6 cm outer diameter, ~7 cm inner diameter) were collected as two core types: a shorter push core (PC, ~30 cm long) and long core (LC, ~1.22 m long).

SMM 800-I

SMM 800-I (33.799447N, 118.647171W) is located at an outcrop of seep carbonate on the western flank of the SMM 800 (NE) mound. This site was characterized by a light peach colored microbial mat adjacent to a white mat, shown in Fig. 1.11. At this site, the sediment was sufficiently deep to insert 1.22 m long cores with the ROV manipulator. LC62 was taken directly within the light peach mat, with full insertion into the sediment. Upon recovery, we observed bubble textures throughout the core, with large void spaces at 30-cmbsf.

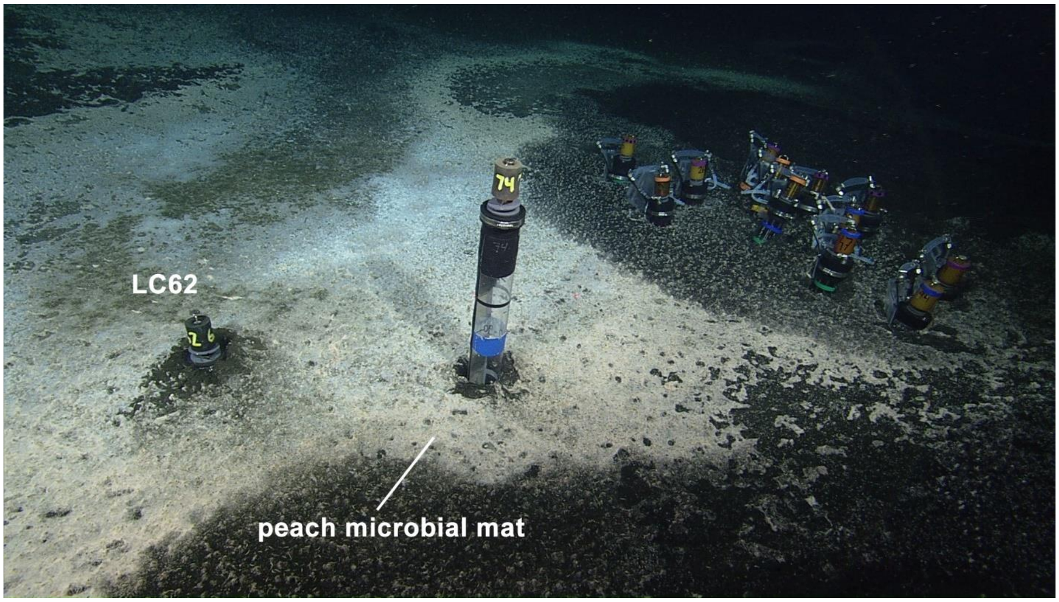

Fig. 1.11 – In situ image of the sampling site at SMM 800-I during the WF05-21 cruise. LC62 was sampled over a microbial mat (shown, left). Additional cores were taken (shown, right) but not used for this study. Core diameter is ~7 centimeters.

SMM 800-II

SMM 800-II (33.799662N, 118.646947W) is located on the northern flank of the primary SMM 800 mound, about 1 meter down the mound from SMM 800-I. We observed white and thin, grey microbial mats and small clams, shown in Fig. 1.12A. An initial push coring attempt on the white microbial mat region failed due to a hard layer observed at ~8-10 cmbsf, presumed to be carbonate platform. A second, successful coring attempt was made on the sparser, grey microbial mat. Due to this success, PC44 was taken directly on top of the grey mat, with full insertion into the sediment. The site's appearance in 2021 was notably different than when it was previously sampled in 2020. During the 02-20 Southern California oceanographic expedition of the *R/V Western Flyer*, we observed thick, white and peach-colored microbial mats, which suggested a previously higher degree of methane seepage activity. PC64 was taken on the white microbial mat adjacent to the peach-colored mat, shown in Fig. 1.12B. The full length (30 cm) was not recovered due to encountering a hard layer at 9 cmbsf (presumed to be carbonate platform), though active bubbling was observed prior to sectioning.

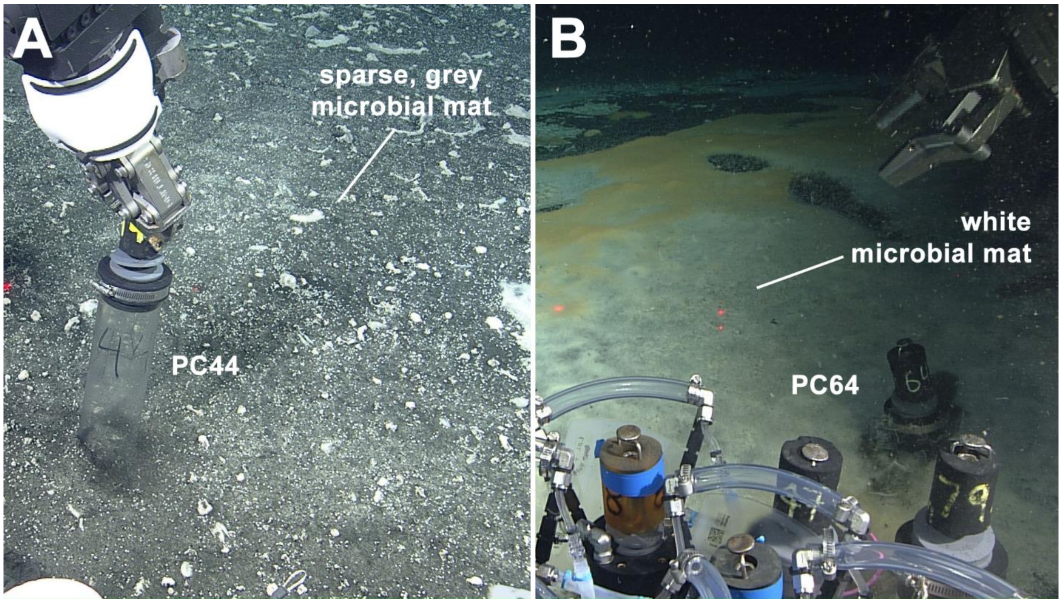

Fig. 1.12 – *In situ* images of the sampling site at SMM 800-II. A) PC44 was sampled over a sparse microbial mat during the WF05-21 cruise. B) In contrast, PC64 was sampled over a thicker microbial mat during the WF02-20 cruise at the same site, suggesting a decrease in the degree of methane seepage activity. Core diameters shown are ~7 centimeters. Laser dots in the images are 29 cm apart.

SMM 800-III

SMM 800-III (33.798962N, -118.646264W) is located on the southeastern flank of the primary SMM 800 mound, about 5 meters down the mound from SMM 800-II. We observed a large white microbial mat with a patch of dark sediment in the center. Two cores, PC43 and PC69, were taken directly over the white mat on the eastern end of the mat patch, shown in Fig. 1.13. However, both cores were only half-length cores due to solid carbonate encountered at 9 and 12 cmbsf for PC43 and PC69, respectively. Upon recovery, we observed small white clams at the surface, as well as active bubbling coming from deeper within PC69. For PC43, we observed denser white microbial mat filaments in the top 3-4 cmbsf, and active bubbling as well as trapped gas voids below 8 cmbsf.

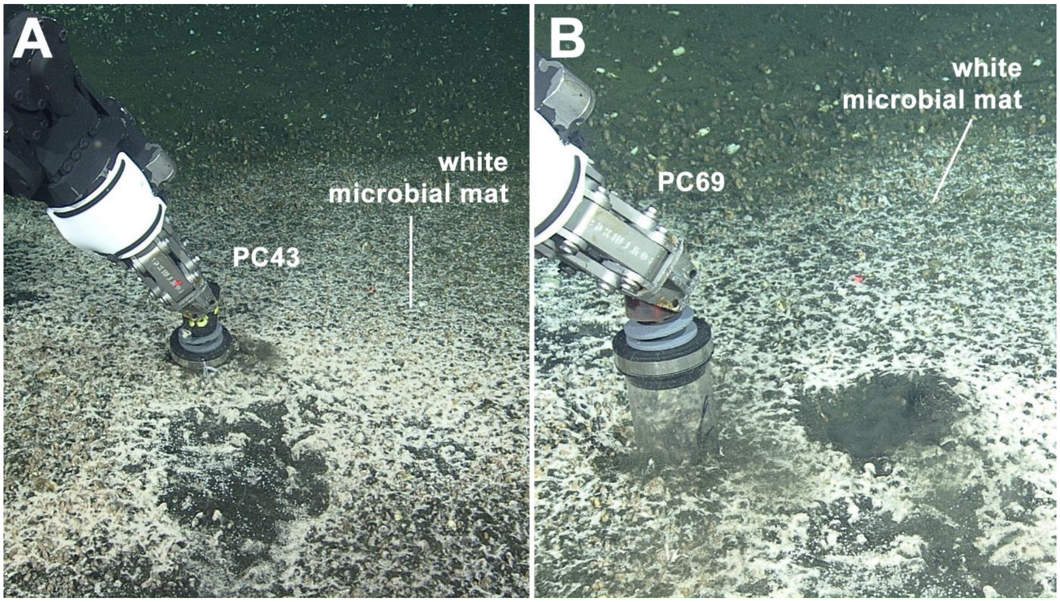

Fig. 1.13 – *In situ* images of the sampling site at SMM 800-III during the WF05-21 cruise. A) PC43 was sampled over a white microbial mat. B) PC69 was sampled to the left of PC43 (dark sediment spot to the right) over the same white microbial mat. Core diameters shown are ~7 centimeters. Laser dots in the images are 29 cm apart.

SMM 863

SMM 863 (33.788977N, -118.647171W) is located on the southern flank of the primary mound at Site 863 (863m depth), about 2.25km SW of SMM 800. We observed orange and white microbial mats, shown in Fig. 1.14. LC66 and LC74 were taken directly over the orange mat. Both cores were only able to be partially inserted due to a hard substrate (presumed to be carbonate pavement) at depth, 50-cmbsf for LC74, and 65-cmbsf for LC66.

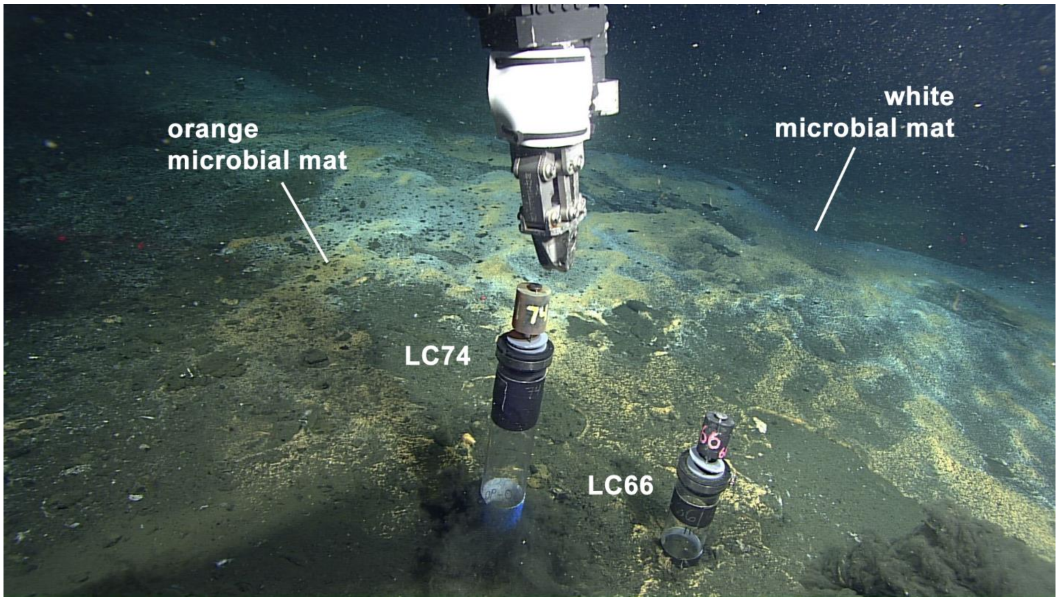

Fig. 1.14 – *In situ* images of the sampling site at SMM 863 during the WF05-21 cruise. LC66 and LC74 were sampled over the same orange microbial mat. Core diameters shown are ~7 centimeters.

Sediment Push Core Descriptions

Sediment cores from all four sites in this study featured three primary material components: black to olive-colored mud; white bivalve shell fragments ranging from large, >cm-scale shards to mm-scale 'shell hash'; and hardened, grey-brown calcitic material ranging in size from <cm rubble to >cm nodules (Fig. 1.15). We also observed a mm-sized layer of microbial mat material overlying all the cores. Calcitic rubble was found at distinct depth intervals in the sediment at all four sites and was not exclusively associated with the bivalve shell fragments. Additionally, sites with long push core (LC, ~122 cm core barrel length) sampling (SMM 800-I and SMM 863) featured calcitic rubble and nodules as deep as 57 cmbsf and 48 cmbsf, respectively. The deeper cores did not feature nodules (>cm concretions) until 24-27 cmbsf, compared to the shallower nodules (3-12 cm cmbsf) recovered within the shorter push cores (PCs) at SMM 800-II and SMM 800-III. While nodules were observed in cores PC64 and PC43 (Fig. 1.15), these were not recovered for further analysis. Table 1.5 summarizes the site-specific, nodule-bearing sediment horizons included in this study.

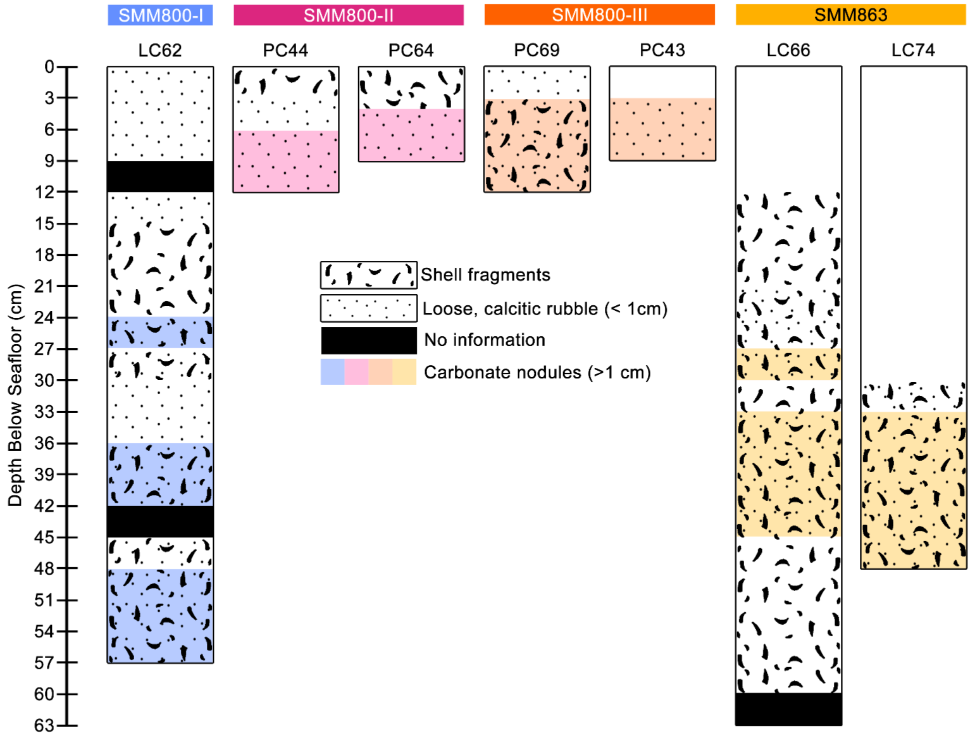

Fig. 1.15 – Pseudo-stratigraphical characterizations of all the sediment push cores collected for this study, including shorter push cores (PC) and longer cores (LC). Here, we distinguish calcitic rubble from nodules on a size-basis, where the presence of concretions >1cm were considered nodules and anything smaller was excluded.

Table 1.5
Nodule ‘horizons’ recovered for this study

Site	**SMM 800 - Site I**	**SMM 800 - Site II**	**SMM 800- Site III**	**SMM 863**	
Core ID	LC62	PC44	PC69	LC66	LC74
Nodule Horizon (cmbsf)	24-27 36-42 48-51 51-57	6-9 9-12	3-12	36-39 39-42 42-45	33-39 42-45

Geochemistry Supplemental Data

Table 1.6
Individual $\delta^{13}C$ for recovered nodules

Site	Core ID	Depth (cmbsf)	$\delta^{13}C$ (‰)
SMM 800-I	LC62	24-27	-30.49 -29.70
		48-51	-45.80 -46.25
SMM 800-II	PC44	9-12	-51.92 -51.84
SMM 800-III	PC69	3-12	-53.67 -53.92
SMM 863	LC74	33-39	-31.85 -34.53
	LC66	39-42	-49.94 -49.15

Note: values listed for each nodule horizon are replicate analyses from a single, representative nodule

16S Sequencing Methods & Supplemental Data

DNA Extraction, SSU rRNA Gene Amplification, and Illumina Sequencing

During core sectioning on the WF05-21 and the WF02-20 cruises, 2mL of sediment from each core horizon were sampled and immediately stored at -80°C for later sequencing. During nodule extraction, rinsed nodules designated for sequencing were additionally treated to minimize sedimentary contamination according to the methods optimized in (4). Briefly, each nodule was rinsed in fresh, 0.22-µm-filtered, 1X PBS and sonicated at 8W for 45 seconds in fresh, 0.22-µm-filtered, 1X PBS. Rinsing and sonication was done three times using fresh 1X PBS each time before nodules were centrifuged in fresh, 0.22-µm-filtered, 1X PBS at 4,000g for 5 minutes and removed from the supernatant. After the 'decontamination' treatment, the nodules were finely ground with a sterile agate mortar and pestle. The mortar and pestle were washed with bleach, DI H_2O, and flame sterilized with ethanol prior to each use. DNA was extracted from 0.15-0.3g (wet weight) of thawed sediment or ground nodules with the DNeasy PowerSoil Pro Kit (Qiagen). The extraction protocol was modified for nodule samples to increase DNA yields according to methods developed by (5). After confirming satisfactory yields from sediment and nodules with a Qubit 2.0 fluorometer (Invitrogen), we performed a series of PCR amplifications for a 2-step Illumina sequencing strategy, detailed in (6). For this, we first performed a duplicate initial PCR amplification of the 16S rRNA gene using the 515f and 926r primer sets with Illumina adapters (515f; 5’-TCGTCGGCAGCGTCAGATGTGTATAAGAGACAG-GTGYCAGCMGCCGCGGTAA-3’; 926r; 5’-GTCTCGTGGGCTCGGAGATGTGTATAAGAGACAG-CCGYCAATTYMTTTRAGTTT-3’, Illumina adapter show on the 5’ end). The 515f and 926r primer set covers the V4 and V5 regions of the 16S rRNA gene and amplifies both bacterial and archaeal DNA, while excluding eukaryotic DNA. PCR reaction mixes were prepared with Q5 Hot Start High-Fidelity 2x Master Mix (New England Biolabs) in a 15 μL reaction volume according to manufacturer’s directions with annealing conditions of 54°C for 30-35 cycles. With each PCR run, we ran a negative control using 1 μL of solution from a blank sample extracted with the PowerSoil Pro Kit instead of the DNA template and another negative control using 1 μL of DI H_2O. Following validation of the desired amplified sequence, duplicate samples were pooled and barcoded with Illumina Nextera XT index 2 primers that included unique 8-bp barcodes (P5; 5’-

AATGATACGGCGACCACCGAGATCTACAC-XXXXXXXX-TCGTCGGCAGCGTC-3’ and P7; 5’-CAAGCAGAAGACGGCATACGAGAT-XXXXXXXX-GTCTCGTGGGCTCGG-3’). Amplification with barcoded primers was done with Q5 Hot Start PCR mixture and 3 µL of the pooled product in a 30 µL reaction volume, annealed at 66°C, and cycled 11 times. After further validation, the barcoded PCR products were then combined in equimolar amounts into a single tube and 300uL of this pooled sample was run on a 1.5% low melt agarose gel (Fisher#BP165-25) and purified using Promega’s Wizard SV Gel and PCR Clean-up System, Promega#A9281. Finally, amplicons were sequenced (2 x 300 bp) using the MiSeq Reagent Kit v3 (600-cycle) #MS-102-3003 on Illumina’s MiSeq platform with the addition of 15-20% PhiX at Laragen (Culver City, USA).

Read Processing and Taxonomic Assignment

At Laragen, the de-multiplexed forward and reverse reads were passed through a barcode filter that removed any reads with >1 bp mismatch. Filtered reads were then assigned a quality (Q) score, and adapter, index, and sequencing primer sequences were removed prior to arrival at the laboratory. Following hand-off of the paired-end sequences, further processing was performed on the reads with a Python-based pipeline. First, samples were filtered for the correct read length before the reads were trimmed to remove degenerate primer sequences using ‘Cutadapt’ (v2.9), (7). We kept reads within 10% of the expected read length after primer removal (between 252 and 308bp in length). Trimmed reads were then input into QIIME2 (v2020.11), (8), where they were filtered and denoised with a DADA2 pipeline (v1.14.1), (9). Filtering was accomplished in DADA2 by manually specified truncation of reads in order to remove low quality base calls while retaining enough overlap between forward and reverse reads for merging (12 nucleotides minimum). Because reads were compiled from 5 separate sequencing runs, 5 different truncation value pairs were used to account for run variability. Truncation values thus ranged from 242-267 for the forward reads and 156-226 for the reverse reads. After filtering, additional reads were removed based on a maximum expected error limit of 2 and a quality score threshold of 2. Chimeric sequence removal was also accomplished with DADA2, identified by consensus across samples. The DADA2 pipeline merged the remaining paired-end sequences.

ASVs with assigned taxonomy were generated from the merged, non-chimeric sequences in QIIME2 using the Silva V138.1 SSURef database feature classifier (10). Further thinning of the assigned reads was performed to remove ASVs unique to the negative controls from the dual-amplification steps, as well as singleton ASVs introduced by removing samples. Additionally, we used the ‘decontam’ R package’s prevalence-based identification to remove likely contaminants based on the dual-amplicon negative controls, using a prevalence threshold of 0.5 (11). We also removed unassigned and Eukaryotic taxonomic assignments at the domain level, as well as any chloroplast taxonomic assignments to limit our focus to Bacterial and Archaeal diversity. After all processing was completed, the final data set had a mean sampling depth of 7148 reads. Samples with <1000 reads were dropped from the study.

Phylum 16S rRNA gene Relative Abundances

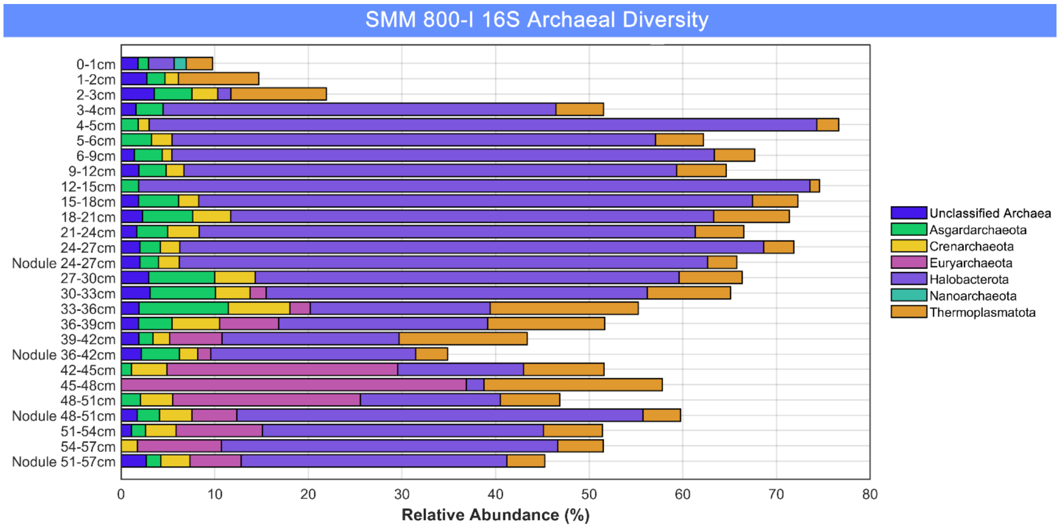

Fig. 1.16 – Stacked bar charts summarizing the depth-resolved, phylum-level 16S archaeal abundances above 1% relative to total 16S abundances in LC62 at SMM 800-I.

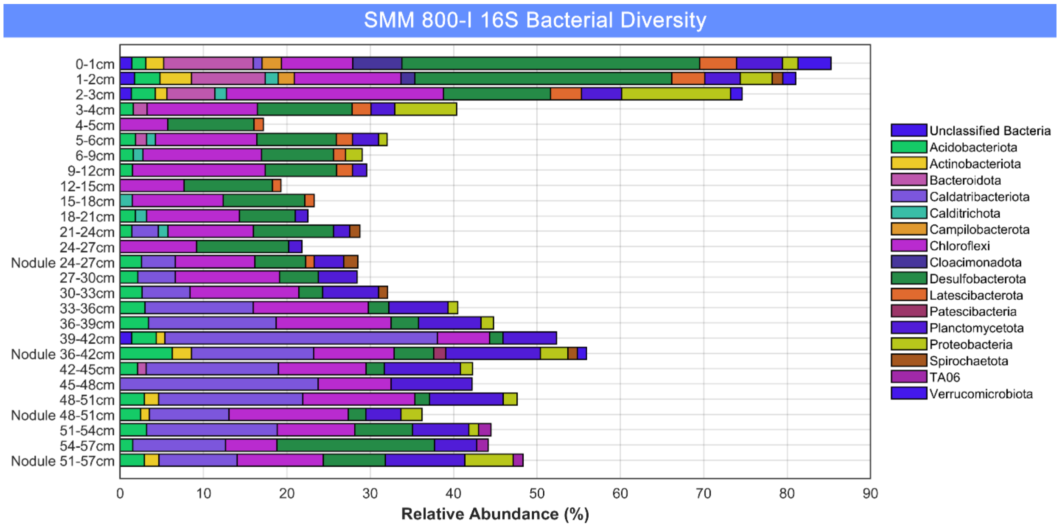

Fig. 1.17 – Stacked bar charts summarizing the depth-resolved, phylum-level 16S bacterial abundances above 1% relative to total 16S abundances in LC62 at SMM 800-I.

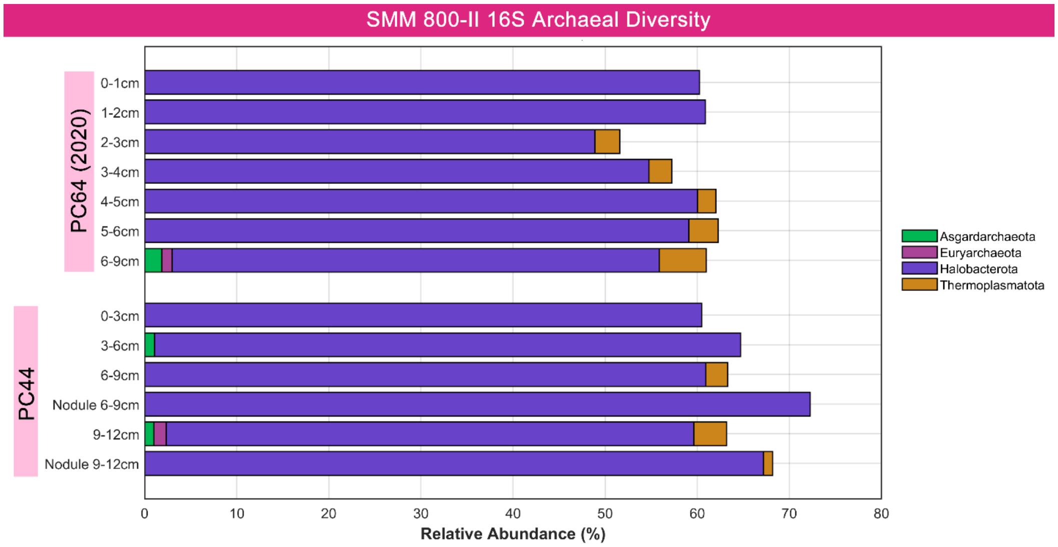

Fig. 1.18 – Stacked bar charts summarizing the depth-resolved, phylum-level 16S archaeal abundances above 1% relative to total 16S abundances in PC64 and PC44 at SMM 800-II.

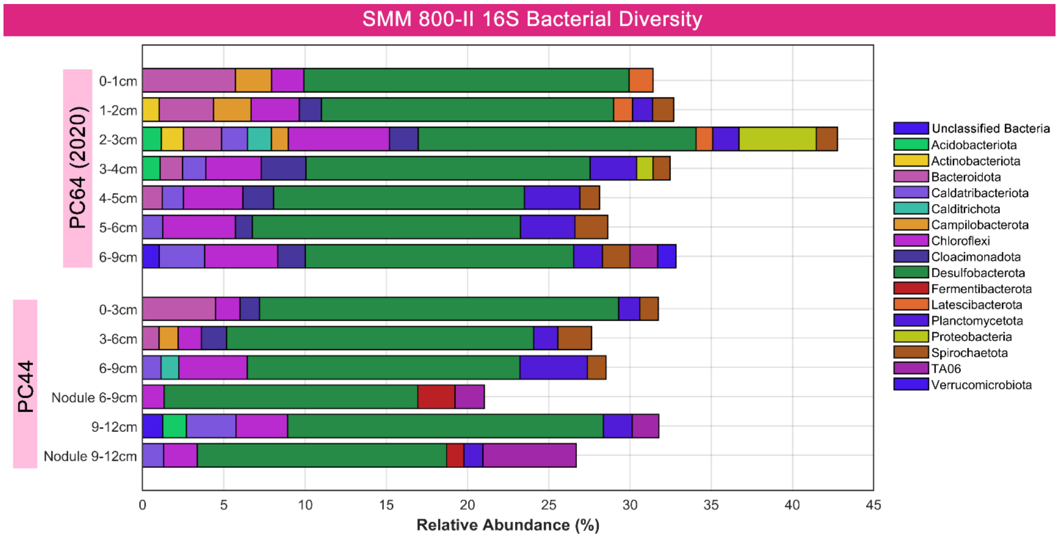

Fig. 1.19 – Stacked bar charts summarizing the depth-resolved, phylum-level 16S bacterial abundances above 1% relative to total 16S abundances in PC64 and PC44 at SMM 800-II.

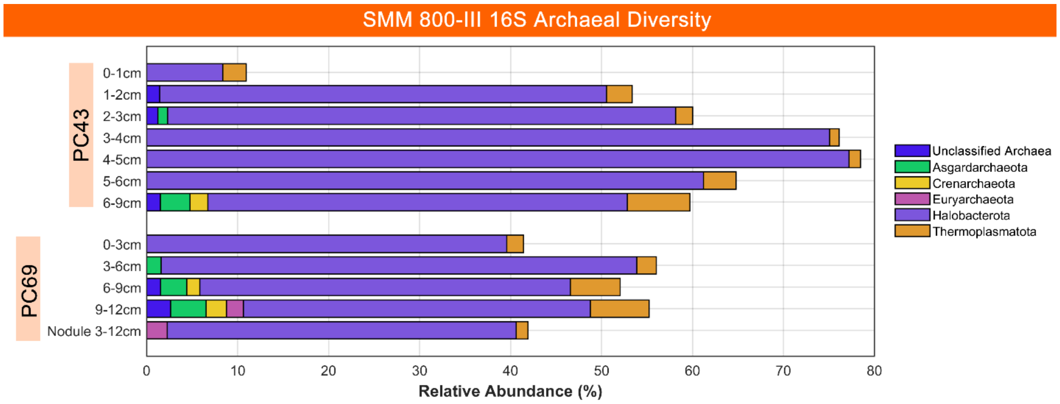

Fig. 1.20 – Stacked bar charts summarizing the depth-resolved, phylum-level 16S archaeal abundances above 1% relative to total 16S abundances in PC43 and PC69 at SMM 800-III.

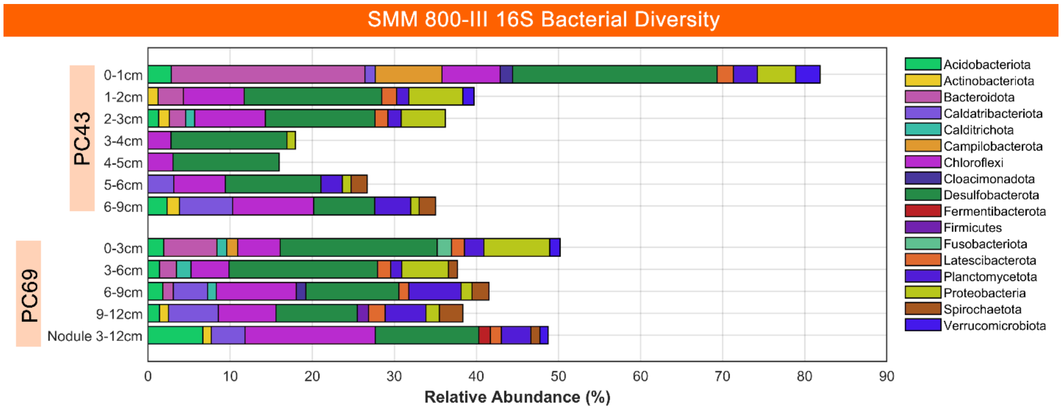

Fig. 1.21 – Stacked bar charts summarizing the depth-resolved, phylum-level 16S bacterial abundances above 1% relative to total 16S abundances in PC43 and PC69 at SMM 800-III.

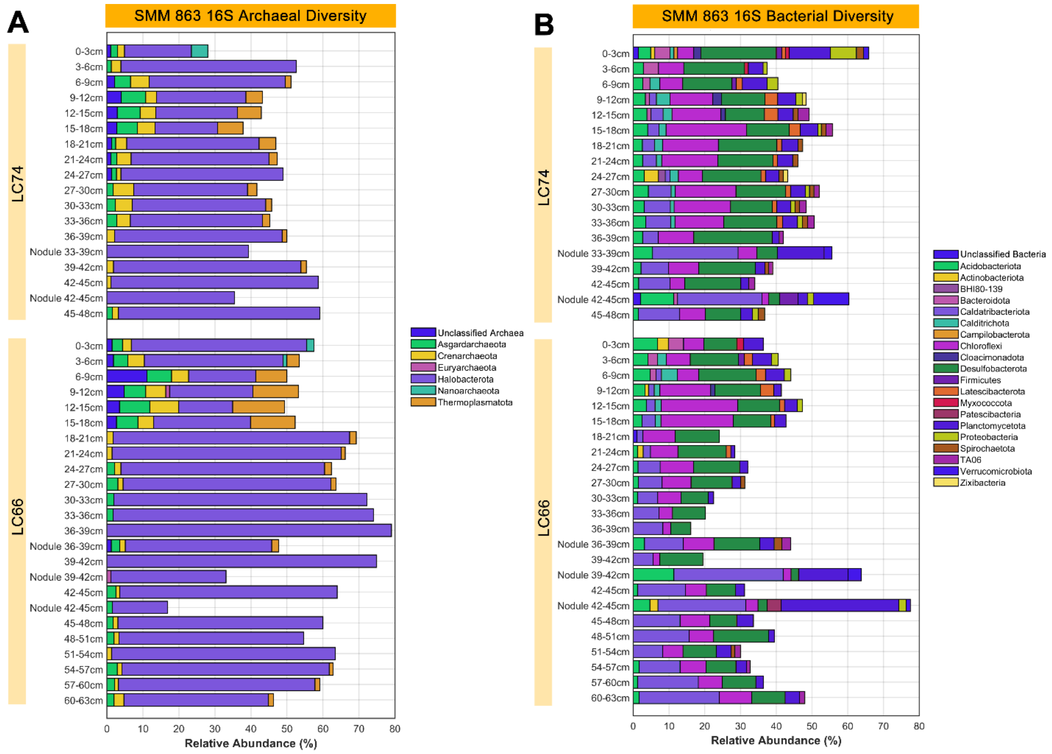

Fig. 1.22 – Stacked bar charts summarizing the depth-resolved, phylum-level 16S A) archaeal and B) bacterial abundances above 1% relative to total 16S abundances in LC74 and LC66 at SMM 863.

Diversity Index Calculations

Both Shannon-Wiener and Inverse Simpson indices for archaeal and bacterial ASVs were calculated by sectioning the sequenced ASVs into bacterial and archaeal groups for each sample. The Shannon-Wiener indices were calculated per sample according to Eq. 2:

$$-\sum_{i=1}^{s} r_i \ln\,(r_i) \tag{2}$$

where r_i is the proportional relative abundance of each individual ASV (i) relative to the total number of archaeal or bacterial ASVs on a per sample basis (s). The Inverse Simpson indices were calculated per sample according to Eq. 3:

$$\frac{1}{\sum_{i=1}^{s} r_i^2} \tag{3}$$

where r_i is the proportional relative abundance of each individual ASV (i) relative to the total archaeal or bacterial ASV pool on a per sample basis (s).

Table 1.7
Archaeal and bacterial diversity indices for recovered nodules (N) and their host sediment horizons at each of the four sites in this study, calculated from domain-specific, 16S ASV proportional abundances

Site	**Core ID**	**Core Horizon (cmbsf)**	**Shannon-Wiener Index**				**Inverse Simpson Index**			
			Archaea		**Bacteria**		**Archaea**		**Bacteria**	
			Sediment	N	Sediment	N	Sediment	N	Sediment	N
SMM 800-I	LC62	24-27	2.3	2.9	3.8	4.7	4.0	6.1	29.9	64.7
		36-39	3.1	2.9	3.9	5.1	13.8	5.3	20.6	48.3
		39-42	2.7		3.0		10.7		8.0	
		48-51	2.6	2.7	4.0	4.2	5.9	5.0	22.3	29.2
		51-54	3.4	3.4	4.1	4.7	17.2	15.6	19.8	38.8
		54-57	3.1		3.3		12.3		13.8	
SMM 800-II	PC44	6-9	2.3	1.7	4.1	3.5	5.2	2.7	32.9	12.1
		9-12	2.6	1.8	3.6	3.3	7.5	3.0	14.9	11.0
SMM800 -III	PC69	3-6	2.6	2.3	4.5	4.4	6.9	5.6	48.3	25.1
		6-9	3.3		4.8		11.2		61.9	
		9-12	3.1		4.3		13.9		43.5	
SMM 863	LC66	36-39	1.6	2.7	3.4	4.7	2.1	5.0	15.0	43.8
		39-42	1.9	2.1	3.3	2.9	2.4	3.4	13.4	8.9
		42-45	2.5	2.2	3.9	3.4	3.8	3.4	22.6	9.3
	LC74	33-36	2.2	2.1	4.3	3.6	4.3	2.8	41.8	13.7
		36-39	2.7		4.2		4.7		18.2	
		42-45	2.2	1.4	4.0	3.5	3.1	1.8	21.7	9.7

Neither index demonstrated a correlation with the number of bacterial or archaeal ASVs recovered.

Community Statistical Analysis

Non-metric multi-dimensional scaling (NMDS) ordination was done in MATLAB (v.2022a) using the open-source Fathom toolbox designed by (12) at USF's College of Marine Science. The Bray-Cutris dissimilarity matrix was first calculated using all ASV total relative abundances (on a per sample basis) with Fathom's f_braycurtis function. The NMDS was generated using MATLAB's mdscale with the 'stress' criterion specified, which normalizes stress by the sum of squares of the interpoint distances.

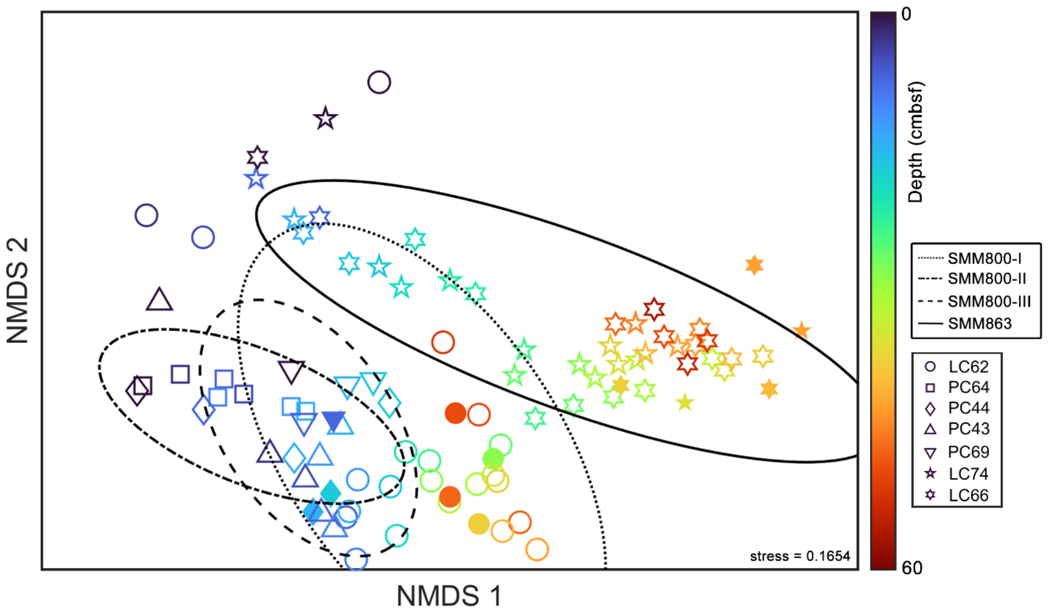

Fig. 1.23 – Nonmetric multidimensional scaling (NMDS) ordination of all 16S ASV relative abundances in the sediment horizons and their nodules, where collected. Empty and filled in markers correspond to horizon-specific sediment and nodule communities, respectively. The shape colors denote depth in cm below seafloor (cmbsf). The four sampling sites (SMM 800-I, SMM 800-II, SMM 800-III, and SMM 863) are indicated with 95% confidence interval ellipses.

Fluorescence *In Situ* Hybridization

Table 1.8
FISH hybridization probe mix 1 (40% formamide, per 101-µL)

Reagent	Amount (in µL)
5M NaCl	18
1M Tris-HCl (pH 8)	2
EUB338 + EUB338 II + EUB338 III (each at 50 ng/µL in PCR-quality, ultrapure DI H_2O)	10
ANME1-350 (50 ng/µL in PCR-quality, ultrapure DI H_2O)	10
ANME1-728 (50 ng/µL in PCR-quality, ultrapure DI H_2O)	10
ARCH-915 (50 ng/µL in PCR-quality, ultrapure DI H_2O)	10
Formamide	40
1% SDS (by weight in sterile, ultrapure DI H_2O)	1

Table 1.9
FISH hybridization wash (for 40% formamide hybridization, per 2-mL)

Reagent	Amount (in µL)
5M NaCl	18.4
1M Tris-HCl (pH 8)	40
0.5M EDTA	20
Sterile, ultrapure DI H_2O	1921.6

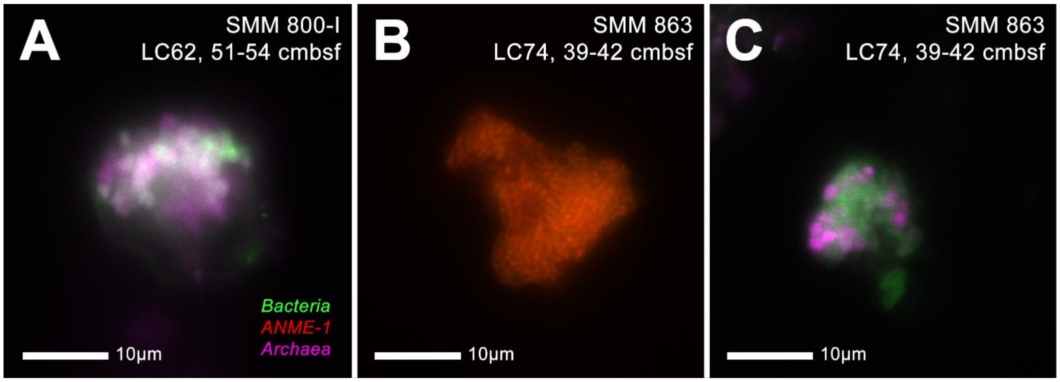

Fig. 1.24 – Observations of aggregate morphologies extracted from deeper sediment horizons at SMM 800-I and SMM 863, including those consistent with ANME-SRB consortia and positive fluorescence in-situ hybridization (FISH) signal from archaeal (ARCH915, in pink; ANME1-350, ANME-728, in red) and bacterial (EUB338, EUB338 II, EUB338 III, in green) probes.

Single Cell Translational Activity Measurements with BONCAT

Recovered nodules were incubated in artificial seawater (ASW) medium. The ASW was prepared according to the amounts listed below, modified from (13) and (14) using Wolin' vitamin solution from DSMZ 141 medium. Notable changes from other ASW media include reducing the as the buffer and modified salt concentrations to ensure $\Omega_{calcite}$ and $\Omega_{aragonite}$ were close to 1 (minimizing the impact of carbonate precipitation/dissolution, see (13)). Reagents were dissolved in deionized water at room temperature, then 0.2-µm filter-sterilized and sparged with N_2 until anoxic. Media was chilled at 4°C overnight prior to use.

Table 1.10
Artificial seawater media (per 1-L DI H_2O)

Reagent	Amount	Final Concentration [mM]
$MgCl_2 \cdot 6H_2O$	9.47 g	46.60
$CaCl_2 \cdot 2H_2O$	1.47 g	10.00
NaCl	25.70 g	439.77
KCl	0.52 g	7.00
Na_2SO_4	1.42 g	10.00
K_2HPO_4	0.17 g	1.00
NH_4Cl	0.11 g	2.00
HEPES Buffer (250mM, pH 7.5)	100.0 mL	25.00
Vitamins DSMZ 141 (1000x)	1.0 mL	*varies per vitamin*
$NaHCO_3$ (1M)	5.0 mL	5.00
Se/W Solution as in (14), containing per 1L:		
Na_2SeO_3	0.017 g	-
$Na_2WO_4 \cdot 2H_2O$	0.033 g	-
Trace Element Solution as in (14), containing per 1L:		
Nitrilotriacetic acid (NTA)	0.15 g	-
$MnCl_2 \cdot 4H2O$	0.61 g	-
$CoCl_2 \cdot 6H2O$	0.42 g	-
$ZnCl_2$	0.09 g	-
$CuCl_2 \cdot 2H_2O$	0.007 g	-
$AlCl_3$	0.006 g	-
H_3BO_3	0.01 g	-
$Na_2MoO_4 \cdot 2H_2O$	0.03 g	-
$SrCl_2 \cdot 6H_2O$	0.01 g	-
NaBr	0.01 g	-
KI	0.07 g	-
$FeCl_3 \cdot 6H_2O$	0.5 g	-
$NiCl_2 \cdot 6H_2O$	0.025 g	-

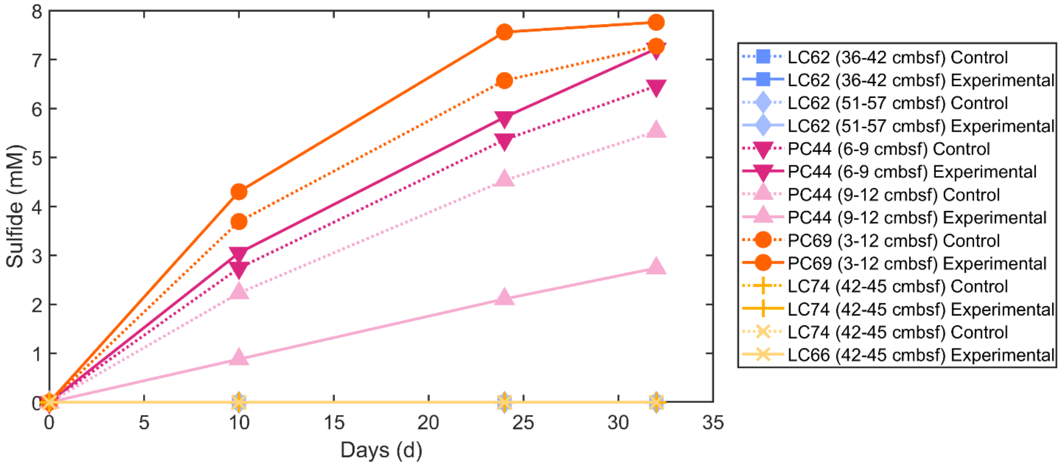

Fig. 1.25 – Sulfide production in the 5-week period after separation of incubated nodules into control and experimental groups, but before addition of HPG, as observed by dissolved sulfide in media and measured by Cline assay. Comparable sulfide production attests to sulfate-coupled AOM activity in both bottles. Notably, both control and experimental groups for nodules from SMM 800-I and SMM 863 did not produce a detectable amount of sulfide.

Table 1.11
BONCAT azide dye solution (per 250-µL)

Reagent	Amount (in µL)
100mM Aminoguanidine (in ultrapure DI H_2O)	12.5
100mM Ascorbate (in 1X PBS)	12.5
20mM $CuSO_4$ (in ultrapure DI H_2O)	1.25
50mM BTTAA (in ultrapure DI H_2O)	2.5
10mM Oregon Green 488 Azide dye (VectorLabs)	0.5
1X PBS	221

Note: A dye 'pre-mix' containing the azide dye, BTTAA, and $CuSO_4$ was incubated under Ar in the dark for 3 minutes prior to the addition of the rest of the reagents).

Table 1.12
FISH hybridization probe mix 2 (35% formamide, per 100-µL)

Reagent	Amount (in µL)
5M NaCl	18
1M Tris-HCl (pH 8)	2
EUB338 + EUB 338 II + EUB338 III (each at 50 ng/µL in PCR-quality, ultrapure DI H_2O)	10
ARCH-915 (50 ng/µL in PCR-quality, ultrapure DI H_2O)	10
Formamide	35
1% SDS (by weight in sterile, ultrapure DI H_2O)	1
PCR-quality, ultrapure DI H_2O	24
5M NaCl	18

Table 1.13
FISH hybridization wash (for 35% formamide hybridization, per 2-mL)

Reagent	Amount (in µL)
5M NaCl	28
1M Tris-HCl (pH 8)	40
0.5M EDTA	20
Sterile, ultrapure DI H_2O	1912

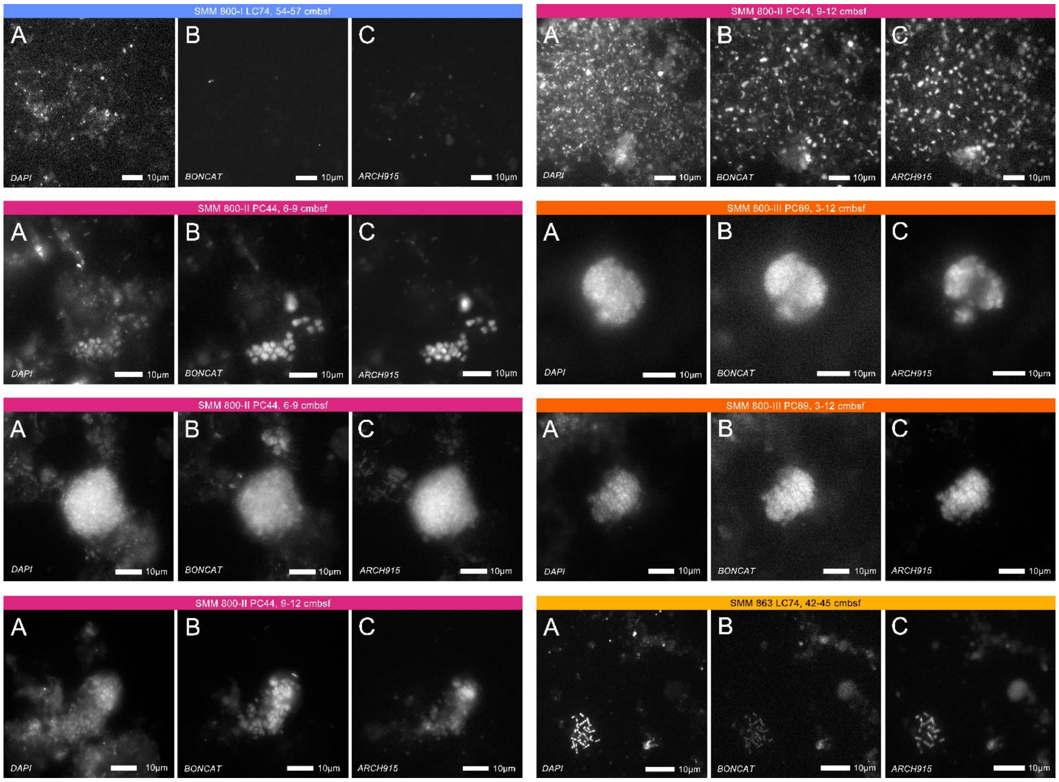

Fig. 1.26 – Individual fluorescent channels from BONCAT-FISH observations of cells from incubated nodules shown in Fig. 13 where A) corresponds to DAPI signal; B) is signal from BONCAT click dye Oregon Green; C) reflects signal from archaeal probe ARCH915.

References

1. Treude T, Boetius A, Knittel K, Wallmann K, Barker Jørgensen B. 2003. Anaerobic oxidation of methane above gas hydrates at Hydrate Ridge, NE Pacific Ocean. Mar Ecol Prog Ser 264:1–14.

2. Case DH, Pasulka AL, Marlow JJ, Grupe BM, Levin LA, Orphan VJ. 2015. Methane Seep Carbonates Host Distinct, Diverse, and Dynamic Microbial Assemblages. mBio 6.

3. Marlow JJ, Hoer D, Jungbluth SP, Reynard LM, Gartman A, Chavez MS, El-Naggar MY, Tuross N, Orphan VJ, Girguis PR. 2021. Carbonate-hosted microbial communities are prolific and pervasive methane oxidizers at geologically diverse marine methane seep sites. Proc Natl Acad Sci 118.

4. Mason OU, Case DH, Naehr TH, Lee RW, Thomas RB, Bailey JV, Orphan VJ. 2015. Comparison of Archaeal and Bacterial Diversity in Methane Seep Carbonate Nodules and Host Sediments, Eel River Basin and Hydrate Ridge, USA. Microb Ecol 70:766–784.

5. Mullin SW, Wanger G, Kruger BR, Sackett JD, Hamilton-Brehm SD, Bhartia R, Amend JP, Moser DP, Orphan VJ. 2020. Patterns of in situ Mineral Colonization by Microorganisms in a ~60°C Deep Continental Subsurface Aquifer. Front Microbiol 11.

6. Kozich JJ, Westcott SL, Baxter NT, Highlander SK, Schloss PD. 2013. Development of a Dual-Index Sequencing Strategy and Curation Pipeline for Analyzing Amplicon Sequence Data on the MiSeq Illumina Sequencing Platform. Appl Environ Microbiol 79:5112–5120.

7. Martin M. 2011. Cutadapt removes adapter sequences from high-throughput sequencing reads. 1. EMBnet.journal 17:10–12.

8. Bolyen E, Rideout JR, Dillon MR, Bokulich NA, Abnet CC, Al-Ghalith GA, Alexander H, et al. 2019. Reproducible, interactive, scalable and extensible microbiome data science using QIIME 2. Nat Biotechnol 37:852–857.

9. Callahan BJ, McMurdie PJ, Rosen MJ, Han AW, Johnson AJA, Holmes SP. 2016. DADA2: High-resolution sample inference from Illumina amplicon data. Nat Methods 13:581–583.

10. Quast C, Pruesse E, Yilmaz P, Gerken J, Schweer T, Yarza P, Peplies J, Glöckner FO. 2013. The SILVA ribosomal RNA gene database project: improved data processing and web-based tools. Nucleic Acids Res 41:D590–D596.

11. Davis NM, Proctor DM, Holmes SP, Relman DA, Callahan BJ. 2018. Simple statistical identification and removal of contaminant sequences in marker-gene and metagenomics data. Microbiome 6:226.

9. Jones DL. 2017. Fathom Toolbox for Matlab | USF College of Marine Science. https://www.usf.edu/marine-science/research/matlab-resources/fathom-toolbox-for-matlab.aspx.

13. Scheller S, Yu H, Chadwick GL, McGlynn SE, Orphan VJ. 2016. Artificial electron acceptors decouple archaeal methane oxidation from sulfate reduction. Science 351:703–707.

14. Imachi H, Nobu MK, Miyazaki M, Tasumi E, Saito Y, Sakai S, Ogawara M, Ohashi A, Takai K. 2022. Cultivation of previously uncultured microorganisms with a continuous-flow down-flow hanging sponge (DHS) bioreactor, using a syntrophic archaeon culture obtained from deep marine sediment as a case study. Nat Protoc 17:2784–2814.

Chapter 2

OBSERVATIONS OF TRIPARTITE, INTER-ANME ASSOCIATIONS AT SANTA MONICA BASIN, CA

Sergio A. Parra[a], Magdalena J. Mayr[a,b], Daniel R. Utter[a], Ranjani Murali[c],
Victoria J. Orphan[a,b]

[a]Division of Geological and Planetary Sciences, California Institute of Technology,
Pasadena, California, USA

[b]Division of Biology and Biological Engineering, California Institute of Technology,
Pasadena, California, USA

[c]Department of Life Sciences, University of Nevada, Las Vegas,
Las Vegas, Nevada, USA

Abstract

This study investigates three-membered, or ‘tripartite’ associations involving 2 distinct clades of anaerobic methanotrophic archaea (ANME) and a bacterial partner, observed across diverse substrates at a methane seep in the Santa Monica Basin, including sediments, sediment-hosted carbonate nodules, and seafloor carbonate pavements. Observations from 16S rRNA sequencing supported likely associations between ANME-1a, ANME-2c, and sulfate-reducing bacteria (SRB), where fluorescence in-situ hybridization (FISH) confirmed the presence of ANME-1 and ANME-2c in close association with a bacterial partner. These associations were morphologically diverse and resembled more common ANME-SRB configurations, ranging from segregated clusters to mixed aggregates. Phylogenetic analyses suggested that the ANME-1a and ANME-2c likely forming these associations are globally distributed across other seep environments, including the Hydrate Ridge, OR and Elba seep sites. Translational activity measurements using bioorthogonal non-canonical amino acid tagging (BONCAT) further revealed that while bacterial and non-ANME-1 archaeal partners were active, ANME-1 appeared inactive in these associations, implying potential competitive advantages for ANME-2 in methane-rich environments. Our findings suggest that tripartite, inter-ANME associations may represent a more widespread and flexible mode of methane drawdown than previously characterized. Further research into the metabolic activity and ecological function of these associations, including potential competitive or cooperative dynamics between ANME clades, promises to expand

our understanding of microbially-mediated anaerobic oxidation of methane (AOM) and microbial evolution at hydrocarbon seeps.

1. Introduction

Anaerobic oxidation of methane (AOM) at coastal, submarine hydrocarbon seeps is a key global methane sink mediated by a specialized consortium of archaeal anaerobic methanotrophs (ANME) and sulfate-reducing bacteria (SRB; Boetius et al., 2000; Orphan et al., 2001; Reeburgh et al., 2007; Knittel & Boetius, 2009). This syntrophic interaction has been observed to be driven by direct, interspecies electron transfer that is thought to necessitate their proximal spatial associations in the form of cell aggregates, often in 1:1 archaeal/bacterial ratios (McGlynn et al., 2015; Wegener et al., 2015; Scheller et al., 2016). However, ANME-SRB consortia are genetically and morphologically diverse, suggestive of further diversified, niche-specific relationships that require greater characterization.

For example, ANME diversity in hydrocarbon seeps is largely approached at the comparatively broad taxonomic levels of the ANME-1 and ANME-2 clades (representing approximately family- or order-level units from separate classes) (Knittel & Boetius, 2009). While ANME-1 and ANME-2 co-occur in diverse seep environments (Orphan et al., 2002; Treude et al., 2007; Hatzenpichler et al., 2016; Ruff et al., 2016; Chapter 1), abundance and metabolic activity patterns have suggested niche distinctions between these two clades. ANME-1, for example, has historically been observed to dominate in deeper, and/or more geochemically diverse (i.e., methane-, sulfate-poor) seep environments (Orphan et al., 2001; Orphan et al., 2002; Blumenberg et al., 2004; Harrison et al., 2009; Rossel et al., 2011; Yanagawa et al., 2011; Biddle et al., 2012), where ANME-2 has been observed more frequently in shallower, sulfate-rich environments (Yanagawa et al., 2011; Biddle et al., 2012; Vigneron et al., 2013).

Furthermore, the environmental distribution of ANME clades may also depend on the prevalence of a particular sulfate-reducing partner, as different clades exhibit varying degrees of partner specificity. ANME-1, for example, has been documented to partner with several members of *Desulfobacterota*, including Seep-SRB2 and HotSeep-1 (Holler et al., 2011; Wegener et al., 2015; Hatzenpichler et al., 2016; Krukenberg et al., 2016, 2018). ANME-2a, by contrast, has only been observed to partner with Seep-SRB1a (Schreiber et al., 2010; Hatzenpichler et al., 2016; Yu et al., 2022a). Similarly, ANME-2b demonstrates a specificity for Seep-SRB1g (Metcalfe et al., 2021), where ANME-2c has been observed to partner with multiple sulfate-reducers in *Desulfobacterota*, including Seep-SRB1a (Schreiber et al., 2010, McGlynn et al., 2015), Seep-SRB2 (Kleindienst et al., 2012; Krukenberg et al., 2018), and others in *Desulfobulbaceae* (Pernthaler et al., 2008).

In addition to a diverse range of partners, these consortia also display a range of morphological configurations ranging from ‘shell-type’ cell aggregates, where the SRB partner surrounds an ANME ‘core’, to ‘mixed-type’ aggregates, where ANME/SRB cells are more homogenously integrated — either at the single-cell, ‘checkerboard’ level, or the ‘segregated’/’bubble’ level, featuring distinct clusters of SRB or ANME (Orphan et al., 2002; Knittel et al., 2005; Knittel & Boetius, 2009;

McGlynn et al., 2015; Ruff et al., 2016). In some cases, ANME/SRB cells have also been observed growing as dense microbial mats, as observed in sediments and carbonate ‘reefs’ in the Black Sea (Michaelis et al., 2002; Treude et al., 2005; Treude et al., 2007; Krüger et al., 2008). While drivers for this morphological variability have not been systematically explored, these spatial configurations are thought to be informed at least in part by the need for direct interspecies electron transfer (McGlynn et al., 2015). Still, ANME have also been observed without SRB partners, present and active as single cells or mono-specific aggregates (Orphan et al., 2002; Durisch-Kaiser et al., 2005; Knittel et al., 2005; Treude et al., 2005; Treude et al., 2007; House et al., 2009; Orphan et al., 2009; Vigneron et al., 2013; Ruff et al., 2016), suggestive of partner-independent AOM capabilities or a different metabolism entirely, as has been proposed for ANME-1 (House et al., 2009; Biddle et al., 2012; McGlynn et al., 2015; Laso-Pérez et al., 2023) and demonstrated in the freshwater ANME-2d (also known as *Candidatus Methanoperedenaceae)* (Cai et al., 2018; Li et al., 2021).

More strikingly, there are documented in-situ observations of ANME associations with more than one ANME clade represented. Treude et al. (2007) reported observations of distinct, direct, cell-to-cell contact between clusters of ANME-2c and ANME-1 distributed throughout a stratified microbial mat sampled from the surface of a methanotrophic reef structure in the Black Sea (Michaelis et al., 2002). This contact was found both in the ANME-1-rich, pink-colored mat interior, as well as in the black ‘rind’ of ANME-2c rich mat on the exterior surface, alongside SRB from the *Desulfococcus-Desulfosarcina* cluster (Treude et al., 2007). Elsewhere, sandy sediment samples from a shallow methane seep off the coast of Elba, Italy also featured several cell-to-cell associations (<10-µm) between ANME-1, ANME-2, and Seep-SRB1a (Ruff et al., 2016). As far as we know, these are the only documented in-situ instances of explicit, ANME-1/ANME-2/SRB associations, and as such they remain the most poorly characterized mode of ANME habitation at hydrocarbon seeps. More specifically, the frequency of occurrence and range of potential identities and morphologies for these types of associations are yet unexplored.

In this study we present additional observations of distinct, morphologically diverse associations between ANME-1, a bacterial partner, and another archaeal participant from diverse substrates at a methane seep in Santa Monica Basin, CA. We also make advances on previous observations by presenting 16S rRNA sequence-based, ASV-specific candidates for these three membered, or 'tripartite' associations as well as measuring their translational activity in lab-based incubations with fluorescence in-situ hybridization (FISH) and bioorthogonal, non-canonical amino acid tagging (BONCAT). Our results confirm the presence of significantly under-characterized diversity among consortia mediating AOM at hydrocarbon seeps and inform further studies to interrogate the drivers and mechanisms for this unique mode of association.

2. Materials and Methods

2.1 Site Description and Sample Collection

The 3 (1 pavement, 1 sediment push core, 1 carbonate concretion, or 'nodule') samples in this study were recovered from an active methane seep site previously identified at Santa Monica Basin: Santa Monica Mound Site 800 - also known as the

NE mound (SMM 800: 33.799438N /118.64672E; 805m; Normark et al., 2006; Paull et al., 2008). Specifically, the samples were collected with *ROV Doc Ricketts* during dive DR1329 in May 2021 on the 05-21 Southern California Cruise of the *R/V Western Flyer*. We provide further information on sampling site context and additional sample recovery details in the Appendix. Sample processing for the recovered sediment push core and carbonate nodule, including core sectioning and removal of sediment from nodules, was performed as described in Chapter 1.

Immediately following recovery, we kept the recovered pavement immersed in bottom water at 4°C until processing. The carbonate pavement was studied, documented, and then prepared for transport within hours of collection. Here, the pavement was transferred to 0.22 µm-Sterivex^{TM} filtered (Millipore Sigma) bottom water collected at the seep during the dive and sealed in an Ar-flushed Mylar bag (IMPAK Corporation) for transport to land.

In the laboratory (<5 months after sample collection), the carbonate pavement upper and lower surfaces were first scraped and sampled with a flame-sterilized spatula. The pavement was then sectioned into several vertical transects using an ethanol-cleaned tile saw (WorkForce THD550) with a wet diamond saw blade (BOSCH, 5/8" arbor, 0.051 in thick). Certain pavement sections were further sectioned into four, horizontally resolved sections for various microbiological analyses (Appendix, Fig. 2.7). To maintain the pavements wet for sectioning, N_2-sparged, 0.22-µm-filtered basal salts medium (artificial seawater with only prominent salts, Appendix Table 2.3) was continuously pumped over the pavement. To minimize oxygen exposure, the pavement was also kept under continuous Ar flow during sectioning. Horizontal sections intended for DNA sequencing and visualization with fluorescence microscopy were additionally treated to minimize contamination from processing according to the methods optimized by (Mason et al., 2015). This treatment included additional rinses with 0.22-μm-filtered 3X PBS, sonication, and centrifugation, where details are briefly summarized in Chapter 1's Supplemental Material. Intact, vertical transects designated for activity measurements with bioorthogonal, non-canonical amino acid tagging (BONCAT) were transferred to separate, sterile, acid-washed bottles and then submerged in 0.22 μm-filtered, N_2-sparged artificial seawater, prepared as described in Chapter 1's Supplemental Material. After immersion, bottle headspaces were flushed with pure CH_4 for 1 minute and pressurized to 2 bar. Samples were then stored in the dark at 4°C.

2.2 16S rRNA Gene Sequencing

Sequencing of the V4 and V5 regions of the 16S rRNA gene within DNA extracts of our recovered samples allowed us to interrogate microbial community identity and structure. Sample processing and DNA extraction for the relevant sediment core section, sediment-hosted nodule, and horizontal pavement sections were performed as described in Chapter 1. In the laboratory, rinsed horizontal pavement transects were also immediately finely ground and frozen at -80°C during sectioning. Later, DNA was extracted from 0.15-0.3 g (wet weight) of sediment or ground nodule/sectioned pavement transect with the DNeasy PowerSoil Pro Kit (Qiagen). We then amplified target sequences using a two-step Illumina sequencing approach (Kozich et al., 2013). The first step involved amplification with 515f (5’-GTGYCAGCMGCCGCGGTAA -3’) and 926r (5’-CCGYCAATTYMTTTRAGTTT -3’) primers, followed by a second amplification to add the required Illumina barcodes before sequencing.

Adapters from paired-end sequences were removed using 'Cutadapt' (v2.9, Martin, 2011). Trimmed reads were processed in QIIME2 (v2020.11, Bolyen et al., 2019), where a DADA2 pipeline (1.14.1, Callahan et al., 2016) filtered and denoised the reads before removing chimeric sequences. Amplicon sequence variants (ASVs) with assigned taxonomy were generated from the paired-end non-chimeric sequences in QIIME2 using the Silva V138.1 SSURef database feature classifier (Quast et al., 2013). Further information on modified DNA extraction protocols, gene sequencing, and read processing are detailed in Chapter 1’s Supplemental Material.

2.3 Phylogenetic Analysis

Prospective 16S rRNA ASVs for the candidate tripartite, inter-ANME associations were determined by excluding any ASVs that were not classified as a member of the *Halobacteriota* archaeal or the *Desulfobacterota* bacterial phyla. Additionally, a minimum occurrence threshold of 1% relative abundance was applied to the resulting ASVs. The remaining ASVs were then added to previously assembled collections of *Halobacteriota* and *Desulfobacterota* 16S rRNA gene sequences, respectively.

Each collection of 16S rRNA ASVs was aligned using MUSCLE v3.8.1551 by Edgar, (2004), where alignments were exported to a. fasta file. Both ANME and *Desulfobacterota* phylogenetic trees and accompanying bootstrap values were generated with IQ-TREE multicore version 2.1.2 using the following parameters: iqtree -B 1000 -T 8. Trees were visualized using ITOL. Reference sequences, including full-length sequences, that aligned with 100% percent identity onto the 'dominant' ASVs (i.e., recurring ASVs with the greatest consistent relative abundance) were noted. Additional details, including aggregation of additional *Halobacteriota* and *Desulfobacterota* 16S rRNA gene sequences, are listed in the Appendix.

2.4 Fluorescence In-Situ Hybridization (FISH)

All samples intended for visualization with fluorescence microscopy were processed as described in Chapter 1. Briefly, sediment, ground nodule, and ground, sectioned pavement transects were fixed in 4% paraformaldehyde overnight at 4°C, washed twice, resuspended in 50% ethanol, and stored at -20°C. We then performed a density separation using percoll to minimize the impact of sediment and mineral particles. The separated cells were washed twice before being mounted for viewing onto a 0.2 µm black polycarbonate filter via vacuum filtration. We then cut each filter into 8 roughly equal slices with a flame-sterilized razor blade to facilitate further processing for visualization.

To document and count the frequency of tripartite, inter-ANME associations, we used fluorescence in-situ hybridization (FISH). Based on the 16S ASV classifications during sequence processing, we selected the hybridization probes EUB338 [5’-GCTGCCTCCCGTAGGAGT-3’ (Amann et al., 1990), dual-labeled Alexa Fluor™ 488 dye], EUB338 II [5’- GCAGCCACCCGTAGGTGT-3’ (Daims et al., 1999), dual-labeled Alexa Fluor™ 488 dye], EUB338 III [5’-GCTGCCACCCGTAGGTGT-3’ (Daims et al., 1999), dual-labeled Alexa Fluor™ 488 dye], ANME1-350 [5’-AGTTTTCGCGCCTGATGC-3’ (Boetius et al., 2000), dual-labeled Alexa Fluor™ 546 dye], ANME1-728 [5’-GGTCTGGTCAGACGCCTT-3’ designed using ARB (Westram et al., 2011) to hit the ANME1 Clade of the SILVA 138 database, 5’ conjugated Alexa Fluor™ 546 dye], and ARCH-915 [5’-GTGCTCCCCCGCCAATTCCT-3’ (Stahl & Amann, 1991), dual-labeled Alexa Fluor™ 647 dye] for visualization of all cell extracts, including pavement, sediment, and nodule. A following hybridization of the same pavement cell extracts used the ANME2c-760 [5’- CGCCCCCAGCTTTCGTCC-3’ (Knittel et al., 2005), dual-labeled Alexa Fluor™ 647 dye] probe instead of the ARCH915 probe. We prepared all hybridization probe mixes in sterile, 40% formamide, with each probe (Integrated DNA Technologies) at a final concentration of 5 ng/µL.

50 µL of probe mix per was then placed onto a parafilm-coated glass slide over which a section of a cut filter was placed, where three filter sections from each mounted sample were hybridized per slide. We then incubated the hybridizations overnight, in the dark, at 46°C. The following day, we incubated the hybridized filter sections in a pre-warmed hybridization wash in the dark for 10 minutes at

48°C. We then rinsed the filters in ultrapure DI H_2O and allowed them to air dry in the dark. For nucleic acid visualization, we then added 10-µL of a 90% Citifluor^{TM} mounting medium (Electron Microscopy Sciences) with 4.5-ng/uL 4',6-diamidino-2-phenylindole (DAPI) to each filter section before placing the coverslip. We provide FISH hybridization probe and wash recipes in Appendix Tables 2.4-2.6.

We used an Olympus BX51 fluorescence microscope using a 100x objective lens (Olympus) to visualize the prepared filter sections. To quantify the number of tripartite, inter-ANME associations observed in the sectioned pavement transects, we counted number of occurrences per filtered sample. These counts were normalized per unit dry mass of crushed pavement. For control experiments, a filter section was subjected to the entire FISH protocol but used ultrapure DI H_2O instead of probes. For these wells, we observed a negligible signal.

2.5 Translational Activity Measurements with BONCAT

Translational activity was detected by treating a subset of the bottled, sectioned pavements with an aqueous solution of L-Homopropargylglycine (HPG). HPG acts as a methionine analog and is incorporated into proteins during synthesis without significantly affecting the community composition or metabolic activity (Hatzenpichler et al. 2014, 2016). Once incorporated, HPG-labeled proteins can be visualized using azide-alkyne ‘click’ chemistry, allowing for detection through fluorescence microscopy (Sletten and Bertozzi 2009; Hatzenpichler and Orphan 2015).

In this study, we separated a subset of the vertical pavement transects previously bottled and maintained in N_2-sparged artificial seawater with a 2-bar CH_4 headspace into experimental and control groups of roughly equivalent mass. After sulfide production indicative of sulfate-coupled AOM was first confirmed to ensure roughly equivalent activity between the control and experimental groups (Appendix, Fig. 2.13), we then performed a 12-week incubation, following the procedures previously described for BONCAT activity measurements in Chapter 1. Here, the medium was refreshed and the experimental bottle received aqueous 0.22 µm-filtered, N_2-sparged HPG to a final concentration of 200-µM. After 12 weeks of incubation, the vertical transects were then further sub-sectioned into 2 horizontal 'horizons': upper, and lower subsections following the same procedures used for the other horizontal subsections used for 16S gene sequencing and fluorescence microscopy. These horizons were ground, fixed overnight in 4% paraformaldehyde, washed, and then subjected to a percoll density separation to minimize the impact of sediment and mineral particles as previously described and detailed in Chapter 1. Instead of filter mounting, experimental and control cell suspensions in ultrapure DI H_2O were simply pipetted into separate 6-mm wells on PTFE- and L-lysine-coated glass slides (Tekdon) and dried at room temperature. We then dehydrated the glass-mounted cell extracts for BONCAT dye click reaction by sequential immersion in 50% (1 minute), 80% (3 minutes), and 90% (3 minutes) ethanol: DI H_2O baths before we allowed the slides to dry again at room temperature.

We then added 10 μL of an Oregon Green 488 azide dye (VectorLabs) solution to each well at a final concentration of 20 μM and placed the slides in a dark sample container that was flushed with Ar to incubate for 30 minutes. After incubation, we washed the slides in 0.22 μm-filtered 1X PBS for 10 minutes, rinsed in ultrapure DI H_2O, and air dried at room temperature before FISH hybridization. Slides were maintained in the dark throughout all these steps. To investigate which archaeal members in these ANME associations were translationally active, we used ANME1-350 [dual-labeled Alexa Fluor™ 546 dye], ANME1-728 [5' conjugated Alexa Fluor™ 546 dye], and ARCH-915 [dual-labeled Alexa Fluor™ 647 dye] for visualization. The probe mix was also prepared following the same procedures as for the filter-mounted cell extracts (40% formamide, 5-ng/μL of probe). 10-μL of probe mix were then added to each well and incubated in the dark, overnight at 46°C. The rest of the hybridization, subsequent washing, and addition of DAPI/Citifluor™ solution occurred as detailed for the filter-mounted cell extracts. BONCAT azide dye solution, FISH hybridization probe mix, and hybridization wash recipes are further detailed in Appendix Tables 2.9-2.10.

We visualized click-dyed, hybridized cells with an ELYRA S.1 / Axio Observer Z1 super resolution microscope equipped with a 100x objective lens (Zeiss). For FISH-specific control experiments, each glass slide included a well with mounted, non-HPG labeled cells that underwent the full FISH protocol but with ultrapure DI H_2O instead of probes. We observed negligible FISH signal for these wells (Appendix, Fig. 2.14).

3. Results

3.1 Characterization of Methane Seep-Associated Samples

The samples presented in this study originate from diverse substrates from active seep sites at Santa Monica Mound 800 (SMM 800), shown in Figure 2.1 and summarized in Table 2.1. Sediment cores PC44 and PC69 were taken from the northeastern and southwestern flanks of the mound, respectively (Chapter 1). Lab-based analyses of these cores revealed a sharp drawdown of methane and sulfate (i.e., the sulfate-methane transition zone, SMTZ) in the upper centimeters of the sediment, coupled with the occurrence of calcitic rubble that included larger, cm-sized carbonate concretions, or 'nodules', suggestive of a history of anerobic oxidation of methane (AOM) in the sediments (Chapter 1). By contrast, R1 was a sediment-poor carbonate crust, or pavement, collected near the top of the mound (coordinates in the Appendix). Most notably, R1 featured a distinct microbial mat and bivalve clams on its surface, as well as dense gas hydrate underneath (Figure 2.1BC), which dissolved during ascent to the sea surface.

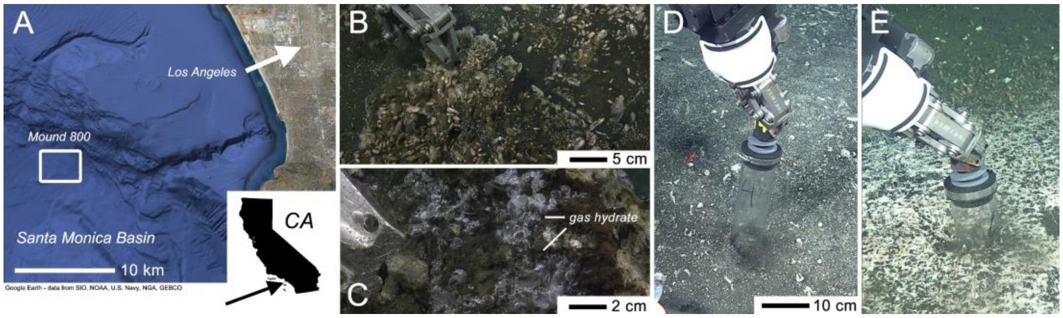

Figure 2.1: A) Map detailing the location of Mound 800 at Santa Monica Basin, CA — adapted from Chapter 1; B) Dive footage from *ROV Doc Ricketts* of seep pavement (R1) sampling, with macrofauna visible on its surface; C) Observations of gas hydrate trapped underneath the sampled pavement (R1); D)-E) Dive footage of sediment push core (PC44, PC69, respectively) sampling above sites with characteristic surface expressions of methanotrophic activity at Mound 800, as shown in Chapter 1's Supplemental Material.

Table 2.1
Seep-associated samples presented in this study

Sample ID	**R1**	**PC44**	**PC69**
Substrate Type	Seep Pavement	Seep Sediment	Seep Sediment-Hosted ‘Nodule’
Depth (cmbsf)	Surface (0)	6-9	3-12

3.2 Observations of Tripartite, Inter-ANME Associations at SMM 800

We surveyed the diversity and morphology of anerobic methanotrophic (ANME) archaeal and sulfate-reducing bacterial (SRB) aggregates at SMM 800 with 16S rRNA-targeted fluorescence in-situ hybridization (FISH). While most of the observed cellular aggregates resembled the traditional monospecific ANME or ANME-SRB morphologies observed in seep environments (Appendix, Fig. 2.11), we also found the rare but recurrent association of a third archaeal member associated with ANME-1 and partner bacteria (Figure 2.2A-D). These three-member consortia, which we term ‘tripartite’ associations, were found across diverse substrates of sectioned seep pavement (R1), sediments (PC 44), and sediment-hosted carbonate nodules (Figure 2.2, Table 2.1).

Comparison of tripartite association morphologies across samples also revealed trends in the aggregate ultrastructure, where cells from either archaeal member appeared to respond to the morphology of the other archaeal member — often by direct proximity, bordering the other. In each of these instances, the unidentified archaeal member also displayed coccoidal, densely packed morphologies consistent with ANME-2 subclades (Orphan et al., 2002; Knittel et al., 2005; Treude et al., 2007).

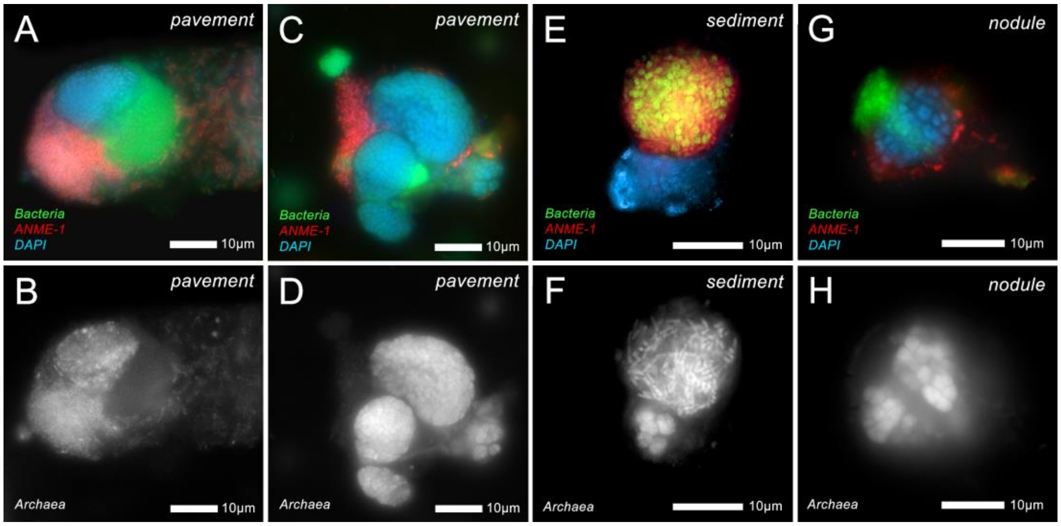

Figure 2.2: Fluorescence in-situ hybridization (FISH) images of tripartite, inter-ANME associations observed in and/or association with several seep-derived substrates (sediment, nodule, pavement) at Santa Monica Mound 800. Panels A, C, E, G show ANME-1 (in red), bacteria (in green), and one other archaeal member (shown with DAPI in blue); panels B, D, F, H show associated archaeal channel separately in white. Individual channels are shown in Appendix Fig. 2.10.

3.3 16S Amplicon-Based Identity in Tripartite Association-Bearing Samples

To identify potential candidate members for these associations, we examined the microbial community composition across the samples where tripartite associations were observed as reflected by 16S ribosomal rRNA gene sequencing. Sequenced lower pavement horizons revealed two dominant, co-occurring ANME subclades — ANME-1a and ANME-2c (Fig. 2.3A). This dominance extended to the amplicon sequence variant (ASV) level, where one ANME-1a ASV and one ANME-2c ASV were consistently over- or singularly represented above the others. Interestingly, ANME-1a and ANME-2c were not equally represented throughout the pavement sections, but rather enriched in ANME-1a in the sample interior and dominated by ANME-2c at the lower surface. By contrast, the sediment and nodule samples revealed a more even distribution of ANME subclades and constituent ASVs, including ANME-1a, ANME-2b, and ANME-2c. Still, we observed the only ANME-

1a ASV in the seep sediment and nodule was the same dominant ANME-1a ASV observed in the seep pavement.

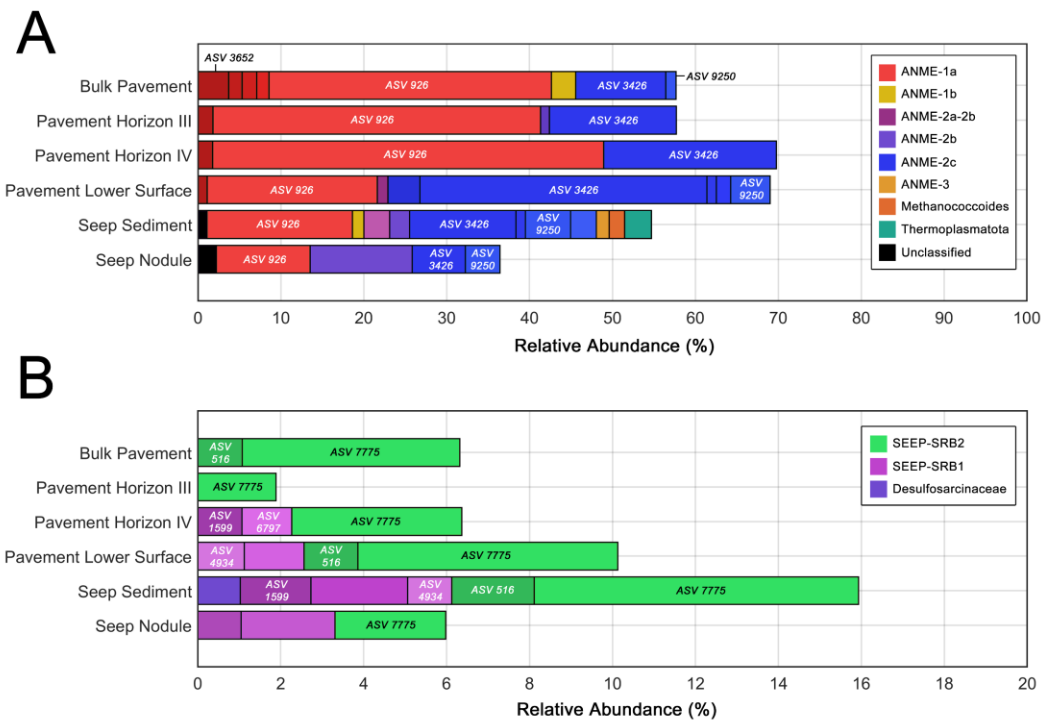

Figure 2.3: ASV-level 16S relative abundances within A) Archaea and B) *Desulfobacterota* for all sampled substrates where tripartite, inter-ANME associations were observed. Bars are colored by genus-level classification according to the Silva V138.1 SSURef database (Quast et al., 2013), where distinct shades correspond to different ASVs within the same genus. Recurring ASVs are labeled. Note that the scale for B) *Desulfobacterota* ASV abundances only goes up to 20%.

In addition to archaeal identity and diversity, we also examined bacterial identity, focusing on *Desulfobacterota* as the parent phylum of the known syntrophic sulfate-reducing partners in ANME-SRB consortia (Fig. 2.3B). We observed all sequenced samples contained *Desulfobacterota* at lower relative abundances (<16%) across all sequenced samples, potentially due to the biases inherent in amplicon sequencing methods. However, the *Desulfobacterota* members present were heavily dominated by Seep-SRB2, known to partner with ANME-1 and ANME-2c, and Seep-SRB1, which contains diverse lineages some of which partner with ANME-2 subclades. As with ANME-1, Seep-SRB2 ASVs were dominated by a single ASV. This did not extend to the Seep-SRB1 ASVs, which were far more diverse and inconsistent across the substrates where the tripartite associations were observed.

Recurring ANME and *Desulfobacterota* ASVs (378 bp) from these samples were compared to similar 16S sequences isolated from hydrocarbon seeps, shown in Figure 2.4. We observed that recurring ANME-1a ASVs were most closely related to sequences from a candidate ANME-1a species (*gen. nov. 3, sp. nov. 1*), which contains sequences identified from diverse, globally distributed methane seeps, including several from Hydrate Ridge, OR (sediment sample #3730, Hatzenpichler et al., 2016). Due to the comparatively short length of the 16S rRNA gene sequenced in this study, the majority of known sequences from this candidate species are identical over the sequenced region, limiting our ability to discern its closest relatives within the species. Nevertheless, the dominant ANME-1a ASV was also identical over its sequenced length to an ANME-1a sequence from the Pomonte seep site off the coast of Mediterranean island Elba, where previous ANME-1/ANME-2 tripartite associations had been microscopically identified (Ruff et al., 2016).

ANME-2c ASVs from SMM 800 samples also were identical over the sequenced region with ANME-2c from the same source sediment at Hydrate Ridge, OR (Hatzenpichler et al., 2016). Despite distinct placement from other ANME subclades, poor intra-clade bootstrap values due to the limited signal available in the V4V5 region of the 16S rRNA gene precluded defining more highly resolved relationships within the ANME-2c sequences. Within the recurring *Desulfobacterota* ASVs from

SMM 800, the dominant Seep-SRB2 ASV was related to Seep-SRB2 from globally distributed seep sites, including the same source sediment at Hydrate Ridge, OR as for the dominant ANME-1a and ANME-2c ASVs (Hatzenpichler et al., 2016), as well as mesophilic (20°C) enrichments of cells from the same cold seeps off the coast of Elba where tripartite associations were identified (Wegener et al., 2016). Of the recurring Seep-SRB1 sequences, one ASV was more closely related to members of the syntrophic Seep-SRB1a subclade, while the other two were more closely placed within the non-syntrophic Seep-SRB1c clade (Murali et al., 2023).

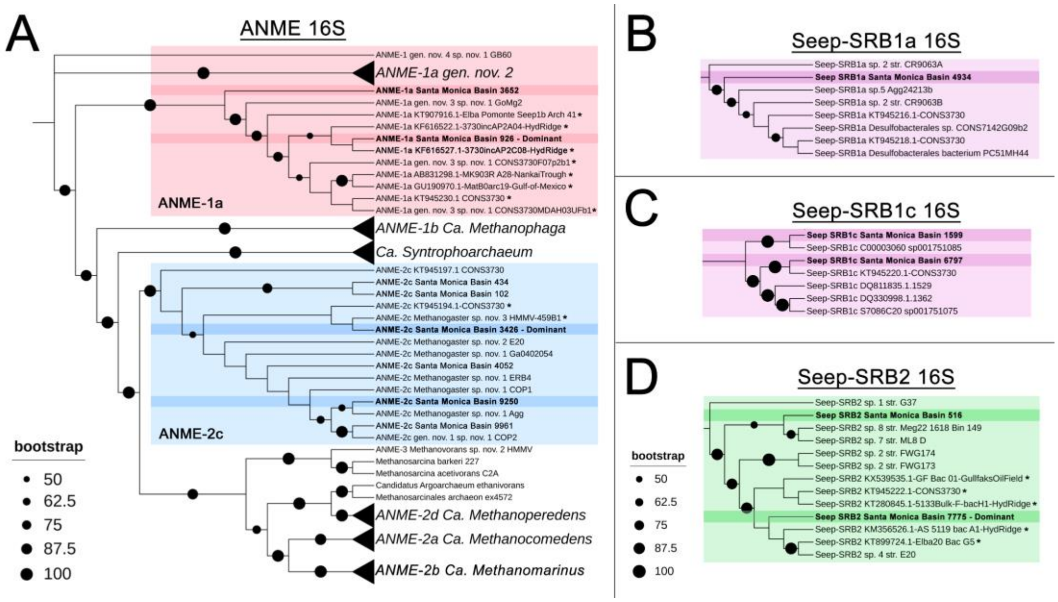

Figure 2.4: A) Maximum-likelihood phylogenetic tree of various ANME archaeal subclades, built with closely related 16S rRNA gene sequences to recurring ASVs in samples included in this study (highlighted, in bold). B)-D) Phylogenetic tree of various *Desulfobacterota* subclades, including 16S rRNA sequences from sulfate-reducing bacteria (SRB) previously observed in syntrophic consortia with ANME archaea. Reference sequences, including full-length sequences, that aligned with 100% percent identity onto the 'dominant' ASVs from each genus are indicated with asterisks. Branch support values >50% are indicated by closed black circles of increasing size as they approach 100%. The full tree is shown in Appendix Fig. 2.9. Tree construction parameters are found in the Methods section.

3.4 Identity, Morphology, and Frequency of Tripartite Associations in R1 Seep Pavement

Based on the prevalence of ANME-2c found from the 16S rRNA-based community profiles, we hypothesized ANME-2c was the second archaeal member in the tripartite associations observed in the pavement samples (R1). To test this hypothesis, we re-imaged the same samples using an ANME-2c-specific FISH probe (ANME2c-760) along with the same bacterial (EUB338 mix) and ANME-1 (ANME1-350, ANME1-728) probes as from the initial survey (Fig. 2.5).

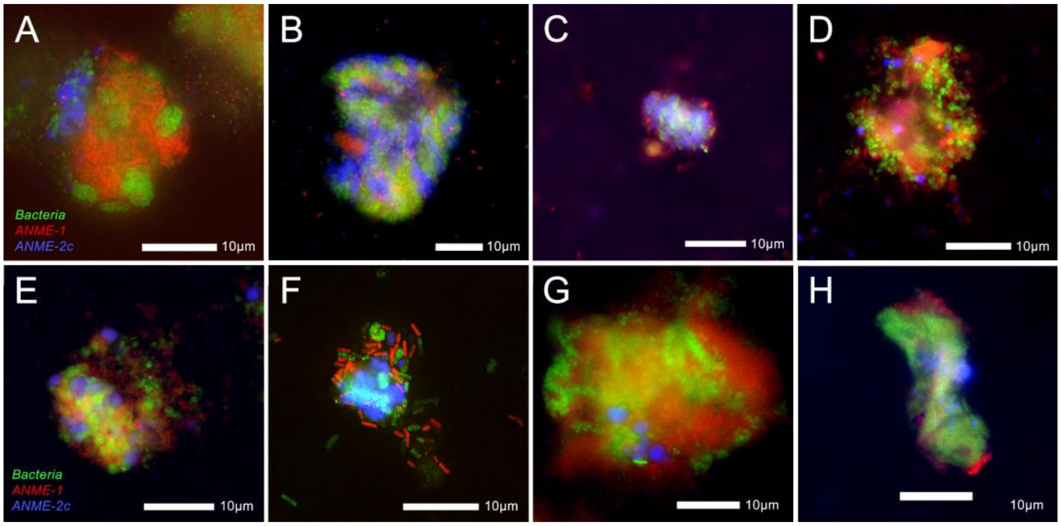

Figure 2.5: Fluorescence in-situ hybridization (FISH) images of ANME-1/ANME-2c tripartite associations observed in and/or association with hydrate-bearing seep pavement (R1) at Santa Monica Mound 800, with ANME-1 (in red), bacteria (in green), and ANME-2c (in blue).

These FISH experiments confirmed the presence of ANME-1/ANME-2c/bacteria tripartite associations in the lower two horizons of the seep pavement, as well as on the pavement’s lower surface. We note that tripartite associations were only observed in these subsamples, where most ANME/bacteria aggregates within R1 were of the typical two-partner form commonly observed in seep substrates (Appendix, Fig. 2.11). Tripartite association abundance per mg sample relative to single cells and non-tripartite cell aggregates is shown in Table 2.2. Notably, tripartite aggregates in R1 were proportionally rare but not vanishingly so, comprising approximately 10% of the ANME aggregates in a given horizon.

Table 2.2
In-situ ANME-1 / ANME-2c association frequency in seep pavement (R1)

Sample ID	**Horizon III**	**Horizon IV**	**Lower Surface**
Tripartite Associations / mg Sample	249	3.15×10^3	1.15×10^5
Non-Tripartite Aggregates / mg Sample	5.76×10^3 (2.00×10^3)	2.39×10^4 (5.06×10^3)	7.77×10^5 (1.42×10^5)
Single Cells / mg Sample	8.90×10^5 (3.91×10^4)	5.53×10^6 (5.47×10^5)	1.07×10^8 (1.01×10^7)

Note: Tripartite associations consisting of loose cell groupings <10-µm were not considered for frequency as these were ambiguous. Standard error values for the single cell and aggregate cell counts are in parentheses.

Despite their proportional rarity within the seep pavement samples, we observed a consistent increase in absolute number of ANME-1/ANME-2c tripartite associations moving from the interior to the exterior of the sample, which mirrored the trends in non-tripartite aggregate and single cell abundances. We also observed a diversity of morphologies employed by the tripartite associations, including those previously observed in ANME-SRB aggregates (e.g., mixed, segmented, shell-type; Orphan et al., 2002; Knittel & Boetius, 2009; McGlynn et al., 2015). More specifically, we saw heterogeneous tripartite associations that suggested interactions between two distinct, ANME-specific aggregates (Fig. 2.5ABH) as well as more homogeneous, mixed associations that could range from associations of segmented clusters of ANME and bacteria (Fig. 2.5DE) to single-cell level associations (Fig. 2.5F). Larger, denser tripartite associations (Fig. 2.5H) reminiscent of the segmented ANME-1/ANME-2c associations previously observed in microbial mats associated with methanotrophic reefs in the Black Sea (Treude et al., 2007) were also observed in cell extracts sampled from the pavement's lower surface. A brief catalog of these associations across the pavement samples is provided in Appendix Tables 2.7-2.8. Interestingly, we also observed occasional tripartite associations where the non-ANME-1 archaeal partner was not labeled by the ANME-2c probe in several of the pavement horizons, though their morphologies still resembled those observed in the ANME-1/ANME-2c associations (Appendix, Fig. 2.12). Similarly, these unlabeled cells still had the coccoidal forms traditional associated with ANME-2 cells (Orphan et al., 2002; Knittel et al., 2005; Treude et al., 2007). More strikingly, while most of these unidentified associations occurred between ANME-1 and a coccoidal, unlabeled partner, we did document one instance of ANME-2c in association with a coccoidal, non-ANME-1, non-ANME-2c partner (Appendix, Fig. 2.12).

3.5 Detection of Cell-Specific Translational Activity Among Tripartite Association Members

12-week incubations of the tripartite association-bearing lower seep pavement (R1) sections with L-Homopropargylglycine (HPG), a clickable methionine analog, under sulfate- and methane-rich conditions revealed continued translational activity in tripartite aggregates (Fig 2.6). Assimilation of HPG as indicated by BONCAT signal was broadly observed across single cells, ANME-1-only aggregates, ANME-1/bacterial aggregates, non-ANME-1 archaeal/bacterial aggregates, and tripartite archaeal associations (Fig. 2.6, Appendix Fig. 2.15).

Interestingly, while ANME-1 were confirmed to be translationally active when in association with a single bacterial partner, i.e., typical bipartite ANME/SRB aggregates, we could not observe concurrent ANME-1 and non-ANME-1 archaeal HPG assimilation in tripartite associations. Instead, all limited observations of tripartite associations from the lower half of the seep pavement showed BONCAT signal consistently and exclusively localized to the bacterial and non-ANME-1 members (Fig. 2.6).

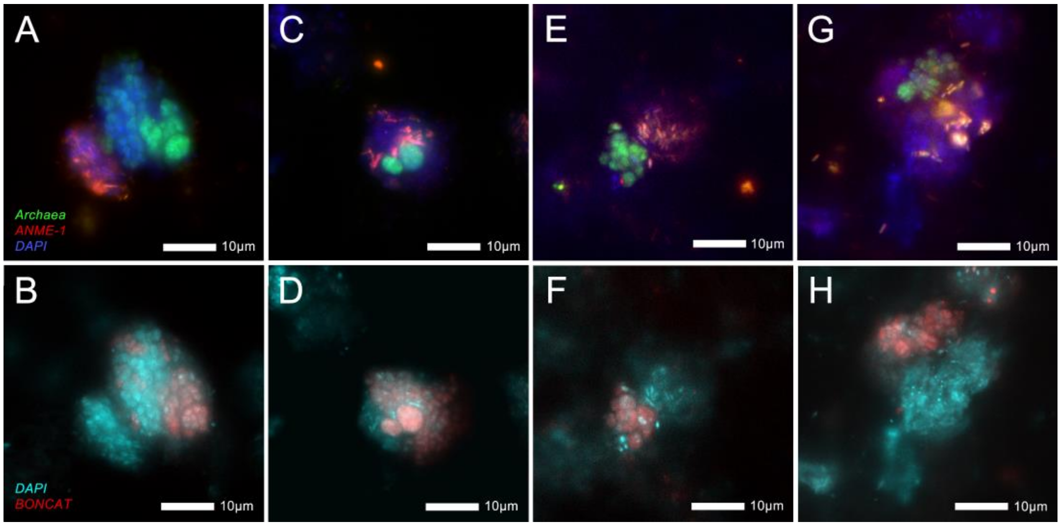

Figure 2.6: BONCAT-FISH images of translational activity within tripartite associations from hydrate-bearing seep pavement (R1) at Santa Monica Mound 800. Panels A), C), E) and G) show FISH identity and are paired to corresponding BONCAT signal in B), D), F), and H), respectively. FISH/DAPI signal in channels overlap such that ANME-1 cells are orange, non-ANME-1 archaeal cells are greenish-cyan, and non-archaeal cells are in blue. Of the tripartite associations imaged, the strongest BONCAT signal appears consistently connected to bacterial cells and non-ANME-1 archaea. Individual channels are shown in Appendix Fig. 2.16.

4. Discussion

4.1 Occurrence and Settings of Inter-ANME Associations

Despite a limited number of documented sightings, direct, cell-to-cell associations between archaeal anaerobic methanotroph (ANME) clades appear to be a globally distributed and substrate-independent phenomenon associated with high advective methane flux in diverse marine seep environments. Including the present work, there are now confirmed observations from microbial mats on carbonate ‘reefs’ (Treude et al., 2007), shallow sand (Ruff et al., 2016), cold seep mud, sediment-hosted carbonate nodules, and gas hydrate-bearing seep pavement. Interestingly, these sites also encompass a diversity of physical and geochemical conditions. Ruff et al. (2016)’s documentation of inter-ANME associations were found in permeable sands under warm water (19°C) and hallmarked by high-sulfate (~28mM), low-sulfide (<2mM) concentrations with advective porewater circulation (Janssen et al., 2005). By contrast, the carbonate reefs at the northwestern Black Sea featuring these microbial mat-hosted tripartite associations were in stratified, permanently anoxic, and sulfide-rich waters (Michaelis et al., 2002), averaging around 9°C (Murray & Izdar, 1989). The sampled locations at Santa Monica Mound 800 (SMM 800) with tripartite associations were colder (4°C) and more closely resembled diffusion-driven cold methane seep environments, though geochemical conditions varied between sulfate- and methane-rich (hydrate-bearing seep pavement), to sulfide-rich and methane-poor (sediment and sediment-hosted nodule, Chapter 1). The presence of tripartite associations across such a range of environments underscores the role of microbial syntrophy in overcoming diverse environmental challenges and prompts further study into the ecological flexibility of individual ANME subclades.

Generally, ANME-2 in seep environments have been observed to show less ecological flexibility than ANME-1 and as such are found in a narrower range of environments. For example, ANME-2 are reported to be restricted to colder temperatures compared to ANME-1 (Nauhaus et al., 2005; Knittel et al., 2005; Holler et al., 2011; Rossel et al., 2011; Biddle et al., 2012; Vigneron et al., 2013). ANME-2 has also been observed to be more sensitive to ambient methane and sulfate/sulfide concentrations than ANME-1 (Blumenberg et al., 2004; Nauhaus et al., 2007; Rossel et al., 2011; Yanagawa et al., 2011; Biddle et al., 2012; Vigneron et al., 2013). Interestingly, ANME-2 has shown evidence of higher oxidative stress tolerance, which reinforces its dominance in sulfate-rich, sometimes micro-oxic environments (Knittel et al., 2005; Rossel et al., 2011; Chen et al., 2023). Together, these observations align with general patterns of centimeter-scale stratification of ANME observed at hydrocarbon seeps, but they do not sufficiently explain repeated genetic and microscopic evidence of ANME co-occurrence in these diverse environments (Orphan et al., 2002; Treude et al., 2007; Hatzenpichler et al., 2016; Ruff et al., 2016; Chapter 1). Such regimes of co-occurrence have been documented more extensively with the rise of 16S-based community surveys of hydrocarbon seeps, and by pairing such bulk sequencing with microscopy, our work suggests that tripartite, inter-ANME associations may be more common in these regions than previously thought. As such, a concentrated effort to identify inter-ANME associations in seep environments featuring these co-occurrences may expand our understanding of ecological niches traditionally associated with specific ANME clades.

4.2 Implications for Identity and Specificity in Tripartite, Inter-ANME Associations

Fluorescence in-situ hybridization (FISH) observations of tripartite associations within and on the surface of hydrate-bearing seep pavement (R1) provide the most definitive visual confirmation of tripartite associations between ANME-1, ANME-2c, and a yet-unidentified bacterial partner. Importantly, this cell-specific identification of the ANME-2c member aligned with its dominant presence in the amplicon sequencing data. Based on the clear dominance of ANME-1a above other ANME-1 subclades in these 16S rRNA data, we therefore interpret the ANME-1a member as the likely taxonomic designation of the ANME-1 partner in R1. Similarly, the dominance of Seep-SRB2 across all substrates also suggests it may be the bacterial partner in these tripartite associations. Indeed, Seep-SRB2 has been observed in separate, syntrophic aggregates with ANME-1 as well as with ANME-2 (Kleindienst et al., 2012; Krukenberg et al., 2018).

By contrast, 16S pyrosequencing by Ruff et al. (2016) revealed a clearer dominance by ANME-2a and ANME-1b in the samples from which tripartite associations were observed, with minor to minimal (<10%) contributions from ANME-2c and ANME-1a. Combined with FISH-based evidence of Seep-SRB1a's participation in the tripartite associations at the Elba seep site, this suggests that tripartite associations may exist across multiple ANME/SRB subclades and are thus not likely to be a specialized behavior. Indeed, occasional observations of a coccoidal, third archaeal partner from the R1 seep pavement may also point to more than one ANME-2 subclade forming these tripartite associations within the same sample. In support of this interpretation, multiple ANME subclades have also been observed to demonstrate diverse spatial associations with non-SRB, including uncultured alpha- and beta-proteobacteria (Knittel & Boetius, 2009), gamma-proteobacteria, *Verrucomicrobia* (Hatzenpichler et al., 2016), *Anaerolineales*, and *Methanococcoides* (Yu et al., 2022b).

Furthermore, the phylogenetic proximity of recurring ASVs to other globally sourced, seep-related ASVs across both ANME and *Desulfobacterota* subclades supports that inter-ANME tripartite associations are not unique to distal outgroups. Indeed, the recurring ASVs from the ANME-1a, ANME-2c, and SEEP-SRB2 subclades were also routinely present in non-tripartite association bearing sediments throughout SMM 800 (Supplemental Table T2), suggestive that the candidate ASVs participating in these associations were not limited to this configuration. Moreover, observations of more common ANME-SRB configurations (i.e., monospecific or two-membered aggregates) with cell morphologies resembling those from tripartite associations in the same samples further posit that tripartite associations are not obligate behavior, but instead facultatively displayed by the same ANME and SRB that also participate in these more common configurations.

Even so, 16S-based community assays are limited in their ability to constrain taxonomic identity in these tripartite associations. Such community profiles are still subject to various biases informed by amplification protocol (Brooks, 2016; Sinha et al., 2017; McLaren et al., 2019), primer selection (Sipos et al., 2007), and even differences in 16S copy number between taxa (Kembel et al. 2012; Louca et al., 2018) that may distort true relative abundances and favor one taxon over another. It may be that these phenomena are uniquely caused by rare ASVs that were not amplified above the 1% threshold in our evaluation. Alternatively, these associations may not be attributed to a singular ASV and instead be a mode of association accessible to several members of a subclade and beyond. The limited phylogenetic resolution afforded by FISH microscopy ultimately precludes definitive ASV- or species-specific taxonomic assignation of members in the SMM800 tripartite associations beyond bacteria, ANME-1, ANME-2c, but 16S-based community assays nonetheless constrain the set of co-occurring ANME subclades and inform further targeted observations of these associations with FISH.

Beyond taxonomic specificity, the observed range of tripartite association morphologies and cell-to-cell contacts with FISH suggests that these associations are not exclusive to a particular spatial arrangement, nor dependent on adjacence to an archaeal or bacterial member. These morphologies were all reminiscent of those employed by ‘standard’ ANME-SRB consortia, including segregated to well-mixed associations (Orphan et al., 2002; Knittel et al., 2005; Knittel & Boetius, 2009; McGlynn et al., 2015; Ruff et al., 2016), and while many featured direct ANME-SRB contact, ANME-ANME contact was as equal if not more present. Interestingly, the more heterogeneous associations from the seep pavement were often portioned into ANME-1-rich or ANME-2c-rich regions and sometimes adopted a more ‘lobate’ form that may suggest that these associations began as distinct ANME-1 and ANME-

2 aggregates (either monospecific or paired with SRB) prior to their interaction. Similarly, observations of ANME-1 single cells forming a ‘shell’ around other non-ANME-1 archaeal aggregates suggests that the ANME-1 cells may have arrived after the non-ANME-1 archaeal aggregate had already formed. This may also align with the stratification of ANME clades at the mat-covered methanotrophic reefs in the Black Sea (Treude et al., 2007), where inter-ANME associations may have arisen from the sequential growth of ANME-1, followed by ANME-2. Still, observations of well-mixed tripartite associations, both as heterogeneous clusters as well as more evenly mixed single cells evocative of the associations documented by Ruff et al. (2016) may suggest a more syngenetic origin. Here, long-term studies of lab-based incubations of these associations may shed further light on drivers governing how and when these associations originate.

4.3 Metabolic Implications in Tripartite, Inter-ANME Associations

Our BONCAT data suggest that ANME-1 in tripartite associations were translationally inactive over the 12-week incubation. Because we did identify active ANME-1 aggregates (both monospecific and paired with SRB) in the same samples, this may suggest the nature of the inter-ANME association is competitive and that ANME-2 was able to out-compete ANME-1 for essential metabolites. Along these lines, the environmental conditions around the lower half of the seep pavement may have favored the ANME-2 partner previously reported to dominate in sulfate- and methane-rich environments (Yanagawa et al., 2011; Biddle et al., 2012; Vigneron et al., 2013). Interestingly, secondary ion mass spectrometry (SIMS) imaging of the

ANME-1/ANME-2-rich microbial mats from Treude et al. (2007) observed more depleted ^{13}C-content in ANME-2-rich biomass, which corroborates our assessment of ANME-2's competitive advantage over ANME-1 when in close proximity.

Advantages stemming from inter-ANME associations may be conferred from exchange of secondary metabolites, protections against environmental stresses, or even metabolic processes inaccessible or unfavorable for the other partner. For example, ANME-2b and ANME-2c have been observed to fix nitrogen in association with an SRB partner (Dekas et al., 2009; Dekas & Orphan, 2011; Metcalfe et al., 2021), where this phenomenon has not been observed in ANME-1. Indeed, most inter-ANME associations characterized thus far have been between ANME-1 and ANME-2. This may suggest a functional synergy inherent to their genetic distance and traditional niche differentiation. Evidence of nutritional dependencies between ANME and SRB partners, including cobalamin exchange (Murali et al., 2023), also attest to the potential for additional syntrophic interactions beyond AOM and encourage additional genome-based studies to better characterize the nature of syntrophic associations in ANME-SRB systems.

Regardless of direct drivers for physical association, there are also implications for indirect effects of inter-ANME contact. For example, these associations open another avenue for horizontal gene transfer (HGT) between multiple ANME subtaxa. Chadwick et al. (2022) reported a higher similarity in PAAR-domain spike proteins between ANME-2b and ANME-1 than other ANME-2 subtaxa, suggestive of exchange facilitated by either interaction with the same syntrophic partner or, in the case of tripartite associations, with each other. As such, these tripartite, inter-ANME associations may enable evolutionary opportunities for expansion of interaction and/or syntrophic partner promiscuity.

Broadly, these tripartite, inter-ANME associations establish a previously underrecognized mode of syntrophic interactions in AOM consortia. Physiological studies targeting individual members in these associations should seek to improve on connecting identity with spatial distribution and substrate-specific activity. Here, stable isotope probing (SIP) methods coupled to taxon-specific observations with fluorescence microscopy (e.g., FISH-nanoSIMS) may provide improved resolution towards defining metabolic activity beyond AOM informing these tripartite associations (Dekas & Orphan, 2011). Furthermore, specific taxonomic identification conferred through activity-based cell sorting coupled to multiple displacement amplification (MDA, as in Hatzenpichler et al., 2016) may be especially useful for minimizing sampling bias by increasing throughput and providing the most direct connection of translational activity to genetic identity. Multi-omic studies, including metagenomic and metatranscriptomic sequencing of environmental samples with and without tripartite associations could also shed light on physiological behaviors unique to these configurations. We expect such further studies, coupled with improved sampling depth, will better shape our understanding of the diversity and complexity reflected in AOM consortia and their ultimate role as an important global methane sink.

5. References

Amann, R.I., Binder, B.J., Olson, R.J., Chisholm, S.W., Devereux, R., Stahl, D.A., 1990. Combination of 16S rRNA-targeted oligonucleotide probes with flow cytometry for analyzing mixed microbial populations. Applied and Environmental Microbiology 56, 1919—1925. https://doi.org/10.1128/aem.56.6.1919-1925.1990

Biddle, J.F., Cardman, Z., Mendlovitz, H., Albert, D.B., Lloyd, K.G., Boetius, A., Teske, A., 2012. Anaerobic oxidation of methane at different temperature regimes in Guaymas Basin hydrothermal sediments. ISME J 6, 1018—1031. https://doi.org/10.1038/ismej.2011.164

Blumenberg, M., Seifert, R., Reitner, J., Pape, T., Michaelis, W., 2004. Membrane lipid patterns typify distinct anaerobic methanotrophic consortia. Proceedings of the National Academy of Sciences 101, 11111—11116. https://doi.org/10.1073/pnas.0401188101

Boetius, A., Ravenschlag, K., Schubert, C.J., Rickert, D., Widdel, F., Gieseke, A., Amann, R., Jørgensen, B.B., Witte, U., Pfannkuche, O., 2000. A marine microbial consortium apparently mediating anaerobic oxidation of methane. Nature 407, 623—626. https://doi.org/10.1038/35036572

Bolyen, E., Rideout, J.R., Dillon, M.R., Bokulich, N.A., Abnet, C.C., Al-Ghalith, G.A., Alexander, H., Alm, E.J., Arumugam, M., Asnicar, F., Bai, Y., Bisanz, J.E., Bittinger, K., Brejnrod, et al., 2019. Reproducible, interactive, scalable and extensible microbiome data science using QIIME 2. Nat Biotechnol 37, 852—857. https://doi.org/10.1038/s41587-019-0209-9

Brooks, J.P., 2016. Challenges for case-control studies with microbiome data. Annals of Epidemiology, The Microbiome and Epidemiology 26, 336-341.e1. https://doi.org/10.1016/j.annepidem.2016.03.009

Cai, C., Leu, A.O., Xie, G.-J., Guo, J., Feng, Y., Zhao, J.-X., Tyson, G.W., Yuan, Z., Hu, S., 2018. A methanotrophic archaeon couples anaerobic oxidation of methane to Fe(III) reduction. The ISME Journal 12, 1929—1939. https://doi.org/10.1038/s41396-018-0109-x

Callahan, B.J., McMurdie, P.J., Rosen, M.J., Han, A.W., Johnson, A.J.A., Holmes, S.P., 2016. DADA2: High-resolution sample inference from Illumina amplicon data. Nat Methods 13, 581—583. https://doi.org/10.1038/nmeth.3869

Chadwick, G.L., Skennerton, C.T., Laso-Pérez, R., Leu, A.O., Speth, D.R., Yu, H., Morgan-Lang, C., Hatzenpichler, R., Goudeau, D., Malmstrom, R., Brazelton, W.J., Woyke, T., Hallam, S.J., Tyson, G.W., Wegener, G., Boetius, A., Orphan, V.J., 2022. Comparative genomics reveals electron transfer and syntrophic mechanisms differentiating methanotrophic and methanogenic archaea. PLOS Biology 20, e3001508. https://doi.org/10.1371/journal.pbio.3001508

Chen, J., Li, Y., Zhong, C., Xu, Z., Lu, G., Jing, H., Liu, H., 2023. Genomic Insights into Niche Partitioning across Sediment Depth among Anaerobic Methane-Oxidizing Archaea in Global Methane Seeps. mSystems 8, e01179-22. https://doi.org/10.1128/msystems.01179-22

Daims, H., Brühl, A., Amann, R., Schleifer, K.-H., Wagner, M., 1999. The Domain-specific Probe EUB338 is Insufficient for the Detection of all *Bacteria*: Development and Evaluation of a more Comprehensive Probe Set. Systematic and Applied Microbiology 22, 434—444. https://doi.org/10.1016/S0723-2020(99)80053-8

Dekas, A.E., Orphan, V.J., 2011. Identification of Diazotrophic Microorganisms in Marine Sediment via Fluorescence *In Situ* Hybridization Coupled to Nanoscale Secondary Ion Mass Spectrometry (FISH-NanoSIMS), in: Klotz, M.G. (Ed.), Methods in Enzymology, Research on Nitrification and Related Processes, Part A. Academic Press, pp. 281—305. https://doi.org/10.1016/B978-0-12-381294-0.00012-2

Dekas, A.E., Poretsky, R.S., Orphan, V.J., 2009. Deep-Sea Archaea Fix and Share Nitrogen in Methane-Consuming Microbial Consortia. Science 326, 422—426. https://doi.org/10.1126/science.1178223

Durisch-Kaiser, E., Klauser, L., Wehrli, B., Schubert, C., 2005. Evidence of Intense Archaeal and Bacterial Methanotrophic Activity in the Black Sea Water Column. Applied and Environmental Microbiology 71, 8099—8106. https://doi.org/10.1128/AEM.71.12.8099-8106.2005

Edgar, R.C., 2004. MUSCLE: multiple sequence alignment with high accuracy and high throughput. Nucleic Acids Research 32, 1792—1797. https://doi.org/10.1093/nar/gkh340

Harrison, B.K., Zhang, H., Berelson, W., Orphan, V.J., 2009. Variations in Archaeal and Bacterial Diversity Associated with the Sulfate-Methane Transition Zone in Continental Margin Sediments (Santa Barbara Basin, California). Applied and Environmental Microbiology 75, 1487—1499. https://doi.org/10.1128/AEM.01812-08

Hatzenpichler, R., Connon, S.A., Goudeau, D., Malmstrom, R.R., Woyke, T., Orphan, V.J., 2016. Visualizing in situ translational activity for identifying and sorting slow-growing archaeal−bacterial consortia. Proceedings of the

National Academy of Sciences 113, E4069—E4078. https://doi.org/10.1073/pnas.1603757113

Hatzenpichler, R., Orphan, V.J., 2016. Detection of Protein-Synthesizing Microorganisms in the Environment via Bioorthogonal Noncanonical Amino Acid Tagging (BONCAT), in: McGenity, T.J., Timmis, K.N., Nogales, B. (Eds.), Hydrocarbon and Lipid Microbiology Protocols: Single-Cell and Single-Molecule Methods. Springer, Berlin, Heidelberg, pp. 145—157. https://doi.org/10.1007/8623_2015_61

Hatzenpichler, R., Scheller, S., Tavormina, P.L., Babin, B.M., Tirrell, D.A., Orphan, V.J., 2014. In-situ visualization of newly synthesized proteins in environmental microbes using amino acid tagging and click chemistry. Environmental Microbiology 16, 2568—2590. https://doi.org/10.1111/1462-2920.12436

Holler, T., Widdel, F., Knittel, K., Amann, R., Kellermann, M.Y., Hinrichs, K.-U., Teske, A., Boetius, A., Wegener, G., 2011. Thermophilic anaerobic oxidation of methane by marine microbial consortia. The ISME Journal 5, 1946—1956. https://doi.org/10.1038/ismej.2011.77

House, C.H., Orphan, V.J., Turk, K.A., Thomas, B., Pernthaler, A., Vrentas, J.M., Joye, S.B., 2009. Extensive carbon isotopic heterogeneity among methane seep microbiota. Environmental Microbiology 11, 2207—2215. https://doi.org/10.1111/j.1462-2920.2009.01934.x

Janssen, F., Huettel, M., Witte, U., 2005. Pore-water advection and solute fluxes in permeable marine sediments (II): Benthic respiration at three sandy sites with different permeabilities (German Bight, North Sea). Limnology and Oceanography 50, 779—792. https://doi.org/10.4319/lo.2005.50.3.0779

Kembel, S.W., Wu, M., Eisen, J.A., Green, J.L., 2012. Incorporating 16S Gene Copy Number Information Improves Estimates of Microbial Diversity and Abundance. PLOS Computational Biology 8, e1002743. https://doi.org/10.1371/journal.pcbi.1002743

Kleindienst, S., Ramette, A., Amann, R., Knittel, K., 2012. Distribution and in situ abundance of sulfate-reducing bacteria in diverse marine hydrocarbon seep sediments. Environmental Microbiology 14, 2689—2710. https://doi.org/10.1111/j.1462-2920.2012.02832.x

Knittel, K., Boetius, A., 2009. Anaerobic Oxidation of Methane: Progress with an Unknown Process. Annu. Rev. Microbiol. 63, 311—334. https://doi.org/10.1146/annurev.micro.61.080706.093130

Knittel, K., Lösekann, T., Boetius, A., Kort, R., Amann, R., 2005. Diversity and Distribution of Methanotrophic Archaea at Cold Seeps. Applied and

Environmental Microbiology 71, 467—479. https://doi.org/10.1128/AEM.71.1.467-479.2005

Kozich, J.J., Westcott, S.L., Baxter, N.T., Highlander, S.K., Schloss, P.D., 2013. Development of a Dual-Index Sequencing Strategy and Curation Pipeline for Analyzing Amplicon Sequence Data on the MiSeq Illumina Sequencing Platform. Appl Environ Microbiol 79, 5112—5120. https://doi.org/10.1128/AEM.01043-13

Krüger, M., Blumenberg, M., Kasten, S., Wieland, A., Känel, L., Klock, J.-H., Michaelis, W., Seifert, R., 2008. A novel, multi-layered methanotrophic microbial mat system growing on the sediment of the Black Sea. Environmental Microbiology 10, 1934—1947. https://doi.org/10.1111/j.1462-2920.2008.01607.x

Krukenberg, V., Harding, K., Richter, M., Glöckner, F.O., Gruber-Vodicka, H.R., Adam, B., Berg, J.S., Knittel, K., Tegetmeyer, H.E., Boetius, A., Wegener, G., 2016. Candidatus Desulfofervidus auxilii, a hydrogenotrophic sulfate-reducing bacterium involved in the thermophilic anaerobic oxidation of methane. Environmental Microbiology 18, 3073—3091. https://doi.org/10.1111/1462-2920.13283

Krukenberg, V., Riedel, D., Gruber-Vodicka, H.R., Buttigieg, P.L., Tegetmeyer, H.E., Boetius, A., Wegener, G., 2018. Gene expression and ultrastructure of meso- and thermophilic methanotrophic consortia. Environmental Microbiology 20, 1651—1666. https://doi.org/10.1111/1462-2920.14077

Laso-Pérez, R., Wu, F., Crémière, A., Speth, D.R., Magyar, J.S., Zhao, K., Krupovic, M., Orphan, V.J., 2023. Evolutionary diversification of methanotrophic ANME-1 archaea and their expansive virome. Nat Microbiol 8, 231—245. https://doi.org/10.1038/s41564-022-01297-4

Li, W., Cai, C., Song, Y., Ni, G., Zhang, X., Lu, P., 2021. The Role of Crystalline Iron Oxides in Methane Mitigation through Anaerobic Oxidation of Methane. ACS EST Water 1, 1153—1160. https://doi.org/10.1021/acsestwater.0c00199

Louca, S., Doebeli, M., Parfrey, L.W., 2018. Correcting for 16S rRNA gene copy numbers in microbiome surveys remains an unsolved problem. Microbiome 6, 41. https://doi.org/10.1186/s40168-018-0420-9

Martin, M., 2011. Cutadapt removes adapter sequences from high-throughput sequencing reads. EMBnet.journal 17, 10—12. https://doi.org/10.14806/ej.17.1.200

Mason, O. U., Case, D. H., Naehr, T. H., Lee, R. W., Thomas, R. B., Bailey, J. V., & Orphan, V. J. (2015). Comparison of Archaeal and Bacterial Diversity in

Methane Seep Carbonate Nodules and Host Sediments, Eel River Basin and Hydrate Ridge, USA. Microbial Ecology, 70(3), 766—784. https://doi.org/10.1007/s00248-015-0615-6

McGlynn, S.E., Chadwick, G.L., Kempes, C.P., Orphan, V.J., 2015. Single cell activity reveals direct electron transfer in methanotrophic consortia. Nature 526, 531—535. https://doi.org/10.1038/nature15512

McLaren, M.R., Willis, A.D., Callahan, B.J., 2019. Consistent and correctable bias in metagenomic sequencing experiments. eLife 8, e46923. https://doi.org/10.7554/eLife.46923

Metcalfe, K.S., Murali, R., Mullin, S.W., Connon, S.A., Orphan, V.J., 2021. Experimentally-validated correlation analysis reveals new anaerobic methane oxidation partnerships with consortium-level heterogeneity in diazotrophy. ISME J 15, 377—396. https://doi.org/10.1038/s41396-020-00757-1

Michaelis, W., Seifert, R., Nauhaus, K., Treude, T., Thiel, V., Blumenberg, M., Knittel, K., Gieseke, A., Peterknecht, K., Pape, T., Boetius, A., Amann, R., Jørgensen, B.B., Widdel, F., Peckmann, J., Pimenov, N.V., Gulin, M.B., 2002. Microbial Reefs in the Black Sea Fueled by Anaerobic Oxidation of Methane. Science 297, 1013—1015. https://doi.org/10.1126/science.1072502

Murali, R., Yu, H., Speth, D.R., Wu, F., Metcalfe, K.S., Crémière, A., Laso-Pèrez, R., Malmstrom, R.R., Goudeau, D., Woyke, T., Hatzenpichler, R., Chadwick, G.L., Connon, S.A., Orphan, V.J., 2023. Physiological potential and evolutionary trajectories of syntrophic sulfate-reducing bacterial partners of anaerobic methanotrophic archaea. PLOS Biology 21, e3002292. https://doi.org/10.1371/journal.pbio.3002292

Murray, J.W., İzdar, E., 1989. The 1988 Black Sea Oceanographic Expedition: Overview and New Discoveries. Oceanography 2, 15—21.

Nauhaus, K., Treude, T., Boetius, A., Krüger, M., 2005. Environmental regulation of the anaerobic oxidation of methane: a comparison of ANME-I and ANME-II communities. Environmental Microbiology 7, 98—106. https://doi.org/10.1111/j.1462-2920.2004.00669.x

Nauhaus, K., Albrecht, M., Elvert, M., Boetius, A., Widdel, F., 2007. In vitro cell growth of marine archaeal-bacterial consortia during anaerobic oxidation of methane with sulfate. Environ Microbiol 9, 187—196. https://doi.org/10.1111/j.1462-2920.2006.01127.x

Normark, W.R., Piper, D.J.W., Sliter, R., 2006. Sea-level and tectonic control of middle to late Pleistocene turbidite systems in Santa Monica Basin, offshore California. Sedimentology 53, 867—897. https://doi.org/10.1111/j.1365-3091.2006.00797.x

Orphan, V.J., House, C.H., Hinrichs, K.-U., McKeegan, K.D., DeLong, E.F., 2002. Multiple archaeal groups mediate methane oxidation in anoxic cold seep sediments. Proceedings of the National Academy of Sciences 99, 7663—7668. https://doi.org/10.1073/pnas.072210299

Orphan, V.J., House, C.H., Hinrichs, K.-U., McKeegan, K.D., DeLong, E.F., 2001. Methane-Consuming Archaea Revealed by Directly Coupled Isotopic and Phylogenetic Analysis. Science 293, 484—487. https://doi.org/10.1126/science.1061338

Orphan, V.J., Turk, K.A., Green, A.M., House, C.H., 2009. Patterns of 15N assimilation and growth of methanotrophic ANME-2 archaea and sulfate-reducing bacteria within structured syntrophic consortia revealed by FISH-SIMS. Environmental Microbiology 11, 1777—1791. https://doi.org/10.1111/j.1462-2920.2009.01903.x

Paull, C.K., Normark, W.R., Ussler, W., Caress, D.W., Keaten, R., 2008. Association among active seafloor deformation, mound formation, and gas hydrate growth and accumulation within the seafloor of the Santa Monica Basin, offshore California. Marine Geology 250, 258—275. https://doi.org/10.1016/j.margeo.2008.01.011

Pernthaler, A., Dekas, A.E., Brown, C.T., Goffredi, S.K., Embaye, T., Orphan, V.J., 2008. Diverse syntrophic partnerships from deep-sea methane vents revealed by direct cell capture and metagenomics. Proceedings of the National Academy of Sciences 105, 7052—7057. https://doi.org/10.1073/pnas.0711303105

Quast, C., Pruesse, E., Yilmaz, P., Gerken, J., Schweer, T., Yarza, P., Peplies, J., Glöckner, F.O., 2013. The SILVA ribosomal RNA gene database project: improved data processing and web-based tools. Nucleic Acids Research 41, D590—D596. https://doi.org/10.1093/nar/gks1219

Reeburgh, W.S., 2007. Oceanic Methane Biogeochemistry. Chem. Rev. 107, 486—513. https://doi.org/10.1021/cr050362v

Rossel, P.E., Elvert, M., Ramette, A., Boetius, A., Hinrichs, K.-U., 2011. Factors controlling the distribution of anaerobic methanotrophic communities in marine environments: Evidence from intact polar membrane lipids. Geochimica et Cosmochimica Acta 75, 164—184. https://doi.org/10.1016/j.gca.2010.09.031

Ruff, S.E., Kuhfuss, H., Wegener, G., Lott, C., Ramette, A., Wiedling, J., Knittel, K., Weber, M., 2016. Methane Seep in Shallow-Water Permeable Sediment Harbors High Diversity of Anaerobic Methanotrophic Communities, Elba, Italy. Frontiers in Microbiology 7.

Scheller, S., Yu, H., Chadwick, G.L., McGlynn, S.E., Orphan, V.J., 2016. Artificial electron acceptors decouple archaeal methane oxidation from sulfate reduction. Science 351, 703—707. https://doi.org/10.1126/science.aad7154

Schreiber, L., Holler, T., Knittel, K., Meyerdierks, A., Amann, R., 2010. Identification of the dominant sulfate-reducing bacterial partner of anaerobic methanotrophs of the ANME-2 clade. Environmental Microbiology 12, 2327—2340. https://doi.org/10.1111/j.1462-2920.2010.02275.x

Sinha, R., Abu-Ali, G., Vogtmann, E., Fodor, A.A., Ren, B., Amir, A., Schwager, E., Crabtree, J., Ma, S., Abnet, C.C., Knight, R., White, O., Huttenhower, C., 2017. Assessment of variation in microbial community amplicon sequencing by the Microbiome Quality Control (MBQC) project consortium. Nat Biotechnol 35, 1077—1086. https://doi.org/10.1038/nbt.3981

Sipos, R., Székely, A.J., Palatinszky, M., Révész, S., Márialigeti, K., Nikolausz, M., 2007. Effect of primer mismatch, annealing temperature and PCR cycle number on 16S rRNA gene-targetting bacterial community analysis. FEMS Microbiology Ecology 60, 341—350. https://doi.org/10.1111/j.1574-6941.2007.00283.x

Sletten, E.M., Bertozzi, C.R., 2009. Bioorthogonal Chemistry: Fishing for Selectivity in a Sea of Functionality. Angewandte Chemie International Edition 48, 6974—6998. https://doi.org/10.1002/anie.200900942

Stahl, D.A. and Amann, R., 1991. Development and Application of Nucleic Acid Probes in Bacterial Systematics, in: Stackebrandt, E. and Goodfellow, M., (Eds.), Nucleic Acid Techniques in Bacterial Systematics, John Wiley & Sons Ltd., Chichester, pp. 205-248.

Treude, T., Knittel, K., Blumenberg, M., Seifert, R., Boetius, A., 2005. Subsurface Microbial Methanotrophic Mats in the Black Sea. Applied and Environmental Microbiology 71, 6375—6378. https://doi.org/10.1128/AEM.71.10.6375-6378.2005

Treude, T., Orphan, V., Knittel, K., Gieseke, A., House, C.H., Boetius, A., 2007. Consumption of Methane and CO2 by Methanotrophic Microbial Mats from Gas Seeps of the Anoxic Black Sea. Applied and Environmental Microbiology 73, 2271—2283. https://doi.org/10.1128/AEM.02685-06

Vigneron, A., Cruaud, P., Pignet, P., Caprais, J.-C., Cambon-Bonavita, M.-A., Godfroy, A., Toffin, L., 2013. Archaeal and anaerobic methane oxidizer communities in the Sonora Margin cold seeps, Guaymas Basin (Gulf of California). ISME J 7, 1595—1608. https://doi.org/10.1038/ismej.2013.18

Wegener, G., Krukenberg, V., Riedel, D., Tegetmeyer, H.E., Boetius, A., 2015. Intercellular wiring enables electron transfer between methanotrophic archaea and bacteria. Nature 526, 587—590. https://doi.org/10.1038/nature15733

Wegener, G., Krukenberg, V., Ruff, S.E., Kellermann, M.Y., Knittel, K., 2016. Metabolic Capabilities of Microorganisms Involved in and Associated with the Anaerobic Oxidation of Methane. Front. Microbiol. 7. https://doi.org/10.3389/fmicb.2016.00046

Westram, R., Bader, K., Prüsse, E., Kumar, Y., Meier, H., Glöckner, F.O. et al., 2011. ARB: a software environment for sequence data, in: de Bruijn F.J. (Ed.). Handbook of Molecular Microbial Ecology I, John Wiley & Sons, Ltd., Hoboken, N.J., pp. 399—406.

Yanagawa, K., Sunamura, M., Lever, M.A., Morono, Y., Hiruta, A., Ishizaki, O., Matsumoto, R., Urabe, T., Inagaki, F., 2011. Niche Separation of Methanotrophic Archaea (ANME-1 and -2) in Methane-Seep Sediments of the Eastern Japan Sea Offshore Joetsu. Geomicrobiology Journal 28, 118—129. https://doi.org/10.1080/01490451003709334

Yu, H., Skennerton, C.T., Chadwick, G.L., Leu, A.O., Aoki, M., Tyson, G.W., Orphan, V.J., 2022a. Sulfate differentially stimulates but is not respired by diverse anaerobic methanotrophic archaea. The ISME Journal 16, 168—177. https://doi.org/10.1038/s41396-021-01047-0

Yu, H., Speth, D.R., Connon, S.A., Goudeau, D., Malmstrom, R.R., Woyke, T., Orphan, V.J., 2022b. Community Structure and Microbial Associations in Sediment-Free Methanotrophic Enrichment Cultures from a Marine Methane Seep. Applied and Environmental Microbiology 88, e02109-21. https://doi.org/10.1128/aem.02109-21

6. Appendix

Sample Collection & Processing

Site Classification and Sample Collection

Seep pavement 15590-R1, or R1 in this study (33.799615N, 118.646763W), was collected on the northern flank of the topmost region of the mound. Geological site context for Santa Monica Basin, as well as site and recovery details for the sediment push cores studied (PC44 and PC69) are detailed further in Chapter 1's Supplemental Material. Confirmation of local methane seep activity based on locally identified sites of gas ebullition, microbial mats, and seep macrofauna (e.g., clam beds) is consistent with previous biological and geological surveys of globally distributed cold seeps (Treude et al., 2003; Case et al., 2015; Marlow et al., 2021).

Seep Pavement (R1) Sectioning

Figure 2.7: Seep-associated, non-sediment samples included in this study; A) intact seep pavement (R1), with light-colored, fine-grained sediment overlying its surface — no macrofauna were observed to have remained on the sample after collection; B) sample vertical transects during pavement (R1) sectioning after the cruise. Some transects were immediately bottled for activity studies, while others were further sectioned into horizontal sections for analysis; C) carbonate concretions, or 'nodules' recovered from sediment core PC69 at Mound 800, nodules were combined across the depth of the core sampled, as described in Chapter 1.

Table 2.3

Basal salts medium for seep pavement sectioning (per 1 L DI H_2O)

Reagent	Amount (in g)
NaCl	21.6
$MgCl_2 \cdot 6H_2O$	10.9
Na_2SO_4	3.98
$NaHCO_3$	0.2
KCl	0.76
$CaCl_2 \cdot 2H_2O$	1.47

Community Identity & Phylogenetic Analysis

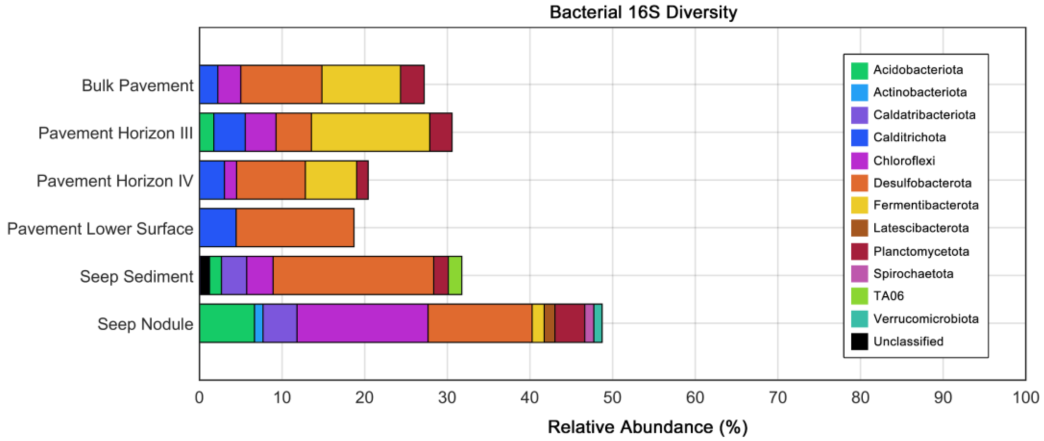

Figure 2.8: Bacterial, 16S relative abundances for all sampled substrates where tripartite, inter-ANME associations were observed. Bars are colored by subphylum-level classification according to the Silva V138.1 SSURef database (Quast et al., 2013).

Phylogenetic Analyses

Desulfobacterota 16S rRNA gene sequences used in the maximum-likelihood phylogenetic tree (Fig. A4) were sourced from Murali et al. (2023) and Eitel et al. (2024). *Halobacteriota* 16S sequences were sourced from and Chadwick et al. (2022), Laso-Pérez et al. (2023), and Eitel et al. (2024).

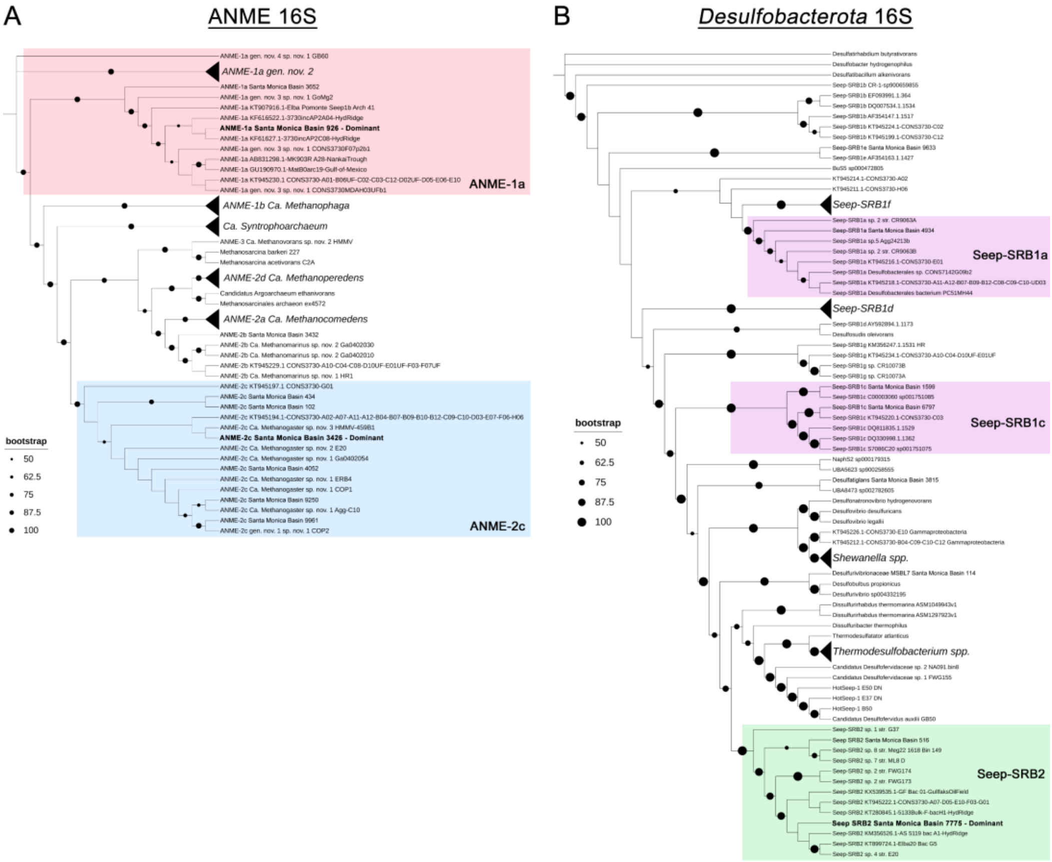

Figure 2.9: A) Maximum-likelihood phylogenetic tree of various ANME archaeal subclades, built with closely related 16S rRNA gene sequences to recurring ASVs in the hydrate-associated seep pavement (R1) from Santa Monica Mound 800. B) Phylogenetic tree of various *Desulfobacterota* subtaxa, including 16S rRNA sequences from SRBs previously observed in syntrophic consortia with ANME archaea. 100% percent identity observed between 'dominant' ASVs from the samples in this study and others are indicated with an asterisk. Branch support values >50% are indicated by closed black circles of increasing size as they approach 100%.

Fluorescence Microscopy

Table 2.4

FISH hybridization probe mix 1 (40% formamide, per 101 µL)

Reagent	Amount (in µL)
5M NaCl	18
1M Tris-HCl (pH 8)	2
EUB338 + EUB338 II + EUB338 III (each at 50 ng/µL in PCR-quality, ultrapure DI H_2O)	10
ANME1-350 (50 ng/µL in PCR-quality, ultrapure DI H_2O)	10
ANME1-728 (50 ng/µL in PCR-quality, ultrapure DI H_2O)	10
ARCH-915 (50 ng/µL in PCR-quality, ultrapure DI H_2O)	10
Formamide	40
1% SDS (by weight in sterile, ultrapure DI H_2O)	1

Table 2.5

FISH hybridization probe mix 2 (40% formamide, per 101 µL)

Reagent	Amount (in µL)
5M NaCl	18
1M Tris-HCl (pH 8)	2
EUB338 + EUB338 II + EUB338 III (each at 50 ng/µL in PCR-quality, ultrapure DI H_2O)	10
ANME1-350 (50 ng/µL in PCR-quality, ultrapure DI H_2O)	10
ANME1-728 (50 ng/µL in PCR-quality, ultrapure DI H_2O)	10
ANME2c-760 (50 ng/µL in PCR-quality, ultrapure DI H_2O)	10
Formamide	40
1% SDS (by weight in sterile, ultrapure DI H_2O)	1

Table 2.6

FISH hybridization wash (for 40% formamide hybridization, per 2 mL)

Reagent	Amount (in µL)
5M NaCl	18.4
1M Tris-HCl (pH 8)	40
0.5M EDTA	20
Sterile, ultrapure DI H_2O	1921.6

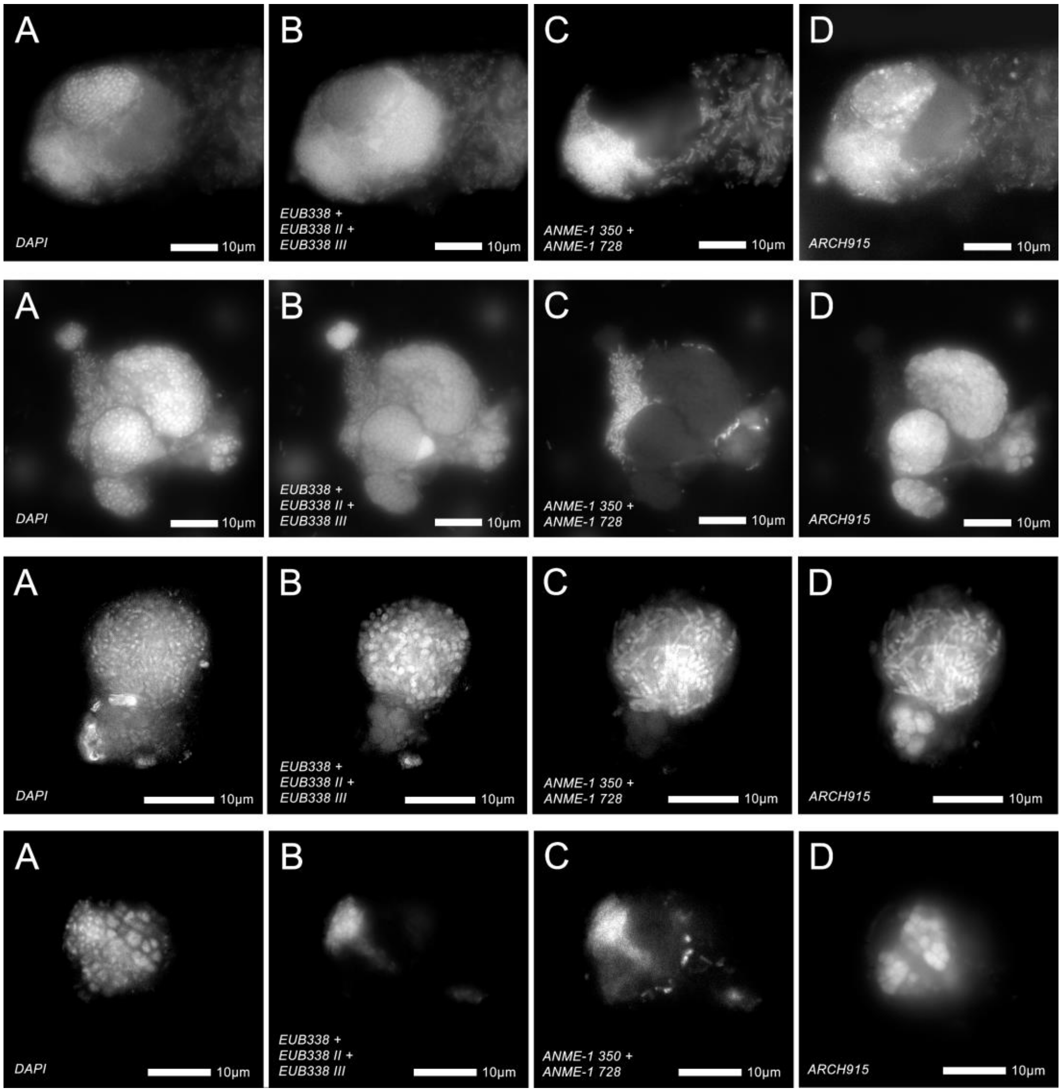

Figure 2.10: Constituent fluorescent channels from FISH observations of tripartite, inter-ANME associations shown in Fig. 2.3, where A) corresponds to DAPI signal; B) is signal from a combination of EUB338, EUB338 II, and EUB338 IIII bacterial FISH probes; C) reflects signal from ANME-1 350 and ANME1-728 FISH probes; and D) is signal from archaeal probe ARCH915. In certain instances, strong signal from cell or auto-fluorescent particulate matter drowned out weaker, though real signal from an adjacent cell. In these cases, we have calibrated the image to the brighter signal to minimize over-exposure.

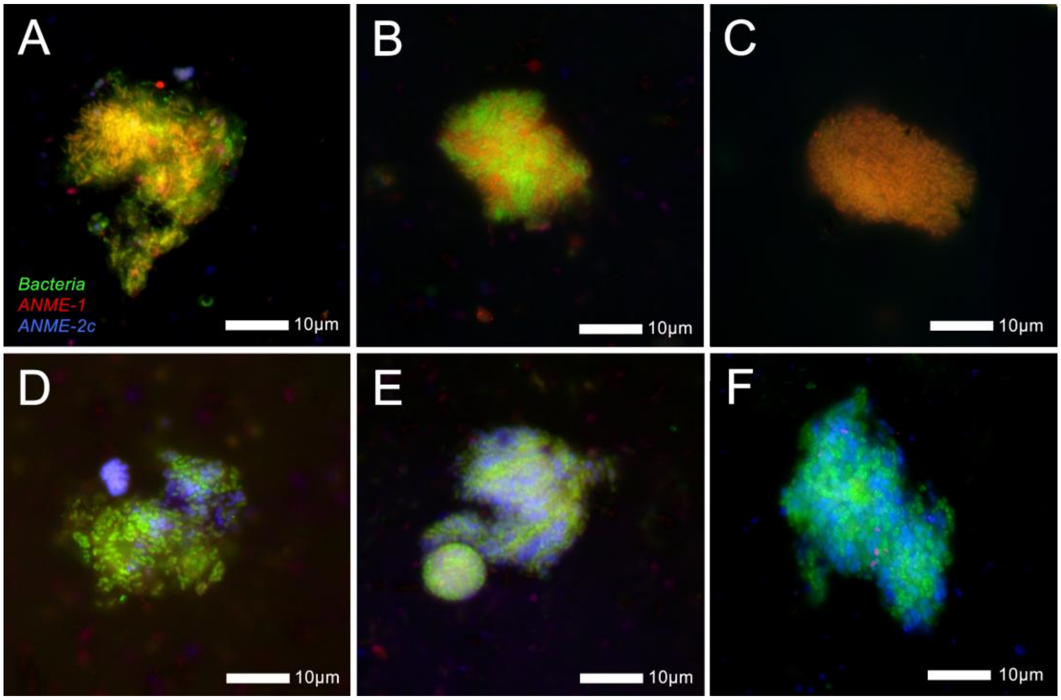

Figure 2.11: Examples of typical monospecific and two-membered ANME aggregates from seep pavement (R1) sections where tripartite, inter-ANME associations were observed.

Table 2.7
ANME-1 / ANME-2c association morphotypes in seep pavement (R1)

Morphotype 1	ANME-1 Segregated Aggregate + ANME-2C Segregated Aggregate
Morphotype 2	ANME-1 Monospecific Aggregate + ANME-2C Segregated Aggregate
Morphotype 3	ANME-1 Single Cells + ANME-2C Segregated Aggregate
Morphotype 4	ANME-1 Segregated Aggregate + ANME-2C Single Cells
Morphotype 5	Mixed ANME-1 + ANME-2c Association
Morphotype 6	Mixed Single-Cell Association

Table 2.8
In-situ ANME-1 / ANME-2c association frequency by morphotype in seep pavement (R1)

Sample ID	**Horizon III**	**Horizon IV**	**Lower Surface**
Morphotype 1	-	2	1
Morphotype 2	1	1	-
Morphotype 3	-	1	3
Morphotype 4	-	3	-
Morphotype 5	-	1	9

Note: Tripartite associations consisting of loose cell groupings <10-μm (Morphotype 6) were not considered for frequency as these were typically more difficult to spot and conclusively assign.

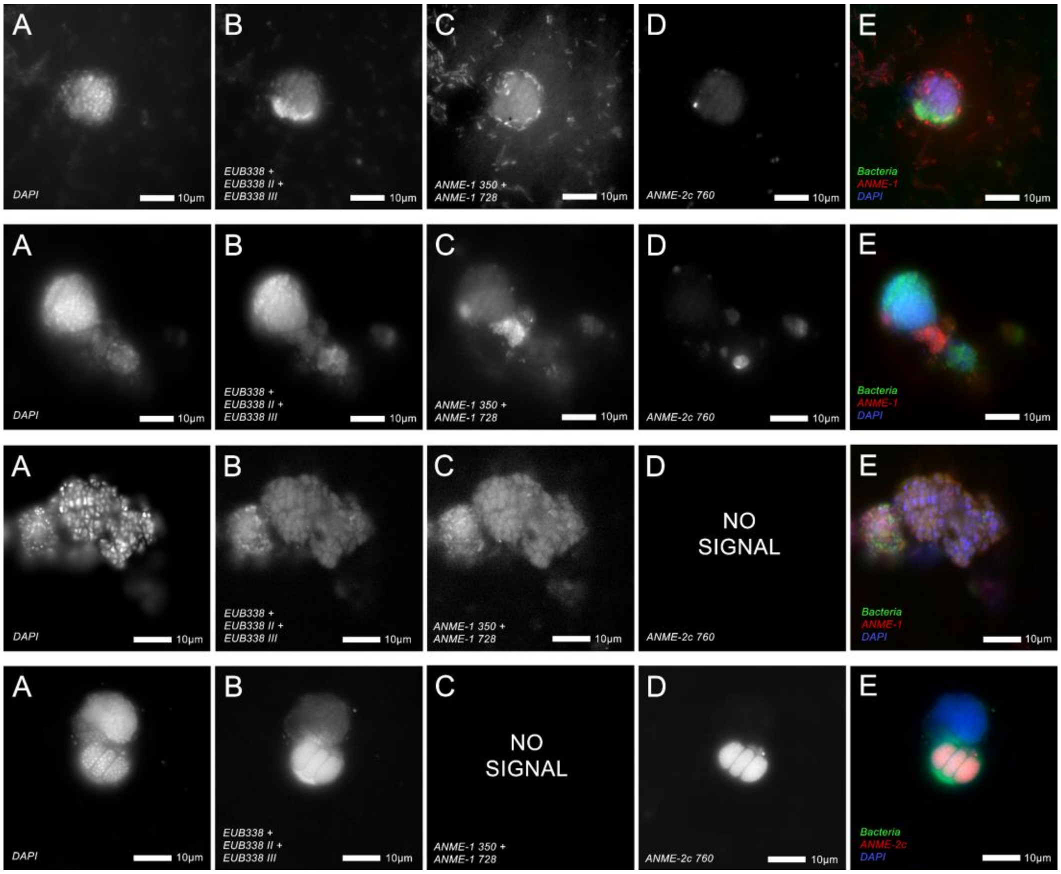

Figure 2.12: Examples of tripartite ANME associations with a third, coccoidal partner unresponsive to the ANME-1 or ANME-2c probe; A) corresponds to DAPI signal; B) is signal from a combination of EUB338, EUB338 II, and EUB338 IIII bacterial FISH probes; C) reflects signal from ANME-1 350 and ANME1-728 FISH probes; D) is signal from archaeal probe ANME-2c 760; E) is a composite image from the channels with recorded signal. We note that panels D) and C) from the third and fourth set of observations were not recorded.

Translational Activity Measurements with BONCAT

Pre-Incubation Activity Assessments

Prior to media refreshment and addition methionine analog, L-Homopropargylglycine (HPG), both control and experimental bottles were monitored for sulfide production, which we interpret to be indicative of sulfate-reduction coupled to anaerobic oxidation of methane (AOM). The media in each bottle was sampled 4 times over the course of ~5 weeks. During sampling, 0.5mL of extracted media from each bottle was added to 0.5-mL of 0.5M zinc acetate to precipitate zinc sulfide. The precipitated sulfide was then quantified spectrophotometrically according to the Cline sulfide assay protocol (Cline, 1969). Concentrations were calculated after subtracting absorbance values from DI H_2O blanks from concurrently measured zinc sulfide standards prepared from sodium sulfide solutions (0.12-mM to 12.5-mM). The resulting sulfide concentrations in both control and experimental bottles are shown in Figure 2.13.

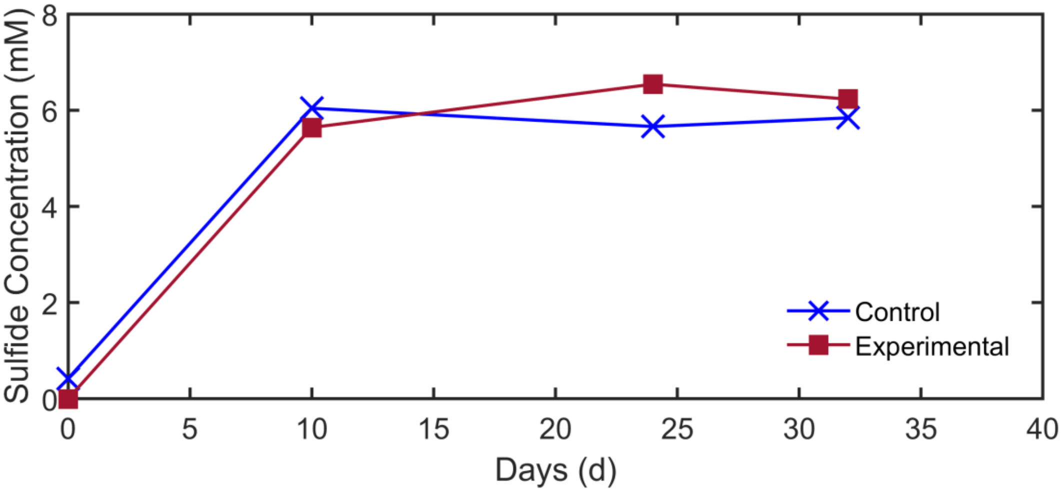

Figure 2.13: Sulfide production in the 5-week period after separation of incubated seep pavement (R1) transects into control and experimental groups, but before addition of HPG, as observed by dissolved sulfide in media and measured by Cline assay. Comparable sulfide production attests to sulfate-coupled AOM activity in both bottles.

Table 2.9
BONCAT azide dye solution (per 250 µL)

Reagent	**Amount (in µL)**
100mM Aminoguanidine (in ultrapure DI H_2O)	12.5
100mM Ascorbate (in 1X PBS)	12.5
20mM $CuSO_4$ (in ultrapure DI H_2O)	1.25
50mM BTTAA (in ultrapure DI H_2O)	2.5
10mM Oregon Green 488 Azide dye (VectorLabs)	0.5
1X PBS	221

Note: A dye ‘pre-mix’ containing the azide dye, BTTAA, and $CuSO_4$ was incubated under Ar in the dark for 3 minutes prior to the addition of the rest of the reagents).

Table 2.10

FISH hybridization probe mix 3 (40% formamide, per 100 µL)

Reagent	Amount (in µL)
5M NaCl	18
1M Tris-HCl (pH 8)	2
ANME1-350 (50 ng/µL in PCR-quality, ultrapure DI H_2O)	10
ANME1-728 (50 ng/µL in PCR-quality, ultrapure DI H_2O)	10
ARCH-915 (50 ng/µL in PCR-quality, ultrapure DI H_2O)	10
Formamide	40
1% SDS (by weight in sterile, ultrapure DI H_2O)	1
PCR-quality, ultrapure DI H_2O	9

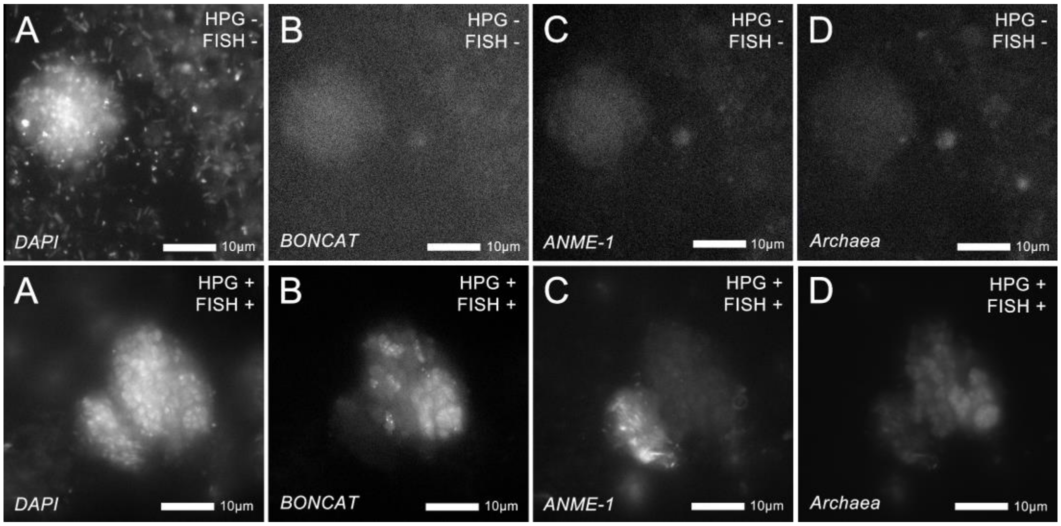

Figure 2.14: Sample BONCAT-FISH control detailing the negligible signal in each non-DAPI channel visualized for this study compared to an HPG-labeled/click-dyed, hybridized well, where A) corresponds to DAPI signal; B) is signal from BONCAT click dye Oregon Green; C) reflects Alexa Fluor™ 546-equivalent signal from hybridization with and without ANME-1 probes, respectively; and D) reflects Alexa Fluor™ 647-equivalent signal from hybridization with and without ARCH915 probe, respectively.

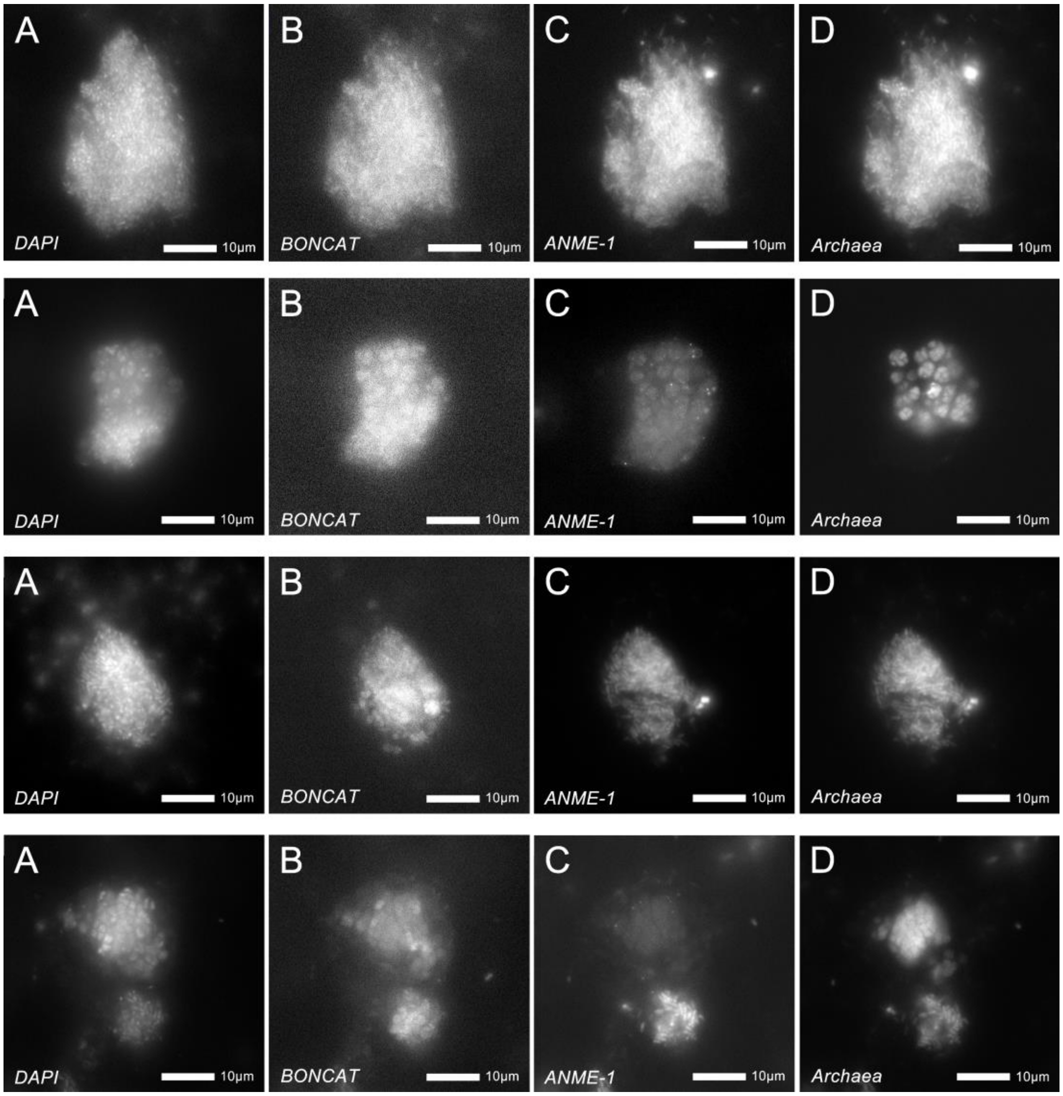

Figure 2.15: Constituent fluorescent channels from BONCAT-FISH observations of other ANME associations from the lower section of the incubated seep pavement transects, where A) corresponds to DAPI signal; B) is signal from BONCAT click dye Oregon Green; C) reflects signal from ANME-1 350 and ANME1-728 FISH probes; and D) is signal from archaeal probe ARCH915.

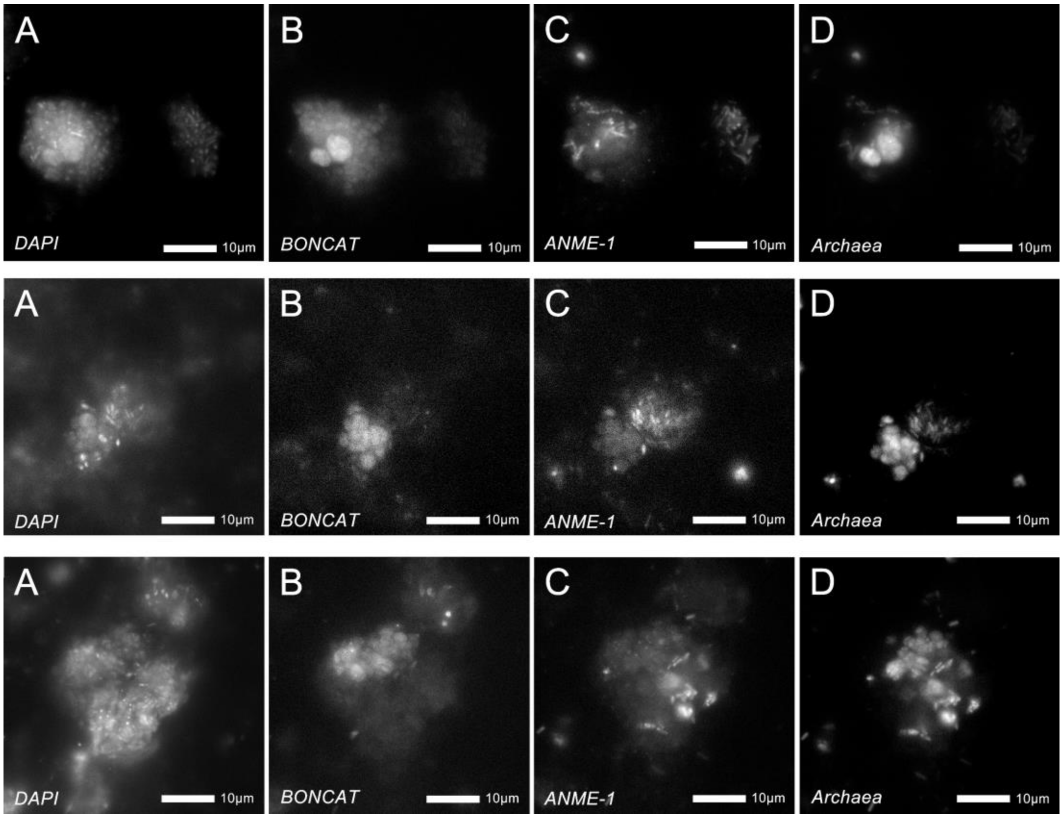

Figure 2.16: Constituent fluorescent channels from BONCAT-FISH observations of tripartite, inter-ANME associations shown in Fig. 6, where A) corresponds to DAPI signal; B) is signal from BONCAT click dye Oregon Green; C) reflects signal from ANME-1 350 and ANME1-728 FISH probes; and D) is signal from archaeal probe ARCH915.

Chapter 3

INSIGHTS FROM SEEP CARBONATE PAVEMENT INTERIORS AND SPATIAL DISTRIBUTIONS OF ENDOLITHIC MICROBIAL COMMUNITIES

Sergio A. Parra[a], Magdalena J. Mayr[a,b], Laura K. Quinn[c], Miguel Vasquez[d], Victoria J. Orphan[a,b]

[a]Division of Geological and Planetary Sciences, California Institute of Technology, Pasadena, California, USA

[b]Division of Biology and Biological Engineering, California Institute of Technology, Pasadena, California, USA

[c]Division of Chemistry and Chemical Engineering, California Institute of Technology, Pasadena, California, USA

[d]National Center for Microscopy and Imaging Research, University of California San Diego, La Jolla, California, USA

Abstract

Carbonate pavements are seafloor-exposed, cemented crusts formed at marine methane seeps by microbially driven anaerobic oxidation of methane (AOM). Previous studies have observed these pavements continue to host active, dynamic, and diverse endolithic microbial communities. However, the impact of internal carbonate structure on the diverse spatial patterns in the hosted microbial community, particularly as a result of seep pavement formation and diagenesis, remains relatively underexplored. This study investigates the spatial distribution of microbial communities in three carbonate pavements from active methane seep sites in the Santa Monica Basin, characterized by varying degrees of porosity and carbonate mineral composition. Porosity and pore size distribution measurements coupled to quantified DNA yields and visualized cell abundances highlight the potential influence of porosity on microbial community size and distribution, where reduced pore connectivity may effectively hinder and/or separate endolithic communities. Further, 16S-rRNA-based community profiles reveal that microbial community composition can vary between seep pavements, with different groups dominating across distinct pavements, suggesting a greater diversity of conditions at the local scale shaping endolithic communities than previously considered. We discuss potential differences in formation and diagenetic histories between seep pavements as evidenced by differences in mineralogy, porosity, and hosted community profiles. Collectively, these insights highlight the likely complex and diverse record of past and/or ongoing microbial habitation within seep pavements that invites further study. In this context, we underscore the need for improved spatial resolution and coverage of seep pavement structures and endolithic communities to better understand their role in methane cycling at marine seeps.

1. Introduction

Anaerobic oxidation of methane (AOM) is a key microbial metabolism responsible for consuming a majority of the subsurface methane emitted from marine methane seeps (Reeburgh et al., 2007; Boetius & Wenzhofer, 2013). This phenomenon is also responsible for precipitating authigenic carbonates, which are often abundant and account for a large volumetric fraction of seep sites around the world. Moreover, these rocks can host active AOM and thus play a significant, but understudied, role in methane drawdown compared to seep sediments (Marlow et al., 2014b; Marlow et al., 2015; Marlow et al., 2021). A particularly under-characterized facet shaping this role is the impact of the physical seep carbonate environment itself.

Porosity and permeability are key factors in governing habitable volume and exchange of microbes, nutrients, and toxins with the exterior environment (Onstott et al., 2019). In seep carbonates, both porosity and permeability are functions of formation and diagenetic processes that act to both create and fill in voids within these authigenic structures. Indeed, seep carbonate-hosted communities represent a distinct type of ‘rock-hosted life’, which differ from other endolithic microorganisms by directly precipitating their mineral substrate around them, thereby ‘entombing’ themselves (Marlow et al., 2015). Such a capability suggests a strong relationship between the resulting physical structure of the seep carbonate and the distribution of the AOM-capable endolithic community within that has not yet been clearly defined. Besides pore structures informed by microbially mediated precipitation, petrographic characterizations of seep carbonates have also identified brecciation voids and fractures from the millimeter to centimeter-scale, potentially caused by vigorous upward gas advection (Greinert et al., 2001; Naehr et al., 2007; Crémière et al., 2016; Weidlich et al., 2023), thereby creating additional, post-depositional spaces for substrate diffusion and microbial habitation. These observations further underscore a heterogeneous physical environment informing spatial distribution in carbonate-hosted microbial communities that ultimately impact the degree to which these communities continue to drive methane drawdown in seep carbonates.

Furthermore, seep sediments often feature sharp geochemical gradients (e.g., the sulfate-methane transition zone, or SMTZ) occurring in intervals as small as a few centimeters (Hoehler et al., 1994; Boetius et al., 2000; Orphan et al., 2001; Chapter 1). Previous studies of methane seep sediments (Blumenberg et al., 2004; Nauhaus et al., 2005; Knittel et al., 2005; Nauhaus et al., 2007; Holler et al., 2011; Rossel et al., 2011; Yanagawa et al., 2011; Biddle et al., 2012; Vigneron et al., 2013; Chapter 1) have similarly documented how these geochemical conditions are reflected in the hosted microbial community, especially in the niche differentiation among subclades of anaerobic methanotrophic archaea (ANME) and their respective sulfate-reducing bacterial (SRB) partners. As such, similarly sharp geochemical transitions made possible by porosity/permeability patterns in seep pavements may lead to a stratification of the microbial communities best adapted to the local environment. A recent study by Schroedl et al. (2024) observed both centimeter and millimeter-scale changes in community identity in chimney-like, seep carbonate chemoherms, where ANME-2 subclades typically associated with higher methane fluxes and potentially more resistant to microoxic conditions (Knittel et al., 2005; Rossel et al., 2011; Chen et al., 2023) were often enriched closer to the carbonate-seawater interface. More broadly, Marlow et al. (2021) caution that seep carbonate environments may be subject to sulfate and methane diffusion limitations, which would act to restrict the 'habitable volume' for AOM-capable communities within seep carbonates. This bears significant implications for current estimates of the global extent of carbonate-hosted AOM, which are based on bulk observations of seep carbonate samples incubated under ideal conditions, and which Marlow et al. (2021) suggest are likely to exceed true *in situ* values.

Aside from geochemically-informed spatial heterogeneity, seep carbonate-hosted communities may also reflect distinct structural patterns associated with processes of their formation and subsequent evolution. These drivers are particularly under-characterized. Previous transplant and colonization experiments by Case et al. (2015) reveal that carbonate-hosted microbial communities can both remain stable or change across intervals as short as 13 months. In Chapter 1, we observed that communities in highly porous, sediment-hosted carbonate nodules were likely in constant exchange with their sediment surroundings, though Mason et al. (2015) record evidence of a preserved bacterial community 'thumbprint' in a similar system. Here, seep carbonates subject to repeated precipitation/dissolution periods and continued diagenesis over geologic timescales are likely to reflect a complex microbial community with both original and colonizing, or 'exchangeable', members whose spatial extents remain unknown, but are likely to be informed by the connectivity of internal voids to the carbonate exterior environment.

Cemented, seafloor-exposed carbonate pavements represent an ideal substrate to examine the role of internal structure on the spatial distribution of the hosted microbial community. In addition to the established body of literature on these seep carbonates (Hovland et al., 1987, Naehr et al., 2007, Paull et al., 2008), seep pavements are the most volumetrically abundant carbonate type at methane seep sites (Teichert et al., 2005; Klaucke et al., 2008, 2012) and have been observed to host endolithic communities capable of performing AOM (Marlow et al., 2014ab, 2021; Case et al., 2015). Still, previous studies characterizing persistent endolithic microbial communities in seep pavements have largely been done at the bulk, centimeter-scale. Such observations preclude insights on the potential spatial extent of AOM-capable microbial communities and how heterogeneous they may be in seep carbonates.

In this study, we advance on past characterizations of carbonate pavements by examining the connections between carbonate composition, internal pore structure, and the resulting spatial distribution of the hosted endolithic community at the sub-centimeter-scale. Specifically, we present an analysis of seep pavement porosities and pore geometries coupled to higher spatial resolution surveys of microbial community identity. This combined approach represents another preliminary step towards determining fine-scale drivers of community identity and distribution in seep carbonates.

2. Materials and Methods

2.1 Site Description and Sample Collection

We recovered the 3 carbonate pavements in this study from the two active methane seep sites at Santa Monica Basin: Santa Monica Mound Site 800 (SMM 800: 33.799438N /118.64672E; 805m depth; also known as the NE mound) and Santa Monica Mound Site 863 (SMM 863: 33.7888N /118.6683W; 863 m; also known as the SW mound). Specifically, the samples (Fig. 3.1) were collected with *ROV Doc Ricketts* during dives DR1329 and DR 1333 in May 2021 on the 05-21 Southern California Cruise of the *R/V Western Flyer*. All collected carbonate structures were dense pavements recovered from sites of previously confirmed methane seepage activity, including gas ebullition, microbial mats, and seep macrofauna (Chapter 1, Supplemental Material) that align with past characterizations of active cold seeps (Treude et al., 2003; Case et al., 2015; Marlow et al., 2021).

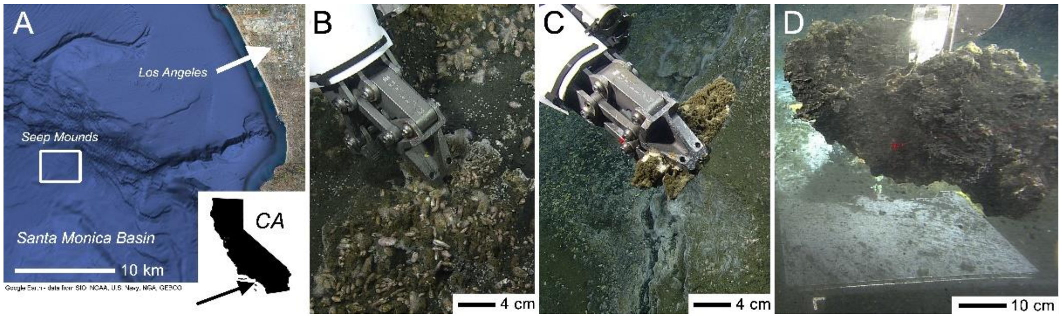

Figure 3.1: A) Map detailing the location of the seep mounds at Santa Monica Basin, CA — adapted from Chapter 1; B) Dive footage from *ROV Doc Ricketts* of seep pavement (15590-R1) sampling from SMM 800, as shown in Chapter 2; C) Dive footage from *ROV Doc Ricketts* of seep pavement (15597-R4) sampling from SMM 800; D) Dive footage of seep pavement (15949-R1) sampling from SMM 863

Both samples from SMM 800, 15590-R1 and 15597-R4, were ~1-2 cm thin crusts collected from sediment-poor, exposed carbonate near the top of the seep mound. Both samples' upper surfaces were covered in ~1-2 mm thin microbial mat, though 15590-R1 was unique in featuring live bivalve clams on the upper surface and gas hydrate underneath. By contrast, 15949-R1 from Santa Monica Mound 863 (SMM 863), was a much larger, carbonate chemoherm-like sample protruding from exposed carbonate near the top of SMM 863. As such, the 'upper' surface facing the water column was contiguous with a partial 'lower' surface still in contact with seawater, such that we simply distinguish an 'exterior' surface, from the sample interior connected to the larger massive carbonate. Though there were no live macrofauna, we observed two distinct microbial mat types on its exterior surface — an orange mat and a black mat. Additional details regarding sampling site context and additional sample observations for 15590-R1 are covered in Chapters 1 and 2.

All pavements were sectioned into ~1 cm wide vertical transects and processed for microbiological characterization, as described for the seep pavement (15590-R1) in

Chapter 2. During pavement sectioning in the laboratory, additionally recovered vertical transects were also allocated for structural and mineralogical analyses.

2.2 Seep Carbonate Bulk Structural and Mineralogical Profiles

2.2.1 Open porosity and pore size distribution measurements

During pavement sectioning, transects from each pavement sample (where sufficient material allowed) were additionally rinsed in deionized water to remove any salts and dried at room temperature for structural and mineralogical analysis. We first measured the open porosities (i.e., pores accessible from the exterior) for sample pavement transects using a water intrusion method, also known as the Archimedes method, using Method A of ASTM D792 (ASTM D792-20), as described in detail in Chapter 1. Further, we measured sample transect pore size distributions with Hg-porosimetry, also following the methods defined in Chapter 1.

2.2.2 Micro-computed X-ray tomography (μ-CT)

To capture seep pavement pore geometries and pore connectivity in greater detail, we also used micro-computed X-ray tomography (μ-CT) to image a sample transect from 15590-R1. μ-CT collects sequential X-ray image cross sections at the <mm-scale/pixel resolution that may be 'stacked' to produce a 3D model of the transect. For this method, a sectioned pavement transect from 15590-R1 was immediately fixed in 4% paraformaldehyde overnight at 4°C, washed twice, resuspended in 50% ethanol, and sent to the National Center for Microscopy and Imaging Research (NCMIR) in San Diego, CA. At NCMIR, the transect was air dried and mounted onto

a mounting pin, where three copper gilder grids (Ted Pella) were affixed using ethyl cyanoacrylate adhesive (Krazy Glue) onto one vertical face as fiducial markers. The transect was scanned with a Zeiss Xradia 510 Versa 3D X-ray microscope at 160V and target power of 10W. An initial, whole-sample scan with a FOV of 29mm x 29mm with 28.6um voxel size. Higher resolution scans were performed over sample regions of interest at 4.9um voxel size and 4.5mm x 4.5mm FOV.Scans were visualized on Fiji v2.16.0 (Schindelin et al., 2012).

2.2.3 XRD

Additional pavement transects from all samples were air-dried and ground into a fine powder for mineralogical analysis via X-ray diffraction (XRD). For this analysis, we used a Rigaku SmartLab powder diffractometer at the X-Ray Crystallography Facility in the Beckman Institute at the California Institute of Technology, following the methods used in Chapter 1. As in Chapter 1, we examined the semi-quantitative content of calcite, Mg-calcite (i.e., $(Ca_{0.9}Mg_{0.1})O_3$, as measured by Althoff, 1977), dolomite, aragonite, and quartz.

2.3 Seep Carbonate Biological Profiles

2.3.1 16S rRNA gene sequencing

We sequenced the V4 and V5 regions of the 16S rRNA gene to characterize and compare the changes in microbial communities within the vertical pavement transects. After initial sectioning, additional material was collected (where sufficient) by scraping various external surfaces using a flame-sterilized spatula.

Pavements transects were then further subsampled into 2 (15949-R1) or 4 (15590-R1 and 15597-R4) separate horizontal horizons with an ethanol-cleaned Dremel diamond-bladed wheel saw (Grainger, 1/32-in thick). After sectioning, the horizons were rinsed in 0.22 µm-filtered artificial seawater and then additionally treated to minimize processing contamination according to the methods optimized by Mason et al. (2015) and briefly summarized in Chapter 1's Supplemental Material. DNA was then extracted from 0.23-0.33 g (wet weight) of scraped external material or rinsed, ground pavement horizons with the DNeasy PowerSoil Pro Kit (Qiagen). Extracted DNA yield from each subsample was then quantified with a NanoDrop 1000 Spectrophotometer (Thermo Fisher) based on sample absorbance at 260 nm. Concentrations were calculated according to Beer's Law and calibration with blanks using the extraction kit elution buffer.

Target sequences were then amplified with a 2-step Illumina sequencing strategy (Kozich et al., 2013). Briefly, this involved in an initial amplification with 515f (5'-TCGTCGGCAGCGTCAGATGTGTATAAGAGACAG-GTGYCAGCMGCCGCGGTAA-3') and 926r (5'-GTCTCGTGGGCTCGGAGATGTGTATAAGAGACAG-CCGYCAATTYMTTTRAGTTT-3') primers, followed by a second amplification to include the necessary Illumina barcodes prior to being sequenced.

Paired-end sequences were filtered and trimmed using 'Cutadapt' (v2.9, Martin, 2011). Trimmed reads were then input into QIIME2 (v2020.11, Bolyen et al., 2019), where we filtered and denoised the reads before removing chimeric sequences through a DADA2 pipeline (1.14.1, Callahan et al., 2016). ASVs with assigned taxonomy were generated from the paired-end non-chimeric sequences in QIIME2 using the Silva V138 SSURef database feature classifier (Quast et al., 2013). Additional details on DNA extraction, gene sequencing, and read processing are discussed in Chapter 1's Supplemental Material.

2.3.2 Fluorescence microscopy

Sub-centimeter horizons from a 15590-R1 transect were further prepared for visualization with fluorescence microscopy following the methods described in Chapter 1. Briefly, ground, sectioned pavement transects were fixed in 4% paraformaldehyde overnight at 4°C, washed twice, resuspended in 50% ethanol, and stored at -20°C. We then performed a density separation using percoll to minimize the impact of sediment and mineral particles. The separated cells were washed twice and stained with a SYBR® Gold (Thermo Fisher) solution at a 25X final concentration before being mounted for viewing onto a 0.2 µm black polycarbonate filter via vacuum filtration.

For counts, we used an Olympus BX51 fluorescence microscope using a 100x objective lens (Olympus). 25 fields of view per filtered sample were surveyed to determine the number of cell aggregates and single cells. For these counts, any close association of cells larger than 2 µm were considered aggregates. Cell and aggregate counts were normalized per unit dry mass of crushed pavement.

3. Results

3.1 Carbonate Observations

Seep pavement transects (Fig. 3.2) revealed distinct textures in the sample interiors, though we observed several recurring features. All sampled pavements had a distinct, crystalline rind, or cap at the upper surface, ranging from ~1-2 mm (15597-R4 and 15949-R1) to 3-4-mm (15590-R1) and roughly encompassed by Horizon I (Fig. 3.2E) during sectioning. Under these rinds, all pavements were mostly a massive matrix hosting various lithic fragments (including shell fragments) and irregularly shaped voids ranging from sub-millimeter to several millimeters in size.

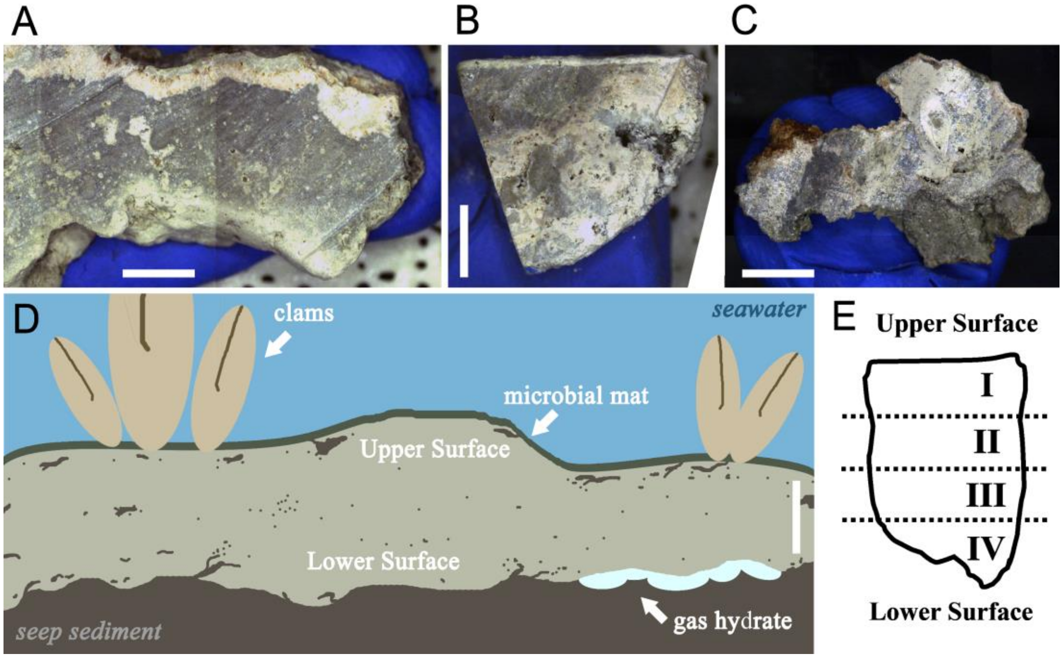

Figure 3.2: A) Image mosaic of the transect from 15590-R1, oriented as it was recovered *in situ* (i.e., upper surface is surface that was facing water column, see Fig. 3.2D). B) Image mosaic of sample transect from 15597-R4 oriented as it was recovered *in situ*. C) Image mosaic from 15949-R1, oriented as it was recovered *in situ*. D) Schematic showing the *in situ* context for transects sectioned from 15590-R1 and 15597-R4 shown in Fig. 3.1, where the upper surface is in contact with seawater, microbial mats, and macrofauna. Scale bars are all 8 mm; E) Diagram illustrating sub-sectioning approach for vertical transects. 15949-R1 was only sectioned into an upper and lower horizon.

In the transect from 15590-R1 (Fig. 3.2A), we observed a light pink, coarse crystalline rind overlying a massive, darker matrix with lighter lithic fragments and a fine-grained, almost silt-like layer at the bottom, where we had previously identified gas hydrates (Chapter 2, Fig. 2.1). By contrast, 15597-R4 (Fig. 3.2B) had a thin, uniform white rind overlying a mixed, multi-colored array of patchy petrographic textures ranging from dark grey to yellow-grey to white. Here, we observed noticeably larger (>mm) voids than those in 15590-R1. 15949-R4 (Fig. 3.2C), which had been sampled from a chemoherm and whose lower surface was not in contact with seep sediment, had a similarly patchy, multi-colored matrix as 15597-R4. Notable differences were observations of large bivalve shell fragments and the color of the overlying rind, which was a rust-like orange and white color.

3.2 Seep Carbonate Bulk Structural and Mineralogical Profiles

3.2.1 Open porosity and pore size distribution

Open porosity captures the fraction of connected pores compared to the total volume of the bulk carbonate, thus the degree to which the sample interior may exchange with the exterior environment. Water intrusion of sample transects (Table 3.1) showed a range of open porosities, where 15949-R1 had more than twice the amount of connected pore space than 15590-R1. Despite the wide range, these porosities aligned with the porosities reported for similar carbonate structures (8-34.4%, Marlow et al., 2014b), though we note that 15590-R1’s lower open porosity aligned more closely with the ‘low activity massive’ carbonate structures identified by

Marlow et al. than the higher porosities in 15597-R4 and 15949-R1 that shared porosities with previously characterized 'active massive' carbonates.

Table 3.1
Water intrusion-derived open porosities of seep pavements

Sample ID	**15590-R1**	**15597-R4**	**15949-R1**
Open Porosity (%)	18.23±0.27	28.27±1.17	38.31±1.81

Hg-porosimetry measurements of pore size distribution between 6- and 350-µm in diameter indicated strong similarities between 15590-R1 and 15597-R4 (Fig. 3.3), with a distinct pore regime in the 10-20 µm diameter range, and a general increase in pores with diameters >100 µm.

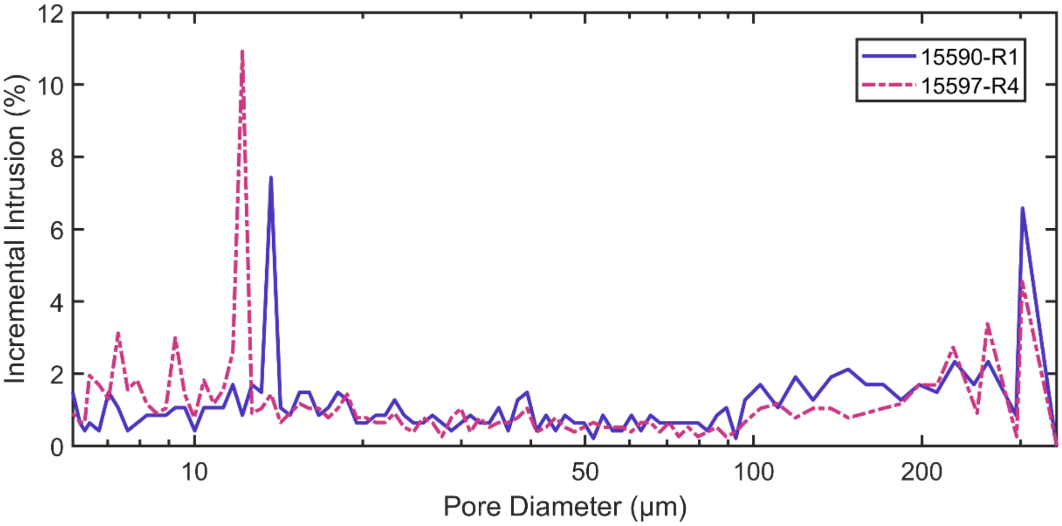

Figure 3.3: Hg-porosimetry curves detailing pore diameter versus incremental Hg intrusion (i.e., fraction of pores at increasingly smaller diameters) for two pavements sampled from SMM 800. Pore sizes observable with porosimetry range from 6- to 350-µm.

3.2.3 Micro-computed X-ray tomography (µ-CT)

µ-CT scans of a characteristic transect from 15590-R1 revealed a heterogenous distribution of mm- and sub-mm-sized pores, including scattered, more isolated pores and larger fracture-like networks (Fig. 3.4C, Supplementary Video V1).

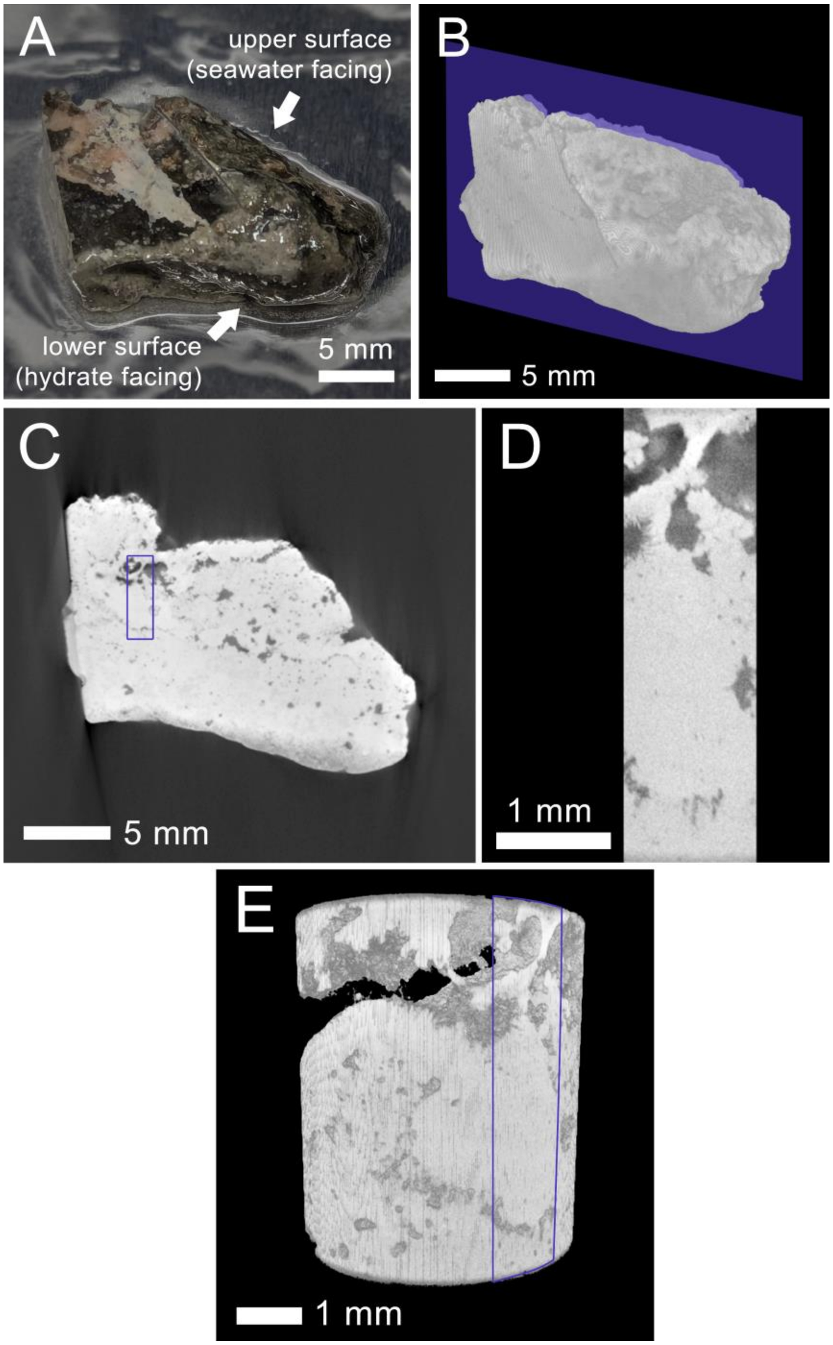

Figure 3.4: A) color image of 15590-R1 transect imaged with μ-CT, where the upper surface corresponds to the clam-bearing, seawater-facing surface *in situ* and the lower surface reflects the *in situ* surface in contact with gas hydrate; B) 3D reconstruction of the of 15590-R1 transect in A) as scanned with μ-CT. The bump on the left side of the sample is the mount used for imaging. The purple surface is a slice through the transect shown in C); C) a representative X-ray cross-section of 15590-R1 reflective of the internal pore structures (dark) versus the carbonate matrix (light), where the upper and lower surfaces match those described in A); The purple box outlines a sample region of interest shown in D); D) a zoomed-in, higher resolution X-ray cross section of the pores seen in C), where large mm-sized pores featuring crystalline fan structures are connected by thin μm-sized channels; E) a 3D reconstruction of the volume imaged in D) (shown in the purple box), where mm-sized and sub-mm pore geometries are more clearly observed.

Visible pore geometries also varied by shape and connectivity, where the more isolated pores were typically rounded and ranged in size below 1 mm. Other voids (or void systems) in the sample were more irregularly shaped and fracture-like, with visible crystal fan-like pore linings and arranged in laminar networks horizontally across the transect (Fig. 3.4, Supplementary Video V1), parallel to the observed petrographic structures previously observed (Fig. 3.2), instead of vertical or diagonal cross-cuts.

Higher resolution scans revealed much smaller pores (<0.1 mm), many of which were frequently isolated compared to the larger pores that were connected by thin, µm-sized channels (Fig. 3.4DE). Besides dark-colored voids, we also observed distinctly shaded textures suggestive of different material densities, where brighter regions correspond to denser, likely mineral content (Fig. 3.4, Supplementary Video V1). In particular, we observed a several mm-thick, bright rind of material near the upper surface of the transect, roughly correlated with the pink mineral rind shown in Fig. 3.2.

3.2.2 Bulk powder mineralogy

Across all pavements, bulk powder XRD-based mineralogy indicated a strong dominance by aragonite (Table 3.2), with consistent, though lesser contributions from quartz and Mg-calcite, the latter of which forms from secondary alteration of aragonitic or other primary metastable carbonate phases during burial and further diagenesis (Naehr et al., 2007; Joseph et al., 2013). These phases were all consistent with previous mineralogical characterization of seep carbonates (Greinert et al., 2001; Naehr et al., 2007; Liebetrau et al., 2014; Crémière et al., 2016; Marlow et al., 2021; Schroedl et al., 2024).

Table 3.2

Key mineral phases for seep pavements

Sample ID	Aragonite	Mg-Calcite	Calcite	Dolomite	Quartz
15590-R1	69.3%	11.3%	1.5%	0%	18%
15597-R4	76.6%	0.07%	2.7%	0.8%	19.8%
15949-R1	89.0%	3.3%	3.1%	0.6%	3.9%

Note: Mg-Calcite corresponds to $(Ca_{0.9}Mg_{0.1})O_3$, as measured by Althoff (1977)

3.3 Seep Carbonate Biological Profiles

3.3.1 16S rRNA-based community profiles

Compared to previous studies (Marlow et al., 2014a, 2021; Case et al., 2015) that have assessed community composition at the bulk sample level, 16S rRNA gene sequencing at the subsample level enabled us to visualize spatial trends in microbial community composition within each of these carbonate pavements. At the bacterial phylum level, all seep pavements were consistently dominated by members of the *Desulfobacterota*, though *Chloroflexi*, *Calditrichota*, and *Fermentibacterota* were also consistently present above 1% (Fig. 3.5A). Of these phyla, *Desulfobacterota* (previously part of the Deltaproteobacteria), and *Chloroflexi* have previously been identified in seep carbonates from various seep environments around the world (Marlow et al., 2014a, 2021; Case et al., 2015; Schroedl et al., 2024), though we observed these and members of the *Calditrichota* and *Fermentibacterota* in other seep carbonates and seep sediments at Santa Monica Basin (Chapter 1). Most bacterial phylum-level diversity was routinely associated with the upper surface to upper horizons of the seep transects, but we observed a noticeable enrichment of

Bacteroidota and *Planctomycetot*a throughout the horizons from 15597-R4, both of which have also been observed in seep carbonates (Marlow et al., 2014a, 2021; Case et al., 2015). Interestingly, archaeal phylum diversity was considerably lower, where all archaeal sequences recovered from the seep pavements were nearly exclusively in *Halobacteriota* (Fig. 3.5).

We also examined groups within the dominant bacterial and archaeal phyla, *Desulfobacterota* and *Halobacteriota*. Specifically, we grouped ASVs at the genus-level where possible, or otherwise at the next highest taxonomic level possible, before removing groups below a 1% minimum total relative abundance. Within the *Desulfobacterota* in 15590-R1, we observed a noticeable transition between Horizons I and II (Fig. 3.5B). Here, the nearly exclusive presence of lineages in *Desulfatiglans*, a group unrelated to anaerobic oxidation of methane (AOM), was succeeded by Seep-SRB1 and Seep-SRB2, which are the main sulfate-reducing, syntrophic partners to anaerobic methanotrophic archaea (ANME). Here, both Seep-SRB1 and Seep-SRB2 abundances increased with proximity to the pavement's lower surface. By comparison, 15597-R4's interior and lower surface were consistently dominated by Seep-SRB1 (and other unclassified *Desulfosarcinaceae*), where Seep-SRB2 was only observed in Horizon I and the lower surface. We also observed the dominance of Seep-SRB1 in 15949-R1, though Seep-SRB2 was present in both upper and lower horizons. Interestingly, while we did not observe Seep-SRB1 in the upper surface of 15590-R1 or 15597-R4, both the black and orange mats overlying 15949-R1 featured Seep-SRB1.

Across all seep transects, community identity within *Halobacteriota* was exclusively composed of different ANME, in line with past observations of seep carbonate-hosted bulk community composition (Marlow et al., 2014a, 2021; Case et al., 2015). Furthermore, localization of ANME subclades roughly aligned with the distribution of their typical sulfate-reducing partners (Schreiber et al., 2010; Holler et al., 2011; Wegener et al., 2015; Hatzenpichler et al., 2016; Krukenberg et al., 2016, 2018; Metcalfe et al., 2021; Yu et al., 2022). In 15590-R1, we observed ANME-1a present from the upper to lower surfaces, though there was a noticeable transition between Horizons I and II (Fig. 3.5C). Here, the dominance of ANME-1b was succeeded by the co-dominance of ANME-1a and ANME-2c, mirroring the transition of sulfate-reducing partners identified in 15590-R1. By contrast, ANME-1a was sparsely present in 15597-R4, co-occurring with ANME-2a-2b. Horizons I, IV and lower surface were instead dominated by ANME-2b, with the inner two horizons dominated by ANME-2c. In contrast to the surfaces of 15590-R1 and 15597-R4, both mat types on 15949-R1's upper surface were clearly dominated by ANME-2c, where the transect interior was populated by both ANME-2c and ANME-1a.

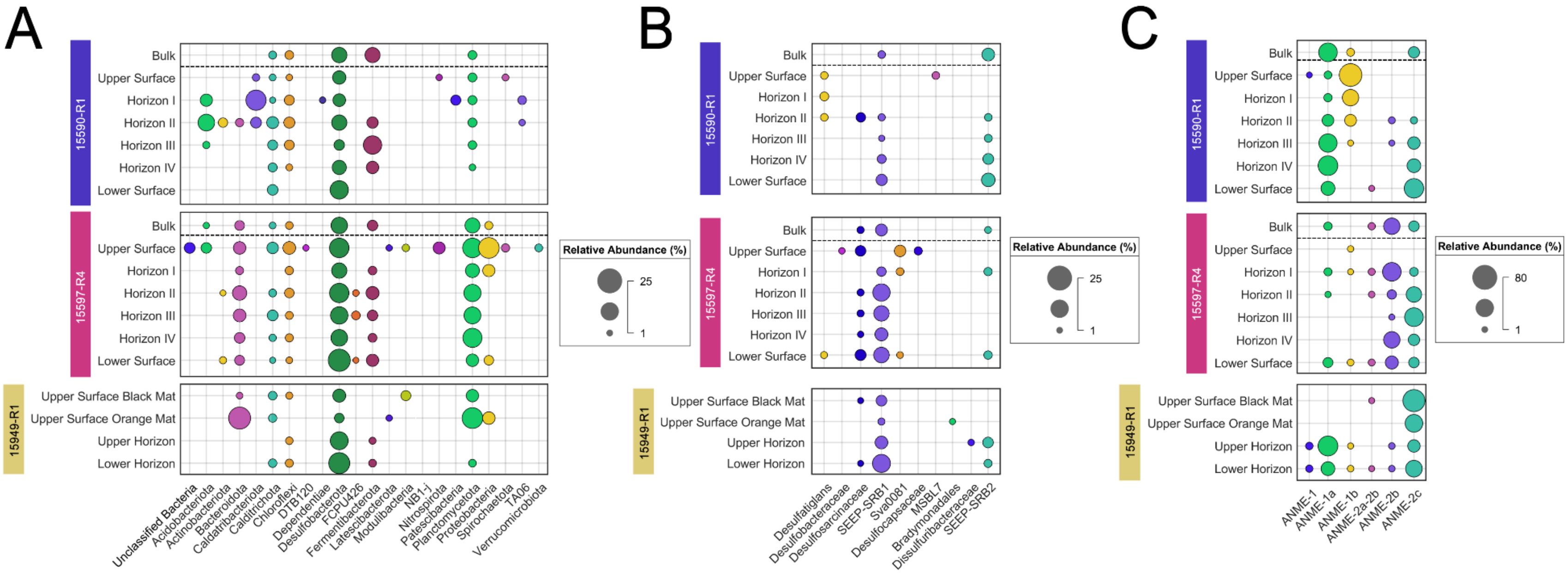

Figure 3.5: Bubble plots summarizing spatially-resolved, 16S relative abundances for groups above 1% total relative abundance in the seep pavements included in this study; A) Relative abundances of bacterial phyla; B) Relative abundances within *Desulfobacterota* — the phylum with sulfate-reducing partners to ANME; C) Relative abundances of groups within prominent phylum *Halobacteriota* (featuring ANME). Groups reflect down to genus-level classification where possible.

3.3.2 Biomass distribution profiles

In addition to identity, we examined the abundance of biomass within the seep pavements based on normalized DNA yields from pavement subsamples, which we compared with cell and aggregate counts from 15590-R1. Across all transects, we observed noticeably increased DNA yields from the upper and lower pavement surfaces (Table 3.3). Interestingly, the lower surface of 15590-R1 was an order of magnitude more enriched in DNA than its upper surface. We also observed the lowest yields were usually from the interior-most horizons, though the DNA yields from 15949-R1's horizons from were noticeably and consistently higher than those from the other pavements.

Table 3.3
Normalized, extracted DNA yields from seep pavements based on absorption at 260 nm

Sample ID	Subsection	Extracted DNA (ng/mg wet sample)
15590-R1	**Upper Surface**	11.5
	Horizon I	1.6
	Horizon II	0.8
	Horizon III	1.8
	Horizon IV	5.6
	Lower Surface	104.8
15597-R4	**Upper Surface**	30.8
	Horizon I	2.0
	Horizon II	1.4
	Horizon III	1.1
	Horizon IV	1.3
	Lower Surface	68.6
15949-R1	**Upper Surface Black Mat**	56.6
	Upper Surface Orange Mat	58.6
	Upper Horizon	27.2
	Lower Horizon	18.6

Cell and aggregate counts (Table 3.4) for subsamples from 15590-R1 aligned strongly with the previously quantified DNA yields (R^2 = 0.9983, 0.9932, respectively, Appendix, Fig. 3.7), where we observed similar horizon-to-horizon changes across both DNA yields and cell/aggregate counts. Here, Horizon II had both the lowest cell and aggregate abundances by three orders of magnitude compared to the highest cell and aggregate abundances observed for the seep pavements lower surface. Notably, these counts are lower than previous quantification of cells and aggregates for active seep carbonates by Marlow et al. (2014a), even if assuming a non-porous, uniform carbonate density of 2.94 g/cm^3, where the cell and aggregate abundances for 15590-R1 are even lower than those previously cited for the 'low activity' massive carbonates (10^9 and 10^7 per cm^3, respectively). Aggregate diameters did not vary with aggregate abundances, however, though the aggregates in the lower two horizons and bottom surface had slightly larger diameters compared to the upper half of the pavement. Generally, these diameters agree with the range of diameters previously quantified for aggregates in bulk seep carbonate samples (Marlow et al., 2014ab). Interestingly the highest mean diameter, which was almost twice the next highest mean diameter, was observed in Horizon III.

Table 3.4
SYBR Gold-based counts of single cell and cell aggregate abundances in 15590-R1

Subsection	Single cells / mg sample	Cell aggregates / mg sample	Mean aggregate diameter (µm)
Upper Surface	6.86×10^6 (6.02×10^5)	1.31×10^4 (2.07×10^3)	3.7 (0.4)
Horizon I	7.51×10^5 (8.25×10^4)	1.61×10^3 (2.82×10^2)	7.0 (0.8)
Horizon II	3.13×10^5 (4.78×10^4)	4.17×10^2 (1.33×10^2)	5.1 (1.0)
Horizon III	8.90×10^5 (3.91×10^4)	5.76×10^3 (2.00×10^3)	17.4 (3.2)
Horizon IV	5.53×10^6 (5.47×10^5)	2.39×10^4 (5.06×10^3)	8.8 (1.0)
Lower Surface	1.07×10^8 (1.01×10^7)	7.77×10^5 (1.42×10^5)	7.9 (0.7)

Note: Cell aggregates were counted as any close association of cells larger than 2-µm. Standard error values for the single cell and aggregate cell counts were calculated from field of view differences and are in parentheses. Values for Horizons III, IV, and Lower Surface are also presented in Chapter 2.

4. Discussion

4.1 Internal pore structures, compositions record an integrated history of growth and diagenetic processes in seep carbonate pavements

The observed range in bulk porosities and mineral content of the seep pavements in this study agree with those previously observed for similar pavements at other marine methane seeps, suggestive of shared formation and diagenetic mechanisms (Greinert et al., 2001; Naehr et al., 2007; Liebetrau et al., 2014; Crémière et al., 2016; Marlow et al., 2014ab, 2021; Weidlich et al., 2023). Together with added measurements of pore size distributions, connectivity, and petrographic textures, we can observe the role of these processes in shaping the identity and distribution of their respective endolithic communities.

For example, the laminar mineral and void structures observed visually across the pavements and confirmed with µ-CT in 15590-R1 suggest lateral uniformity and growth along the vertical axis. This agrees with the growth and accretion models proposed for sediment-emplaced cold seep carbonate pavements, where U-Th dating and ^{18}O signatures suggest that crusts formed through AOM-driven changes in sediment porewater grow predominantly downwards into the sediment (Bayon et al., 2005; Stadnitskaia et al., 2008; Liebetrau et al., 2014; Weidlich et al., 2023). As these pavements grow, porosity is thought to be incorporated by pre-existing gaps between distinct carbonate nucleation sites and/or through pressure-driven brecciation/disruption caused by upwards advective gas migration (Greinert et al., 2001; Naehr et al., 2007; Crémière et al., 2016; Weidlich et al., 2023). Here, Crémière et al. (2016) posit that these fracture episodes lead to porewater ‘flushing’ of created cavities, thereby colonizing the pores with sediment-based endolithic communities capable of continuing AOM and carbonate precipitation. Furthermore, these initial growth and void incorporation processes are generally followed by a second stage of accretion, where sparitic or botryoidal aragonite have been observed to fill and line void networks within previously precipitated carbonate matrices (Naehr et al., 2007; Liebetrau et al., 2014; Crémière et al., 2016; Weidlich et al., 2023). This agrees with our observations of fan-like crystal structures (likely aragonite, based on XRD) lining larger void structures in 15590-R1 (Fig. 3.4).

Collectively, we may conclude that the spatial distributions of porous regimes allowing for habitable volume and/or exchange of nutrient and microbes are thus governed by the rate and duration of initial carbonate precipitation, the frequency of pore-creation episodes, and the rate and duration of secondary pore-filling precipitation that act to ‘seal’ the interior. Lower porosity pavements are thus likely to represent 1) extensive initial cementation during precipitation, 2) low instances of gas-driven brecciation/disruption, and/or 3) extensive secondary pore-in-fill, where 1) and 3) could be associated with high and/or sustained AOM activity. Here, pavement mineralogy and porosimetry can offer additional insights into the relative contributions of these processes.

For example, aragonite abundance in seep carbonates is often driven by high porewater sulfate concentrations and high, advective methane fluxes in seep sediments (Peckmann et al., 2001; Greinert et al., 2001; Weidlich et al., 2023). As such, the higher aragonite fraction observed in 15949-R1 (89%) compared to 15590-

R1 (69.3%) is suggestive of a longer time spent closer to the seafloor in a site of high, advective methane seepage. The higher open porosity observed for 15949-R1 compared to 15590-R1 (~38% vs. ~18%) may thus be evidence of greater pore-creating events driven by strong gas migration. By contrast, the lower open porosity observed in 15590-R1 may reflect a greater accumulated history of carbonate precipitation and thus reduced opportunities for continued habitation and nutrient delivery. Indeed, we observed lower extracted DNA volumes in the pavement interiors associated with 15590-R1 (0.8-1.8 ng/mg wet sample) than 15949-R1 (18.6-27.2 ng/mg wet sample), suggestive of less habitable volume. Furthermore, cell and aggregate abundances from 15590-R1 were 1-2 orders of magnitude below those associated with ‘low-activity’ pavements characterized by Marlow et al. (2014b), despite its location in a site of high methane flux and direct contact with gas hydrates, suggestive of additional barriers to endolithic habitation besides seep activity.

Interestingly, the stark resemblance of pore size distributions between 15590-R1 and 15597-R4 suggests that any potential differences in diagenetic history (encompassing a ~10% difference in porosity) did not affect major pore regimes between the 6-350 μm range, most notably a distinct peak in pores 10-20 μm in diameter. How the 10-20 μm pore regime forms and how common it is within seep pavements remains unaddressed, but its presence and similar prevalence across both pavement transects suggest a common origin — either abiotic (e.g., gas hydrate growth and dissolution dynamics), or informed by the entombed endolithic community (e.g., average size of distinct biomass clusters or cell aggregates that are ultimately surrounded). Despite these similarities, it is likely that much of the porosity in the sampled seep pavements stemmed from voids larger than 350 μm, based on visual analysis of all the transects in addition to μ-CT coverage of 15590-R1 that showed a notable abundance of large, irregularly-shaped void networks with pores as large as several millimeters in diameter. The morphology of these pores more closely resembled those emblematic of brecciation features in other seep pavements (Crémière et al., 2016), which emphasizes the role of pressure-driven fracturing in informing habitable volume.

4.2 Spatial patterns in seep pavement microbial communities suggest influence of interior environment

Broadly, synthesis of 16S-rRNA based community profiles, DNA yields, and cell/aggregate abundances from horizontal transect subsections also indicate a vertically heterogeneous interior environment informing community identity and structure within seep pavements. For example, DNA yields across all samples as well as cell abundances in 15590-R1 showed a consistent increase in biomass with proximity to the pavement exterior surfaces. Further, the presence of macrofauna, biofilms, and increased diversity of bacterial phyla closer to pavement upper surfaces support a distinct, ‘outer’ microbial community compared to the interior horizons. At a cursory level, this exterior vs. interior trend may reflect a greater impact from colonization informed by surrounding sediments or seawater, as observed by Case et al. (2015), or a generally more favorable environment for endolithic communities near the pavement exteriors compared to the interior pavement horizons. Here, reduced interior biomass and community diversity may be considered evidence for a more closed-pore interior structure that acts to hinder exchange with, and nutrient influx from, the pavement surroundings. Indeed, we can consider the spatial patterns in ANME subclades in 15590-R1 as another potential indicator of reduced porosity or pore connectivity focused on the transect interior.

As discussed in Chapter 2, patterns of ANME clade abundance and metabolic activity in seep environments have suggested niche distinctions that lead to distinct regimes typically dominated by one clade. Briefly, these differences are thought to be rooted in local geochemical drivers, where ANME-2 has historically demonstrated a preference for shallow, methane- and sulfate-rich environments (Blumenberg et al., 2004; Yanagawa et al., 2011; Biddle et al., 2012; Vigneron et al., 2013; Chapter 1) compared to ANME-1, which has been found in a wider range of environments, including comparatively methane- and sulfate-poor sediments (Orphan et al., 2001; Orphan et al., 2002; Blumenberg et al., 2004; Harrison et al., 2009; Rossel et al., 2011; Yanagawa et al., 2011; Biddle et al., 2012; Chapter 1).

In 15590-R1, the stronger presence of ANME-2c in the lower horizons suggests a more methane-rich environment, which is supported by the observations of gas hydrate underneath the seep pavement. Still, the sudden decline of ANME-2c lineages by Horizon II coupled with the rise and relative dominance of ANME-1b suggests a transition that may indicate a methane or sulfate limitation between Horizons II and III. Indeed, Horizons II and III also had the lowest extracted volumes of DNA and concentration of cells and aggregates, which we interpreted earlier as a sign of reduced habitable space. This sharp community change across <2 centimeters of host rock is thus potentially further indicative of *in situ* structural barriers to methane flux between the lower and upper pavement surfaces, i.e., reduced pore connectivity in the sample interior. Still, this stratification may be biologically driven, with kinetic limitations from competitive methane drawdown by ANME-2c closer to 15590-R1's lower surface that might also be responsible for the reduced cell abundances in the pavement interior. Notably, μ-CT imaging of a transect from 15590-R1 also did not corroborate a noticeably reduced porosity corresponding to Horizons II and III, where we still observed large void networks in these regions capable of accommodating an endolithic community. However, it may be that lateral variations in seep pavement pore structures preclude direct comparisons between transects. Alternatively, while large pore structures may persist in sample interiors, reduced pore connectivity may also ultimately preclude them from continuing to host an endolithic community. This possibility thus underscores a key distinction between porosity and pore connectivity in shaping seep pavement community structures.

4.3 Implications for continued exchange vs microbial community entrapment in seep pavements

In addition to the observed stratification of cellular abundance and identity within the seep pavements in this study, we also observed differences in these patterns between the seep pavements. We posit these differences may reflect a complex record of the historic and current potential for both nutrient and microbial exchange with the exterior environment (i.e., sediment and/or seawater) as a result of the seep pavement's likely formation in the sediment and exposure at the seafloor.

For example, the inter-pavement diversity in bacterial phyla observed in the biofilms and upper pavement transects suggests there is not a consistent ‘exterior’ seep pavement community, despite their relative proximity within a site of active methane seepage that would suggest broadly similar environmental pressures. Similarly, there is an inter-sample diversity of interior spatial trends within ANME clades, such as the transition from ANME-1b to ANME-1a in 15590-R1, and the ANME-2c-rich interior vs the ANME-2b-rich exterior in 15597-R4. This diversity may therefore reflect adaptations to unique, geochemical ‘micro-gradients’ experienced *in situ* (whether due to kinetic or diffusive constraints), or the relatively uncharacterized role of seep macrofauna (e.g., clams) in shaping carbonate-hosted communities. Additionally, partitioning between and within ANME lineages in seep pavements may also be attributed to a partially preserved record of community succession.

Previous analyses combining carbonate mineralogy, petrographic thin sections, and lipid biomarkers have confirmed statistical connections between aragonitic fabrics and ANME-2 lipid biomarkers and comparatively more Mg-rich calcitic fabrics and ANME-1 lipid biomarkers (Leefmann et al., 2008; Stadnitskaia et al., 2008; Ge et al., 2015), such that spatial patterns of ANME lineages may simply mirror the seep pavement’s formation and diagenetic history. This further highlights the potential for seep pavement communities to not just reflect a niche-adapted community, but instead reflect a mosaic of originally entombed as well as colonizing microbial lineages from subsequent translocation through the seep sediment and exhumation. For example, the consistent, intra-sample presence of the archaeal *Halobacteriota* and bacterial phyla common to seep sediments (e.g., *Chloroflexi*, *Calditrichota*, *Desulfobacterota*, *Planctomycetota*) might reflect microorganisms (metabolically active or dormant or a combination thereof) already present in sediment at the pavement's formation that were 'baked in' prior to exhumation, thus supportive of the carbonate's role as a passive recorder of the local sediment community. Here, the noticeably increased dominance of *Planctomycetota* and *Bacteroidota* in 15597-R4 may be evidence of the stronger influence of host sediments during precipitation and diagenesis. Indeed, the higher quartz fraction in 15597-R4 observed from bulk powder XRD supports a higher degree of sediment incorporation. *Bacteroidota* were also observed to be limited to the shallow (<10 cm depth) sediments at Santa Monica Basin (Chapter 1, Supplemental Material), such that the greater abundance of this phylum within the seep pavement may be evidence of at least partial entrapment of native sediment communities closer to the seawater interface. This near-surface formation is further supported by the increased aragonite fraction and near-zero abundance of Mg-calcite.

Alternatively, the prevalence of this shallow sediment-associated bacterial phylum may also suggest a post-formation exchange with the shallow sediment environment prior to exhumation. In this scenario, the original community is overwritten and instead partially reflects the last instance of exchange with the surrounding sediment. However, the noticeable absence of *Bacteroidota* inside the comparatively more porous 15949-R1 horizons argues against any consistent preservation of exchange or entrapment of sediment-hosted communities. The sample-wide presence of

Bacteroidota and other phyla may instead simply reflect a community adapted to unique interior conditions different from those in the other pavements. Indeed, Case et al. (2015) and Mayr et al. (2025) observed that seafloor seep carbonates host diverse microbial communities that remain distinct from those in surrounding sediments and sediment-hosted carbonates (‘nodules’). Ultimately, these findings underscore the gap in understanding when and how sediment communities can infiltrate seep carbonates and inform their resulting community structure.

4.4 Conclusions and future avenues of inquiry

Across three different seafloor pavements from the methane seeps at Santa Monica Basin, we showed diversity reflected across carbonate structures and associated endolithic microbial communities. We demonstrated evidence for reduced biomass in pavement interiors and changing community identity across pavement transects as thin as ~ 2 cm, with potential connections to pavement porosity and diagenetic history. Furthermore, we saw inter-sample diversity within hosted bacterial and archaeal lineages, particularly ANME clades, that may reflect unique, sample-specific records of past and *in situ* controls on seep pavement communities.

While this study presents a preliminary exploration of the role of seep pavement structure on endolithic community identity and spatial distribution, these data further underscore the relatively under-characterized diversity and complexity of seep carbonates as hosts for diverse, endolithic microbial life, with potentially overlapping thumbprints of past and current microbial communities. In particular, there remains a significant gap in the characterization of porosity in seep carbonates. Much of the current literature has focused on morphological and compositional studies of seep carbonate pores, where comprehensive quantification of bulk and spatially-resolved porosity, pore connectivity, and pore geometry in seep carbonates remains relatively undefined. These data are critical to connecting formation and diagenetic processes observed at the pore (µm/mm) scale to their broader impact on habitability and permeability at the seep deposit (>m) scale. As such, additional structural characterizations of seep carbonate structures should seek to capture the frequency, connectivity, and systematic location, if any, of hosted pore sizes across a wider range of diameters.

Here, the use of µ-CT in particular represents a valuable and underutilized technique to observe seep carbonate porosity for its ability to non-destructively image highly resolved spatial relationships in 3D. µ-CT has already been used to quantitatively characterize pore networks in larger rock and soil volumes, including marine hydrothermal chimneys and seafloor sediments (Spanne et al., 1994; Cnudde & Boone, 2013; Uramoto et al., 2014; Stanulla et al., 2017). Combined with petrographic observations (e.g., thin sectioning), U/Th dating, spatially resolved quantification of relevant carbonate phases (e.g., XRF or imaging spectroscopy), and even $\delta^{13}C$ measurements as done in Schroedl et al. (2024), these data could better constrain the time-resolved effect of burial and diagenetic processes on the internal structure of seep pavements informing continued AOM and other microbial activity.

Furthermore, direct correlation of these highly-resolved structural and compositional maps with a more spatially-resolved localization of biomass may help to distinguish fracture-associated communities that may reflect a secondary colonization from isolated, pore-associated communities that may reflect the precipitating/primary endoliths. Here, use of µ-CT and contrast stains typically used to image cells with SEM can also provide centimeter-scale maps of biomass distribution in context with their porous environment (Van Loo et al., 2014; Védère et al., 2022). Beyond µ-CT, correlative microscopy coupled to composite scanning electron microscopy (SEM) images of host rock is also capable of identifying endolithic communities within their host rock (Marlow et al., 2020, 2021; Osorio-Rodríguez et al., 2023ab).

Another critical aspect ready for further exploration is spatially resolved, contextualized observations of metabolic activity in seep pavements. In Chapter 1, we discussed the potential for 16S-based community profiles from seep carbonates to reflect a combination of active and relict, or 'fossil' DNA, as posited by Stadnitskaia et al. (2005, 2008). Although recent studies have asserted that the impact of 'fossil' DNA on taxonomic surveys of environmental samples is negligible (Lennon et al., 2018; Torti et al., 2018), there remains a distinct potential for pavement-hosted communities to reflect a combination of activity and metabolically quiescent, or dormant, members that ultimately determine the degree to which these pavements continue to serve as methane sinks. While we presented observations of AOM-driven translational activity from lab-based incubations of lower seep pavement horizons in Chapter 2, these observations were based on cell extracts, which precluded localization of this activity. Here, correlative microscopy also represents a valuable tool to preserve spatial context in assessing metabolic activity as demonstrated by spatially resolved observations of translational activity on intact fumarole sediments by Marlow et al. (2020).

Ultimately, these observations emphasize the need for additional characterizations of seep carbonates and improved spatial context to better constrain the role these substrates play in methane drawdown at marine seep sites.

5. References

Althoff, P.L., 1977. Structural refinements of dolomite and a magnesian calcite and implications for dolomite formation in the marine environment. American Mineralogist 62, 772-783.

ASTM D792-20., 2020. Standard Test Methods for Density and Specific Gravity (Relative Density) of Plastics by Displacement. https://doi.org/10.1520/D0792-20.

Bayon, G., Henderson, G.M., Pierre, C., Bohn, M., Fouquet, Y., 2005. Temporal activity of fluid seepage on the Nile Deep-Sea Fan inferred from U-Th dating of authigenic carbonates. CIESM Workshop Monogr., 29, pp. 111-114

Biddle, J.F., Cardman, Z., Mendlovitz, H., Albert, D.B., Lloyd, K.G., Boetius, A., Teske, A., 2012. Anaerobic oxidation of methane at different temperature regimes in Guaymas Basin hydrothermal sediments. ISME J 6, 1018-1031. https://doi.org/10.1038/ismej.2011.164

Blumenberg, M., Seifert, R., Reitner, J., Pape, T., Michaelis, W., 2004. Membrane lipid patterns typify distinct anaerobic methanotrophic consortia. Proceedings of the National Academy of Sciences 101, 11111-11116. https://doi.org/10.1073/pnas.0401188101

Boetius, A., Ravenschlag, K., Schubert, C.J., Rickert, D., Widdel, F., Gieseke, A., Amann, R., Jørgensen, B.B., Witte, U., Pfannkuche, O., 2000. A marine microbial consortium apparently mediating anaerobic oxidation of methane. Nature 407, 623-626. https://doi.org/10.1038/35036572

Boetius, A., Wenzhöfer, F., 2013. Seafloor oxygen consumption fuelled by methane from cold seeps. Nature Geosci 6, 725-734. https://doi.org/10.1038/ngeo1926

Bolyen, E., Rideout, J.R., Dillon, M.R., Bokulich, N.A., Abnet, C.C., Al-Ghalith, G.A., Alexander, H., Alm, E.J., Arumugam, M., Asnicar, F., Bai, Y., Bisanz, J.E., Bittinger, K., et al., 2019. Reproducible, interactive, scalable and extensible microbiome data science using QIIME 2. Nat Biotechnol 37, 852-857. https://doi.org/10.1038/s41587-019-0209-9

Callahan, B.J., McMurdie, P.J., Rosen, M.J., Han, A.W., Johnson, A.J.A., Holmes, S.P., 2016. DADA2: High-resolution sample inference from Illumina amplicon data. Nat Methods 13, 581-583. https://doi.org/10.1038/nmeth.3869

Case, D.H., Pasulka, A.L., Marlow, J.J., Grupe, B.M., Levin, L.A., Orphan, V.J., 2015. Methane Seep Carbonates Host Distinct, Diverse, and Dynamic Microbial Assemblages. mBio 6. https://doi.org/10.1128/mBio.01348-15

Chen, J., Li, Y., Zhong, C., Xu, Z., Lu, G., Jing, H., Liu, H., 2023. Genomic Insights into Niche Partitioning across Sediment Depth among Anaerobic Methane-Oxidizing Archaea in Global Methane Seeps. mSystems 8, e01179-22. https://doi.org/10.1128/msystems.01179-22

Cnudde, V., Boone, M.N., 2013. High-resolution X-ray computed tomography in geosciences: A review of the current technology and applications. Earth-Science Reviews 123, 1-17. https://doi.org/10.1016/j.earscirev.2013.04.003

Crémière, A., Lepland, A., Chand, S., Sahy, D., Kirsimäe, K., Bau, M., Whitehouse, M.J., Noble, S.R., Martma, T., Thorsnes, T., Brunstad, H., 2016. Fluid source and methane-related diagenetic processes recorded in cold seep carbonates from the Alvheim channel, central North Sea. Chemical Geology 432, 16–33. https://doi.org/10.1016/j.chemgeo.2016.03.019

Ge, L., Jiang, S.-Y., Blumenberg, M., Reitner, J., 2015. Lipid biomarkers and their specific carbon isotopic compositions of cold seep carbonates from the South China Sea. Marine and Petroleum Geology, Carbonate conduits linked to hydrocarbon-enriched fluid escape 66, 501–510. https://doi.org/10.1016/j.marpetgeo.2015.02.005

Greinert, J., Bohrmann, G., Suess, E., 2001. Gas Hydrate-Associated Carbonates and Methane-Venting at Hydrate Ridge: Classification, Distribution, and Origin of Authigenic Lithologies, in: Natural Gas Hydrates: Occurrence, Distribution, and Detection. American Geophysical Union (AGU), pp. 99-113. https://doi.org/10.1029/GM124p0099

Harrison, B.K., Zhang, H., Berelson, W., Orphan, V.J., 2009. Variations in Archaeal and Bacterial Diversity Associated with the Sulfate-Methane Transition Zone in Continental Margin Sediments (Santa Barbara Basin, California). Applied and Environmental Microbiology 75, 1487-1499. https://doi.org/10.1128/AEM.01812-08

Hatzenpichler, R., Connon, S.A., Goudeau, D., Malmstrom, R.R., Woyke, T., Orphan, V.J., 2016. Visualizing in situ translational activity for identifying and sorting slow-growing archaeal−bacterial consortia. Proceedings of the National Academy of Sciences 113, E4069-E4078. https://doi.org/10.1073/pnas.1603757113

Hoehler, T.M., Alperin, M.J., Albert, D.B., Martens, C.S., 1994. Field and laboratory studies of methane oxidation in an anoxic marine sediment: Evidence for a methanogen-sulfate reducer consortium. Global Biogeochemical Cycles 8, 451-463. https://doi.org/10.1029/94GB01800

Holler, T., Widdel, F., Knittel, K., Amann, R., Kellermann, M.Y., Hinrichs, K.-U., Teske, A., Boetius, A., Wegener, G., 2011. Thermophilic anaerobic oxidation of methane by marine microbial consortia. The ISME Journal 5, 1946-1956. https://doi.org/10.1038/ismej.2011.77

Hovland, M., Talbot, M.R., Qvale, H., Olaussen, S., Aasberg, L., 1987. Methane-related carbonate cements in pockmarks of the North Sea. Journal of Sedimentary Research 57, 881-892. https://doi.org/10.1306/212F8C92-2B24-11D7-8648000102C1865D

Joseph, C., Campbell, K.A., Torres, M.E., Martin, R.A., Pohlman, J.W., Riedel, M., Rose, K., 2013. Methane-derived authigenic carbonates from modern and paleoseeps on the Cascadia margin: Mechanisms of formation and diagenetic signals. Palaeogeography, Palaeoclimatology, Palaeoecology, Tracing Phanerozoic hydrocarbon seepage from local basins to the global Earth system 390, 52-67. https://doi.org/10.1016/j.palaeo.2013.01.012

Klaucke, I., Masson, D.G., Petersen, C.J., Weinrebe, W., Ranero, C.R., 2008. Multifrequency geoacoustic imaging of fluid escape structures offshore Costa Rica: Implications for the quantification of seep processes. Geochemistry, Geophysics, Geosystems 9. https://doi.org/10.1029/2007GC001708

Klaucke, I., Weinrebe, W., Linke, P., Kläschen, D., Bialas, J., 2012. Sidescan sonar imagery of widespread fossil and active cold seeps along the central Chilean continental margin. Geo-Mar Lett 32, 489-499. https://doi.org/10.1007/s00367-012-0283-1

Knittel, K., Lösekann, T., Boetius, A., Kort, R., Amann, R., 2005. Diversity and Distribution of Methanotrophic Archaea at Cold Seeps. Applied and Environmental Microbiology 71, 467-479. https://doi.org/10.1128/AEM.71.1.467-479.2005

Kozich, J.J., Westcott, S.L., Baxter, N.T., Highlander, S.K., Schloss, P.D., 2013. Development of a Dual-Index Sequencing Strategy and Curation Pipeline for Analyzing Amplicon Sequence Data on the MiSeq Illumina Sequencing Platform. Appl Environ Microbiol 79, 5112-5120. https://doi.org/10.1128/AEM.01043-13

Krukenberg, V., Harding, K., Richter, M., Glöckner, F.O., Gruber-Vodicka, H.R., Adam, B., Berg, J.S., Knittel, K., Tegetmeyer, H.E., Boetius, A., Wegener, G., 2016. Candidatus Desulfofervidus auxilii, a hydrogenotrophic sulfate-reducing bacterium involved in the thermophilic anaerobic oxidation of methane. Environmental Microbiology 18, 3073-3091. https://doi.org/10.1111/1462-2920.13283

Krukenberg, V., Riedel, D., Gruber-Vodicka, H.R., Buttigieg, P.L., Tegetmeyer, H.E., Boetius, A., Wegener, G., 2018. Gene expression and ultrastructure of meso- and thermophilic methanotrophic consortia. Environmental Microbiology 20, 1651-1666. https://doi.org/10.1111/1462-2920.14077

Leefmann, T., Bauermeister, J., Kronz, A., Liebetrau, V., Reitner, J., Thiel, V., 2008. Miniaturized biosignature analysis reveals implications for the formation of cold seep carbonates at Hydrate Ridge (off Oregon, USA). Biogeosciences 5, 731–738. https://doi.org/10.5194/bg-5-731-2008

Lennon, J.T., Muscarella, M.E., Placella, S.A., Lehmkuhl, B.K., 2018. How, When, and Where Relic DNA Affects Microbial Diversity. mBio 9, 10.1128/mbio.00637-18. https://doi.org/10.1128/mbio.00637-18

Marlow, J., Peckmann, J., Orphan, V., 2015. Autoendoliths: a distinct type of rock-hosted microbial life. Geobiology 13, 303-307. https://doi.org/10.1111/gbi.12131

Marlow, J.J., Colocci, I., Jungbluth, S.P., Weber, N.M., Gartman, A., Kallmeyer, J., 2020. Mapping metabolic activity at single cell resolution in intact volcanic fumarole sediment. FEMS Microbiology Letters 367, fnaa031. https://doi.org/10.1093/femsle/fnaa031

Marlow, J.J., Hoer, D., Jungbluth, S.P., Reynard, L.M., Gartman, A., Chavez, M.S., El-Naggar, M.Y., Tuross, N., Orphan, V.J., Girguis, P.R., 2021. Carbonate-hosted microbial communities are prolific and pervasive methane oxidizers at geologically diverse marine methane seep sites. PNAS 118. https://doi.org/10.1073/pnas.2006857118

Marlow, J.J., Steele, J.A., Case, D.H., Connon, S.A., Levin, L.A., Orphan, V.J., 2014a. Microbial abundance and diversity patterns associated with sediments and carbonates from the methane seep environments of Hydrate Ridge, OR. Front. Mar. Sci. 1. https://doi.org/10.3389/fmars.2014.00044

Marlow, J.J., Steele, J.A., Ziebis, W., Thurber, A.R., Levin, L.A., Orphan, V.J., 2014b. Carbonate-hosted methanotrophy represents an unrecognized methane sink in the deep sea. Nature Communications 5, 5094. https://doi.org/10.1038/ncomms6094

Martin, M., 2011. Cutadapt removes adapter sequences from high-throughput sequencing reads. EMBnet.journal 17, 10-12. https://doi.org/10.14806/ej.17.1.200

Mason, O.U., Case, D.H., Naehr, T.H., Lee, R.W., Thomas, R.B., Bailey, J.V., Orphan, V.J., 2015. Comparison of Archaeal and Bacterial Diversity in Methane Seep Carbonate Nodules and Host Sediments, Eel River Basin and Hydrate Ridge, USA. Microb Ecol 70, 766-784. https://doi.org/10.1007/s00248-015-0615-6

Mayr MJ, Parra SA, Connon SA, Narayanan AK, Murali R, Cremiere A, Orphan VJ. 2025. Distinct Microbial Communities Within and On Seep Carbonates Support Long-term Anaerobic Oxidation of Methane and Novel pMMO Diversity. bioRxiv https://doi.org/10.1101/2025.02.04.636526.

Metcalfe, K.S., Murali, R., Mullin, S.W., Connon, S.A., Orphan, V.J., 2021. Experimentally-validated correlation analysis reveals new anaerobic methane oxidation partnerships with consortium-level heterogeneity in diazotrophy. ISME J 15, 377-396. https://doi.org/10.1038/s41396-020-00757-1

Naehr, T.H., Eichhubl, P., Orphan, V.J., Hovland, M., Paull, C.K., Ussler, W., Lorenson, T.D., Greene, H.G., 2007. Authigenic carbonate formation at hydrocarbon seeps in continental margin sediments: A comparative study. Deep Sea Research Part II: Topical Studies in Oceanography, Authigenic Mineral Formation in the Marine Environment; Pathways, Processes and Products 54, 1268-1291. https://doi.org/10.1016/j.dsr2.2007.04.010

Nauhaus, K., Albrecht, M., Elvert, M., Boetius, A., Widdel, F., 2007. In vitro cell growth of marine archaeal-bacterial consortia during anaerobic oxidation of methane with sulfate. Environ Microbiol 9, 187-196. https://doi.org/10.1111/j.1462-2920.2006.01127.x

Nauhaus, K., Treude, T., Boetius, A., Krüger, M., 2005. Environmental regulation of the anaerobic oxidation of methane: a comparison of ANME-I and ANME-II communities. Environmental Microbiology 7, 98-106. https://doi.org/10.1111/j.1462-2920.2004.00669.x

Onstott, T. c., Ehlmann, B. l., Sapers, H., Coleman, M., Ivarsson, M., Marlow, J. j., Neubeck, A., Niles, P., 2019. Paleo-Rock-Hosted Life on Earth and the Search on Mars: A Review and Strategy for Exploration. Astrobiology 19, 1230-1262. https://doi.org/10.1089/ast.2018.1960

Orphan, V.J., House, C.H., Hinrichs, K.-U., McKeegan, K.D., DeLong, E.F., 2002. Multiple archaeal groups mediate methane oxidation in anoxic cold seep sediments. Proceedings of the National Academy of Sciences 99, 7663-7668. https://doi.org/10.1073/pnas.072210299

Orphan, V.J., House, C.H., Hinrichs, K.-U., McKeegan, K.D., DeLong, E.F., 2001. Methane-Consuming Archaea Revealed by Directly Coupled Isotopic and Phylogenetic Analysis. Science 293, 484-487. https://doi.org/10.1126/science.1061338

Osorio-Rodríguez, D., 2023. Microbial Transformations of Sulfur: Environmental and (Paleo) Ecological Implications (phd). California Institute of Technology. https://doi.org/10.7907/9bn5-z794

Osorio-Rodríguez, D., Metcalfe, K.S., McGlynn, S.E., Yu, H., Dekas, A.E., Ellisman, M., Deerinck, T., Aristilde, L., Grotzinger, J.P., Orphan, V.J., 2023. Microbially induced precipitation of silica by anaerobic methane-oxidizing consortia and implications for microbial fossil preservation. Proceedings of the National Academy of Sciences 120, e2302156120. https://doi.org/10.1073/pnas.2302156120

Paull, C.K., Normark, W.R., Ussler, W., Caress, D.W., Keaten, R., 2008. Association among active seafloor deformation, mound formation, and gas hydrate growth and accumulation within the seafloor of the Santa Monica Basin, offshore California. Marine Geology 250, 258-275. https://doi.org/10.1016/j.margeo.2008.01.011

Peckmann, J., Reimer, A., Luth, U., Luth, C., Hansen, B.T., Heinicke, C., Hoefs, J., Reitner, J., 2001. Methane-derived carbonates and authigenic pyrite from the northwestern Black Sea. Marine Geology 177, 129–150. https://doi.org/10.1016/S0025-3227(01)00128-1

Quast, C., Pruesse, E., Yilmaz, P., Gerken, J., Schweer, T., Yarza, P., Peplies, J., Glöckner, F.O., 2013. The SILVA ribosomal RNA gene database project: improved data processing and web-based tools. Nucleic Acids Research 41, D590-D596. https://doi.org/10.1093/nar/gks1219

Reeburgh, W.S., 2007. Oceanic Methane Biogeochemistry. Chem. Rev. 107, 486-513. https://doi.org/10.1021/cr050362v

Rossel, P.E., Elvert, M., Ramette, A., Boetius, A., Hinrichs, K.-U., 2011. Factors controlling the distribution of anaerobic methanotrophic communities in marine environments: Evidence from intact polar membrane lipids. Geochimica et Cosmochimica Acta 75, 164-184. https://doi.org/10.1016/j.gca.2010.09.031

Schreiber, L., Holler, T., Knittel, K., Meyerdierks, A., Amann, R., 2010. Identification of the dominant sulfate-reducing bacterial partner of anaerobic methanotrophs of the ANME-2 clade. Environmental Microbiology 12, 2327-2340. https://doi.org/10.1111/j.1462-2920.2010.02275.x

Schroedl, P., Silverstein, M., DiGregorio, D., Blättler, C.L., Loyd, S., Bradbury, H.J., Edwards, R.L., Marlow, J., 2024. Carbonate chimneys at the highly productive point Dume methane seep: Fine-scale mineralogical, geochemical, and microbiological heterogeneity reflects dynamic and long-lived methane-metabolizing habitats. Geobiology 22, e12608. https://doi.org/10.1111/gbi.12608

Schindelin, J., Arganda-Carreras, I., Frise, E., Kaynig, V., Longair, M., Pietzsch, T., Preibisch, S., Rueden, C., Saalfeld, S., Schmid, B., Tinevez, J.-Y., White, D.J., Hartenstein, V., Eliceiri, K., Tomancak, P., Cardona, A., 2012. Fiji: an open-source platform for biological-image analysis. Nat Methods 9, 676–682. https://doi.org/10.1038/nmeth.2019

Spanne, P., Thovert, J.F., Jacquin, C.J., Lindquist, W.B., Jones, K.W., Adler, P.M., 1994. Synchrotron Computed Microtomography of Porous Media: Topology and Transports. Phys. Rev. Lett. 73, 2001-2004. https://doi.org/10.1103/PhysRevLett.73.2001

Stadnitskaia, A., Muyzer, G., Abbas, B., Coolen, M.J.L., Hopmans, E.C., Baas, M., van Weering, T.C.E., Ivanov, M.K., Poludetkina, E., Sinninghe Damsté, J.S., 2005. Biomarker and 16S rDNA evidence for anaerobic oxidation of methane and related carbonate precipitation in deep-sea mud volcanoes of the Sorokin Trough, Black Sea. Marine Geology 217, 67-96. https://doi.org/10.1016/j.margeo.2005.02.023

Stadnitskaia, A., Nadezhkin, D., Abbas, B., Blinova, V., Ivanov, M.K., Sinninghe Damsté, J.S., 2008. Carbonate formation by anaerobic oxidation of methane: Evidence from lipid biomarker and fossil 16S rDNA. Geochimica et Cosmochimica Acta 72, 1824-1836. https://doi.org/10.1016/j.gca.2008.01.020

Stanulla, R., Stanulla, C., Bogason, E., Pohl, T., Merkel, B., 2017. Structural, geochemical, and mineralogical investigation of active hydrothermal fluid discharges at Strýtan hydrothermal chimney, Akureyri Bay, Eyjafjörður region, Iceland. Geothermal Energy 5, 8. https://doi.org/10.1186/s40517-017-0065-0

Teichert, B.M.A., Bohrmann, G., Suess, E., 2005. Chemoherms on Hydrate Ridge - Unique microbially-mediated carbonate build-ups growing into the water column. Palaeogeography, Palaeoclimatology, Palaeoecology, Geobiology of Ancient and Modern Methane-Seeps 227, 67-85. https://doi.org/10.1016/j.palaeo.2005.04.029

Torti, A., Jørgensen, B.B., Lever, M.A., 2018. Preservation of microbial DNA in marine sediments: insights from extracellular DNA pools. Environmental Microbiology 20, 4526-4542. https://doi.org/10.1111/1462-2920.14401

Treude, T., Boetius, A., Knittel, K., Wallmann, K., Barker Jørgensen, B., 2003. Anaerobic oxidation of methane above gas hydrates at Hydrate Ridge, NE Pacific Ocean. Mar. Ecol. Prog. Ser. 264, 1-14. https://doi.org/10.3354/meps264001

Uramoto, G.-I., Morono, Y., Uematsu, K., Inagaki, F., 2014. An improved sample preparation method for imaging microstructures of fine-grained marine sediment using microfocus X-ray computed tomography and scanning electron microscopy. Limnology and Oceanography: Methods 12, 469–483. https://doi.org/10.4319/lom.2014.12.469

Van Loo, D., Bouckaert, L., Leroux, O., Pauwels, E., Dierick, M., Van Hoorebeke, L., Cnudde, V., De Neve, S., Sleutel, S., 2014. Contrast agents for soil investigation with X-ray computed tomography. Geoderma 213, 485-491. https://doi.org/10.1016/j.geoderma.2013.08.036

Védère, C., Vieublé Gonod, L., Nunan, N., Chenu, C., 2022. Opportunities and limits in imaging microorganisms and their activities in soil microhabitats. Soil Biology and Biochemistry 174, 108807. https://doi.org/10.1016/j.soilbio.2022.108807

Vigneron, A., Cruaud, P., Pignet, P., Caprais, J.-C., Cambon-Bonavita, M.-A., Godfroy, A., Toffin, L., 2013. Archaeal and anaerobic methane oxidizer communities in the Sonora Margin cold seeps, Guaymas Basin (Gulf of California). ISME J 7, 1595-1608. https://doi.org/10.1038/ismej.2013.18

Wegener, G., Krukenberg, V., Riedel, D., Tegetmeyer, H.E., Boetius, A., 2015. Intercellular wiring enables electron transfer between methanotrophic archaea and bacteria. Nature 526, 587-590. https://doi.org/10.1038/nature15733

Weidlich, R., Bialik, O.M., Rüggeberg, A., Grobéty, B., Vennemann, T., Neuman, A., Makovsky, Y., Foubert, A., 2023. Occurrence and Genesis of Cold-Seep Authigenic Carbonates from the South-Eastern Mediterranean Sea. The Depositional Record 9, 844–870. https://doi.org/10.1002/dep2.239

Yanagawa, K., Sunamura, M., Lever, M.A., Morono, Y., Hiruta, A., Ishizaki, O., Matsumoto, R., Urabe, T., Inagaki, F., 2011. Niche Separation of Methanotrophic Archaea (ANME-1 and -2) in Methane-Seep Sediments of the Eastern Japan Sea Offshore Joetsu. Geomicrobiology Journal 28, 118-129. https://doi.org/10.1080/01490451003709334

Yu, H., Speth, D.R., Connon, S.A., Goudeau, D., Malmstrom, R.R., Woyke, T., Orphan, V.J., 2022. Community Structure and Microbial Associations in

Sediment-Free Methanotrophic Enrichment Cultures from a Marine Methane Seep. Applied and Environmental Microbiology 88, e02109-21. https://doi.org/10.1128/aem.02109-21

6. Appendix

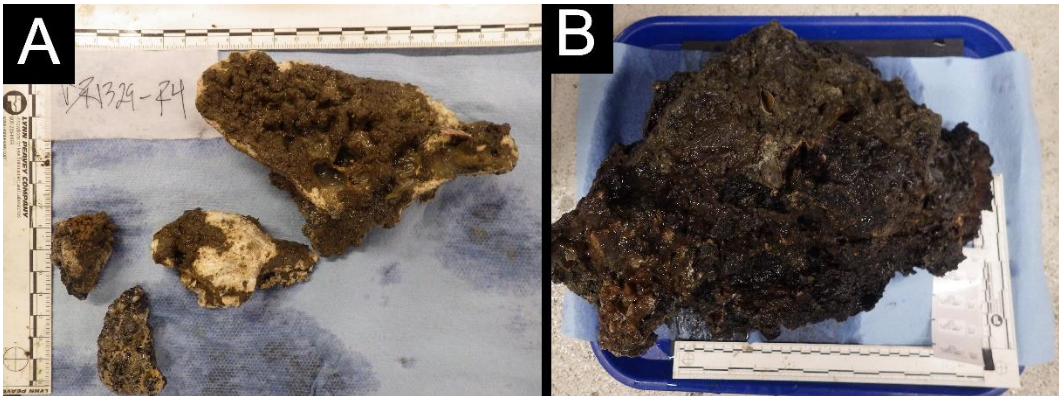

Figure 3.6: Laboratory images of seep pavements recovered for this study, where 15590-R1 is shown in Parra et al. (Chapter 2); A) seep pavement 15597-R4 from SMM 800, with a leathery, dark brown microbial mat on its upper surface; B) seep pavement 15949-R1 from SMM 863, where the upper surface was covered in a black and dark orange microbial mat; we also observed bivalve shells incorporated into the matrix.

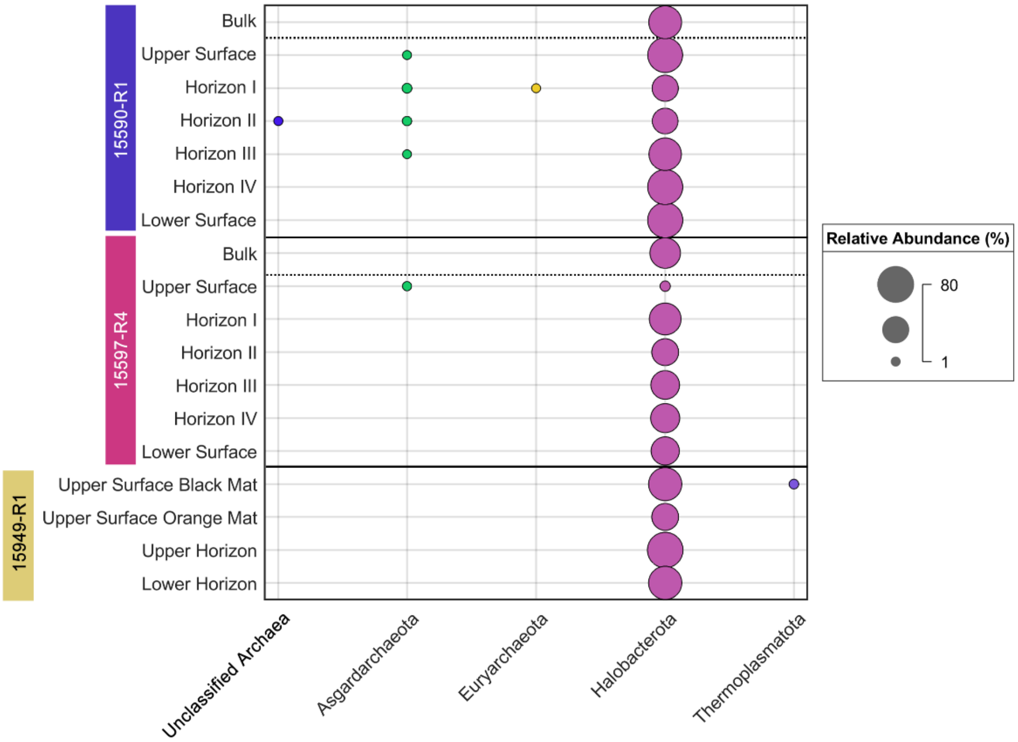

Figure 3.7: Bubble plots summarizing the spatially-resolved, phylum-level 16S archaeal abundances above 1% relative to total 16S abundances in the seep pavements included in this study.

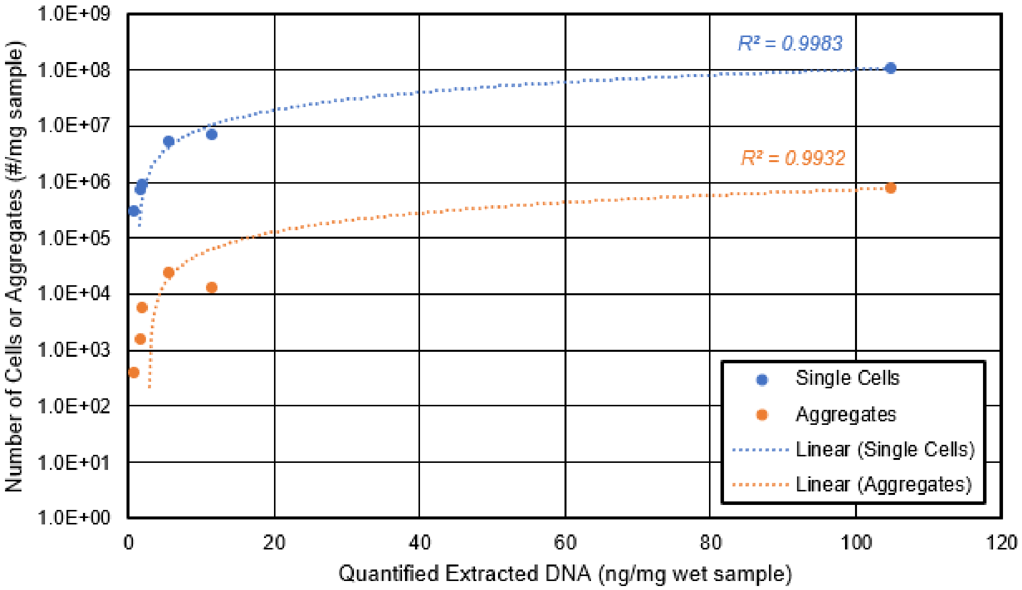

Figure 3.8: Semi-log scale plot comparing trends in cell and cell aggregate counts (#/mg sample) to corresponding volume of extracted DNA (ng/mg wet sample) for sample transects from SMM 800 seep pavement, 15590-R1.

Intermission

CURRENT AND FUTURE PERSPECTIVES ON STUDIES OF SEEP CARBONATES AND THEIR MICROBIAL COMMUNITIES

Diversity and spatial patterns of seep carbonate-hosted communities reflect responses to *in situ* environmental pressures

Throughout the work presented in these first three chapters, we have investigated a range of diverse, spatially-resolved, seep carbonate-hosted microbial communities within their environmental contexts (e.g., porewater geochemistry, carbonate mineralogy, carbonate pore structures) with the express goal of elucidating the complex network of mechanisms that shape them. From these data, we have observed the direct influence of localized methane and sulfate availability (particularly on the potential for methane cycling by the hosted communities), but have also observed how diagenetic history (i.e., burial, exhumation, precipitation dynamics) likely plays a poorly understood role in permitting continued perfusion and colonization from the carbonate's immediate surroundings. Further, this approach has highlighted understudied diversity and metabolic flexibility in seep-associated microbial communities, particularly with regards to the physiological plasticity of methanotrophic archaea within the ANME-1 lineage.

An exploration of key processes shaping seep carbonate microbial communities

While proposing a complete, biogeochemical model of seep carbonate formation, colonization, diagenesis, and continued habitation by endolithic microbes is outside the scope of the work presented here, our correlative approach leveraging several spatially-resolved observations of diverse seep carbonate substrates has outlined various processes that act over different time and spatial scales to produce the diversity of seep carbonates (and their associated microbial communities) observed at methane seeps. At the core of these processes, these carbonates at least partially originate within seep sediments where microbially-driven AOM has produced sufficient bicarbonate-driven alkalinity (measured as ^{13}C-depleted DIC) to exceed the local saturation states of carbonate minerals (e.g., $\Omega_{calcite}$) and trigger net carbonate precipitation. Beyond this shared formation mechanism, however, we can hypothesize there are several evolutionary scenarios leading to distinct seep carbonate microbial habitats.

Scenario I: Carbonate formation in shallow, advective seep sediments

In this hypothetical system, we may consider an 8 m-wide, circular patch of seep sediments experiencing a localized, advective plume of methane-rich porewater, rising at a rate of 10 cm/yr (e.g., Luff and Wallman, 2003; Blouet et al., 2021). This elevated fluid flow regime is the latest in a concentrated series of advective episodes driven by the decomposition of a large reservoir of gas hydrates at depth. This most recent period of elevated fluid flow has been stable long enough to maintain methane delivery to the shallow (<12 cm below seafloor, cmbsf) subsurface and feed a localized region enriched in ANME archaea (particularly ANME-2), that together with sulfate-reducing bacteria (SRB) have driven a substantially elevated rate of AOM (perhaps 30 mmol/m^2 day, e.g., Treude et al., 2003) localized to these upper centimeters and below which all of the porewater sulfate diffusing into the sediments has been consumed. Equally as important, this is occurring in marine sediments along continental margins where the equivalent sedimentation rates have stayed around a typical 0.01 cm/yr over the past 1000 years (per Sadler, 1981, 1999; Schumer & Jerolmack, 2009) and other processes including bioirrigation, bioturbation, sediment winnowing, and seismic activity are sufficiently minimal such that sediment layers are mostly undisrupted.

Here, we might expect to find a zone of sediments — perhaps in the upper 6 cm and roughly bounded laterally by the edges of the upwards-migrating methane rich fluid — bearing actively precipitating, aragonite-rich concretions, or ‘nodules’ ranging in size from <cm to as large as 5-6 cm wide. From the mean size of these nodules, we may infer that this region of incipient carbonates represents anywhere from 500-1000 years of accumulated growth, based on rates estimated by Luff and Wallmann, (2003), Bayon et al., (2009), and Blouet et al., (2021). Notably, any individual concretion would likely not represent a single, continuous period of isotropic growth from a particular nucleation event, but ‘bursts’ of many distinct nucleation instances that might fuse loosely together over years-long growth periods to form a consolidated, though porous matrix, with voids as large as several mms that comprise as much as 50% of the nodule’s volume.

Most importantly, advective fluid and gas transport would play a critical role in flushing sediment porewater and even unconsolidated sediment through pre-existing nodule voids (e.g., Crémière et al., 2016), thereby perfusing the void networks within the growing carbonate system with the surrounding, sediment-based microbial communities, including ANME-SRB consortia performing AOM. Based on this mechanism of exchange, we could expect the nodules in the shallow sediments of this hypothetical site to maintain a local habitation environment mostly continuous with their immediate surroundings, in this case the microbial communities predominantly performing AOM in the shallow sediment sulfate-methane transition zone (SMTZ).

Still, as we have seen in Chapter 1, nodule-hosted communities tend to be smaller and often less diverse than their sediment counterparts. These observations agree with comparatively reduced metabolic activity observed in nodules from radiotracer incubations by Marlow et al., (2014), which together are potentially indicative of a locally diffusion-limited regime within the nodules caused by the growing tortuosity of the nodule voids. Indeed, the removal of sediments from the nodules for study (as done in Chapter 1, Mason et al., 2015) likely only selects for the communities that are sufficiently removed from the nodule exterior. Along these lines, the uncharacterized, effective diffusivity of nodules may reduce methane or sulfate delivery enough to lead to diffusion-limited AOM rates within the innermost regions of the nodules, but not sufficient enough to trigger major community shifts between nodules and sediments.

Scenario II: Low seep activity on shorter vs. longer timescales

After 10 years of elevated methane flux (with some negligible interruptions) and observed nodule growth in the upper cms of seep sediment, our hypothetical system might suddenly experience a longer period, perhaps 20 years, of low seep activity (e.g., fluid velocities <1cm/yr). In this scenario, the shallow SMTZ would start to expand, growing deeper into the sediment with reduced methane delivery and deeper penetration of sulfate. During this period, the nodule-hosted communities would naturally shift in response to local conditions, likely on the order of months to a few years after the initial drop in methane delivery (e.g., Case et al., 2015). In a weaker, more diffusive seep regime we might observe a shallow nodule community more enriched by ANME-1 archaea, as observed in the surrounding seep sediments. Instead of the pore-flushing and active colonization observed in more advective fluid regimes, this community shift may be mostly driven by selection of existing lineages that were not as favored under the higher methane flux conditions.

Here, AOM is still feasible, but reduced rates closer to the seafloor may mean shallow nodule growth rates are slowed or altogether paused. Instead, we may observe slightly elevated AOM rates at depth (e.g., 60 cmbsf). Given the slow rates of carbonate growth however (e.g., 4.5 cm/kyr, Luff and Wallmann, 2003), a 20-year period of quiescence would not be sufficient to create a new carbonate formation regime at this depth. Instead, with the return of elevated methane fluxes and advective fluid flow, the SMTZ would once again shallow substantially (i.e., back to <12 cmbsf) and we'd observe the months-to-years long return of ANME-2 dominant lineages in the sediment and nodules as well as previously observed AOM and associated carbonate precipitation rates in the shallow sediment.

By contrast, a longer accumulated period of low seep activity (e.g., 500 years) could feasibly sustain a new carbonate-forming regime deeper in the sediment (e.g., Ussler and Paul, 2008). At these depths, any precipitated carbonate would be comparatively enriched in Mg-calcite, and the absence of pore-pressure driven by advective fluid flow may mean these nodules are also much less porous, such that diffusion-limited AOM rates within the nodules are much more likely, thereby excluding lineages more sensitive to methane or sulfate limitations.

Scenario III: Prolonged carbonate lifetime in sulfate-depleted conditions

Assuming a steady rate of burial (e.g., 0.01 cm/yr) and a predominantly shallow SMTZ (i.e., advective seep environment) over 1000's of years at our hypothetical seep site, the nodules forming in the sediment are also increasingly likely to spend longer intervals of time in sulfate-depleted conditions. Below some time-integrated depth (e.g., 21 cmbsf), these seep nodules would stop growing altogether, as AOM is no feasible at high enough rates to sustain the alkalinity required for carbonate precipitation. As such, we would observe an effective 'conveyor belt' of sediment horizons bearing increasingly older, similarly sized nodules with depth. Indeed, nodule sizes are likely an integrated record of burial rates and methane fluxes, as has been proposed from previous site-driven studies and reaction-transport models (e.g., Luff and Wallmann, 2003; Luff et al., 2004; Aloisi et al., 2004; Luff et al., 2005; Karaca et al., 2010, 2014; Blouet et al., 2021).

Because these integrated growth histories are sufficiently brief to maintain high porosities (e.g., 50%, see Chapter 1), periods of advective fluid flow at depth may still 'flush' these nodules, thereby replenishing them with a weakly metabolically active sediment community more dominated by ANME-1 lineages, organic carbon fermenters, and/or methylotrophic methanogens that are no longer driving sufficient levels of AOM to sustain continued nodule growth. Nonetheless, these nodules may still experience a second, if weak or short-lived phase of growth triggered by the input of porewater alkalinity from methanogenesis.

Scenario IV: Carbonate crust formation under elevated, advective methane flux

Instead of a routine 'conveyor belt' delivering porous nodules at depth, we might instead observe the formation of a comparatively denser crust in the shallow sediment. Although there remains a large gap in our understanding of the distinction between porous, sediment-hosted nodules and cemented, seafloor-exposed carbonate slabs and pavements, it may be that a 'sweet spot' of elevated fluid flow rates (e.g., 20-60 cm/yr as in Luff et al., 2004) and associated increases in methane delivery to the subsurface leads to the precipitation and cementation of a less porous (e.g., 20-30%) aragonitic crust several cm thick over the same 500-1000 year interval (e.g., Luff et al., 2004, 2005). During this interval, we might observe the fluid flow velocity through this increasingly cemented regime plummet from 20 or 30 cm/yr to 1-2 cm/yr, leading to increasingly diffusive fluid regimes within the carbonate. Over the next several 1000's of years, the crust might continue growing downwards in bursts associated with shifts in seep activity and complex carbonate precipitation/dissolution dynamics, entombing local sediment-based community transitions in deeper, increasingly Mg-calcite rich layers.

With time, however, these crusts are eventually exhumed by uplift, perhaps associated with tectonic movements (e.g., Greinert et al., 2001; Naehr et al., 2007) or even pressure from expanding gas hydrate layers at depth (e.g., Paull et al., 2008). Now under less sulfate-depleted conditions, these cemented assemblages might be re-exposed to increased alkalinity stemming from AOM, where they may experience additional phases of carbonate precipitation, including new, aragonite-rich pore-infill and surface cap layers fueled by renewed growth in advective regimes (e.g., Weidlich et al., 2023, Chapter 3). Notably, these porosity-reducing processes are also balanced by instances of pore creation. High advective fluid flow sometimes associated with gas ebullition (i.e., a bubble plume) can lead to gas accumulation within particularly tortuous carbonate pavements or slabs, causing a buildup of pore pressure that suddenly releases and creates additional fracture cavities that are flushed by the surrounding sediments or seawater.

Importantly, these substrates, while less porous than their potential nodule predecessors, maintain pore structures that are able to sustain a constantly evolving endolithic population. This population is likely to reflect a complex mixture of the microbes that may have persisted from initial cementation, microbes that were seeded by advective perfusion from the surrounding sediment during carbonate uplift, and microbes that were seeded by exposure to the seawater interface, such that these communities become notably distinct from both nearby sediments and the overlying seawater. Here, pore structures are much more likely to exhibit more heterogeneity than that observed in comparatively younger nodules, perhaps reflective of regions exhibiting higher rates of brecciation or cementation associated with the continuous shifting of the SMTZ and strength of methane delivery.

While all of these simplified scenarios are likely not wholly representative of the factors informing seep carbonate formation and evolution, they serve to underscore the likely connection between seep carbonate diagenetic histories and their hosted endolithic microbial communities. In turn, this connection further outlines the need for comprehensive, spatially-resolved characterization of seep carbonate interiors, (such as with µ-CT, discussed in Chapter 3) that may shed more information on how exactly the microenvironment varies across these distinct scenarios. This need may be readily met by incorporating another commonly employed method to understand the interplay of various processes at the sample scale: pore-scale, reaction-transport models.

Application of pore-scale, reaction-transport models to interrogate seep carbonate habitability as a function of interior structure

Spatially-resolved scans of seep carbonate interiors with µ-CT provide a readily adaptable model domain through which to explore the impact of porosity, pore connectivity, and fluid flow on the hosted microbial community's metabolic activity using a reaction-transport model (RTM). RTMs have an established history of use in modelling nutrient transport and microbial reactions in heterogeneous porous media (e.g., Jung and Meile, 2019, 2020, 2021), where structural and fluid flow properties, such as pore geometries, pore connectivity, and biomass density may be artificially varied to map regions of elevated or reduced substrate concentrations.

By applying these techniques, a two-phase approach may be employed. In the first phase, µ-CT image cubes from various recovered seep carbonate substrates may be binarized (i.e., each voxel is set as solid or void) into 3D domains, where arbitrary boundary conditions and pressure regimes can be set to create numerical fluid flow scenarios from which permeability values may be numerically calculated. In turn, these permeability values can be compared between domains as an indicator of pore connectivity. By introducing solute transport (i.e., advective methane flux and sulfate diffusion) into these domains, we may then model the spatial distribution of critical species such as methane and sulfate that can indicate candidate regions where AOM may be favored under the modeled fluid flow environment.

In the second phase, these ‘habitability’ zones may be directly compared to μ-CT image cubes of the same seep carbonate substrates, this time with biomass contrast stains (e.g., Van Loo et al., 2014; Védère et al., 2022) that provide an *in situ* spatial validation for the zones previously modeled. Through this approach, we may be able to approximate the interior conditions that led to the observed distribution of biomass in the seep carbonates and provide a more explicit integration of structure to endolithic habitation.

This convergence of *in situ* sample observations with modelling approaches represents a high value next step that can subsequently inform future studies seeking to investigate environmental controls on seep carbonate habitability. Future possibilities include the modelling and subsequent *in situ* deployment of artificial porous media and even integration with a diagenetic model incorporating variable methane seep fluxes and carbonate precipitation dynamics over longer ($>10^2$) timescales.

Collectively, these future avenues of inquiry represent only a few of many possibilities that seek to maximize the value of spatially-resolved observations of seep carbonates to answer long standing questions about these globally prevalent and under characterized microbial environments.

References

Aloisi, G., Wallmann, K., Bollwerk, S.M., Derkachev, A., Bohrmann, G., Suess, E., 2004. The effect of dissolved barium on biogeochemical processes at cold seeps. Geochimica et Cosmochimica Acta 68, 1735–1748. https://doi.org/10.1016/j.gca.2003.10.010

Bayon, G., Henderson, G.M., Bohn, M., 2009. U–Th stratigraphy of a cold seep carbonate crust. Chemical Geology 260, 47–56. https://doi.org/10.1016/j.chemgeo.2008.11.020

Blouet, J.-P., Arndt, S., Imbert, P., Regnier, P., 2021. Are seep carbonates quantitative proxies of CH4 leakage? Modeling the influence of sulfate reduction and anaerobic oxidation of methane on pH and carbonate precipitation. Chemical Geology 577, 120254. https://doi.org/10.1016/j.chemgeo.2021.120254

Case, D.H., Pasulka, A.L., Marlow, J.J., Grupe, B.M., Levin, L.A., Orphan, V.J., 2015. Methane Seep Carbonates Host Distinct, Diverse, and Dynamic Microbial Assemblages. mBio 6. https://doi.org/10.1128/mBio.01348-15

Crémière, A., Lepland, A., Chand, S., Sahy, D., Kirsimäe, K., Bau, M., Whitehouse, M.J., Noble, S.R., Martma, T., Thorsnes, T., Brunstad, H., 2016. Fluid source and methane-related diagenetic processes recorded in cold seep carbonates from the Alvheim channel, central North Sea. Chemical Geology 432, 16–33. https://doi.org/10.1016/j.chemgeo.2016.03.019

Greinert, J., Bohrmann, G., Suess, E., 2001. Gas Hydrate-Associated Carbonates and Methane-Venting at Hydrate Ridge: Classification, Distribution, and Origin of Authigenic Lithologies, in: Natural Gas Hydrates: Occurrence, Distribution, and Detection. American Geophysical Union (AGU), pp. 99–113. https://doi.org/10.1029/GM124p0099

Jung, H., Meile, C., 2021. Pore-Scale Numerical Investigation of Evolving Porosity and Permeability Driven by Biofilm Growth. Transp Porous Med 139, 203–221. https://doi.org/10.1007/s11242-021-01654-7

Jung, H., Meile, C., 2019. Upscaling of microbially driven first-order reactions in heterogeneous porous media. Journal of Contaminant Hydrology 224, 103483. https://doi.org/10.1016/j.jconhyd.2019.04.006

Jung, H., Meile, C.D., 2020. Numerical investigation of microbial quorum sensing under various flow conditions. PeerJ 8, e9942. https://doi.org/10.7717/peerj.9942

Karaca, D., Hensen, C., Wallmann, K., 2010. Controls on authigenic carbonate precipitation at cold seeps along the convergent margin off Costa Rica. Geochemistry, Geophysics, Geosystems 11. https://doi.org/10.1029/2010GC003062

Karaca, D., Schleicher, T., Hensen, C., Linke, P., Wallmann, K., 2014. Quantification of methane emission from bacterial mat sites at Quepos Slide offshore Costa Rica. Int J Earth Sci (Geol Rundsch) 103, 1817–1829. https://doi.org/10.1007/s00531-012-0839-3

Luff, R., Greinert, J., Wallmann, K., Klaucke, I., Suess, E., 2005. Simulation of long-term feedbacks from authigenic carbonate crust formation at cold vent sites. Chemical Geology 216, 157–174. https://doi.org/10.1016/j.chemgeo.2004.11.002

Luff, R., Wallmann, K., 2003. Fluid flow, methane fluxes, carbonate precipitation and biogeochemical turnover in gas hydrate-bearing sediments at Hydrate Ridge, Cascadia Margin: Numerical modeling and mass balances. Geochimica et Cosmochimica Acta 67, 3403–3421. https://doi.org/10.1016/S0016-7037(03)00127-3

Luff, R., Wallmann, K., Aloisi, G., 2004. Numerical modeling of carbonate crust formation at cold vent sites: significance for fluid and methane budgets and chemosynthetic biological communities. Earth and Planetary Science Letters 221, 337–353. https://doi.org/10.1016/S0012-821X(04)00107-4

Marlow, J.J., Steele, J.A., Ziebis, W., Thurber, A.R., Levin, L.A., Orphan, V.J., 2014. Carbonate-hosted methanotrophy represents an unrecognized methane sink in the deep sea. Nature Communications 5, 5094. https://doi.org/10.1038/ncomms6094

Mason, O.U., Case, D.H., Naehr, T.H., Lee, R.W., Thomas, R.B., Bailey, J.V., Orphan, V.J., 2015. Comparison of Archaeal and Bacterial Diversity in Methane Seep Carbonate Nodules and Host Sediments, Eel River Basin and Hydrate Ridge, USA. Microb Ecol 70, 766–784. https://doi.org/10.1007/s00248-015-0615-6

Naehr, T.H., Eichhubl, P., Orphan, V.J., Hovland, M., Paull, C.K., Ussler, W., Lorenson, T.D., Greene, H.G., 2007. Authigenic carbonate formation at hydrocarbon seeps in continental margin sediments: A comparative study. Deep Sea Research Part II: Topical Studies in Oceanography, Authigenic Mineral Formation in the Marine Environment; Pathways, Processes and Products 54, 1268–1291. https://doi.org/10.1016/j.dsr2.2007.04.010

Paull, C.K., Normark, W.R., Ussler, W., Caress, D.W., Keaten, R., 2008. Association among active seafloor deformation, mound formation, and gas hydrate growth and accumulation within the seafloor of the Santa Monica Basin, offshore California. Marine Geology 250, 258–275. https://doi.org/10.1016/j.margeo.2008.01.011

Sadler, P.M., n.d. Determination of Sediment Accumulation Rates. GeoResearch Forum 5, 15–40.

Schumer, R., Jerolmack, D.J., 2009. Real and apparent changes in sediment deposition rates through time. Journal of Geophysical Research: Earth Surface 114. https://doi.org/10.1029/2009JF001266

Treude, T., Boetius, A., Knittel, K., Wallmann, K., Barker Jørgensen, B., 2003. Anaerobic oxidation of methane above gas hydrates at Hydrate Ridge, NE Pacific Ocean. Mar. Ecol. Prog. Ser. 264, 1–14. https://doi.org/10.3354/meps264001

Ussler, W., Paull, C.K., 2008. Rates of anaerobic oxidation of methane and authigenic carbonate mineralization in methane-rich deep-sea sediments inferred from models and geochemical profiles. Earth and Planetary Science Letters 266, 271–287. https://doi.org/10.1016/j.epsl.2007.10.056

Van Loo, D., Bouckaert, L., Leroux, O., Pauwels, E., Dierick, M., Van Hoorebeke, L., Cnudde, V., De Neve, S., Sleutel, S., 2014. Contrast agents for soil investigation with X-ray computed tomography. Geoderma 213, 485–491. https://doi.org/10.1016/j.geoderma.2013.08.036

Védère, C., Vieublé Gonod, L., Nunan, N., Chenu, C., 2022. Opportunities and limits in imaging microorganisms and their activities in soil microhabitats. Soil Biology and Biochemistry 174, 108807. https://doi.org/10.1016/j.soilbio.2022.108807

Weidlich, R., Bialik, O.M., Rüggeberg, A., Grobéty, B., Vennemann, T., Neuman, A., Makovsky, Y., Foubert, A., 2023. Occurrence and Genesis of Cold-Seep Authigenic Carbonates from the South-Eastern Mediterranean Sea. The Depositional Record 9, 844–870. https://doi.org/10.1002/dep2.239

Chapter 4

MICROIMAGING SPECTROSCOPY OF CARBONACEOUS CHONDRITES AND A COMPARISON TO THE SPECTRAL DIVERSITY OF ASTEROIDS

Sergio A. Parra[a], Rebecca N. Greenberger[a], Bethany L. Ehlmann[a]

[a]Division of Geological and Planetary Sciences, California Institute of Technology,
Pasadena, California, USA

as submitted to the AGU Journal of Geophysical Research: Planets

Key Points

- We imaged 20 carbonaceous chondrites across the visible and shortwave infrared spectrum (0.5-2.5 μm) with a microimaging spectrometer
- We present a spectral processing pipeline to characterize chondrite spectral diversity using the Expanded Bus-DeMeo asteroid taxonomy
- Fe-bearing minerals drive shared spectral behavior between carbonaceous chondrites and asteroids and terrestrial weathering is discernible

Abstract

Primitive asteroids and carbonaceous chondrites (CCs) record the history of processes in the early solar system. Visible and shortwave infrared (VSWIR) spectroscopy of primitive asteroids and bulk-powdered CCs has identified shared spectral features suggestive of shared parent body origins. However, bulk powder CC spectra are spatially unresolved and destroy textures, which hinders tying shared spectral features to particular phases, petrologic contexts, and alteration histories. This study presents an analysis of 20 CCs measured using microimaging hyperspectral VSWIR spectroscopy, recording over 700,000 individual spectra at the ~80 μm/pixel scale. We compare CC spectral features with asteroids using the Expanded Bus-DeMeo taxonomy. We introduce a spectral processing pipeline using Savitzky-Golay filtering to better capture subtle spectral features, reduce noise and enhance comparisons between asteroid classes and CC subgroups and constituent phases. Key findings include the close spectral match between CM chondrites and Cgh-class asteroids, as well as between CV3 chondrites with L-class asteroids. Unaltered, iron-bearing silicate CC components are similar to ‘stony’ asteroid spectral classes. Furthermore, taxonomy-based separation of CC spectra also identifies features unique to CCs, e.g., oxidized iron signatures in CR2 chondrite NWA 7502 and other samples indicative of terrestrial weathering. Together these CC data show that primary and secondary Fe-bearing minerals drive the separations in the asteroid classes expressed in the Expanded Bus-DeMeo taxonomy. These findings also underscore the value of microimaging spectroscopy and statistically-motivated frameworks in conducting larger surveys to interrogate the shared record of alteration in the early solar system.

Plain Language Summary

Relatively unaltered (‘primitive’) asteroids and carbonaceous chondrite meteorites (CCs) share visible and infrared light reflection profiles (‘spectra’), suggesting CCs come from primitive asteroids. However, most studies grind CCs to powders in the laboratory and destroy textures bearing diverse spectral features. This hinders understanding why and where exactly CCs share spectra, and therefore origin processes, with asteroids. In this study, we measure 20 CCs using a technique that measures their spectra at high spatial resolution to form an image, permitting us to see the spectra of individual components that make up the meteorite. To compare these spectra to asteroids, we start with a statistical framework previously used to classify asteroid spectra, with modifications to preserve subtle spectral features and enhance asteroid-CC comparisons. Key findings include close spectral matches between distinct CC types, specific CC components, and asteroid spectral classes. Furthermore, the asteroid classification identifies features unique to certain CCs, e.g., oxidized iron signatures indicative of reactions with water. Together, these CC data show that different types of iron-bearing minerals drive classifications of asteroids. These findings also highlight the value of high-resolution spectroscopy and statistically-motivated frameworks in conducting larger studies to observe the shared record of alteration in the early solar system.

1. Introduction

Carbonaceous chondrites are a key class of meteorites that preserve records of the early solar system. These spectrally dark, organic-bearing meteorites represent some of the oldest materials available for laboratory study and therefore inform much of our understanding of early solar system dynamical and alteration processes (Grady et al., 2006; McSween Jr., 1979). Carbonaceous chondrites exhibit compositional diversity, which has been used to classify them into distinct subgroups (e.g., CM, CR, CV-types) associated with a unique origin and alteration history (Cloutis, Hiroi, et al., 2011; Cloutis, Hudon, et al., 2011; Cloutis, Hudon, Hiroi, & Gaffey, 2012b, 2012a; Cloutis, Hudon, Hiroi, Gaffey, et al., 2012; Krot et al., 2007; Weisberg et al., 2006). Additional records of early solar system evolution persist in asteroids — fragments of planetesimals and planetary embryos that were not incorporated into planetary bodies. Although there are now recent advances in returning samples from asteroids for laboratory study (e.g., Lauretta et al., 2017; Pilorget et al., 2022; Tachibana et al., 2022; Yada et al., 2022), much of our understanding of secondary alteration on asteroids comes from interpretation of visible and shortwave infrared (VSWIR) spectral data collected with ground- and space-based observations.

The VSWIR range captures absorption features indicative of both primary condensates from the solar nebula as well as alteration minerals in asteroids and carbonaceous chondrites, including redox-sensitive (e.g., Fe-bearing) minerals, hydrated minerals, and metal-OH bearing minerals (R. N. Clark et al., 1990). Telescopic observations reveal spectral features diagnostic of mineral classes formed through processes such as aqueous alteration and thermal metamorphism (DeMeo et al., 2009; Rivkin et al., 2002; Takir & Emery, 2012; Vilas & Gaffey, 1989). The diversity of spectral properties of asteroids has led to their systematic classification — suggestive of unique origin and evolution histories (Bus, 1999; DeMeo et al., 2009; DeMeo & Carry, 2014; Tholen, 1984). Spectral similarities in the VSWIR range (0.4 µm to 3 µm) observed between carbonaceous chondrites and certain asteroid classes suggest that primitive asteroids (e.g., C-complex, X-complex, B-class asteroids) are the parent bodies from which carbonaceous chondrites originate (e.g., Burbine & Binzel, 2002; B. E. Clark et al., 2011; Cloutis, Hiroi, et al., 2011; Cloutis, Hudon, et al., 2011; Cloutis, Hudon, Hiroi, & Gaffey, 2012a, 2012b; Cloutis, Hudon, Hiroi, Gaffey, et al., 2012; DeMeo & Carry, 2014; Hamilton et al., 2019; Kitazato et al., 2019; Takir & Emery, 2012).

Studies examining the spectral properties of CCs have traditionally been done on ground, bulk powders. These powders do not preserve original sample textures and heterogeneity, including spectral variability of the distinct constituent phases. In addition to losing petrographic/spatial contexts, grinding acts to disrupt original grain size distributions, which are known to affect absorption band strengths as well as spectral slope (Bowen et al., 2023; Cantillo et al., 2023; Reddy et al., 2015). Systematic spectral comparisons between carbonaceous chondrites (preserving their heterogeneity) and asteroids may more accurately reflect compositional (and thus evolutionary) ties between these two populations as well as illuminate the phases causing variation in spectral properties among primitive asteroids and between CC classes. To this end, microimaging hyperspectral VSWIR spectroscopy of carbonaceous chondrites represents a high-throughput technique to study the compositional variability of carbonaceous chondrites at the component level, processes leading to different mineralogies, and causes of the shared spectral attributes between carbonaceous chondrites and asteroids. This non-destructive, lab-based method has been applied successfully to capture thousands of ~100 μm/pixel-scale spectra per sample— allowing for imaging of natural textures and fabrics (Fraeman et al., 2016; Greenberger et al., 2015; Leask et al., 2021; Leask & Ehlmann, 2016; Pilorget et al., 2022).

In this study, we use microimaging hyperspectral VSWIR spectroscopy to image 20 carbonaceous chondrites of different petrologic classes. We examine the nature of processes preserved in the 80 μm/pixel scale record and the variability in spectral properties of the constituent phases of carbonaceous chondrites. We then use the statistical properties of the microimaging spectroscopy dataset to perform a systematic spectral comparison between carbonaceous chondrites and asteroids. To structure this comparison, we visualize shared spectral diversity with the Expanded Bus-DeMeo asteroid taxonomy (DeMeo et al., 2009). This taxonomy has been previously applied to bulk meteorite spectra (Cantillo et al., 2023) and provides a statistically-motivated framework informed by spectral diversity in asteroids in the VSWIR range (0.45-2.45 μm). To improve sensitivity to smaller spectral features, we also present a modified spectral processing pipeline that may be used in future studies of both asteroid and chondrite spectra.

2. Materials and Methods

2.1 Asteroid Data Set

For our asteroid comparison dataset, we employed the telescopic data set used to develop the Expanded Bus DeMeo taxonomy (DeMeo et al., 2009). These data represent 371 objects with visible and near-infrared spectra. The visible (~0.4-0.9

μm) spectra were compiled in the Small Main Belt Asteroid Spectroscopic Survey (SMASS II) data set (Bus & Binzel, 2002) and the near-IR (0.8-2.5 μm) spectra were collected with the SpeX near-IR spectrograph at the 3-meter NASA IRTF on Mauna Kea, Hawaii (DeMeo et al., 2009; Rayner et al., 2003). For a table of all objects used in this comparison, included in the Expanded Bus-DeMeo Taxonomy, see Appendix Table 4.3.

2.2 Carbonaceous Chondrite Data Set

2.2.1 Meteorite sample selection

We selected 20 carbonaceous chondrites for measurement that span several compositional groups and petrologic types (Table 4.1). The sample set was dictated by both logistical and scientific considerations. Logistically, we sought samples that could be borrowed from scientific collections that had a cut, unpolished or minimal-relief face presentable at a single focus distance for the imaging spectrometer and that had sufficient spatial area (>~1cm^2) so as to collect at least 3000 individual spectra of each sample. We obtained multiple examples of CI, CM, CR, and CV classes to cover a range of histories of processing and alteration on the parent bodies. We utilized both falls and finds with a goal of disentangling the effects of terrestrial weathering on composition and spectral properties.

Table 4.1
Carbonaceous chondrites selected for this study

Chondrite	**Composition Group / Petrologic Type**	**Fall/Find**	**Number of Spectra (Number of Cubes)**	**Source Institution**
Tagish Lake	C2, ungrouped	Fall	3,295 (2)	University of Alberta
Y-82162	C 1/2, ungrouped (‘CY’ - Ikeda et al., 1992)	Find	5,024 (1)	National Institute of Polar Research (NIPR)
Y-980115	CI 1 (‘CY’ - Ikeda et al., 1992)	Find	11,859 (2)	NIPR
ALH 83100	CM 1/2	Find	29,628 (2)	NASA Johnson Space Center (JSC)
ALH 83102	CM2	Find	21,264 (2)	NASA JSC
ALH 84044	CM2	Find	14,793 (1)	NASA JSC
Cold Bokkeveld	CM2.2	Fall	50,229 (3)	Caltech
LEW 90500	CM2	Find	16,191 (1)	NASA JSC
LON 94101	CM2	Find	17,553 (1)	NASA JSC
Mighei	CM2	Fall	18,924 (1)	Arizona State University
Murchison	CM2.5 ± 0.1	Fall	14,014 (1)	Arizona State University
SCO 06043	CM1	Find	9,134 (1)	NASA JSC
PCA 91008	CM-anomalous	Find	14,029 (1)	NASA JSC
WIS 91600	CM-anomalous	Find	33,459 (4)	NASA JSC
NWA 7502	CR2	Find	230,271 (2)	Caltech
Renazzo	CR2	Fall	25,774 (3)	Caltech
Allende	CV3	Fall	65,681 (1)	Arizona State University
NWA 3118	CV3	Find	24,344 (1)	Arizona State University
Vigarano	CV3	Fall	86,774 (4)	Caltech

2.2.2 Microimaging spectroscopy with UCIS and calibration to reflectance

The Ultra-Compact Imaging Spectrometer (UCIS) at the NASA Jet Propulsion Laboratory (JPL) (Van Gorp et al., 2014) was used to acquire 34 VSWIR image cubes of the carbonaceous chondrites. The image cubes were taken in microimaging mode at a spectral resolution of 10 nm over wavelengths 0.5-2.5 µm with a spatial resolution of ~80 µm/pixel. Along the track, each slit was generated by averaging 9 frames, with the integration time per frame set at 20 ms. Because of the varying surface area exposed for imaging across the sample set, each image cube contains 10^3 to 10^5 spectra according to the size of the chondrite surface area exposed (Table 4.1). Because most carbonaceous chondrites are spectrally dark, a 20% Spectralon target (SRS-20-020; Labsphere, USA) was used for calibration and correction to absolute reflectance.

Instrument operation for raw image collection and processing was performed using a series of JPL MATLAB routines. Briefly, the routines first collect an image of the calibration target, then close the shutter to collect a dark current image, then identify bad pixels from the dark current image, correct the calibration target and dark images with interpolation, and subtract the bad-pixel-corrected dark current from the bad-pixel-corrected calibration target image. As we measured samples, the calibration target was measured approximately every 10 minutes so that any changes in instrument or illumination source stability would be captured. Then, during meteorite measurement, UCIS routines collect a new dark current image with the shutter closed and move the illuminated sample across the slit at the calculated rate to achieve the scan length, integration time, and frame average specified. To calibrate the image, bad pixels were identified from the new dark image and corrected in the chondrite and dark images using interpolation, the bad-pixel-corrected dark current was subtracted from the bad-pixel-corrected chondrite image, and the result was divided by the latest dark-subtracted calibration target image. A MATLAB routine written for this study performs the final correction to absolute reflectance for each resulting image cube by multiplying the cube by the measured absolute reflectance spectrum for the SRS-20-020 calibration target.

The dark albedo and low spectral contrast of the carbonaceous chondrite targets made accurate removal of the minimal but present spectral properties of the Spectralon calibration target more important than is typical for normal moderate to high albedo geological targets. To obtain this correction spectrum, the JPL SRS-20-020 calibration target was measured at the California Institute of Technology with an ASD Fieldspec 3 spectrometer (Malvern Panalytical, USA) and goniometer setup using a 30° incidence angle and emission angle at nadir (Pilorget et al., 2016). Measurements were conducted relative to 20% Spectralon target SRT-20-050 (Labsphere) and corrected for the reflectance properties of the target with the NIST-traceable spectrum provided by Labsphere for the Caltech target. This was necessary because the absolute reflectance of the JPL target was not available and batches of darkened Spectralon can be subtly different. To remove noise in the resulting spectrum that was largely from the noisy Labsphere calibration spectrum, the spectrum was smoothed with an 80-channel window. This corresponds to an 80 nm with the 1 nm output of the ASD, or ~8 UCIS channels. The resulting spectrum was then resampled to the wavelengths of the UCIS bands. Visual examination verified the smoothing had not shifted any spectral features.

2.2.3 Comparison to prior bulk spectra

To confirm the efficacy of the UCIS meteorite image capture, calibration, and correction pipeline, we calculated spatially averaged spectra for each corrected image cube by averaging the reflectance values at each UCIS spectral channel across the area of the chondrite surface. These spatially averaged spectra were then compared to previous chondrite bulk powder observations in the VSWIR range for the corresponding chondrite (where available) to verify the image cube processing pipeline had not introduced anomalous features into the collected spectra, shown in Fig. 4.1. The spectra used for these comparisons were collected by (Cloutis, Hiroi, et al., 2011; Cloutis, Hudon, et al., 2011; Cloutis, Hudon, Hiroi, & Gaffey, 2012a, 2012b; Cloutis, Hudon, Hiroi, Gaffey, et al., 2012) and sourced from the University of Winnipeg Planetary Spectrophotometer Facility (PSF) and the NASA Reflectance Experiment LABoratory (RELAB) database (Milliken, 2020). Note that the reflectance, continuum shape, and spectral contrast of VSWIR bulk powder spectra differ between rock and powder (Cantillo et al., 2023); thus, it is the similarities with RELAB absorption feature positions that validate the features in the spectral data collected with UCIS.

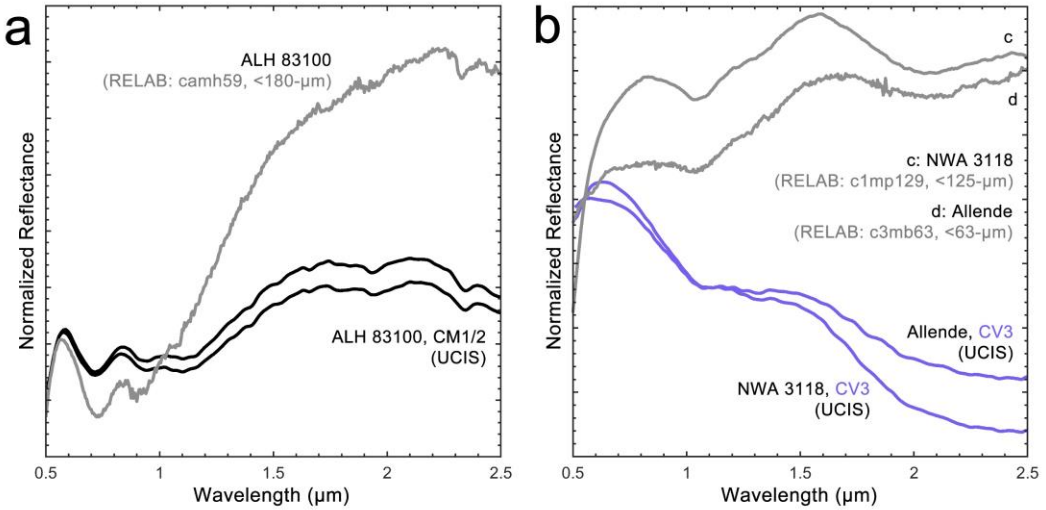

Figure 4.1: a) Averaged UCIS image cube spectra for CM1/2 chondrite ALH83100 compared to a RELAB spectrum of the same meteorite (camh59; Cloutis, Hudon, et al., 2011). b) averaged UCIS image cube spectra for CV3 chondrites NWA 3318 and Allende compared to analog RELAB spectra (c1mp129, c3mb63; Cloutis, Hudon, Hiroi, Gaffey, et al., 2012). Spectra were normalized at 0.55 µm for comparison.

2.3 Adapting the Bus-DeMeo Taxonomy

To utilize the spectral feature-driven Expanded Bus-DeMeo taxonomy and better compare the spectral diversity of chondrites and asteroids, we introduced certain modifications to the data preparation methods used by DeMeo et al. (2009) for processing of the asteroid spectral database they made available (Appendix Table 4.3). In the original Expanded Bus-DeMeo taxonomy, the data are processed to reduce the impact of noise and missing data, as well as highlight desired features. Briefly, the original method first applies *ad hoc* cubic spline fits to the asteroid spectra, which smooth and down-sample the spectra to 41 channels from 0.45-2.45 µm (0.05 µm increments). The splined data are then normalized at 0.55 µm. Following normalization, the slope is removed from the data by dividing the spectra by linear regression lines calculated from the normalized data. Because normalization renders the spectra at 0.55 µm meaningless (all 1), this channel is removed, reducing the final data set to 40 channels. Finally, the slope-removed data are mean-subtracted prior to the first step of the Principal Component Analysis (PCA), which prepares a covariance matrix from the prepared data. The eigenvectors of this covariance matrix are the same used to compute the principal components of the dataset, according to Eq. (1) from DeMeo et al. (2009) below:

$$PC_x = [E_x^T][D^T]. \tag{1}$$

In this study, we present a modified pipeline for processing of both asteroid and chondrite spectra used for PCA-derived classification. This MATLAB-based pipeline largely follows the methods outlined above for asteroid spectra but allows for the inclusion of the chondrite spectral data and more accurately preserves asteroid (and meteorite) spectral features that may be used to compare between asteroid spectral classes and chondrite compositional groups.

2.3.1 Novel noise reduction and spectral re-sampling procedures

Most notably, we build on DeMeo et al. (2009)'s original cubic spline fits by automating a more dynamic noise reduction process that can preserve signal in noisy spectra (Fig. 4.2a, dotted black line vs. dotted red line). To do this, we first introduce a series of Savitsky-Golay (SG) noise filters that reduce noise without distorting or smoothing out tens-of-nm-wide spectral features. The SG filters are based on a noise-filtering algorithm developed for digital signals (Savitzky & Golay, 1964) and have a history of use in asteroid spectral noise reduction (Bhatt et al., 2015; Borisov et al., 2018; Le Corre et al., 2018).

We selectively apply increasingly stronger SG filters in three stages. Prior to applying the filters, we first characterize the level of signal relative to the noise by taking a 10-channel boxcar average of the unprocessed input spectrum. We then compute the percentage by which the input spectrum reflectance values exceed the boxcar average. This allows us to define two statistically motivated "noise cutoffs" for each spectrum by using the mean, μ, and the standard deviation, σ: 1) $\mu+\sigma$ and 2) $\mu+2\sigma$. We use these cutoffs to define two sets of spectrum segments: 1) "intermediate noise" regions in the spectrum that exceed the $\mu+\sigma$ cutoff, and 2) "high noise" regions in the spectrum that exceed the $\mu+2\sigma$ cutoff, as shown in Fig. 4.2.

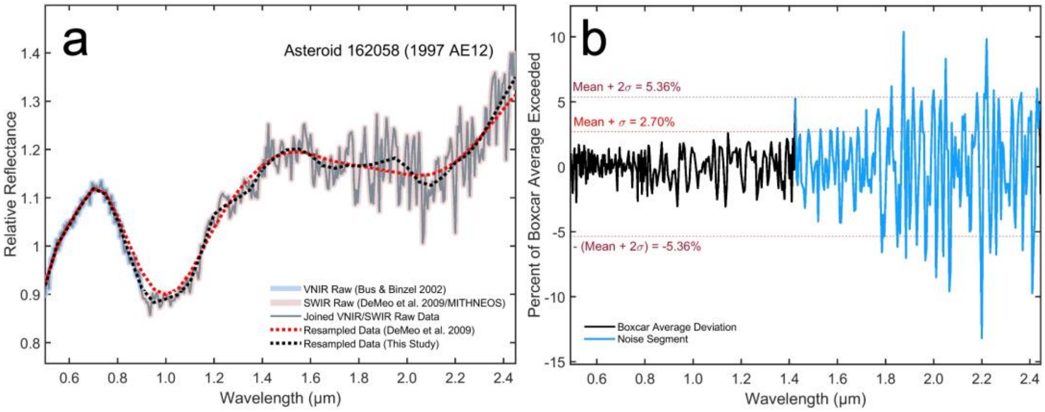

Figure 4.2: a) The new, Savitzky-Golay filter-based down-sampling of asteroid spectra in this study, as shown with 162058 (1997 AE12). The raw data are shown in comparison to the resampled data as computed in DeMeo et al. (2009) (in red) and as computed for this study (in black). b) Two sets of noise thresholds are calculated based on deviations from a 10-channel boxcar average of the raw signal (in black). Increasingly aggressive filters are then applied to specific segments that exceed these thresholds, shown together in blue. This method improves on the spectrum produced with just a cubic spline as in DeMeo et al. (2009) by preserving spectral features more faithfully.

To begin noise reduction, we apply an initial SG filter across the entire input spectrum based on a 2^{nd}-order polynomial and a 31-channel frame. Then, for the "intermediate noise" regions only, we substitute these regions in the initially smoothed spectrum with those from a more aggressively filtered spectrum that applies a 2nd order polynomial and a 51-channel frame over the initially smoothed spectrum. For “high noise” regions, we instead substitute these regions with those from a different, more aggressively filtered spectrum using a 2nd order polynomial and a 71-channel frame after the initial, 31-channel frame filter. Following the SG-filter noise reduction, we finally apply MATLAB’s “fnxtr” and “csaps” routines (based on a 2nd order polynomial) to compute a standardized, less aggressive cubic spline fit that also accounts for extrapolation in spectra where there is missing data at the edges of the desired spectral range.

We also shorten the spectral range originally used for the taxonomy’s PCA (0.45-2.45 μm) to be the intersection with the spectral range captured by the Ultra-Compact Imaging Spectrometer used for chondrite data collection (0.5-2.5 μm). The spectral range in the PC-based comparison is 0.5 to 2.45 μm. We maintain the spectral resolution of DeMeo et al. (2009), 0.05 μm, such that the newly computed spline fits are sampled from 0.5 to 2.45 μm across 40 channels.

2.3.2 Changes to slope removal

Slope removal is performed to make the PCA more sensitive to other spectral drivers likely to be more indicative of compositional differences and because spectral slope in asteroid spectra is often linked to space weathering (DeMeo et al., 2009). We modify their approach by removing the slope from the splined data prior to normalization; this occurred after normalization in the original data preparation for the taxonomy. While relatively unimportant in the asteroid taxonomy, use of a linear regression curve post-normalization was impossible for near-infrared spectra of carbonaceous chondrites, where the existence of spectra with flatter continua, increased dynamic range, and the presence of broad absorption features led to high slope functions and divisions by near-zero. To address this, we translate the reflectance spectrum in the y-direction by 1, calculate the linear regression line, and divide the spectrum by the slope function prior to then normalizing, which is sufficient to eliminate this problem. The rest of the data preparation methods follow as described in DeMeo et al. (2009). A visual summary of the new data preparation pipeline is summarized in Fig. 4.3.

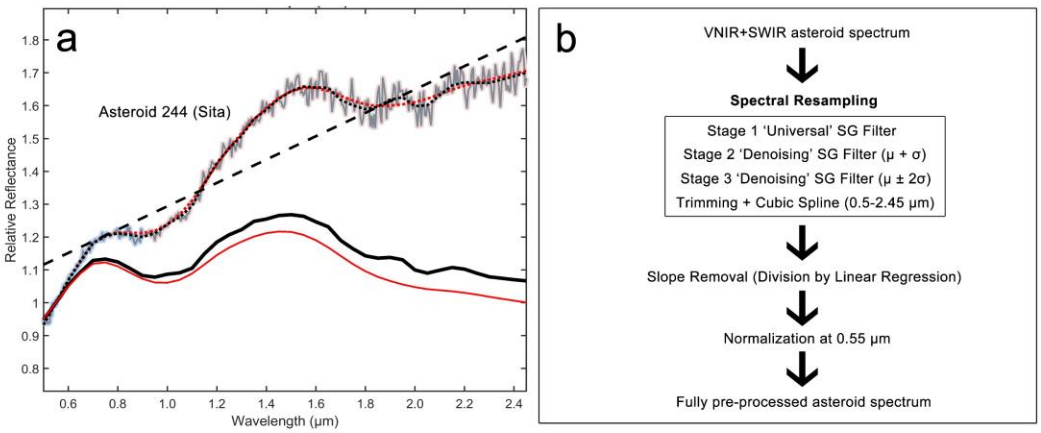

Figure 4.3: The full representation of the novel spectral pre-processing pipeline presented in this study. a) Graphical representation of the raw data, compared to intermediate steps in the preparation pipeline as presented by DeMeo et al. (2009) (in red) and as computed for this study. b) A summary of the individual steps to process asteroid spectra for Principal Component Analysis (PCA) and projection into principal component spaces in this study.

2.4 Validation of Improved Pre-Processing on the Expanded Bus-DeMeo Taxonomy

To evaluate the impact of the novel data preparation pipeline on the original Expanded Bus-DeMeo taxonomy, we re-computed the eigenvectors of the asteroid covariance matrix and re-visualized key principal component spaces used to create the asteroid classification system with the new data preparation pipeline.

2.4.1 Overview of newly represented asteroid spectral diversity

We first looked at the variance captured across the principal components of the data set as prepared in the original Expanded Bus DeMeo taxonomy. DeMeo et al. (2009) observe that the first five principal components were sufficient to capture 99.1% of the variance in the data set, with 87.4% being represented in the first two components. Our modified pipeline preserves this decomposition of the variance, with 99.2% of the variance captured within the first five principal components of the asteroid spectral data, as shown in Table 4.2.

Table 4.2
Comparison of variance captured by principal components

Principal Component (PC)	**Variance (%) — DeMeo et al. (2009)**	**Variance (%) - This Study**
PC1’	63.1	68.6
PC2’	24.3	21.3
PC3’	8.9	7.3
PC4’	2.2	1.6
PC5’	0.6	0.4
Total Variance (%)	**99.1**	**99.2**

Note. Use of the “’” symbol remains as an indicator that the slope has been removed from the asteroid spectra, as in DeMeo et al. (2009).

A graphical comparison between these principal components (shown in Fig. 4.4) shows a high similarity between the first four principal components. The largest differences are in the PC5’ eigenvector, which in the new processing now has higher spectral contrast in the 0.6-1.2 µm and 1.9-2.5 µm ranges. Still, we conclude that the modified data preparation procedures preserve DeMeo et al. (2009)’s first five principal components and thus preserve the key distinctions between asteroid spectral classes established in the principal component spaces selected for the taxonomy.

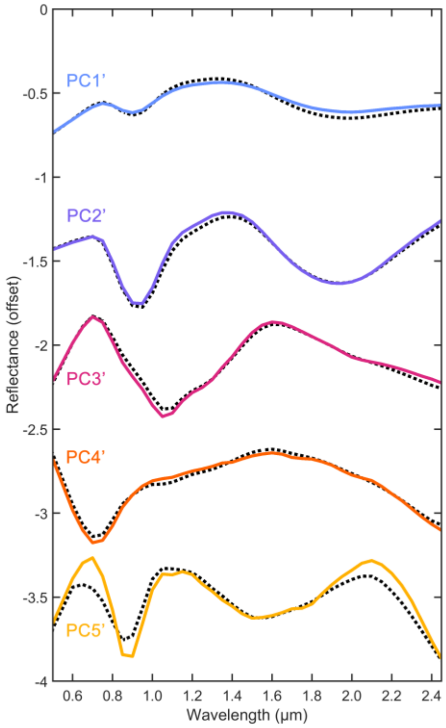

Figure 4.4: The eigenvectors of asteroid spectral data set, as produced by the pre-processing pipeline in this study (solid, colored lines) and overlaid on the eigenvectors as published in DeMeo et al. (2009) (dotted, black lines).

2.4.2 Evaluation of taxonomic principal component spaces

We next examined key principal component spaces used to define asteroid spectral classes, particularly those that effectively separate primitive asteroids (C-complex, X-complex, B, etc.) — as the primitive asteroids are believed to be the parent bodies of carbonaceous chondrites. The most defining feature of the Expanded Bus-

DeMeo taxonomy, the “grand divide” is found in the PC2’ vs. PC1’ (DeMeo et al., 2009). This divide is observed to mostly separate objects with strong 1- or 2-µm absorption features (e.g., S class) from those without (e.g., C, X classes) and is thus used prominently as a classification boundary. Comparison of the resulting positions of all 371 objects in the asteroid data set based on our newly formulated PC2’ and PC1’ to their original positions from DeMeo et al. (2009) shows preservation of the natural separation of objects with and without the 1- and 2- µm absorption features (Fig. 4.5). We also observe the movement of previously distant spectral class objects closer towards other objects in their spectral class, such as Sq-class 138258 (2000 GD2) and Q-class 162058 (1997 AE12). We attribute this to the improved retention of spectral behavior in the near-infrared with the new spectral pre-processing (Figs. 4.2, 4.3). In the new PC2’ vs. PC1’ space, the single A- and Sa- class examples previously to the right of the divide migrate to the left side, joining the others in their class and in accordance with lower PC2’ values reflective of a broader, shallower 2-µm absorption feature. Together, this demonstrates the continued utility of the PC2’ vs. PC1’ space with the pre-processing modifications introduced in this study.

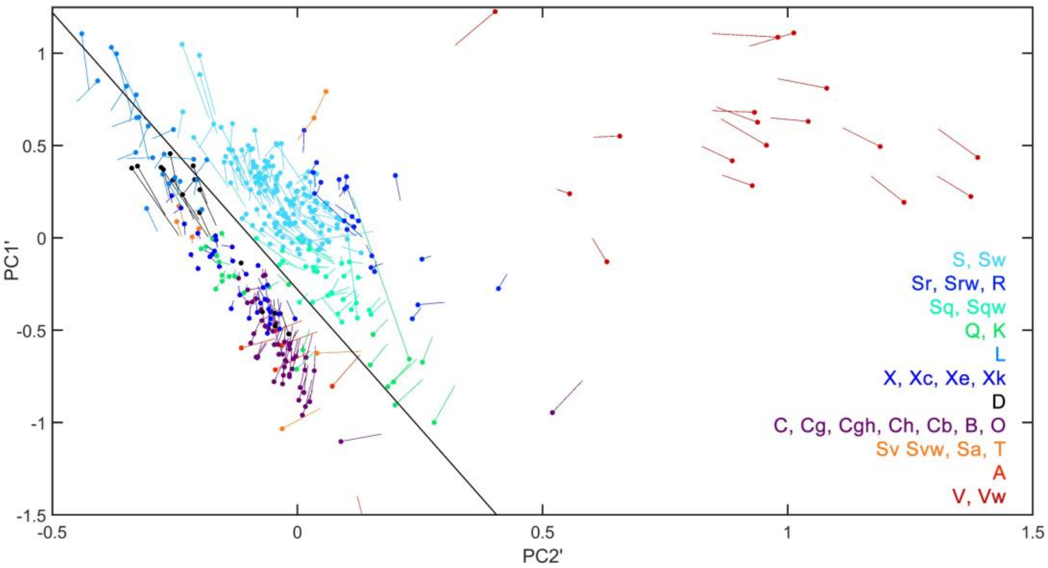

Figure 4.5: The reformulated PC2’ vs. PC1’ space according to the revised spectral processing pipeline in this study. The long black line is the “grand divide” used to separate objects with and without the 1- and 2- µm absorption features. Dots represent the new locations of the 371 asteroid spectra used in the original taxonomy, colored according to their spectral type as defined by DeMeo et al. (2009). The lines connected to each dot point to their original locations in PC2’ vs. PC1’ as generated by DeMeo et al. (2009).

The PC4’ vs. PC1’ space is also a space of interest for comparison of asteroids to carbonaceous chondrites, as it separates X-complex primitive asteroids from various sub-classes within the C-complex primitive asteroids. In the newly reformed PC4’ vs. PC1’ space compared to those of the original taxonomy, we observe that along PC4’, the separation between X-complex and Cgh-class objects is increased, while PC1’ retains the vertical distance between X-complex and C-class objects (Fig. 4.6a). Similarly, the Ch-class objects remain distinct from the C, Cg, and Cb-class objects. This is particularly relevant, due to 0.7-µm features in Ch and Cgh-class asteroids also observed in CM chondrites (Cloutis, Hudon, et al., 2011; DeMeo et al., 2009). As such, we conclude that the novel pre-processing pipeline may increase the value of this space for linking spectral diversity of asteroids and carbonaceous chondrites.

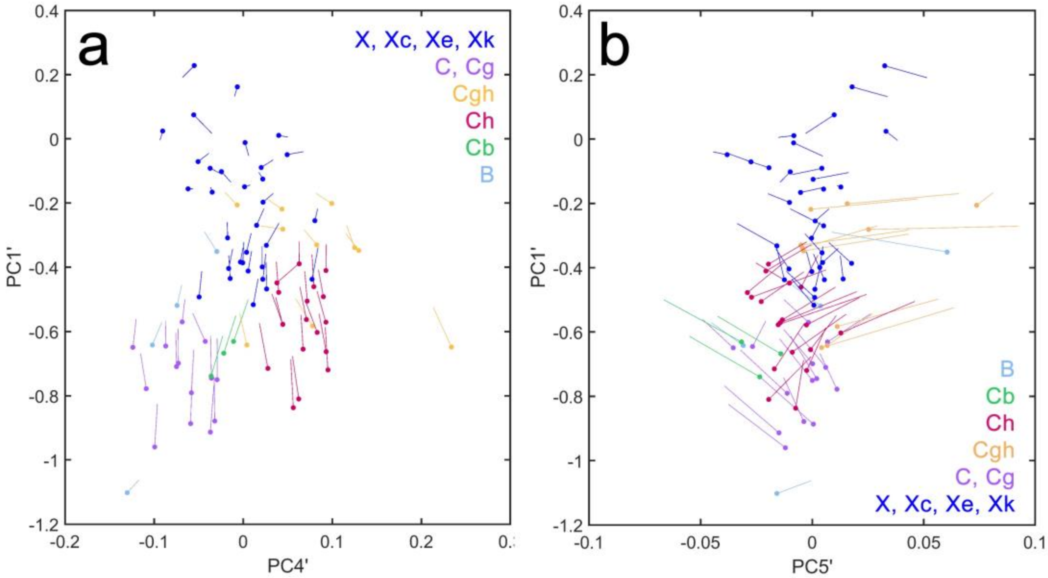

Figure 4.6: a) The re-formulated PC4' and b) PC5' vs. PC1' space according to the revised spectral processing pipeline in this study. Dots represent the new locations of the B, X-, and C-complex asteroid spectra used in the original taxonomy, colored according to their spectral type as defined by DeMeo et al. (2009). The lines connected to each dot point to their original locations in PC4' vs. PC1' and PC5' vs. PC1' as generated by DeMeo et al. (2009).

Lastly, we examine the PC5' vs. PC1' space, which is also used to separate X-complex class objects from C-complex objects and is thus relevant to identifying potential trends shared with carbonaceous chondrites (Fig. 4.6b). Here, we do not improve and instead observe a loss of separation between X-complex and C, Cb, and Cgh-class objects. This is primarily driven by a compression of object positions along PC5'. As stated earlier, PC5' diverged the most from its counterpart in the original Expanded Bus-DeMeo taxonomy after modifications to the pre-processing pipeline. This divergence may be in part driven by the loss of spectral data at the blue/purple wavelengths in this study, which also precludes the definitive classification of certain spectral classes under the original taxonomy, including Xe and Cgh-class objects. Because of this divergence and loss of separation, we do not further consider PC5' vs. PC1' to observe connections between the spectral diversity in carbonaceous chondrites and primitive asteroids, though a future study could incorporate <0.5 µm data of carbonaceous chondrites.

3. Results and Discussion

3.1 Spatially-Resolved Features from Chondrite Spectra

Hyperspectral VSWIR image cubes of carbonaceous chondrites enable us to distinguish spectral features associated with visibly distinct components (Fig. 4.7). For example, CR2 chondrite NWA7502 has broad absorption features at ~0.9 and ~1.8 µm that are typically associated with chondrules (Fig. 4.7b, e). These features are diagnostic of Fe crystal field transitions in low-Ca pyroxene (Burns, 1993) and agree with Greenberger et al. (2015)'s spatially resolved spectra of olivine and pyroxene associated with chondrules in CM2 chondrite Murchison. Furthermore, we observe metal-OH and water vibrational overtones indicative of aqueous alteration (e.g., Fe, Mg-rich clays, water-bearing minerals, Clark et al., 1990; Burns et al., 1993) in the chondrite matrix (Fig. 4.7c-e). These spatially resolved absorption features were also resolved in the Murchison chondrite (Greenberger et al., 2015) and further underscore the value of microimaging spectroscopy to both capture spectral diversity in carbonaceous chondrites (CCs) and discern their spectral drivers in petrographic context. In turn, these data allow us to explore the key components directly responsible for informing spectral similarities and differences between CCs and their asteroid parent bodies.

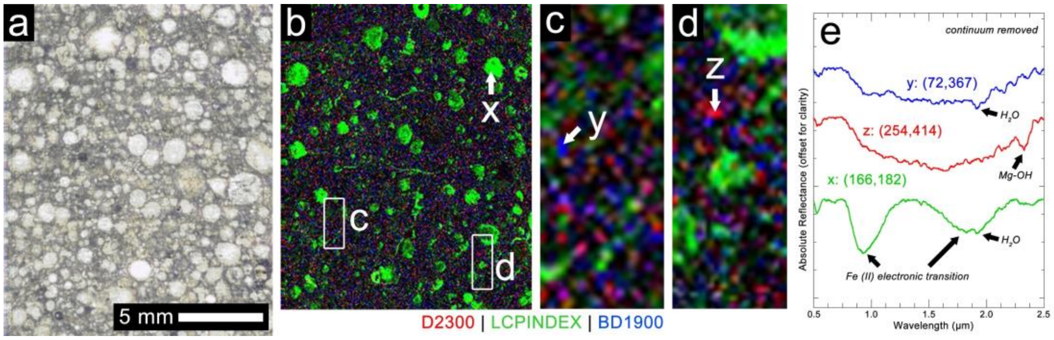

Figure 4.7: a) Near-true color composite image of CR2 chondrite NWA 7502, as taken with UCIS; b) Parameter map of the same field of view as in a) indicating primary vs. altered composition distributions, after the mineral parameters in Viviano et al., (2014), where red is D2300 (Fe/Mg-phyllosilicates), green is LCPINDEX (low-Ca pyroxene), and blue is BD1900 (structural H_2O; c)-d) locations where sample spectrum in e) were taken; e) example spectra for all three parameters.

3.2 Shared Spectral Features Between Chondrites & Asteroids

Slab-like CCs have a bluer slope than particulates (Cantillo et al., 2023), so it is expected that lab-based CC spectra would be bluer than asteroid natural surfaces that have a mixture of cobbles and fine grains. Nonetheless, we observe similarities and shared features between the averaged CC spectra and the asteroid spectra used to generate the PC-driven taxonomy. These include strong “red slopes” longward from the UV, “blue slopes” (downward to longer wavelengths), and absorption features at or near 1 and 2 µm, among others (Fig. 4.8).

In particular, L-class asteroids have previously been connected with CV chondrites based on spectral similarities (Mahlke et al., 2023), including their 1- and 2-µm features, which we observe from comparison of their spectral averages (Fig. 4.9a). Spatial averages of CM chondrite spectra also reveal a strong 0.7 µm absorption (attributed to intervalent Fe^{2+}/Fe^{3+} charge transfer in Cloutis, Hudon, et al., 2011), as well as a pronounced UV-dropoff shared with Cgh asteroids (Fig. 4.9b, DeMeo et al., 2009). These similarities echo past spectral comparisons to Cgh asteroids based on bulk powder measurements (Cloutis, Hudon, et al., 2011; Hiroi et al., 1996; McAdam et al., 2015) and all together suggest close clustering in key PC spaces defined by the Expanded Bus DeMeo taxonomy.

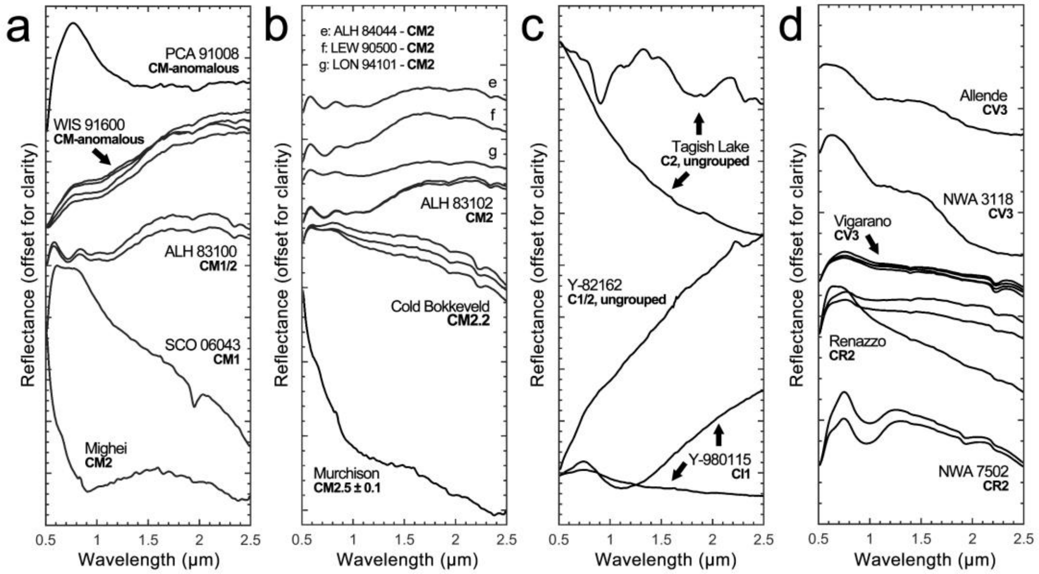

Figure 4.8: Averaged spectra for the carbonaceous chondrites included in this study, where spectra for each image cube were averaged at each UCIS spectral channel across the chondrite surface area. Spectra from different chondrites are offset for clarity. a) CM chondrites of differing petrological grades; b) CM2 chondrites; c) various C-type chondrites; d) CR2 and CV3 chondrites imaged in this study.

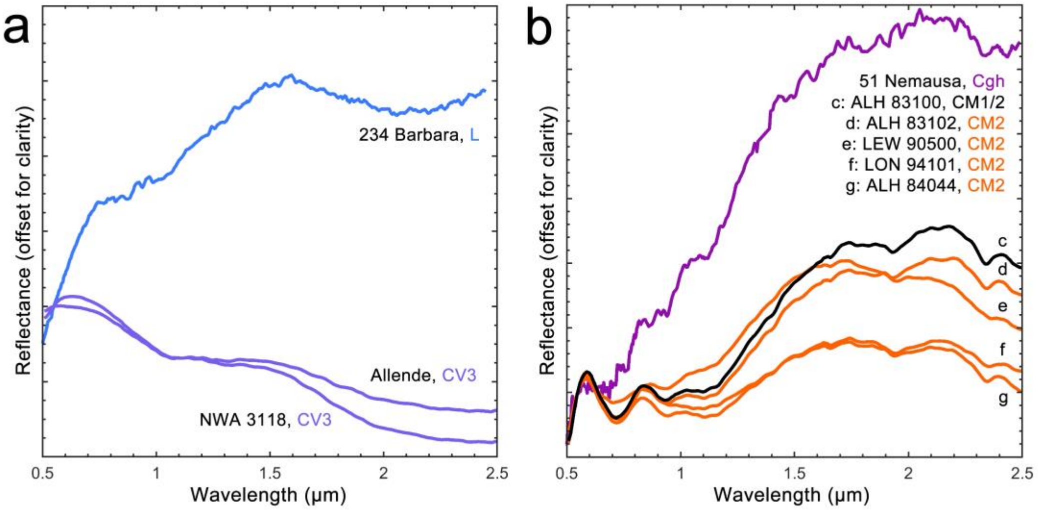

Figure 4.9: a) Averaged spectra for a subset of CV3 chondrites compared to asteroid 234, Barbara — a ‘stony’ asteroid characteristic of features observed in L-type asteroids, particularly its steep red slope short of 0.7 µm and ‘gentle’ blue slope leading into the infrared; b) Averaged spectra for a subset of

CM1/2 and CM2 chondrites (c-d) compared to asteroid 51, Nemausa — a primitive asteroid characteristic of features observed in Cgh-type asteroids, particularly a strong 0.7-µm absorption feature and a sharp dropoff into the UV; all spectra were normalized at 0.55 µm for ease of comparison.

3.3 Carbonaceous Chondrite Spectra in the Asteroid Taxonomy

Unsurprisingly, most averaged CC spectra plot with the relatively feature-poor asteroid classes (including primitive asteroid classes) on the lower left side of the “grand divide” in the PC2’ vs. PC1’ space (Fig. 4.10c). Within these averages, we also note the spatial separation between the CR2/CV3 and CM-type spectra, where CR2 and CV3 chondrites plot closer to the L-type asteroids and the CM-type chondrites place closer to the C-complex asteroids (Fig. 4.10d), aligning with their shared spectral similarities. This separation is in general agreement with that observed from select bulk VSWIR measurements of CC powders and slabs by Cantillo et al. (2023). Comparison of individual chondrite spectral PCs by compositional group in this space (Fig. 4.10a) further reveal this separation of averaged spectra is likely driven by the significantly higher proportion of extremely negative PC2’ and positive PC1’ values belonging to individual CR2 and CV3 spectra compared to the other compositional groups and even the L-type asteroids.

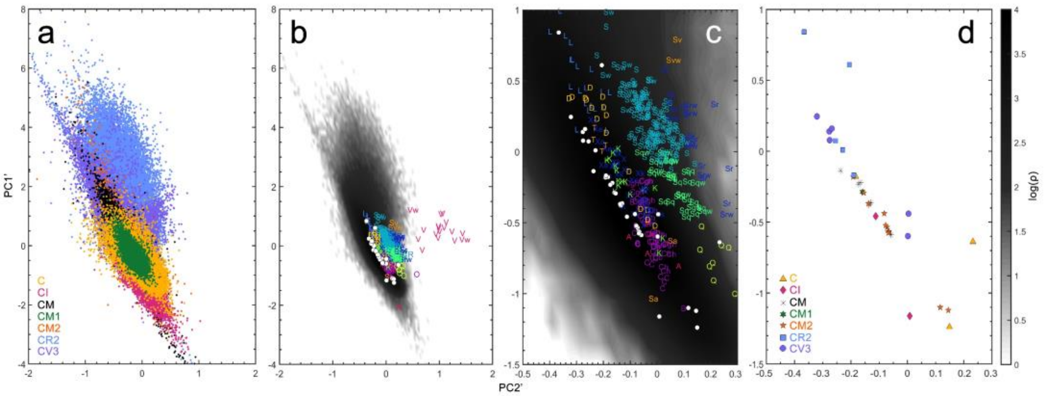

Figure 4.10: a) Reformulated PC2’ vs. PC1’ space, now with the individual carbonaceous chondrite pixel spectra colored by compositional group. Here, C refers to formally ungrouped chondrites and

CM refers to both CM anomalous and CM1/2 chondrites. b) The same space shown in subpanel a), now with a density cloud detailing the spread of individual carbonaceous chondrite image pixels compared to their spectral averages (white circles) and asteroid spectral classes, colored according to their spectral type as defined by DeMeo et al. (2009); c) a zoomed-in view of the PC2’ vs. PC1’ space in subpanel b) where the bulk of the spectrally averaged chondrite image cube PCs lie; d) an identical view of the spectrally averaged chondrite image cube PCs as in sub-panel c), this time distinguished by the chondrite compositional class and petrologic type, where specified, and without the density cloud.

Interestingly, some of the CM2, CI, and the C class Tagish Lake averaged spectra (yellow triangles, orange stars, pink diamonds, Fig. 4.10d) plot much further away from asteroids, indicating either that clasts of this composition are minor compositional types on asteroid surfaces — perhaps representative of interiors — or that these samples’ spectral properties have been influenced by terrestrial alteration.

In DeMeo et al. (2009), Cgh-class asteroid spectra were designated because of their placement in PC4’ vs. PC1’ space, driven in particular by their strong 0.7 μm absorption. In this space (Fig. 4.11), we observe a distinct, negatively sloped trend in the averaged CC spectral PCs not explicitly associated with any trends observed in the primitive asteroid spectral classes, as well as a lateral spread in the averaged spectral PCs at lower PC1’ values. Nonetheless, CR2 and CV3 averaged spectra retain their association with the L-class asteroids (Fig. 4.11c, d), as well as their separation from the CM chondrite groups, which are generally associated with higher PC4’ values, as with Cgh class asteroids bearing the distinct 0.7 μm feature in DeMeo et al. (2009). This includes CM2 chondrites Mighei and Murchison, which populate the right-most part of the lateral spread of averaged spectra at lower PC1’ values. While linear averaging of spatially-resolved CC spectra may not accurately reflect the type of intimate spectral mixing that occurs with observations of asteroid surfaces, these averaged spectra reflect the dominant features driving the spectral diversity of the chondrites included in this study and serve as a point of comparison to spatially resolved spectra from the CCs.

Indeed, individual chondrite spectral PCs in this space reveal a distinct lobe of CR2 chondrite spectra with high PC1’ values that have higher PC4’ values than the CM chondrite spectra (Fig. 4.11a). As this lobe is not as densely populated (Fig. 4.11b), this may reflect a unique, albeit relatively uncommon spectral signature in CR2 chondrites that is insufficient to drive averaged chondrite spectral PCs closer towards those of the CM chondrites.

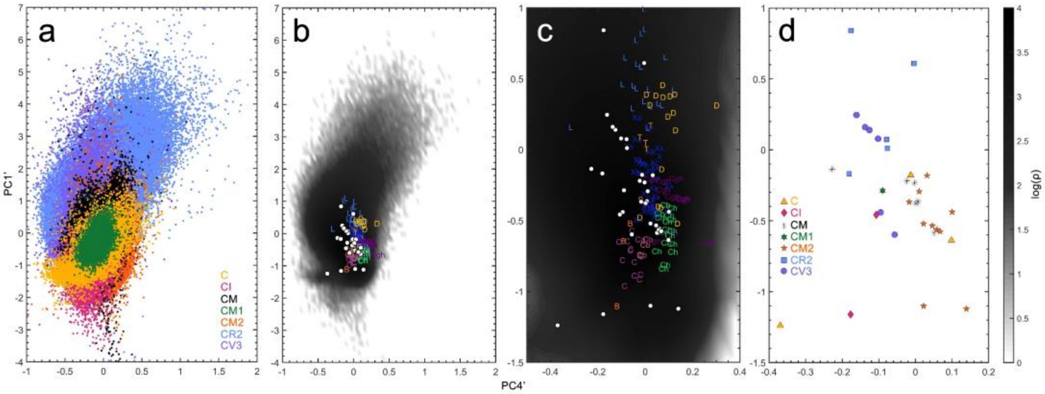

Figure 4.11: a) Reformulated PC4’ vs. PC1’ space, with individual carbonaceous chondrite pixel spectra colored by compositional group. Here, C refers to formally ungrouped chondrites and CM refers to both CM anomalous and CM1/2 chondrites. b) The same space shown in subpanel a), now with a density cloud detailing the spread of individual carbonaceous chondrite image pixels compared to their spectral averages (white circles) and asteroid spectral classes, colored according to their spectral type as defined by DeMeo et al. (2009); c) a zoomed-in view of subpanel b) where the bulk of the spectrally averaged chondrite image cube PCs lie; d) an identical view of the spectrally averaged chondrite image cube PCs as in sub-panel c), this time distinguished by the chondrite compositional class and petrologic type, where specified, and without the density cloud.

3.4 Drivers of Spectral Diversity in the Asteroid Taxonomy

Generally, differences across the spectral properties of spatially resolved chondrite constituents drive a very large spread in the PC spaces examined by the Expanded

Bus DeMeo taxonomy. (Figs. 4.10, 4.11). In particular, we observe a broad, dense extension of the chondrite pixel clouds towards a higher PC1' in the direction defined by the "stony" asteroids (e.g., S-complex, V-complex) as well as the L-class asteroids (Fig. 4.10a, b). This behavior is attributed to distinct unaltered mineral signatures in CCs, such as the strong ~0.9 and 1.8 μm features indicative of low-Ca pyroxene in CR2 chondrite NWA7502 (Fig. 4.7) that more closely reflect the orthopyroxene-driven spectra of V-complex asteroids such as Vesta (e.g., Burbine et al., 2023; De Sanctis et al., 2011) than a C-complex asteroid.

In particular, the PC3'versus PC1' space also separates K-, A-, and Sa-type asteroid spectra from the comparatively feature-poor, primitive asteroid classes (e.g., C-complex, X-complex, Fig. 4.12). Pixel clouds of CC spectra reveal distinct "lobes" loosely associated with certain asteroid spectral classes (e.g., V-complex, A/Sa-type) clustering in the PC3' versus PC1' space, including the broad lobe towards higher PC1' values (Fig. 4.12a, b). Interestingly, lateral separation among the averaged chondrite spectra is notably reduced (Fig. 4.12c), which may suggest an equal contribution from constituent spectra at either extreme, a low abundance of sampled spectra with diversity expressed by PC3', or a combination thereof. Indeed, the density of the chondrite pixel clouds in the lobes defined by the A/Sa- and V-complex asteroids is as much as 3 orders of magnitude less than along the vertical axis defined by the S-complex and C-complex asteroids (Fig. 4.12b).

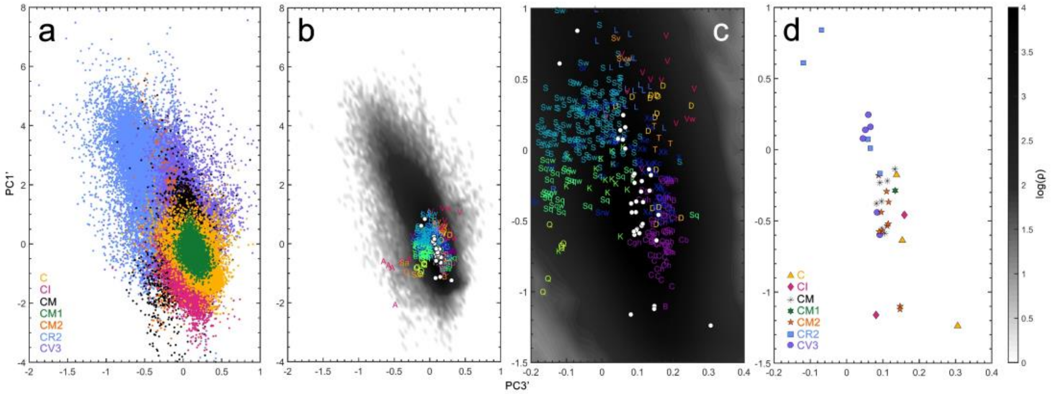

Figure 4.12: a) Reformulated PC3' vs. PC1' space, with individual carbonaceous chondrite pixel spectra colored by compositional group. Here, C refers to formally ungrouped chondrites and CM refers to both CM anomalous and CM1/2 chondrites. b) The same space shown in subpanel a), now with a density cloud detailing the spread of individual carbonaceous chondrite image pixels compared to their spectral averages (white circles) and asteroid spectral classes, colored according to their spectral type as defined by DeMeo et al. (2009); c) a zoomed-in view of subpanel b) where the bulk of the spectrally averaged chondrite image cube PCs lie — here we also see a strong retention of the separation between primitive asteroids (C-complex, X-complex, B, etc.) and the asteroids with a strong 2-μm feature originally seen in the PC2' vs. PC1' space; d) an identical view of the spectrally averaged chondrite image cube PCs as in sub-panel c), this time distinguished by the chondrite compositional class and petrologic type, where specified, and without the density cloud.

A closer examination of the CCs informing the spread of pixel clouds in PC3' vs. PC1' reveals that CR2 chondrite spectra dominate in the broad lobe towards higher PC1', lower PC3' values (Fig. 4.13a), compared to other chondrite spectral classes. Localized, constituent spectra from higher PC1' values and lower PC3' values suggest two distinct spectral drivers are expressed in these regions (Fig. 4.13a, f). Spatially resolved "Region A" spectra from CR2 chondrite NWA 7502 bear chondrule-associated features consistent with olivine's broad absorption feature centered at ~1.05 μm (Fig. 4.13c-g). Unsurprisingly, the spectral signature of Region A also mirrors the broad ~1 μm olivine feature characteristic of A/Sa-class asteroids (e.g., Cruikshank & Hartmann, 1984; DeMeo et al., 2019; Sanchez et al., 2014) and suggests that PC3' may, in part, be informed by the diversity of olivine content among the asteroids in the Expanded Bus-DeMeo taxonomy.

By contrast "Region B" spectra from NWA 7502 show distinct absorption features at ~0.9 µm and are most likely attributed to Fe-oxides (e.g., hematite) or Fe-oxyhydroxides (Fig. 4.13c-g). Unlike olivine's spectral features, the 0.9-µm feature has been routinely observed from whole-sample bulk powders of CR chondrites and is thought to stem from post-fall terrestrial weathering, as posited by Cloutis, Hudon, et al., (2011). Indeed, a further analysis of the spectra informing the broad lobe in PC3' vs. PC1' space reveal this absorption band originates from NWA 7502's chondrules (Fig. 4.13c-g). The spatial dominance of these chondrule-associated features likely explains the distant positions of two CR2 averaged chondrite spectra (both of which correspond to NWA 7502) compared to the other chondrite averaged spectra.

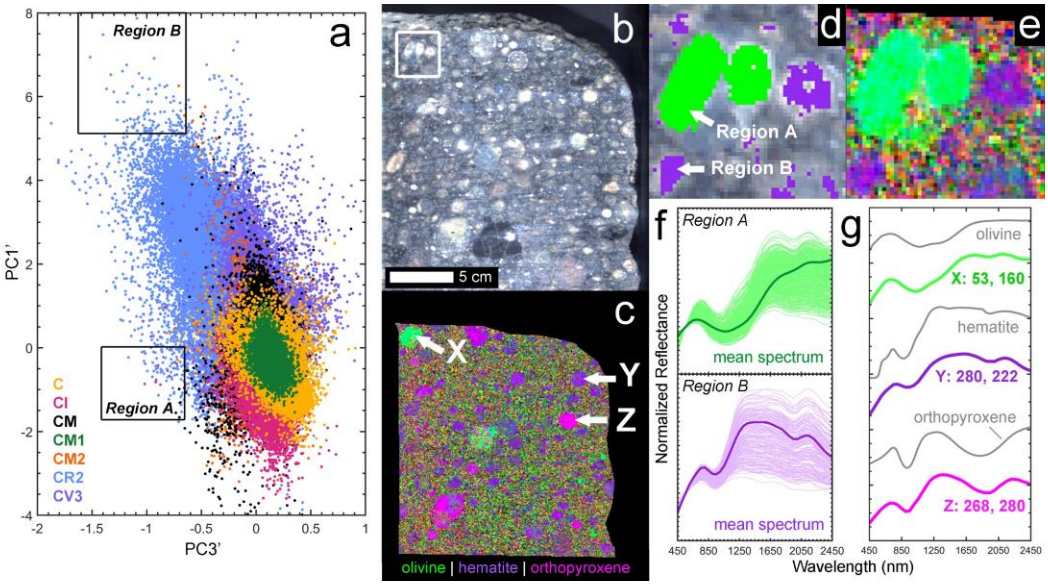

Figure 4.13: a) Reformulated PC3'vs. PC1' space showing the spread of individual carbonaceous chondrite image pixels, as in 4.12a, where select regions reflecting distinct spectral features are in boxes. b) Near true-color image of CR2 chondrite NWA 7502; c) RGB parameter map with key absorptions for low-Ca pyroxene (R: band depth (BD) at 1.9 µm), olivine (G: based on reflectances at 1.05, 1.21, 1.33, 1.47, and 1.695 µm), and ferric iron (B: BD at 0.92 µm). Low-Ca pyroxene-like spectra appear pink, and more hematite-like spectra are purple, see g); d) ROIs for pixels within each indicated region from a); e) a zoomed-in view of c); f) lighter spectra correspond to the member pixels

shown in d) with mean spectrum in bold; g) sample spectra from c) with RELAB spectra for olivine, hematite, and orthopyroxene.

More broadly, the top three eigenvectors informing the Expanded Bus-DeMeo Taxonomy (Table 4.2, Fig. 4.4) suggest that as much as ~96% of the asteroid spectral variance in the 0.5-2.45 μm range may be expressed by linear combinations of spectral signatures strongly resembling those of unaltered (or differentiated) iron-bearing mineral phases, particularly pyroxene and olivine. Confirmation of these mineral phases in CC spectra clustering in the PC spaces defined by the top three eigenvectors further supports the role of these minerals in driving the separation of certain asteroid classes. Indeed, the notable "grand divide" between stony and comparatively more primitive asteroids is very likely attributed to the role of olivine and pyroxene-rich phases, which drive the strong 1- or 2-μm absorption features identified by DeMeo et al., (2009). While specific connections between these mineral phases and asteroid spectral classes have been studied in detail (e.g., olivine in A-type asteroids and pyroxene in V-complex asteroids), these associations in PC space underscore the value of the Expanded Bus-DeMeo taxonomy as a potential tool to evaluate co-occurring patterns of key mineral abundances between multiple asteroid spectral classes and chondrite compositional groups.

In particular, the observed connections between spectral PCs and various Fe-bearing minerals highlights the role of iron (Fe) as a major driver of asteroid spectral diversity in this spectral range (0.5-2.45 μm). Indeed, the separation of spectra indicative of unaltered Fe-bearing minerals in CCs from those reflecting more aqueously altered Fe-bearing minerals (e.g., Fe-phyllosilicates or iron oxides like hematite) shows the taxonomy is explicitly reflective of differing states of iron mineral alteration. While these spectral trends may be used to discover new, or support existing chondrite-parent body connections, the taxonomy can also use spatially resolved chondrite spectra to outline components or regions where Fe-mineral alteration is preferentially expressed, as observed with NWA 7502.

4. Conclusions

Collectively, our observations demonstrate the value of microimaging VSWIR spectroscopy for identifying the constituents driving the spectral properties of carbonaceous chondrites. By extension, these are likely the same constituents driving the majority of spectral variability of the asteroids. Plotting the data in the principal components-based Expanded Bus-DeMeo taxonomy demonstrates shared as well as unique drivers of spectral diversity between carbonaceous chondrites and asteroids as enabled through high-throughput microimaging hyperspectral VSWIR spectroscopy. Furthermore, we build on the spectral processing procedures used by DeMeo et al. (2009) to preserve spectral behavior more accurately and improve the separation of asteroid spectra in the principal component spaces used to develop the taxonomy.

While projection of averaged spectra from individual chondrite image cubes suggests that bulk spectral behavior in the VSWIR roughly aligns with previously examined chondrite-parent body relationships (e.g., L-class asteroids and CV3 chondrites, or CM chondrites and Cgh-class asteroids), spatially-resolved chondrite spectra offer a window into a much broader spectral diversity. Distinct spectral features consistent with primary minerals (e.g., low-Ca pyroxene, olivine) found in chondrules are also shared with differentiated asteroids with "stonier" compositions. By contrast, we also see that the principal components of asteroid spectral diversity can isolate spectral features unique to chondrites, including terrestrially-derived alteration signatures.

More broadly, these observations underscore the role of iron minerals in driving spectral diversity in the VSWIR range. Indeed, much of the variable spectral behavior captured in the top five principal components (PCs) of the Expanded Bus-DeMeo taxonomy may be directly attributed to distinct iron-bearing minerals that reflect various states of alteration. Further investigation promises to outline additional connections as indicated from distinct separation of the chondrite image cube pixels in different PC spaces. Beyond Fe-associated absorption features, hydration features are routinely used to identify records of aqueous alteration and are also prevalent in the dataset presented in this study. Still, the Expanded Bus-DeMeo taxonomy is a limited framework to systematically identify and compare the spectral diversity between asteroids and carbonaceous chondrites. Diagnostic alteration features with shallower absorption bands (e.g., various metal-OH vibrational overtones) may be less likely to shape shared spectral diversity. A novel classification based on the native, spatially resolved spectral diversity of carbonaceous chondrites is another avenue for further investigation afforded by microimaging spectroscopy.

Ultimately, these data represent an initial step towards a wider, structured survey across asteroid and carbonaceous chondrite surfaces to better understand their shared record of alteration during the early solar system.

5. References

Bhatt, M., Reddy, V., Le Corre, L., Sanchez, J. A., Dunn, T., Izawa, M. R. M., et al. (2015). Spectral calibration for deriving surface mineralogy of Asteroid (25143) Itokawa from Hayabusa Near-Infrared Spectrometer (NIRS) data. Icarus, 262, 124–130. https://doi.org/10.1016/j.icarus.2015.08.036

Borisov, G., Christou, A. A., Colas, F., Bagnulo, S., Cellino, A., & Dell'Oro, A. (2018). (121514) 1999 UJ7: A primitive, slow-rotating Martian Trojan. Astronomy & Astrophysics, 618, A178. https://doi.org/10.1051/0004-6361/201732466

Bowen, B., Reddy, V., Florio, M. D., Kareta, T., Pearson, N., Furfaro, R., et al. (2023). Grain Size Effects on Visible and Near-infrared (0.35–2.5 μm) Laboratory Spectra of Ordinary Chondrite and HED Meteorites. The Planetary Science Journal, 4(3), 52. https://doi.org/10.3847/PSJ/acb268

Burbine, T. H., & Binzel, R. P. (2002). Small Main-Belt Asteroid Spectroscopic Survey in the Near-Infrared. Icarus, 159(2), 468–499. https://doi.org/10.1006/icar.2002.6902

Burbine, T. H., P. C, B., Jercinovic, M. J., & Greenwood, R. C. (2023). Determining the Pyroxene Mineralogies of Vestoids. The Planetary Science Journal, 4(5), 96. https://doi.org/10.3847/PSJ/accb98

Burns, R. G. (1993). Mineralogical Applications of Crystal Field Theory (2nd ed.). Cambridge: Cambridge University Press. https://doi.org/10.1017/CBO9780511524899

Bus, S. J., & Binzel, R. P. (2002). Phase II of the Small Main-Belt Asteroid Spectroscopic Survey: A Feature-Based Taxonomy. Icarus, 158(1), 146–177. https://doi.org/10.1006/icar.2002.6856

Bus, S. J. (Schelte J. (1999). Compositional structure in the asteroid belt : results of a spectroscopic survey (Thesis). Massachusetts Institute of Technology. Retrieved from https://dspace.mit.edu/handle/1721.1/9527

Cantillo, D. C., Reddy, V., Battle, A., Sharkey, B. N. L., Pearson, N. C., Campbell, T., et al. (2023). Grain Size Effects on UV–MIR (0.2–14 μm) Spectra of Carbonaceous Chondrite Groups. The Planetary Science Journal, 4(9), 177. https://doi.org/10.3847/PSJ/acf298

Clark, B. E., Binzel, R. P., Howell, E. S., Cloutis, E. A., Ockert-Bell, M., Christensen, P., et al. (2011). Asteroid (101955) 1999 RQ36: Spectroscopy from 0.4 to 2.4µm and meteorite analogs. Icarus, 216(2), 462–475. https://doi.org/10.1016/j.icarus.2011.08.021

Clark, R. N., King, T. V. V., Klejwa, M., Swayze, G. A., & Vergo, N. (1990). High spectral resolution reflectance spectroscopy of minerals. Journal of Geophysical Research: Solid Earth, 95(B8), 12653–12680. https://doi.org/10.1029/JB095iB08p12653

Cloutis, E. A., Hiroi, T., Gaffey, M. J., Alexander, C. M. O., & Mann, P. (2011). Spectral reflectance properties of carbonaceous chondrites: 1. CI chondrites. Icarus, 212(1), 180–209. https://doi.org/10.1016/j.icarus.2010.12.009

Cloutis, E. A., Hudon, P., Hiroi, T., Gaffey, M. J., & Mann, P. (2011). Spectral reflectance properties of carbonaceous chondrites: 2. CM chondrites. Icarus, 216(1), 309–346. https://doi.org/10.1016/j.icarus.2011.09.009

Cloutis, E. A., Hudon, P., Hiroi, T., & Gaffey, M. J. (2012a). Spectral reflectance properties of carbonaceous chondrites: 3. CR chondrites. Icarus, 217(1), 389–407. https://doi.org/10.1016/j.icarus.2011.11.004

Cloutis, E. A., Hudon, P., Hiroi, T., & Gaffey, M. J. (2012b). Spectral reflectance properties of carbonaceous chondrites 4: Aqueously altered and thermally metamorphosed meteorites. Icarus, 220(2), 586–617. https://doi.org/10.1016/j.icarus.2012.05.018

Cloutis, E. A., Hudon, P., Hiroi, T., Gaffey, M. J., Mann, P., & Bell, J. F. (2012). Spectral reflectance properties of carbonaceous chondrites: 6. CV chondrites. Icarus, 221(1), 328–358. https://doi.org/10.1016/j.icarus.2012.07.007

Cruikshank, D. P., & Hartmann, W. K. (1984). The Meteorite-Asteroid Connection: Two Olivine-Rich Asteroids. Science, 223(4633), 281–283. https://doi.org/10.1126/science.223.4633.281

De Sanctis, M. C., Ammannito, E., Migliorini, A., Lazzaro, D., Capria, M. T., & McFadden, L. (2011). Mineralogical characterization of some V-type asteroids, in support of the NASA Dawn mission*. Monthly Notices of the Royal Astronomical Society, 412(4), 2318–2332. https://doi.org/10.1111/j.1365-2966.2010.18058.x

DeMeo, F. E., & Carry, B. (2014). Solar System evolution from compositional mapping of the asteroid belt. Nature, 505(7485), 629–634. https://doi.org/10.1038/nature12908

DeMeo, F. E., Binzel, R. P., Slivan, S. M., & Bus, S. J. (2009). An extension of the Bus asteroid taxonomy into the near-infrared. Icarus, 202(1), 160–180. https://doi.org/10.1016/j.icarus.2009.02.005

DeMeo, F. E., Polishook, D., Carry, B., Burt, B. J., Hsieh, H. H., Binzel, R. P., et al. (2019). Olivine-dominated A-type asteroids in the main belt: Distribution, abundance and relation to families. Icarus, 322, 13–30. https://doi.org/10.1016/j.icarus.2018.12.016

Fraeman, A. A., Ehlmann, B. L., Northwood-Smith, G. W. D., Liu, Y., Wadhwa, M., & Greenberger, R. N. (2016). Using VSWIR microimaging spectroscopy to explore the mineralogical diversity of HED meteorites. In 2016 8th Workshop on Hyperspectral Image and Signal Processing: Evolution in Remote Sensing (WHISPERS) (pp. 1–5). https://doi.org/10.1109/WHISPERS.2016.8071804

Grady, M. M., Wright, I., Binzel, R. P., Walker, R. M., & Cameron, A. G. W. (2006). Types of Extraterrestrial Material Available for Study. In D. S. Lauretta & H. Y. McSween (Eds.), Meteorites and the Early Solar System II (pp. 3–18). University of Arizona Press. https://doi.org/10.2307/j.ctv1v7zdmm.7

Greenberger, R. N., Mustard, J. F., Ehlmann, B. L., Blaney, D. L., Cloutis, E. A., Wilson, J. H., et al. (2015). Imaging spectroscopy of geological samples and outcrops: Novel insights from microns to meters. GSA Today, 25(12), 4–10. https://doi.org/10.1130/GSATG252A.1

Hamilton, V. E., Simon, A. A., Christensen, P. R., Reuter, D. C., Clark, B. E., Barucci, M. A., et al. (2019). Evidence for widespread hydrated minerals on asteroid (101955) Bennu. Nature Astronomy, 3(4), 332–340. https://doi.org/10.1038/s41550-019-0722-2

Hiroi, T., Zolensky, M. E., Pieters, C. M., & Lipschutz, M. E. (1996). Thermal metamorphism of the C, G, B, and F asteroids seen from the 0.7 μm, 3 μm, and UV absorption strengths in comparison with carbonaceous chondrites. Meteoritics & Planetary Science, 31(3), 321–327. https://doi.org/10.1111/j.1945-5100.1996.tb02068.x

Kitazato, K., Milliken, R. E., Iwata, T., Abe, M., Ohtake, M., Matsuura, S., et al. (2019). The surface composition of asteroid 162173 Ryugu from Hayabusa2 near-infrared spectroscopy. Science, 364(6437), 272–275. https://doi.org/10.1126/science.aav7432

Krot, A. N., Keil, K., Scott, E. R. D., Goodrich, C. A., & Weisberg, M. K. (2007). 1.05 - Classification of Meteorites. In H. D. Holland & K. K. Turekian (Eds.), Treatise on Geochemistry (pp. 1–52). Oxford: Pergamon. https://doi.org/10.1016/B0-08-043751-6/01062-8

Lauretta, D. S., Balram-Knutson, S. S., Beshore, E., Boynton, W. V., Drouet d'Aubigny, C., DellaGiustina, D. N., et al. (2017). OSIRIS-REx: Sample Return from Asteroid (101955) Bennu. Space Science Reviews, 212(1), 925–984. https://doi.org/10.1007/s11214-017-0405-1

Le Corre, L., Sanchez, J. A., Reddy, V., Takir, D., Cloutis, E. A., Thirouin, A., et al. (2018). Ground-based characterization of Hayabusa2 mission target asteroid 162173 Ryugu: constraining mineralogical composition in preparation for spacecraft operations. Monthly Notices of the Royal Astronomical Society, 475(1), 614–623. https://doi.org/10.1093/mnras/stx3236

Leask, E. K., & Ehlmann, B. L. (2016). Identifying and quantifying mineral abundance through VSWIR microimaging spectroscopy: A comparison to XRD and SEM. In 2016 8th Workshop on Hyperspectral Image and Signal Processing: Evolution in Remote Sensing (WHISPERS) (pp. 1–5). https://doi.org/10.1109/WHISPERS.2016.8071774

Leask, E. K., Ehlmann, B. L., Greenberger, R. N., Pinet, P., Daydou, Y., Ceuleneer, G., & Kelemen, P. (2021). Tracing Carbonate Formation, Serpentinization, and Biological Materials With Micro-/Meso-Scale Infrared Imaging Spectroscopy in a Mars Analog System, Samail Ophiolite, Oman. Earth and Space Science, 8(11), e2021EA001637. https://doi.org/10.1029/2021EA001637

Mahlke, M., Eschrig, J., Carry, B., Bonal, L., & Beck, P. (2023). Spectral analogues of Barbarian asteroids among CO and CV chondrites. Astronomy & Astrophysics, 676, A94. https://doi.org/10.1051/0004-6361/202346032

McAdam, M. M., Sunshine, J. M., Howard, K. T., & McCoy, T. M. (2015). Aqueous alteration on asteroids: Linking the mineralogy and spectroscopy of CM and CI chondrites. Icarus, 245, 320–332. https://doi.org/10.1016/j.icarus.2014.09.041

McSween Jr., H. Y. (1979). Are carbonaceous chondrites primitive or processed? A review. Reviews of Geophysics, 17(5), 1059–1078. https://doi.org/10.1029/RG017i005p01059

Milliken, R. E. (2020). RELAB Spectral Library Bundle [Data set]. Archive, NASA Planetary Data System. https://doi.org/10.17189/1519032

Pilorget, C., Okada, T., Hamm, V., Brunetto, R., Yada, T., Loizeau, D., et al. (2022). First compositional analysis of Ryugu samples by the MicrOmega hyperspectral microscope. Nature Astronomy, 6(2), 221–225. https://doi.org/10.1038/s41550-021-01549-z

Rayner, J. T., Toomey, D. W., Onaka, P. M., Denault, A. J., Stahlberger, W. E., Vacca, W. D., et al. (2003). SpeX: A Medium-Resolution 0.8–5.5 Micron Spectrograph and Imager for the NASA Infrared Telescope Facility. Publications of the Astronomical Society of the Pacific, 115(805), 362. https://doi.org/10.1086/367745

Reddy, V., Dunn, T. L., Thomas, C. A., Moskovitz, N. A., & Burbine, T. H. (2015). Mineralogy and Surface Composition of Asteroids. In P. Michel, F. E.

DeMeo, W. F. Bottke, & R. Dotson (Eds.), Asteroids IV (pp. 43–64). University of Arizona Press. Retrieved from https://www.jstor.org/stable/j.ctt18gzdvc.9

Rivkin, A. S., Howell, E. S., Vilas, F., Lebofsky, L. A., & Gehrels, T. (2002). Hydrated Minerals on Asteroids: The Astronomical Record. In W. F. Bottke, A. Cellino, P. Paolicchi, & R. P. Binzel (Eds.), Asteroids III (pp. 235–254). University of Arizona Press. https://doi.org/10.2307/j.ctv1v7zdn4.23

Sanchez, J. A., Reddy, V., Kelley, M. S., Cloutis, E. A., Bottke, W. F., Nesvorný, D., et al. (2014). Olivine-dominated asteroids: Mineralogy and origin. Icarus, 228, 288–300. https://doi.org/10.1016/j.icarus.2013.10.006

Savitzky, Abraham., & Golay, M. J. E. (1964). Smoothing and Differentiation of Data by Simplified Least Squares Procedures. Analytical Chemistry, 36(8), 1627–1639. https://doi.org/10.1021/ac60214a047

Tachibana, S., Sawada, H., Okazaki, R., Takano, Y., Sakamoto, K., Miura, Y. N., et al. (2022). Pebbles and sand on asteroid (162173) Ryugu: In situ observation and particles returned to Earth. Science, 375(6584), 1011–1016. https://doi.org/10.1126/science.abj8624

Takir, D., & Emery, J. P. (2012). Outer Main Belt asteroids: Identification and distribution of four 3-μm spectral groups. Icarus, 219(2), 641–654. https://doi.org/10.1016/j.icarus.2012.02.022

The MathWorks Inc. (2019). MATLAB version: 9.6.0.1072779 (R2019a). Natick, Massachusetts, United States: The MathWorks Inc. Retrieved from https://www.mathworks.com

Tholen, D. J. (1984). ASTEROID TAXONOMY FROM CLUSTER ANALYSIS OF PHOTOMETRY. Retrieved from https://repository.arizona.edu/handle/10150/187738

Van Gorp, B., Mouroulis, P., Blaney, D. L., Green, R. O., Ehlmann, B. L., & Rodriguez, J. I. (2014). Ultra-compact imaging spectrometer for remote, in situ, and microscopic planetary mineralogy. Journal of Applied Remote Sensing, 8(1), 084988. https://doi.org/10.1117/1.JRS.8.084988

Vilas, F., & Gaffey, M. J. (1989). Phyllosilicate Absorption Features in Main-Belt and Outer-Belt Asteroid Reflectance Spectra. Science, 246(4931), 790–792. https://doi.org/10.1126/science.246.4931.790

Viviano, C. E., Seelos, F. P., Murchie, S. L., Kahn, E. G., Seelos, K. D., Taylor, H. W., et al. (2014). Revised CRISM spectral parameters and summary products based on the currently detected mineral diversity on Mars. Journal of Geophysical Research: Planets, 119(6), 1403–1431. https://doi.org/10.1002/2014JE004627

Weisberg, M. K., McCoy, T. J., Krot, A. N., Binzel, R. P., Walker, R. M., & Cameron, A. G. W. (2006). Systematics and Evaluation of Meteorite Classification. In D. S. Lauretta & H. Y. McSween (Eds.), Meteorites and the Early Solar System II (pp. 19–52). University of Arizona Press. https://doi.org/10.2307/j.ctv1v7zdmm.8

Yada, T., Abe, M., Okada, T., Nakato, A., Yogata, K., Miyazaki, A., et al. (2022). Preliminary analysis of the Hayabusa2 samples returned from C-type asteroid Ryugu. Nature Astronomy, 6(2), 214–220. https://doi.org/10.1038/s41550-021-01550-6

Additional acknowledgements

Thanks to M. Velbel for help in formulating the sample choices and early scope of the study. We thank Z. Small and P. Mouroulis from the Jet Propulsion Laboratory (JPL) for their help in maintaining and troubleshooting the Ultra-Compact Imaging Spectrometer (UCIS). Thanks to A. Fraeman for acquiring a subset of the dataset and C. Herd, M. Garcia, and M. Wadhwa for help in obtaining samples to scan. Additionally, we thank F. DeMeo for her detailed correspondence on the asteroid classification methodology and help in this study by providing additional asteroid spectral data products to develop the modified processing pipeline.

This work was supported in part by NASA's Emerging Worlds program under Award Number #80NSSC18K0593 as well as NASA's Future Investigators in NASA Earth and Space Science and Technology (FINESST) program under Award Number #80NSSC22K1336.

Open Research

Part of the asteroid data utilized in this publication were obtained by the SMASS: Small Main-Belt Asteroid Spectroscopic Survey and published in Bus & Binzel, (2002). Part of the asteroid data utilized in this publication were obtained and made available by the MITHNEOS MIT-Hawaii Near-Earth Object Spectroscopic Survey. The IRTF is operated by the University of Hawaii under contract 80HQTR19D0030 with the National Aeronautics and Space Administration. The MIT component of this work is supported by NASA grant 80NSSC18K0849. Both SMASS and MITHNEOS data sets are available on the Planetary Spectroscopy at MIT website at: http://smass.mit.edu/home.html (directly from sidebar menu).

The RELAB spectra used were collected by (Cloutis, Hudon, et al., 2011; Cloutis, Hudon, Hiroi, & Gaffey, 2012a; Cloutis, Hudon, Hiroi, Gaffey, et al., 2012) and sourced from the University of Winnipeg Planetary Spectrophotometer Facility (PSF) and the NASA Reflectance Experiment LABoratory (RELAB) database, produced at Brown University, hosted by the PDS Geosciences Node at Washington

University in St. Louis, MO (Milliken, 2020). These data are available at https://pds-geosciences.wustl.edu/speclib/urn-nasa-pds-relab/data_reflectance/.

The code to correct UCIS image cubes, process both asteroid and chondrite spectra, and perform Principal Component analyses was designed using MATLAB Version 9.6.0.1072779 (R2019a, The MathWorks Inc., 2019). The code also includes a modified version of a MATLAB ENVI package and ENVI ROI reader script, redistributed with permissions under the Simplified BSD License. The joined visible/near-IR asteroid spectra and uncorrected carbonaceous chondrite image cubes prepared in this study are included as part of the code package that includes all MATLAB routines used to process the asteroid and chondrite spectra and perform the Principal Component Analysis presented in this study. Upon publication, the combined data and code package will be separately published on the CaltechDATA repository and accessible on GitHub under the MIT license.

Upon publication, the corrected chondrite image cubes collected with UCIS will be separately published on, and accessible from, the CaltechDATA repository.

6. Appendix

Table 4.3
The 371 asteroid spectra used in the original Expanded Bus-DeMeo taxonomy and in this study

Database ID	Asteroid Name	Asteroid Number	DeMeo et al. (2009) Class
a000001.sp41	Ceres	1	C
a000002.sp05	Pallas	2	B
a000003.sp21	Juno	3	Sq
a000004.sp02	Vesta	4	V
a000005.sp28	Astraea	5	S
a000007.sp28	Iris	7	S
a000008.sp17	Flora	8	Sw
a000010.sp28	Hygiea	10	C
a000011.sp47	Parthenope	11	Sq
a000013.sp41	Egeria	13	Ch
a000014.sp25	Irene	14	S
a000015.sp28	Eunomia	15	K
a000016.sp02	Psyche	16	Xk
a000017.sp07	Thetis	17	S
a000018.sp06	Melpomene	18	S
a000019.sp49	Fortuna	19	Ch
a000020.sp06	Massalia	20	S
a000021.sp31	Lutetia	21	Xc

a000022.sp55	Kalliope	22	X
a000024.sp45	Themis	24	C
a000025.sp03	Phocaea	25	S
a000026.sp08	Proserpina	26	S
a000027.sp31	Euterpe	27	S
a000028.sp09	Bellona	28	S
a000029.sp03	Amphitrite	29	S
a000030.sp02	Urania	30	S
a000032.sp03	Pomona	32	Sw
a000033.sp10	Polyhymnia	33	S
a000034.sp28	Circe	34	Ch
a000037.sp07	Fides	37	S
a000038.sp23	Leda	38	Cgh
a000039.sp07	Laetitia	39	Sqw
a000040.sp32	Harmonia	40	S
a000041.sp84	Daphne	41	Ch
a000042.sp06	Isis	42	K
a000043.sp48	Ariadne	43	Sq
a000048.sp45	Doris	48	Ch
a000049.sp24	Pales	49	Ch
a000050.sp23	Virginia	50	Ch
a000051.sp29	Nemausa	51	Cgh
a000052.sp52	Europa	52	C
a000054.sp19	Alexandra	54	Cgh
a000055.sp49	Pandora	55	Xk
a000056.sp31	Melete	56	Xk
a000057.sp14	Mnemosyne	57	S
a000058.sp24	Concordia	58	Ch
a000061.sp02	Danae	61	S
a000063.sp25	Ausonia	63	Sw
a000064.sp03	Angelina	64	Xe
a000065.sp25	Cybele	65	Xk
a000066.sp48	Maja	66	Ch
a000067.sp29	Asia	67	S
a000069.sp40	Hesperia	69	Xk
a000070.sp18	Panopaea	70	Cgh
a000073.sp26	Klytia	73	S
a000076.sp44	Freia	76	C
a000077.sp55	Frigga	77	Xe
a000078.sp46	Diana	78	Ch
a000082.sp08	Alkmene	82	S
a000084.sp24	Klio	84	Ch
a000085.sp24	Io	85	C

a000087.sp44	Sylvia	87	X
a000090.sp44	Antiope	90	C
a000092.sp02	Undina	92	Xk
a000093.sp22	Minerva	93	C
a000096.sp49	Aegle	96	T
a000097.sp45	Klotho	97	Xc
a000099.sp47	Dike	99	Xk
a000101.sp57	Helena	101	S
a000103.sp07	Hera	103	S
a000105.sp24	Artemis	105	Ch
a000106.sp24	Dione	106	Cgh
a000108.sp10	Hecuba	108	Sw
a000110.sp03	Lydia	110	Xk
a000111.sp31	Ate	111	Ch
a000114.sp52	Kassandra	114	K
a000115.sp10	Thyra	115	S
a000119.sp06	Althaea	119	S
a000128.sp24	Nemesis	128	C
a000130.sp05	Elektra	130	Ch
a000131.sp53	Vala	131	K
a000132.sp44	Aethra	132	Xe
a000133.sp06	Cyrene	133	S
a000147.sp24	Protogeneia	147	C
a000150.sp24	Nuwa	150	C
a000151.sp47	Abundantia	151	Sw
a000153.sp40	Hilda	153	X
a000158.sp21	Koronis	158	S
a000160.sp23	Una	160	Xk
a000170.sp06	Maria	170	S
a000175.sp47	Andromache	175	Cg
a000180.sp18	Garumna	180	Sr
a000181.sp25	Eucharis	181	Xk
a000188.sp12	Menippe	188	S
a000191.sp38	Kolga	191	Cb
a000192.sp50	Nausikaa	192	Sw
a000199.sp21	Byblis	199	D
a000201.sp28	Penelope	201	Xk
a000205.sp24	Martha	205	Ch
a000210.sp47	Isabella	210	Cb
a000214.sp33	Aschera	214	Cgh
a000216.sp15	Kleopatra	216	Xe
a000221.sp02	Eos	221	K
a000226.sp10	Weringia	226	S

a000233.sp18	Asterope	233	Xk
a000234	Barbara	234	L
a000236.sp50	Honoria	236	L
a000237.sp12	Coelestina	237	Sr
a000243.sp21	Ida	243	Sw
a000244.sp05	Sita	244	Sw
a000246.sp37	Asporina	246	A
a000250.sp26	Bettina	250	Xk
a000258.sp08	Tyche	258	S
a000264.sp41	Libussa	264	S
a000266.sp44	Aline	266	Ch
a000267.sp24	Tirza	267	D
a000269.sp40	Justitia	269	D
a000278.sp14	Paulina	278	S
a000279.sp35	Thule	279	D
a000288.sp18	Glauke	288	S
a000289.sp01	Nenetta	289	A
a000295.sp18	Theresia	295	Sw
a000308.sp39	Polyxo	308	T
a000322.sp18	Phaeo	322	D
a000337.sp18	Devosa	337	Xk
a000345.sp45	Tercidina	345	Ch
a000346.sp14	Hermentaria	346	S
a000349.sp06	Dembowska	349	R
a000352.sp06	Gisela	352	Sw
a000354.sp12	Eleonora	354	A
a000359.sp03	Georgia	359	Xk
a000371.sp07	Bohemia	371	S
a000378.sp12	Holmia	378	S
a000387.sp22	Aquitania	387	L
a000389.sp08	Industria	389	S
a000402.sp04	Chloe	402	L
a000403.sp22	Cyane	403	S
a000433.sp16	Eros	433	Sw
a000434.sp08	Hungaria	434	Xe
a000444.sp07	Gyptis	444	C
a000446.sp07	Aeternitas	446	A
a000453.sp07	Tea	453	Sw
a000456.sp15	Abnoba	456	S
a000460.sp15	Scania	460	L
a000485.sp10	Genua	485	S
a000512.sp32	Taurinensis	512	Sqw
a000513.sp05	Centesima	513	K

a000532.sp06	Herculina	532	S
a000570.sp28	Kythera	570	D
a000579.sp04	Sidonia	579	K
a000596.sp14	Scheila	596	T
a000599.sp04	Luisa	599	L
a000606.sp18	Brangane	606	L
a000625.sp04	Xenia	625	Sw
a000631.sp18	Philippina	631	S
a000653.sp21	Berenike	653	K
a000661.sp21	Cloelia	661	K
a000670.sp18	Ottegebe	670	S
a000673.sp06	Edda	673	L
a000675.sp12	Ludmilla	675	Sw
a000679.sp04	Pax	679	L
a000688.sp18	Melanie	688	C
a000699.sp35	Hela	699	S
a000706.sp49	Hirundo	706	Cgh
a000716.sp08	Berkeley	716	S
a000719.sp08	Albert	719	S
a000720.sp02	Bohlinia	720	Sq
a000729.sp07	Watsonia	729	L
a000739.sp18	Mandeville	739	Xc
a000742.sp21	Edisona	742	K
a000773.sp31	Irmintraud	773	T
a000776.sp38	Berbericia	776	Cgh
a000782.sp06	Montefiore	782	Sw
a000785.sp41	Zwetana	785	Cb
a000789.sp16	Lena	789	Xk
a000793.sp18	Arizona	793	S
a000808.sp07	Merxia	808	Sr
a000824.sp07	Anastasia	824	L
a000832.sp23	Karin	832	S
a000847.sp04	Agnia	847	S
a000863.sp09	Benkoela	863	A
a000908.sp53	Buda	908	D
a000913.sp07	Otila	913	Sw
a000925.sp18	Alphonsina	925	S
a000929.sp06	Algunde	929	S
a000944.sp31	Hidalgo	944	D
a000984.sp18	Gretia	984	Sa
a000985.sp40	Rosina	985	S
a001011.sp09	Laodamia	1011	Sw
a001020.sp21	Arcadia	1020	Sr

a001036.sp37	Ganymed	1036	S
a001065.sp37	Amundsenia	1065	S
a001094.sp21	Siberia	1094	Xk
a001126.sp04	Otero	1126	Sw
a001131.sp40	Porzia	1131	S
a001139.sp44	Atami	1139	Sw
a001143.sp42	Odysseus	1143	D
a001147.sp07	Stavropolis	1147	Sw
a001148.sp05	Rarahu	1148	K
a001198.sp19	Atlantis	1198	Sw
a001204.sp37	Renzia	1204	Sw
a001228.sp21	Scabiosa	1228	Sr
a001300.sp55	Marcelle	1300	Cgh
a001329.sp16	Eliane	1329	Sqw
a001332.sp42	Marconia	1332	L
a001350.sp06	Rosselia	1350	S
a001374.sp28	Isora	1374	Sq
a001433.sp16	Geramtina	1433	S
a001459.sp04	Magnya	1459	Vw
a001471.sp45	Tornio	1471	D
a001494.sp55	Savo	1494	Sqw
a001508.sp28	Kemi	1508	B
a001542.sp39	Schalen	1542	D
a001565.sp36	Lemaitre	1565	S
a001620.sp03	Geographos	1620	S
a001640.sp37	Nemo	1640	S
a001642.sp07	Hill	1642	S
a001658.sp03	Innes	1658	Sw
a001659.sp11	Punkaharju	1659	S
a001660.sp37	Wood	1660	S
a001662.sp21	Hoffmann	1662	Sr
a001667.sp19	Pels	1667	Sw
a001685.sp37	Toro	1685	Sq
a001751.sp06	Herget	1751	S
a001807.sp30	Slovakia	1807	Sqw
a001839.sp05	Ragazza	1839	S
a001848.sp07	Delvaux	1848	S
a001858.sp12	Lobachevskij	1858	S
a001862.sp47	Apollo	1862	Q
a001864.sp05	Daedalus	1864	Sq
a001866.sp56	Sisyphus	1866	Sw
a001903.sp21	Adzhimushkaj	1903	K
a001904.sp01	Massevitch	1904	V

a001916.sp07	Boreas	1916	Sw
a001929.sp04	Kollaa	1929	V
a001943.sp09	Anteros	1943	Sw
a001980.sp55	Tezcatlipoca	1980	Sw
a002035.sp19	Stearns	2035	Xe
a002042.sp08	Sitarski	2042	Sr
a002045.sp09	Peking	2045	V
a002063.sp41	Bacchus	2063	Sq
a002064.sp52	Thomsen	2064	Sqw
a002074.sp25	Shoemaker	2074	Sw
a002085.sp12	Henan	2085	L
a002099.sp45	Opik	2099	Ch
a002107.sp49	Ilmari	2107	Sw
a002157.sp21	Ashbrook	2157	S
a002246.sp39	Bowell	2246	D
a002335.sp46	James	2335	S
a002353.sp14	Alva	2353	S
a002354.sp21	Lavrov	2354	L
a002378.sp40	Pannekoek	2378	Cgh
a002386.sp15	Nikonov	2386	S
a002396.sp07	Kochi	2396	S
a002401.sp16	Aehlita	2401	S
a002442.sp17	Corbett	2442	V
a002448.sp21	Sholokhov	2448	L
a002501.sp09	Lohja	2501	A
a002504.sp22	Gaviola	2504	Sr
a002521.sp09	Heidi	2521	S
a002566.sp17	Kirghizia	2566	V
a002579.sp02	Spartacus	2579	V
a002715.sp07	Mielikki	2715	Sw
a002732.sp07	Witt	2732	L
a002851.sp08	Harbin	2851	V
a002873.sp09	Binzel	2873	Sq
a002875.sp11	Lagerkvist	2875	S
a002911.sp21	Miahelena	2911	Sw
a002912.sp04	Lapalma	2912	V
a002957.sp21	Tatsuo	2957	K
a002965.sp40	Surikov	2965	Sv
a002977.sp18	Chivilikhin	2977	S
a003028.sp17	Zangguoxi	3028	K
a003102.sp02	Krok	3102	Sqw
a003103.sp06	Eger	3103	Xe
a003122.sp27	Florence	3122	Sqw

a003155.sp06	Lee	3155	V
a003198.sp40	Wallonia	3198	Sqw
a003199.sp36	Nefertiti	3199	K
a003200.sp34	Phaethon	3200	B
a003248.sp39	Farinella	3248	D
a003255.sp17	Tholen	3255	S
a003317.sp50	Paris	3317	D
a003363.sp12	Bowen	3363	Sr
a003395.sp04	Jitka	3395	S
a003402.sp25	Wisdom	3402	S
a003430.sp15	Bradfield	3430	S
a003491.sp15	Fridolin	3491	S
a003511.sp12	Tsvetaeva	3511	Srw
a003628.sp50	Boznemcova	3628	O
a003635.sp47	Kreutz	3635	Srw
a003701.sp07	Purkyne	3701	S
a003734.sp08	Waland	3734	L
a003753.sp45	Cruithne	3753	Q
a003788.sp21	Steyaert	3788	S
a003844.sp22	Lujiaxi	3844	L
a003858.sp28	Dorchester	3858	Srw
a003873.sp19	Roddy	3873	Sw
a003903.sp17	Kliment Ohridski	3903	S
a003908.sp30	Nyx	3908	V
a003910.sp16	Liszt	3910	S
a003920.sp17	Aubignan	3920	Sqw
a003949.sp08	Mach	3949	Sq
a004038.sp19	Kristina	4038	Vw
a004055.sp38	Magellan	4055	V
a004179.sp30	Toutatis	4179	Sq
a004188.sp07	Kitezh	4188	V
a004197.sp25	1982 TA	4197	Sq
a004352.sp15	Kyoto	4352	S
a004407.sp08	Taihaku	4407	Sqw
a004417.sp08	Lecar	4417	Sw
a004451.sp09	Grieve	4451	Svw
a004558.sp29	Janesick	4558	Sr
a004570.sp06	Runcorn	4570	Sw
a004688.sp03	1980 WF	4688	Q
a004713.sp12	Steel	4713	Sw
a004737.sp15	Kiladze	4737	L
a004995.sp19	Griffin	4995	S
a005013.sp09	Suzhousanzhong	5013	Sw

a005111.sp44	Jacliff	5111	V
a005143.sp55	Heracles	5143	Q
a005230.sp44	Asahina	5230	S
a005261.sp41	Eureka	5261	Sa
a005379.sp51	Abehiroshi	5379	Sr
a005401.sp21	Minamioda	5401	Sw
a005407.sp09	1992 AX	5407	S
a005587.sp05	1990 SB	5587	Sr
a005604.sp05	1992 FE	5604	V
a005641.sp38	McCleese	5641	Sw
a005660.sp43	1974 MA	5660	Q
a005685.sp05	Sanenobufukui	5685	S
a005817.sp31	Robertfrazer	5817	Sr
a005840.sp08	Raybrown	5840	L
a006047.sp45	1991 TB1	6047	S
a006239.sp27	Minos	6239	Sqw
a006386.sp36	Keithnoll	6386	S
a006411.sp28	Tamaga	6411	B
a006455.sp19	1992 HE	6455	Srw
a006585.sp55	O'Keefe	6585	S
a007341.sp11	1991 VK	7341	Q
a007763.sp14	Crabeels	7763	L
a008334.sp21	1984 CF	8334	S
a008444.sp25	Popovich	8444	S
a017274.sp02	2000 LC16	17274	D
a018736.sp03	1998 NU	18736	Sw
a019127.sp25	Olegefremov	19127	Srw
a019356.sp03	1997 GH3	19356	Sq
a020786.sp25	2000 RG62	20786	Sq:
a020790.sp03	2000 SE45	20790	S
a022771.sp26	1999 CU3	22771	S
a024475.sp05	2000 VN2	24475	Sw
a025330.sp19	1999 KV4	25330	Xk:
a035107.sp20	1991 VH	35107	Sq
a036284.sp11	2000 DM8	36284	K
a053435.sp55	1999 VM40	53435	Srw
a054690.sp05	2001 EB	54690	S
a066146.sp25	1998 TU3	66146	Q
a086450.sp03	2000 CK33	86450	L
a086819.sp02	2000 GK137	86819	Sq
a089355.sp12	2001 VS78	89355	Sr
a098943.sp33	2001 CC21	98943	Sw
a099907.sp19	1989 VA	99907	Sr

a137062.sp19	1998 WM	137062	Sr
a138258.sp11	2000 GD2	138258	Sq
a162058.sp26	1997 AE12	162058	Q
a162781.sp03	2000 XL44	162781	S
au2000PG3.sp01		2000PG3	D
au2001TX16.sp11		2001TX16	X
au2001XN254.sp12		2001XN254	S
au2002AA.sp09		2002AA	S
au2002AV.sp09		2002AV	S

Note. Spectral data were sourced from the SMASS: Small Main-Belt Asteroid Spectroscopic Survey and the MITHNEOS MIT-Hawaii Near-Earth Object Spectroscopic Survey.